8-2009

Electron Beam Induced Etching

Matthew Gordon Lassiter

To the Graduate Council:

I am submitting herewith a dissertation written by Matthew Gordon Lassiter entitled "Electron Beam Induced Etching." I have examined the final electronic copy of this dissertation for form and content and recommend that it be accepted in partial fulfillment of the requirements for the degree of Doctor of Philosophy, with a major in Materials Science and Engineering.

Philip Rack, Major Professor

We have read this dissertation and recommend its acceptance:

David Joy, David Keffer, Thomas Meek, James Morris

Accepted for the Council:
Dixie L. Thompson

Vice Provost and Dean of the Graduate School

(Original signatures are on file with official student records.)

To the Graduate Council:

I am submitting herewith a dissertation written by Matthew Gordon Lassiter entitled “Electron Beam Induced Etching.” I have examined the final electronic copy of this dissertation for form and content and recommend that it be accepted in partial fulfillment of the requirements for the degree of Doctor of Philosophy, with a major in Materials Science and Engineering.

Philip Rack, Major Professor

We have read this dissertation and recommend its acceptance:

David Joy

David Keffer

Thomas Meek

James Morris

Accepted for the Council:

Carolyn R. Hodges
Vice Provost and Dean of the Graduate School

(Original signatures are on file with official student records.)

Electron Beam Induced Etching

A Dissertation
Presented for the
Doctor of Philosophy
Degree
The University of Tennessee, Knoxville

Matthew Gordon Lassiter
August 2009

Dedication

For Missy

Acknowledgments

To my Lord and God for graciously giving me the wisdom and the means to pursue my graduate education. To my wife, Missy, for patiently standing by me and encouraging me. To my children, Zachary and Samuel, for love and obedience. To my parents, Clyde and Pam Lassiter, and my wife's parents, David and Nancy Woolard, for guidance and support. To the committee members for taking the time to read and advise on this dissertation. To Professor Philip Rack for stepping out on a limb to bring my family to Knoxville, and for guiding my research and forming me into a better scientist.

Abstract

The mechanisms of electron beam induced etching have been studied both experimentally and theoretically. Specifically, a steady-state and a time-dependent continuum model of the process have been developed which uniquely includes the effect of the etch product desorption and diffusion. Both analytical and numerical methods were employed for the modeling, and various experimental designs were used for validation. Initially, a steady-state model was developed to understand an observed so-called “moat” profile which could adequately be described by a finite etch product surface residence time. Subsequently a thorough time-dependent model was written to investigate scanning parameter effects on EBIE. A design of experiments was performed to validate the model and to extract the fundamental parameters for the etching of silica by xenon difluoride. Finally, two technical applications were explored: spontaneous etching passivation on Ta-based extreme ultraviolet lithography masks and carbon nanotube etching.

Table of Contents

List of Figures

Chapter 1: Literature Review

Overview

The nanoscale deposition of material by an electron beam induced reaction has been studied in greater detail than the etching of material. Fortunately, the physical processes are very similar and so most of the literature regarding the deposition processes is applicable to etching.

The electron beam induced etching process involves the adsorption of a gas phase precursor on the surface of the substrate. During exposure of the surface by the electron beam, there is a probability that the impinging primary electrons or the subsequent secondary electrons will cause the otherwise stable, physisorbed precursor to dissociate and react with the surface atoms. In order to accomplish etching, the product(s) of said reaction need to be volatile species. Once these products desorb from the surface, new bulk material is revealed as surface, providing new adsorption sites for precursor gas molecules to repeat the process and etch the material. The primary advantage of electron beam induced etching is that it is site selective to the locations of beam exposure, and because the focused electron beam offers high spatial resolution potential, there is potential for high resolution of the etched feature.

In order to understand the etching process as a whole it is necessary to review the existing relevant literature on the topics of adsorption, surface diffusion, electron probes, electron-solid interactions, and process continuum modeling. This chapter examines some of the most relevant literature to the work of this dissertation.

Thermodynamics of Adsorption and Surface Diffusion

The electron beam induced etching process requires adsorption of gas molecules onto the surface of the substrate to be etched. It is worthwhile to investigate the kinetics of adsorption and desorption as they form the basis of the existing continuum models[1,2]. The Langmuir adsorption model is based on a surface containing equivalent adsorption sites of density Z. The adsorption sites can contain only one adsorbed gas molecule, and there is no interaction between adsorbed molecules, only interaction with the surface is possible[3]. The rate of adsorption of the gas molecules is proportional to the molecular impingement rate (I) times a sticking coefficient (g). If a site is already full, the impinging gas molecule will not adsorb onto the surface[4].

$$\frac{dN}{dt} = gI\left(1 - \frac{N}{Z}\right)$$

where N is the surface concentration of adsorbed gas. The molecular impingement rate is a function of the local pressure (p), the mass of the impinging molecule (m), and the temperature (T)[5]:

$$I = \frac{p}{\sqrt{2\pi mkT}}$$

where k is the Boltzmann constant. The gas is bound to the surface due to an interaction potential with the atoms on the surface and near the surface of the solid. The potential acting on the adsorbed gas is due to the sum of the potentials of the interactions with each of the atoms in the solid. The interaction potential in the z direction normal to the surface takes on a shape similar to that described by the Lennard-Jones Potential[6] (see Figure 1).

The gas desorbs from the surface and returns to the gas phase by random thermal fluctuations that give an adsorbed molecule enough kinetic energy to overcome the binding energy from the molecule-surface interaction. The Boltzmann statistics give an average residence time on the surface (τ):

$$\tau = \frac{1}{\nu_0} e^{\frac{E_{ads}}{kT}}$$

where ν_0 is the lattice vibrational frequency (typically on the order of $10^{12}s^{-1}$) and E_{ads} is the binding energy due to the molecule surface interaction. So, a van der Waals interaction with a binding energy of 0.1eV has an average residence time of only $5.5x10^{-11}$ seconds at room temperature. 1.0eV adsorption energy results in a residence time of $2.4x10^{5}$ seconds at room temperature. The point being there is a large variation in residence time depending upon the interaction forces between adsorbed species and surface. Likewise, a large variation due to temperature can result. In the above example, the 0.1eV residence time can be increased to 1 sec by reducing the temperature to ~43K or the 1.0eV residence time can be reduced to 1 sec by increasing the temperature to ~434K[7]. The rate of desorption from the surface is then:

$$\frac{dN}{dt} = -\frac{N}{\tau}$$

Combining the adsorption and desorption rates gives the detailed balance rate equation:

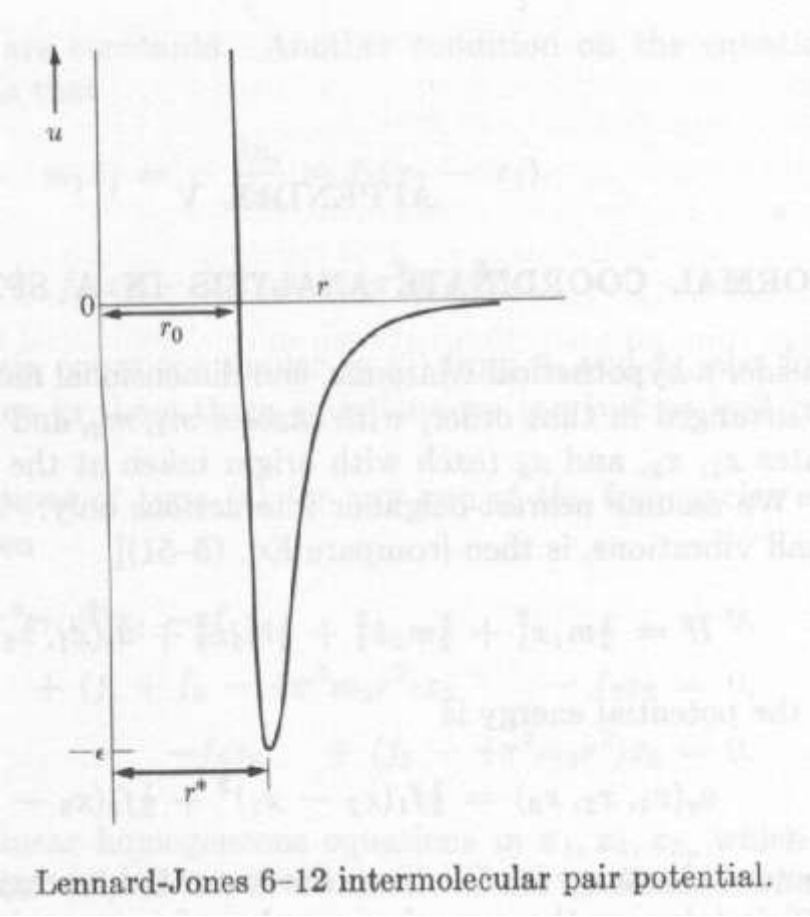

Lennard-Jones 6–12 intermolecular pair potential.

Figure 1: The Lennard-Jones Potential

$$\frac{dN}{dt} = gI\left(1 - \frac{N}{Z}\right) - \frac{N}{\tau}$$

In equilibrium, the surface concentration reaches a steady state:

$$N = \frac{gI}{\frac{gI}{Z} + \frac{1}{\tau}}$$

For small impingement rates (i.e. low pressures) or small residence times such that $(gI/Z) << (1/\tau)$, the surface concentration reduces to:

$$N = gI\tau$$

This is commonly known as Henry Adsorption. The adsorbed gas concentration increases linearly with pressure. When the pressure increases sufficiently high or the residence time is sufficiently large such that the condition $(gI/Z) >> (1/\tau)$ is met, then the surface concentration of adsorbed species approaches Z. Configurational entropy dictates that some sites must be empty for all T>0. As long as the condition $(gI/Z) >> (1/\tau)$ is maintained, the adsorption site coverage level is essentially unity and independent of pressure or temperature[8]. The relationship between pressure, temperature, and surface coverage is illustrated by the Figure 2.

For a given temperature (Isotherm), the coverage initially increases linearly with pressure and then approaches unity asymptotically. For a given pressure (Isobar), the coverage approaches unity below a critical temperature then decreases for increasing temperature. In order for efficient deposition or etching rates to occur, it is desirable to have as high a surface coverage of precursor gas as possible. For this to happen, the condition $(gI/Z) >> (1/\tau)$ must be met. If the residence time of the precursor gas is small, the pressure (i.e. molecular flux) must be increased as much as necessary to reach the desired coverage level.

An eigenanalysis[9] of the single ordinary differential equation gives a single real eigenvalue:

$$\lambda_1 = -\left(\frac{gI}{Z} + \frac{1}{\tau}\right)$$

Inspection reveals that the eigenvalue is always negative; therefore the steady state solution is a stable critical point. The general analytical solution to the ordinary differential equation is:

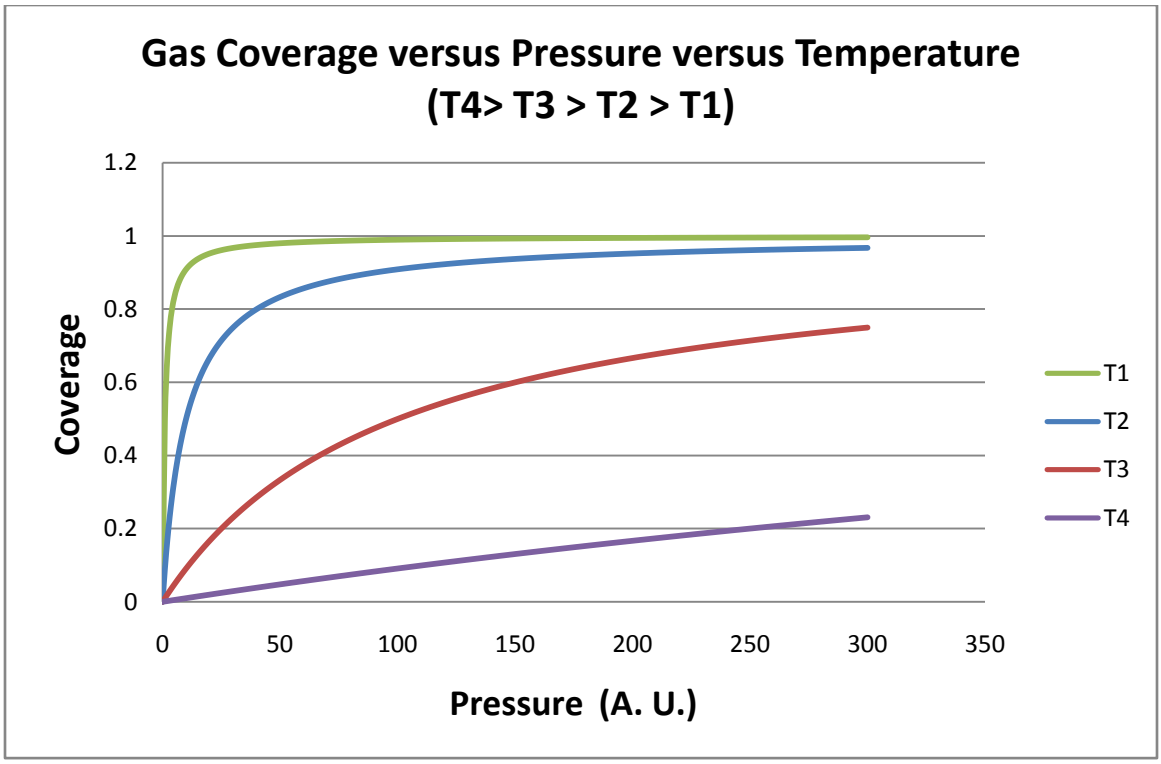

Figure 2: Effect of Temperature and Pressure on Surface Coverage of Adsorbed Gas

$$N(t) = \alpha + \beta e^{\lambda_1 t} = \frac{gI}{\left(\frac{gI}{Z} + \frac{1}{\tau}\right)} + \left(N_0 - \frac{gI}{\left(\frac{gI}{Z} + \frac{1}{\tau}\right)}\right) e^{-\left(\frac{gI}{Z} + \frac{1}{\tau}\right)t}$$

The transient behavior of this system is of interest regarding the gas refresh during the scanning of the electron beam or pulsing of the beam for area etching and spot mode etching, respectively. While the beam probes an area, the precursor gas is depleted, and after the beam moves away the gas refreshes toward the equilibrium concentration. The gas parameters can have a big impact on the amount of refresh time required to return to equilibrium during the beam refresh. Petzold and Heard quantified the importance of beam refresh time during Ga^+ focused ion-beam induced deposition, and noted that the efficiency of deposition is heavily dependent on the refresh time[10]. Too short a refresh time and the gas does not refresh enough for significant deposition during subsequent beam dwell. Too long of a refresh time and there is wasted process time and the overall deposition rate is sub-optimal. The effects of refresh and dwell time are covered more extensively later in this review. Also, the transient behavior of the system is of interest when considering the presence of residual gases on the surface of the substrate after the gas injection system has been shut down and the molecular impingement rate is essentially zero. If the residence time is large and the surface concentration started large, the precursor gas concentration could remain high for a significant amount of time, resulting in potentially adverse effects from subsequent e-beam imaging in the system. This was investigated by Lassiter *et al*[11] and the effect of a long residence time was used to protect the sidewalls of an etched feature from further etching during subsequent edits.

The adsorption sites are separated in the x any y directions by potential energy barriers due to the interaction between the adsorbed molecule and the various surface and near surface atoms. The figure below from Hill (Figure 3) illustrates the potential barrier between adsorption sites due to the sum of the interactions between adsorbed gas and solid atoms[12].

If during thermal fluctuation an adsorbed species acquires enough kinetic energy to overcome the inter-site potential barrier, it can jump to a neighboring empty site. The jump frequency follows an Arrhenius relationship with temperature:

$$\upsilon_{sd} = \upsilon_0 A e^{-\frac{E_{sd}}{kT}}$$

where ν_0 is the x- or y-direction vibrational frequency (typically on the order of 10^{12} s^{-1}), E_{sd} is the potential barrier between adsorption sites, and A is some weak temperature dependence factor[13]. The surface diffusion coefficient for a nearest neighbor jumping mechanism is calculated by:

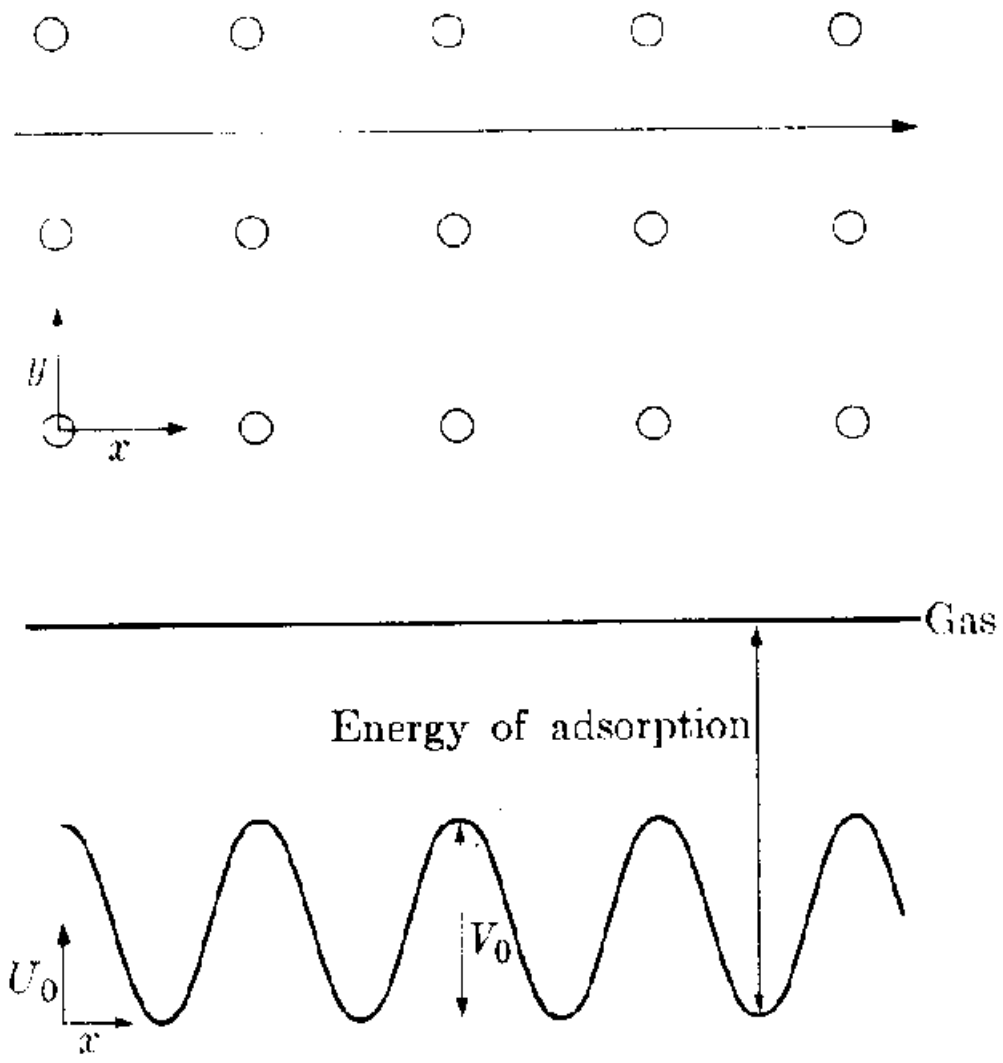

Figure 3: Surface Adsorption Energy Diagram with Diffusion Energy Barrier (V_0)

$$D_s = \frac{1}{4}\alpha^2 \upsilon_{sd}$$

where α is the jump distance and the (1/4) factor is related to the two degrees of freedom in two dimensions (x and y) for surface diffusion[14]. Fick's Second Law gives the relationship between the temporal rate of change of concentration and the spatial distribution of the concentration:

$$\frac{\partial N}{\partial t} = \nabla[D_s \nabla N] = \nabla D_s \nabla N + D_s \nabla^2 N$$

For the case where the diffusion coefficient is not a function of concentration (as in the dilute nearest neighbor jumping mechanism described above), the spatial gradient of D_s is zero and only the second term containing the Laplacian is relevant.

Regarding electron-beam induced chemistry, surface diffusion can affect the shape of the deposit or etch by enhancing the arrival of precursor above that which is adsorbing from the gas phase to the depleted region under the e-beam[15]. Also, surface diffusion can be the dominating refresh mechanism versus molecular impingement, thereby affecting the optimum refresh time for scanning- or pulsed-beam processing.

Electron Probe Shape

In order to understand electron-beam induced chemistry, it is useful to have an understanding of the factors affecting the shape of the beam as it comes into contact with the surface of the substrate. The beam electrons are generated by a source at the top of the column. The electron source can be any of three types: thermal emission, thermal field emitter (Schottky), or cold field emitter. The mechanisms for each emission are different, but the most relevant difference is the relative brightness difference between each of the three types of electron sources.

Thermal emitters generally are the least expensive of the three types. Electrons are emitted by elevating the temperature of a metal (W is ~3000K) until enough electrons are able to overcome the work function of the metal and leave into the vacuum. The Richardson-Dushman equation describes the current density emitted from a metal as a function of its work function (φ) and temperature[16].

$$J_c = A_c T^2 e^{-\frac{\varphi}{kT}}$$

where A_c is a constant. A field generated from a Wehneldt cylinder focuses the electrons emitted from the filament. The focused spot of emitted electrons becomes the virtual source; it is the object that is demagnified by the condenser and objective lenses in the column to form the electron probe. See Figure 4 from Goldstein *et al*.

A second type of electron source is the Schottky thermal field emitter. This type of emitter uses a tungsten tip nano-machined to a fine point (usually using focused ion beam milling) and coated with zirconium oxide to lower the work function. Electrons are emitted by applying a potential to the filament. The field is strongest at the point of the tip. Here the work function is lowered and the temperature of the filament is raised (~1700K) until there is significant thermal emission at the tip, but elsewhere on the filament there is virtually zero emission. This has the advantage of creating a very small source of electrons and does not require refocusing the emitted electrons into a virtual source. Figure 5 is a picture of a spent thermal field emitter from the Hitachi-4300 SEM at The University of Tennessee that has curled onto itself at the end of its lifetime.

The third source type is the field emitter. This is also a finely machined tip, but the mechanism of emission is different. The electric field at the surface is strong enough to allow for sufficient quantum tunneling through the work function potential barrier into the vacuum. Once the emitted electron is in the vacuum, it is accelerated away from the surface by the electric field. There is no heating of the tip, so it is often referred to as a cold field emitter. Figure 6 illustrates the three different types of sources and their respective emission mechanisms.

A major factor in the shape of the electron probe is the brightness of the source. Brightness is defined as the amount of current per area per solid angle. So, the brightness (β) of a spot of electrons impinging on (or emitting from) a surface in a circle of diameter (d) by a cone of angle (α) from normal is:

$$\beta = \frac{i_B}{\left(\frac{\pi}{4}d^2\right)(\pi\alpha^2)} = \frac{4i_B}{\pi^2 d^2 \alpha^2}$$

The brightness is controlled by the source and conserved by the lens. A minimum beam current is required to maintain a signal over the random noise of the detection system; so for a given beam current and solid angle, the spot size can be reduced by increasing the brightness of the system.

Envision the emitted electrons from the source with a kinetic energy normal to the surface controlled by the acceleration voltage (eV_{acc}) and the tangential kinetic energy governed by temperature (kT). The cone projected by these electrons has solid angle equal to ($\pi kT/eV_{acc}$). The maximum brightness of the electron source is thus[17]:

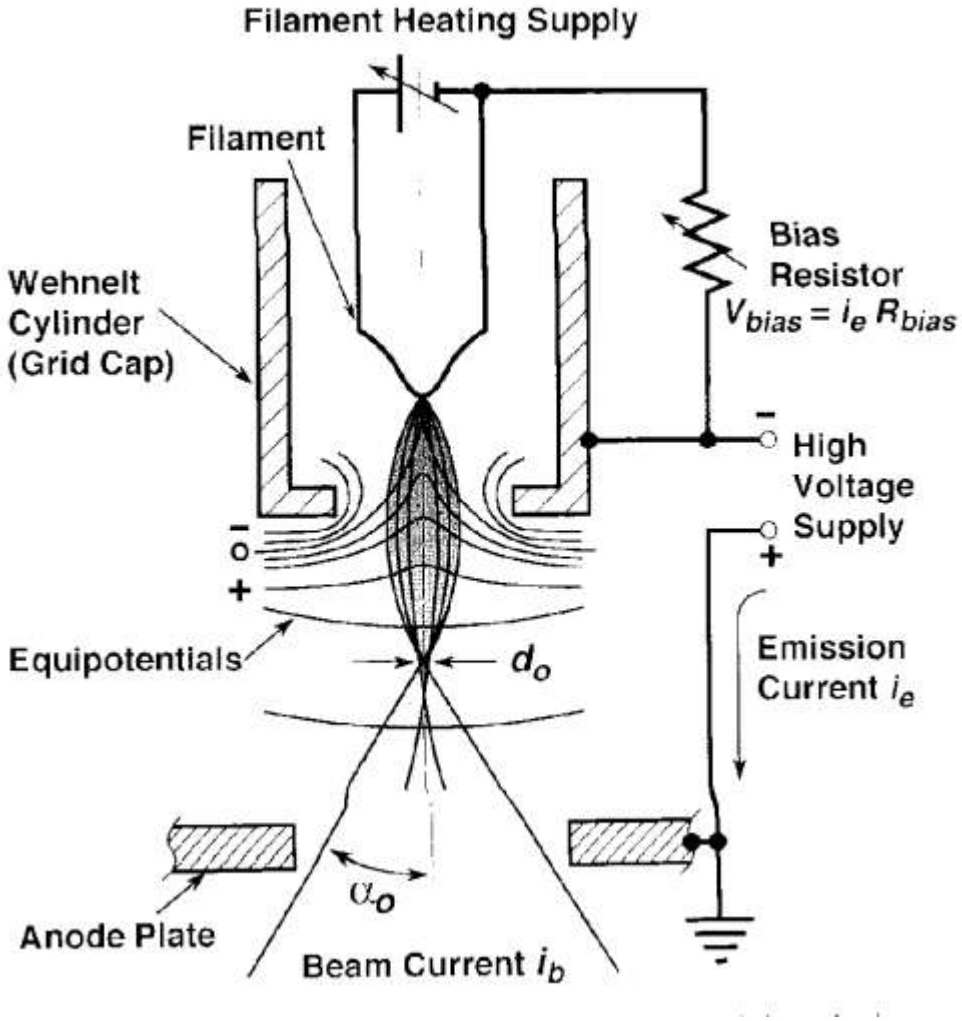

Figure 4: Thermal Emission Electron Source

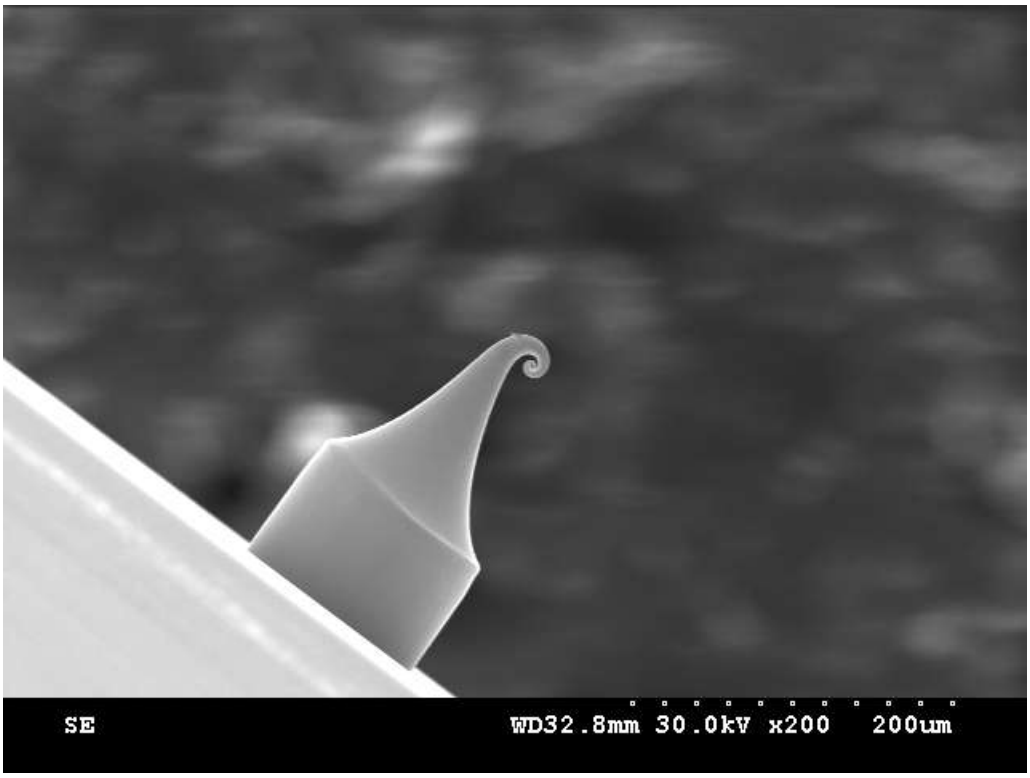

Figure 5: Used Thermal Field Emitter (Spiraled Tip is a defect)

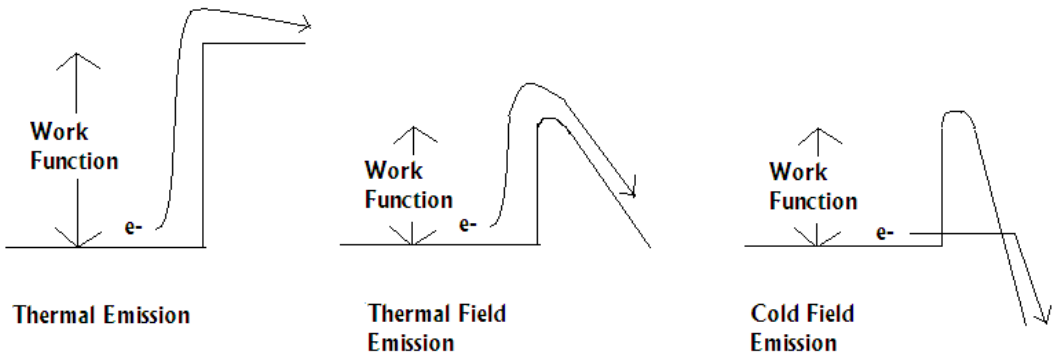

Figure 6: Energy Diagram Comparison of the Electron Emission

$$\beta_{max} = \frac{JeV_{acc}}{\pi kT}$$

In order to increase brightness, the accelerating voltage is increased and/or the temperature is decreased. The thermal emission source operates at about 3000K, while Schottky thermal field emitters operate at a much lower temperature around 1700K, and cold field emitters are generally at room temperature. Thus, for a given accelerating voltage the brightness of the thermionic emitter is least and the cold field emitter is highest. Generally, the Schottky thermal field emitter is the source of choice due to the fact that cold field emitters are limited in the maximum beam current possible, and they require more maintenance during operation due to adsorption of gases on the cold field emitter.

In an aberration free lens, the beam size would only be limited by the current requirement. The brightness equation can be rearranged and substitution used to arrive at:

$$d_\beta = \sqrt{\frac{4i_B}{\pi^2\alpha^2\beta}} = \sqrt{\frac{4i_B kT}{\pi\alpha^2 JeV_{acc}}}$$

The condenser lens can be focused to change the amount of current passing through the limiting aperture. Driving the current towards zero reduces the beam spot size at the sample. For the microscopist, there is a minimum beam current needed to overcome the random noise in the detection system. Therefore given a minimum beam current requirement, increasing the current density of the electron source (J), the accelerating voltage (V_{acc}), or the convergence angle (α) are the options for decreasing the spot size of the electron probe. The current density in the Schottky thermal field emitter is controlled by adjusting the electric field at the tip, but it is limited by the maximum mechanical stress the tip can handle and is generally fixed by the manufacturer during the tip start-up routine. The accelerating voltage gives the microscopist a chance to significantly lower the probe size, but the beam range in the sample can provide significant drawbacks to moving to higher accelerating voltages. The convergence angle (α) is adjustable by changing limiting apertures and by the working distance from the lens. While increasing the convergence angle improves the brightness-limited spot size, real electron lenses have aberrations that limit the imaging performance with increasing convergence angles.

In real charged particle lenses, there exists a deviation from ideal in the radial direction of magnetic field such that electrons of the same energy entering the lens at a larger radius from the center of the lens are focused at a different length than electrons

entering the lens closer to the center. This effect is known as spherical aberration from its analog in photon optics. The variation in focal lengths increases with increasing convergence angle and there is a disc of least confusion that results in a spreading of each point source at the sample.

The size of the minimum disc can be derived to[18]:

$$d_{sph} = \frac{1}{2} C_s \alpha^3$$

where C_S is the spherical aberration coefficient in units of length. The value of C_S is roughly proportional to and is similar in magnitude to the focal length of the lens. The effect of spherical aberration can be reduced by decreasing the convergence angle (α) the electrons on the sample (Figure 7).

Electrons passing through the lens with variation in energy will be focused at different focal lengths. This effect, known as chromatic aberration from its optical counterpart, gives another disc spreading point sources. The size of the disc due to chromatic aberration is[19]:

$$d_{chr} = C_C \left(\frac{\Delta E}{e V_{acc}} \right) \alpha$$

Figure 8 illustrates how the chromatic aberration improves by decreasing the beam convergence angle. As the accelerating volt increases, the effect of chromatic aberration is reduced. As with spherical aberration, the magnitude of the chromatic aberration coefficient is on the order of the focal length.

The wave nature of the electron means that diffraction effects are possible when considering small apertures. The wavelength (λ) of the electron can be calculated from the momentum of the particle[20] (p):

$$\lambda = \frac{h}{p}$$

where h is the Planck constant. Ignoring relativistic effects of very fast electrons (>30keV) approaching the speed of light, the momentum can be calculated classically from:

$$E = \frac{p^2}{2m} = e V_{acc}$$

Substitution of the momentum, mass, and fundamental charge of the electron results in the relationship between accelerating voltage and wavelength in nanometers:

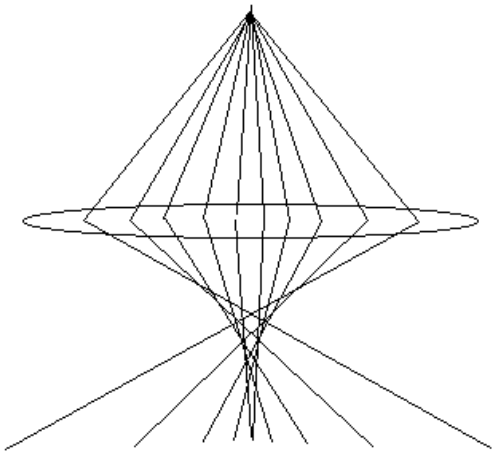

Figure 7: Spherical Aberration

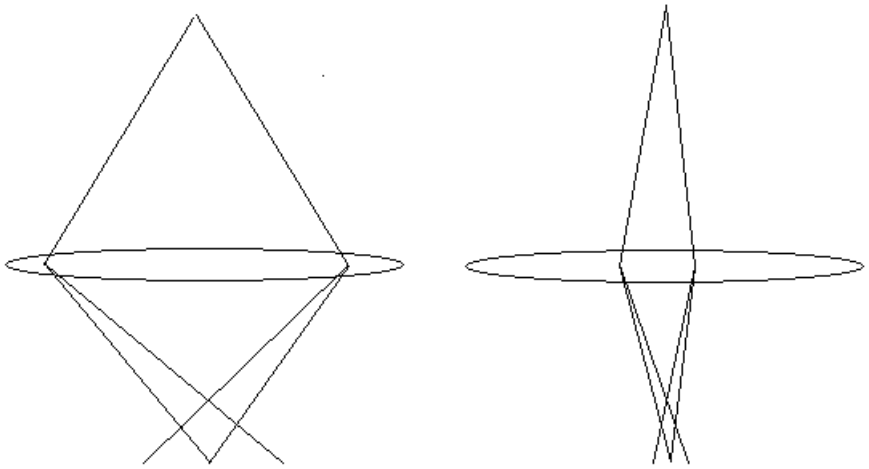

Figure 8: Illustration of Chromatic Aberration Increasing with Angle

$$\lambda = \frac{1.226\, V^{0.5} nm}{\sqrt{V_{acc}}}$$

The electron passing through the lens column is diffracted in the far field and the limiting aperture acts as a low-pass filter in the frequency domain, resulting in the probability distribution of the location of the electron at the sample taking on an Airy disc shape[21]. The full width half maximum of the Airy disc is taken as the contribution of diffraction to the probe size[22]:

$$d_{diff} = \frac{0.61\lambda}{\alpha} = \frac{0.75 V^{0.5} nm}{\alpha\sqrt{V_{acc}}}$$

The effect of diffraction on the probe size can be minimized by increasing the accelerating voltage and the convergence angle.

There is debate within the community on the proper definition of the size of a beam given the fact that shape can vary widely[23]. Many have used the full width half maximum (FWHM) is the past, but this could vary widely for beams of different profiles. For example, a cylinder shaped beam and a Gaussian shaped beam with the same FWHM, could have wildly different peak electron fluxes. The width of fractional content (d_{FCXX}) is proposed where XX is the percentage of the total beam current contained within the diameter of d_{FCXX}. d_{FC50} is likely a better measurement for use in quantifying the size of diffraction or aberration disc[24], though there is not an apparent accepted standard.

The final beam size is due to a two-dimensional convolution of the initial beam shape (the demagnified source) with the lens aberration point spread functions, spherical and chromatic, as well as convolution with the Airy disc diffraction pattern[25]. While other summation methods[26] have been used for the purposes of determining the beam diameter at the sample surface, the quadrature sum of the various discs' diameters is sufficient to estimate the effect of the two-dimensional convolution on the final probe diameter.

$$d_{beam} = \sqrt{{d_\beta}^2 + {d_{sph}}^2 + {d_{chr}}^2 + {d_{diff}}^2}$$

$$d_{beam} = \sqrt{\frac{4 i_B kT}{\pi\alpha^2 J e V_{acc}} + \left(\frac{1}{2} C_s \alpha^3\right)^2 + \left(C_C \left(\frac{\Delta E}{e V_{acc}}\right)\alpha\right)^2 + \frac{0.56[V nm^2]}{\alpha^2 V_{acc}}}$$

Increasing the accelerating voltage reduces the beam size, but as is discussed later, the size of the interaction of high energy electrons in the specimen ultimately limits the imaging resolution. At times it is desirable to use a small accelerating voltage (~1000V) to limit the beam interaction volume to the surface of the specimen. The result is a large diffraction limited disc and large chromatic aberrations.

It can be seen that with regards to the selection of the beam convergence angle, the chromatic and spherical aberrations act in opposition with electron diffraction for the final beam spot size. Optimization is required to minimize the beam size and thus achieve the highest possible spatial resolution. For high beam currents, the size is brightness limited by the first term in the radical. Lowering the beam current for a fixed convergence angle, by adjusting the condenser lens, results in a smaller spot size until the dominant aberration(s) are reached. Further lowering of the beam current has little impact on the beam spot size. David Joy published on the use of complex aberration correctors to reduce the C_S and C_C values to the order of a few micrometers[27]. The result is an ability to increase the beam convergence angle (α), which results in a reduction of the diffraction effect on the beam size and makes a higher beam current possible.

Electron-Solid Interaction

As an energetic electron interacts with a solid, it is scattered by the positive charges in the nuclei of the solid atoms. The scattering can be elastic, resulting in only a directional change with no loss in kinetic energy, or it can be an inelastic scattering event where some of the kinetic energy of the electron is converted to secondary electrons, photons, and phonons. The probability of elastic scattering is proportional to the square of the atomic number of the solid atoms. That is, the higher the atomic number, the larger the positive charge in the nucleus, and thus, the stronger attractive force on the electron. The probability of scattering is also proportional to the inverse square of the electron's energy, so electrons moving rapidly are scattered less than slower moving electrons. Effectively, the electron has less time to interact with the nucleus as it passes in its vicinity, resulting in less scattering. The cross-section of elastic scattering is described mathematically by Goldstein *et al* as[28]:

$$Q(>\phi_0) = 1.62 \times 10^{-20} \frac{Z^2}{E^2} \cot^2 \frac{\phi_0}{2}$$

This is the likelihood of scattering at an angle greater than ϕ_0. At higher scattering angles, there is a lower probability of scattering to that angle. The result of the various scattering angles across multiple scattering events is that some of the incident electrons exit the solid and return to the vacuum. These are known as back-scattered electrons

(BSE) and they are often emitted at large distances from the point where they enter the substrate comparatively to the electron probe size. This is often the reason why the imaging resolution in the SEM is much poorer than the calculated probe size. In regards to electron induced surface chemistry, these BSE can cause the deposition or etching events and therefore have an impact on the shape and rate of the deposit or etch.

At the same time the velocity direction of the electron is being scattered, the velocity magnitude is being reduced as energy from the electron is converted into other forms. Bethe is known among many things for describing the amount of energy lost per unit distance traveled in the solid[29].

$$\frac{dE}{ds} = -7.85 \times 10^4 \frac{Z\rho}{AE} \ln\left(\frac{1.166E}{10^{-3}(9.76Z + 58.5Z^{-0.19})}\right)$$

E is described in units of keV, distance s in terms of cm, Z is the unitless atomic number of the solid material, ρ is the density in g/cm^3, and A is the atomic mass in g/mol. Increasing the atomic number (Z) or the number density of the solid (ρ/A) increases the energy lost per distance traveled of an energetic electron. The total distance travelled in the solid can be approximated by integrating the Bethe equation from the incident electron energy to a small energy threshold. The larger the incident electron energy the further the electron will travel through the solid.

$$s_{Bethe} \approx \int_{E_{th}}^{E_0} \left(\frac{dE}{ds}\right)^{-1} dE$$

The inelastic events that slow the primary electron include conversion to heat, photons, and secondary electrons. The secondary electrons are loosely bound electrons that are knocked free by the beam electrons as they inelastically collide with the solid atoms. While secondary electrons are generated along the entire primary electron path, only the secondary electrons that are generated close to the surface can be emitted from the surface. After a secondary electron is generated, it undergoes inelastic collisions with the solid atoms, so only secondary electrons generated within a few path lengths from the surface are able to be emitted, otherwise they are thermallized[30]. The following figure (Figure 9) from Goldstein *et al* illustrates this effect[31]. For the purpose of electron beam induced surface chemistry, the lower energy secondary electrons are likely more efficient at dissociation of the precursor than the higher energy primary and backscattered electrons[32].

The secondary electron emission yield increases for decreasing primary beam energy due to the fact that the primary electrons are scattered in a shorter range from the surface. There are less total secondary electrons generated, but more are generated in

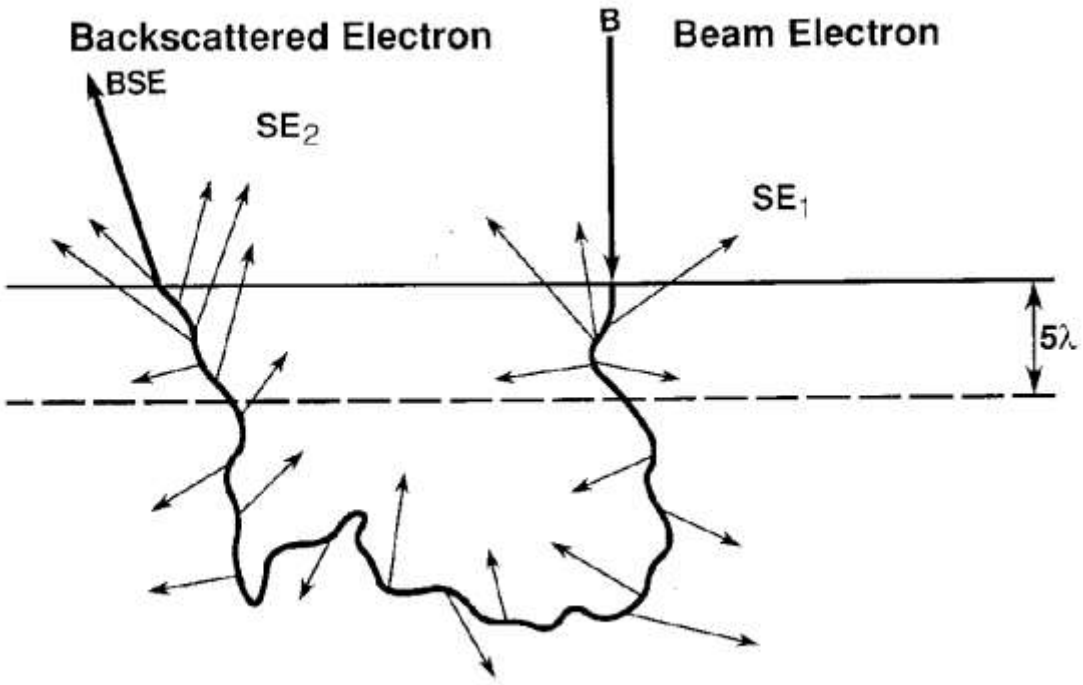

Figure 9: Primary (B), Backscattered (BSE), and Secondary (SE) Electron Emissions

a range where they could escape the solid. The range of backscattered electrons and their secondary electrons has an impact on the shape of the deposit or etch.

Process Simulation

There has been much published in the literature regarding the simulation of electron beam induced processes, mostly regarding deposition. These simulations generally fit into one of two categories: Monte-Carlo based and Continuum models.

The Monte-Carlo simulations simulate individual electron trajectories through the specimen, calculating and tracking secondary electrons and backscattered. Simultaneously, they track the precursor gas dynamics on the surface. When a primary, secondary, or backscattered electron encounters a precursor molecule on the surface, a random decision is made based on the probability of dissociating the precursor molecule. If a dissociation event occurs, the material is deposited, and the surface takes on a new shape.

The continuum models are based upon partial differential equations that describe the various accumulations and depletions of the precursor gas molecule(s). The rates of molecular impingement, thermal desorption, electron induced dissociation, and surface diffusion are considered across a spatial region around the electron beam. Depending upon the model complexity, the electron beam takes on various shapes, and the resulting electron flux is used to calculate the rate of precursor consumption.

Continuum Modeling

The early work on continuum modeling has its beginnings in focused ion beam modeling. Just as in focused electron beam induced chemistry, an ion beam can be used to induce chemistry. While the focused ion beam can be used to mill away material by physical sputtering, it can also be used to deposit material by dissociating an organometallic precursor gas molecule adsorbed on the surface. Petzold and Heard developed a model to understand the rate of depositing tungsten from a $W(CO)_6$ precursor molecule as a means of repairing defects for x-ray lithography masks[33]. They used the rate equation from Scheuer *et al*[34]:

$$\frac{dn}{dt} = g\Phi\left(1 - \frac{n}{n_0}\right) - \frac{n}{\tau_m} - \sigma n i$$

Where n is the adsorbate concentration, g is the sticking coefficient, Φ is the molecular flux, n_0 is the adsorption site density, τ_m is the mean residence time of the adsorbate, σ is the ion induced dissociation cross section, and i is the flux of ions impinging on the surface. The adsorption rate equation can be solved to determine the concentration of precursor adsorbed on the surface as a function of time, n(t), during the dwell time of the beam and the subsequent refresh or loop time while the beam is scanning other pixels. Following the work of Blauner[35] with some modification, the deposition rate can be calculated from the integration over time of the rate of material deposited minus the amount of material sputtered by the gallium ions:

$$R = \frac{i}{\tau_l \delta}\left(\eta\sigma \int_0^{\tau_d} n(t)dt - Y_s\tau_d\right)$$

Where τ_l and τ_d are the loop time and dwell time respectively, δ is the number density of the deposit, η is the sticking probability of the deposit (generally assumed to be unity), and Y_s is the sputter yield (a ratio of number of atoms sputtered per impinging ion). After substitution of n(t), Petzold and Heard had developed an analytical expression, albeit complicated, to describe the deposition rate as a function of all of the process parameters. They were able to reduce the equation considering two regimes. The first is the case where the deposition is dominated by the steady-state behavior of the system. This could happen due to very long dwell times. It also could be due to the ion flux being less than the molecular flux and so there is very little change in the adsorbate gas coverage whether the beam is on or off. The second deposition regime is dominated by the time dependent behavior of the precursor concentration, where the gas coverage changes significantly from after the beam is turned on, and the dwell time is short enough that a steady-state is not achieved.

Petzold and Heard conducted a series of experiments using the dwell time and loop time and were able to fit the dissociation cross section (σ), molecular flux ($g\Phi$), and ion flux (i) from the experimental data. Although the results were all within reasonable expectations, they provide an opportunity to discuss the short comings of the continuum model. The Petzold and Heard model assumes a uniform cylinder of ion flux rather than a shaped profile one might expect from an imperfect ion lens. The ion induced dissociation cross section assumes that the generated secondary electrons and backscattered ions have no impact on the dissociation of the precursor. In their simplification of the regimes, they assume that the residence time of the precursor adsorbate is so large that the equilibrium coverage when the beam is off is unity. There are certainly cases where the surface residence time is small enough that the molecular flux cannot keep the sites full, resulting in a different deposition regime.

Toth *et al* developed a continuum model to describe competitive deposition and etching processes[36]. They observed rings of deposition during exposure to a high pressure of etch gas in a "dirty" SEM environment. They used a two precursor model, one a carbon containing deposition precursor and the other an etch precursor for the carbonaceous deposit. At lower beam current, they observed a pillar deposit under the beam spot, but as the beam current increased, the deposition converted to a pillar shape. They postulated that at low electron flux, the deposition process was more efficient than the etch process due to a higher dissociation cross section and greater gas coverage. As the electron flux increased beyond a certain threshold, the deposition process became limited by the mass transport. The deposition process reached its maximum rate due to the arrival of new precursor, while the etch process was able to continue to increase with increasing electron flux. The result is a switching from net deposition to net zero (or net etching) beyond an electron flux threshold. Figure 10 (Figure 6 from their paper) illustrates the significant change in deposit shape observed with different beam currents. The two precursor continuum model that was used:

$$\frac{dN_e}{dt} = F_e - \frac{N_e}{\tau_e} - f\sigma_e N_e$$

$$\frac{dN_d}{dt} = F_d - \frac{N_d}{\tau_d} - f\sigma_d N_d - (f\sigma_e N_e)\sigma_{rd} N_d$$

The precursors are described by a set of simultaneous differential equations. The first term of the right hand side of each equation describes the arrival rate of the respective precursors, the second term describes the spontaneous thermal desorption rate of the precursor gases, the third term describes the rate of precursor dissociation where f is the electron flux and σ_x is the appropriate dissociation cross section. The fourth term of the deposition precursor rate equation describes the rate at which the deposition precursor is consumed by a reaction with a dissociated etch precursor.

The net deposition rate is then calculated as the rate of deposit precursor pinning minus the rate of etching of any deposited material. The dissociated etch precursor could react either with a deposited (pinned) species or an adsorbed deposition precursor molecule, creating a volatile product species. Toth *et al* made several reasonable assumptions about adsorption energies for hexane and water, and some assumptions about the electron induced dissociation cross sections of the precursor molecules and the reaction cross sections of volatile dissociation species. The results shown below in Figure 11 (Figure 7 from their paper) show the expected deposition rate as a function of electron flux. In the absence of an etch precursor (P_e=0), the deposition takes on the expected form, proportional to the electron flux for low electron fluxes until the mass it becomes mass transport limited at higher electron fluxes. In the case of the presence of the etch gas at low electron fluxes, the net deposition rate is decreased as some of the

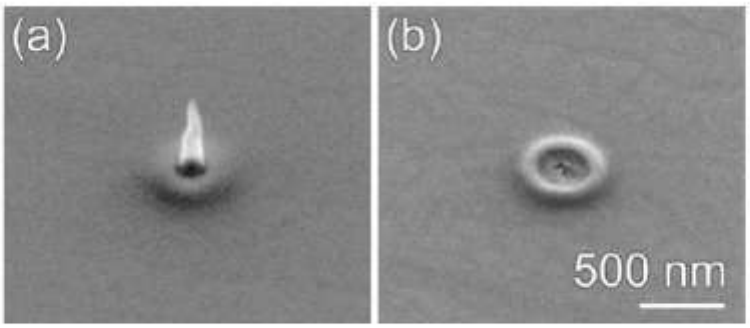

FIG. 6. Carbonaceous deposits on $In_{0.6}Ga_{0.4}As$ produced in a low vacuum environment (P=90 Pa of H_2O) using a stationary electron beam and beam currents of (a) 71 pA and (b) 245 pA. These deposits were generated in the presence of a contaminated cone (see Fig. 1) that acted as an additional deposit precursor source (V_0=5 keV, t=6 min, and ϕ=0°, during imaging ϕ=45°).

Figure 10: Carbonaceous Ring Deposits during Two-Precursor EBIP

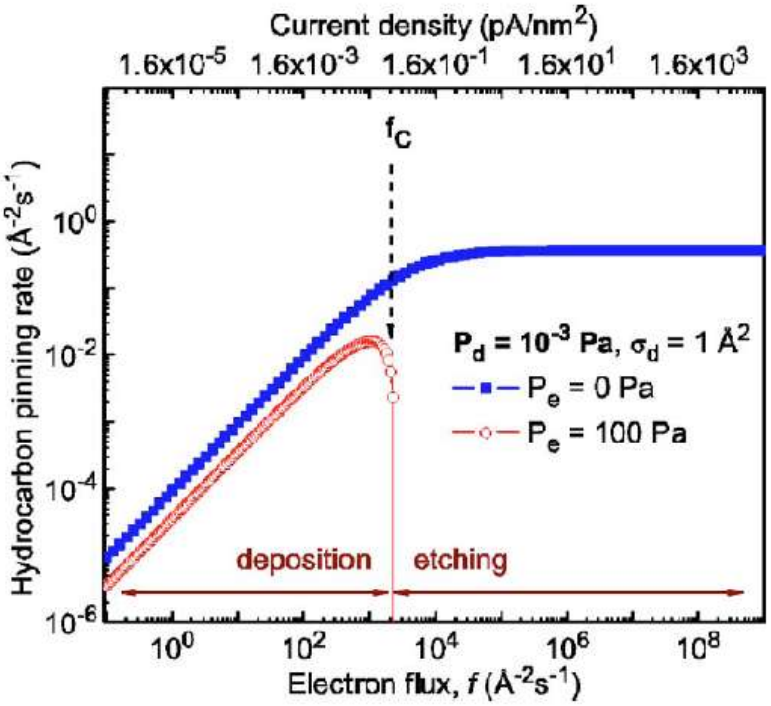

FIG. 7. (Color online) Steady state hydrocarbon pinning rates calculated at 295 K, as a function of electron flux at H_2O partial pressures (P_e) of 0 and 100 Pa (σ_e=10^{-2} $Å^2$).

Figure 11: Hydrocarbon Pinning versus Electron Flux

material that is being deposited is being etched away. But as the electron flux increases, the deposition process is limited while the etch process continues to increase proportional to electron flux. Above a particular electron flux, the etching process overpowers the deposition, and there is a net zero deposit. In this particular case, the etch precursor only etches the deposited carbonaceous material. If the substrate were able to be etched by the etch precursor, this electron flux would be the minimum flux to achieve net etching.

The simulated results of Toth *et al* Figure 7 (Figure 11) explain the behavior observed in their Figure 6 (Figure 10). Assuming the SEM beam spot is diffraction or aberration limited, the peak electron flux would increase with an increase in beam current. So, the electron flux in the center of the 71pA beam is not high enough to switch to etching and overcome the deposition, so a significant deposit is observed. As the beam current is increased to 245pA, the electron flux close the beam center is high enough to switch to a net zero deposit. Meanwhile, the electron flux in the periphery has increased and so the net deposit there is higher.

The key point to take from this paper is the need to reduce the molecular flux of deposit precursors in order accomplish etching. This was found to be very important by Lassiter *et al* while etching tantalum oxide/tantalum nitride thin films[37] and silicon dioxide films[38]. The pressure of etch precursor obtained by Toth *et al* is not attainable in most SEMs, so the molecular flux of etch precursor is many orders of magnitude less in a typical setup. Without the high etch precursor molecular flux, the competitive deposition could not have been overcome in Toth *et al's* experiments. To accomplish electron beam induced etching in high-vacuum mode, where the chamber is not exposed to back-streaming vacuum pump oils, requires cleaning the chamber and sample with an oxygen radical source to remove hydrocarbon species.

One of the exclusions from Toth *et al* etching continuum model, as well as others such as Utke *et al*[39], is handling the volatile etch product's surface residence time. All etching continuum models to date have assumed the etch products have zero residence time on the surface. Lassiter and Rack have shown that under certain process conditions, it is necessary to consider the etch product residence time to explain the experimental etch profiles[40].

Lobo, Toth, and others later modified the set of ordinary differential equation and made them into a set of partial differential equations to model the ring deposits[41]. They added terms for surface diffusion of the precursor molecules. They used a Gaussian shaped primary electron beam added to a Monte-Carlo derived backscattered/secondary electron profile to arrive at a radial electron flux profile. They were able to simulate various process parameters that would give the ring shaped deposit, and proposed a process space for creating smaller rings with resolution below the electron beam size.

Chapter 2: Static Beam Behavior

This chapter is a slightly revised version of a 2008 journal article published in *Nanotechnology* by myself and Philip Rack.

Matthew G. Lassiter and Philip D. Rack, "Nanoscale Electron Beam Induced Etching: A Continuum Model that Correlates the Etch Profile to the Experimental Parameters," *Nanotechnology*, **19** (2008), 455306

The use of "we" refers to my co-author and me. My contributions to the work include: (1) Experimental setup and data collection, (2) model construction, (3) literature searching, (4) almost all of the writing, and (5) interaction with journal editor and referees. My co-author provided direction and funding on the scope of the research, insight into the possible surface processes observed in the experimental data, several rounds of helpful editing of the paper, general advice, and motivation.

Abstract

In this chapter, we relate experimental electron beam induced etching profiles to various electron limited and mass transport limited regimes via a continuum model. In particular, we develop a series of models with increasing complexity and demonstrate the effects and interactions that the precursor gas adsorption kinetics, the electron flux distribution, and the etch product desorption kinetics have on the resultant nanoscale etching profile. Unlike analogous electron beam induced deposition models, it is shown that one must consider the diffusion, desorption, and possible re-dissociation of the resultant etch product to understand the observed etching profiles. To confirm the explanation of the etch results, a defocus experiment was performed showing transitions from the *electron flux limited* to the *mass transport limited* to the *etch product dissociation limited* regimes.

Introduction

Electron beam induced etching (EBIE) is a technique used for nanoscale patterning and editing or repair, and is an alternative to focused ion beam (FIB) etching[42,43,44]. EBIE offers better spatial resolution than FIB due to the smaller beam spot size. Furthermore, the electron beam does far less collateral damage to the substrate than the Ga^+ ion beam. FIB etching processes are mostly due to physical sputtering of the substrate atoms, which can be assisted via a chemical etching component. The physical sputtering mechanism of the gallium ion beam typically leads to poor etch selectivity of the material of interest and underlying film or substrate. EBIE processes lack the physical sputtering mechanism and can offer high etch selectivity between different materials. Electron beam induced etching is analogous to electron beam induced deposition (EBID) which has been studied in more detail and has been used as a nanoscale direct write synthesis technique[42].

In order to accomplish EBIE, a precursor gas is typically injected in the chamber in close proximity to the substrate which directs a flux of precursor species onto the surface and subsequently adsorbs onto the surface for an average residence time determined by the gas-surface interaction and the temperature of the system. When an energetic electron interacts with the adsorbed precursor molecule, there is a probability that some of the electron's energy will be transferred to the precursor molecule and result in the dissociation of the precursor molecule into radical species. These radicals can subsequently react with the atoms of the solid substrate to form volatile species. For etching to occur, the volatile reaction products must subsequently desorb from the surface, which exposes new adsorption sites for impinging precursor gas molecules to

repeat the EBIE cycle. The desorbed etch products are eventually pumped out of the chamber by the evacuation system. The result is a site specific etching process which is directed or induced by the focused electron beam.

Monte Carlo methods have been developed for simulating electron beam induced deposition via an electron by electron process[45,46,47,48]. These methods have been useful in understanding the EBID process, but require significant simulation time to handle the gas kinetics due to the fact that each adsorbed gas molecule is handled individually. Several continuum models have been introduced over the years which have their basis on models originally proposed for focused ion beam processing[49,50,51,52]. Recently, Toth *et al* developed a continuum model to describe deposition of material and the simultaneous etching of the deposit using a two-precursor model[53]. The competitive growth versus etching was examined as a function of the electron flux, and deposition versus etching "switching" was discussed as a function of the precursor pressures, dissociation cross sections, and temperature. Lobo *et al* later extended Toth's model by introducing a spatially resolved current profile that mimics the beam interaction region and also included surface diffusion. This was used to describe the potential for depositing high resolution ring structures that can be fabricated by the simultaneous carbonaceous deposit and subsequent etching of the carbon deposit based on the relative efficiency of the two processes[54]. Utke *et al* developed a continuum model describing the precursor gas distribution to understand the relationship between the EBID deposit shape and the spatially resolved electron beam flux by considering the gas kinetics, the depletion of the precursor due to the e-beam exposure, and the surface diffusion of the precursor molecule[55]. Rykaczewski *et al* developed an adaptive continuum model that describes the shape of the deposit and continuously updates the electron flux distribution as the deposit changes shape during growth[56].

In this paper, we have extended the EBID continuum models to EBIE. We present some experimental results that inspired us to add new terms to the EBIE model that account for the residence time of the volatile etch products. The finite residence time of the etch product leads to the probability of re-dissociating the volatile etch products, and subsequently re-depositing the initial substrate material. The re-dissociation of the etch product can slow the etching rate and can affect the resultant shape of the etched feature.

Experimental Results

A spot mode (constant beam at a fixed position) experiment was performed using a Hitachi 4300 SEM with a thermal field emitter electron source. Before etching, the surface of the substrate and the vacuum chamber surfaces were cleaned using an

oxygen plasma generated by an EVACTRON C Decontaminator. The oxygen plasma removes hydrocarbons by converting them into volatile species of CO, CO_2, and H_2O that are subsequently pumped out of the chamber. Removing carbon-containing species from the system is critical to eliminating competitive deposition processes during etching. In many cases, etching the substrate is not possible unless the system and substrate has been cleaned. A 100nm thick SiO_2 film on Si substrate was etched using XeF_2 as the precursor gas, injected from a needle approximately 2mm from the surface of the substrate. The flow of XeF_2 was adjusted until the background pressure in the chamber reached $2.0x10^{-2}$ Pa. While the exact localized pressure is not specifically known, it is surmised that the localized pressure directly under the injection needle is more than an order of magnitude higher than the background pressure[57,58,59]. The SiO_2 film does not spontaneously react with the XeF_2 molecule[60,61], as no detectable etching occurs from simply flowing the precursor gas. Three time series were run using a 5keV beam and a variable sample current of 10, 100 and 300 pA, respectively. Figure 12 shows the results of a XeF_2-SiO_2 EBIE varying the beam current and etch times. For each current, initially a 10 minute (left most spot) etch was performed, then progressing left to right a 2, 4, 6, and 8 minute etch was done, respectively. From these experimental results, several interesting observations were noted from the etch profiles. It is observed that for higher beam currents, the etch rate decreases directly under the beam in comparison to the periphery. Specifically, a "moat" profile resulted at the two higher beam currents where the spot exposed to the beam has a near zero etch rate and a specific radius in the beam periphery (which is current dependent) has the highest etch rate. As beam current was reduced, the radius of the maximum etching rate is reduced; and below a certain beam current, the etch rate is fastest in the center. At 10pA, the moat profile is not present; the area under the beam center has the highest etch rate and subsequently the highest resolution etch (~ 75nm in diameter). Figure 12 also shows a tilted view of the moat profile showing the reduced etch rate under the center of the beam and the moat profile.

Spontaneous etching of silicon in XeF_2 has been studied in detail by Vugts *et al*[62]. Ibbottson et al. report that the XeF_2 molecule physisorbs at temperatures below 450K, and there is direct impact dissociation at higher temperatures on Si and SiO_2[63]. Below 450K, the physisorbed xenon difluoride molecule reacts with the Si to form a SiF_2 intermediate reaction product, and ultimately a SiF_4 product with a relatively small desorption energy. The etching rate at lower temperatures is limited by the concentration of XeF_2 on the surface, due to the XeF_2 residence time in decreasing with increasing temperature. As the temperature increases, etch rate decreases to a minimum and then begins increasing along a positive activation energy slope. Vugts *et al*[21] attributed the positive activation energy to the desorption of the intermediate reaction product SiF_2. At room temperature, there is no etching spontaneously of SiO_2 because of the non-dissociative physisorption of the XeF_2 molecule. Dissociative chemisorption results in F* radicals, which readily etch SiO_2[22]. Therefore, it is assumed

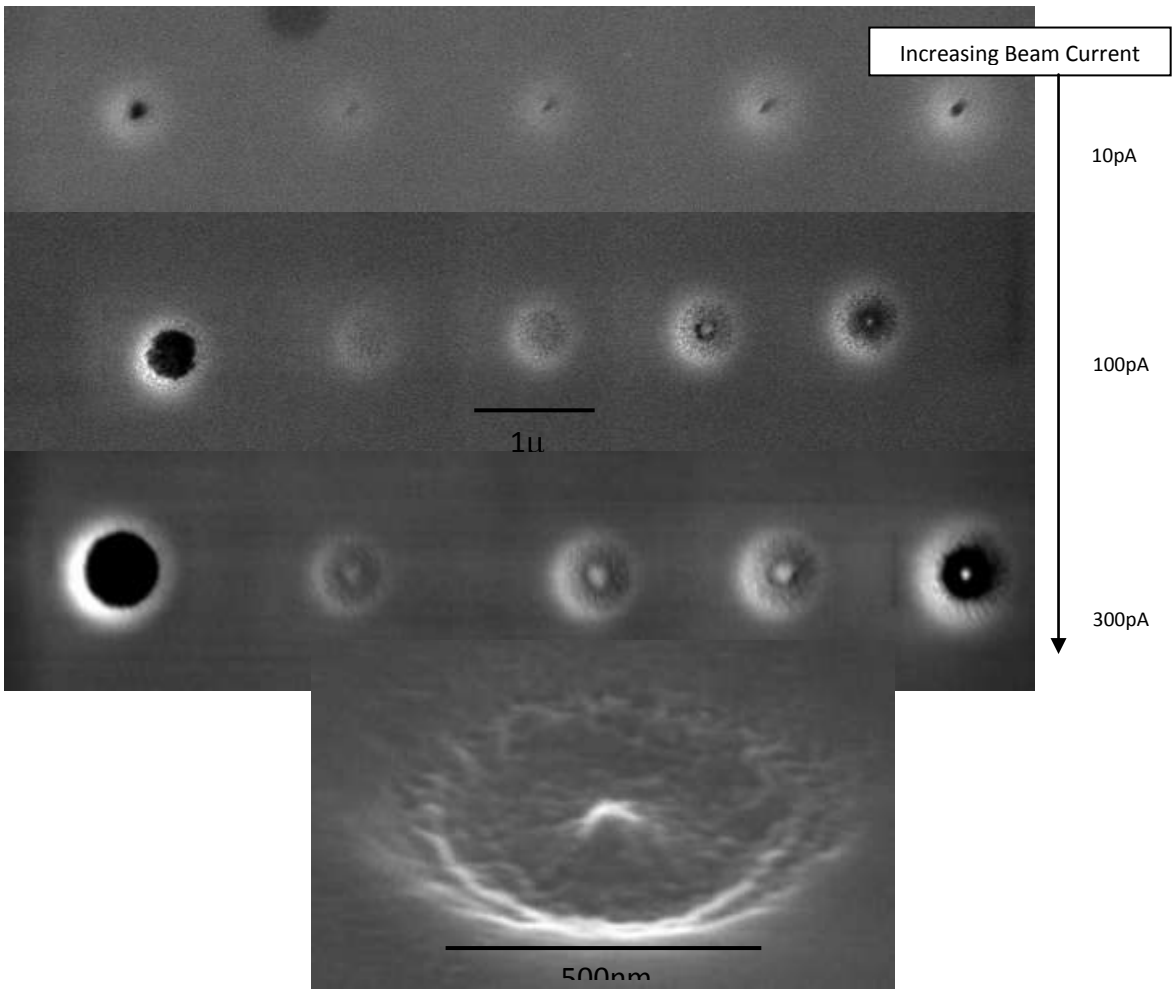

Figure 12: Spot Mode EBIE of 100nm SiO_2 on Si

Under $2.00x10^{-2}$ Pa of XeF_2 and a 5kV e-beam, the columns represent times of 10, 2, 4, 6, and 8 minutes from left to right. The rows are different initial sample currents of 10, 100, and 300 pA from top to bottom. Note that increasing the beam current causes a change in the shape of the etched feature. The moat effect is observed at higher beam currents while the effect disappears at the lowest beam current. Inset: A tilted view of the 2 minute, 300 pA etching site.

that the reaction progresses only after an electron stimulated dissociation of the xenon difluoride molecule. While the dissociation of the XeF_2 could be photon stimulated, we acknowledge any photons are generated by the electron-solid interaction, and therefore the photon intensity profile would take on the same shape as the electron flux profile. For simplicity sake, photon induced dissociation is ignored.

Noting that the thickness of the SiO_2 film is 100nm, and assuming a density of 2.2 g-cm^{-3}, the film thickness is approximately 280 layers of SiO_2[64]. Using the contrast change in the image from SiO_2 to the Si substrate as a rough estimation for the time of etching through the SiO_2 film, the results from Figure 12 indicate that under the 100pA and 300pA beam current, the fastest etching through the 100nm SiO_2 occurred in about 6 minutes. This would require a removal rate of 0.78 monolayers per second. Using a surface density of 7.87×10^{14} per square cm for SiO_2 (from the calculations above), this translates into a removal rate about 6×10^{14} molecules-cm^{-2}s^{-1}. This image contrast method is used as a crude estimate of the peak removal rate for comparison to the continuum model and is not useful for the 10pA etches due to the size of the etched hole and the reduction of the secondary electron yield in the hole due to the proximity of the sidewalls. For the 100pA and 300pA beam currents, the center etching rate is significantly less than the peak rates. Figure 12 tilted view indicates that the etching rate directly under the beam spot is close to zero. We demonstrate that this anomalous etching behavior can be explained by understanding the various accumulation rates and depletion rates of precursor and etch product species.

Process Modeling

Precursor EBIE Model

In order to understand the electron beam induced etching process, it is necessary to understand the relationship between the gas adsorption on the surface and the flux of electrons arriving at the surface. The precursor gas on the surface can be modeled using an ordinary differential equation considering the rates of gas arriving at and leaving the surface. Following the Langmuir model of gas adsorption, the arrival rate of precursor gas to the surface is given by the molecular impingement rate (which is directly proportional to the localized pressure) and the assumption that impinging gas cannot adsorb onto a site that is already occupied. Precursor molecules leave the surface or get consumed by two mechanisms, thermal desorption or an electron induced reaction to form the volatile etch product. The rate equation for the change in precursor concentration as a function of time (t) on the surface is thus:

$$\frac{dN_A}{dt} = gI_A\left[1 - \frac{N_A}{Z}\right] - \frac{N_A}{\tau_A} - \frac{A_\sigma \Gamma_e N_A}{Z} \tag{2.1}$$

where N_A is the surface concentration of adsorbed gas molecules. The first term on the right hand side is the Langmuir adsorption rate where g is the sticking coefficient, I_A is the molecular impingement rate, and Z is the density of adsorption sites. The second term is the thermal desorption rate where τ_A is the average residence time of the precursor species. The third term is the rate of dissociation of the precursor by the electron beam where A_σ is the probability of an energetic electron causing a dissociation event of the precursor gas and Γ_e is the flux of electrons on the surface. Solving for the steady state concentration of the precursor gas we get:

$$(2.2)\quad N_A = \frac{gI_A}{\left(\frac{gI_A}{Z} + \frac{1}{\tau_A} + \frac{A_\sigma \Gamma_e}{Z}\right)}$$

The equilibrium coverage (θ_A) in the absence of the electron beam (Γ_e=0):

$$(2.3)\quad \theta_A = \frac{N_A}{Z} = \frac{gI_A}{Z\left(\frac{gI_A}{Z} + \frac{1}{\tau_A}\right)} = \frac{gI_A}{\left(gI_A + \frac{Z}{\tau_A}\right)}$$

If the assumption is made that once the dissociation of the precursor molecule occurs, the etch product forms and leaves the surface; then the etch rate is directly proportional to the rate at which volatile etch product molecules are created. The rate of product formation is a stoichiometry factor (x) multiplied by the rate of dissociation of the precursor gas. For example, x=0.5 for the etch reaction:

$$(2.4)\quad 2XeF_2 + SiO_2 \xrightarrow{e^-} SiF_4 + 2Xe + O_2$$

(that is, 1 SiF_4 product molecule per 2 XeF_2 precursor molecules). The etching rate becomes:

$$(2.5)\quad EtchRate \propto \frac{xA_\sigma \Gamma_e N_A}{Z} = \frac{xA_\sigma \Gamma_e}{Z} \cdot \frac{gI_A}{\left(\frac{gI_A}{Z} + \frac{1}{\tau_A} + \frac{A_\sigma \Gamma_e}{Z}\right)} = \frac{xA_\sigma \Gamma_e gI_A}{\left(gI_A + \frac{Z}{\tau_A} + A_\sigma \Gamma_e\right)}$$

Considering the above equation for etching rate, different processing regimes exist depending on the precursor gas and beam parameters.

Electron Flux Limited Regime

For the case when the electron flux ($A_\sigma \Gamma_e$) is small compared to molecular impingement rate (gI_A) or the maximum precursor desorption rate (Z/τ_A), the denominator of equation (5) reduces to ($gI_A + Z/\tau_A$), it is seen that the etch rate is proportional to the electron flux and the equilibrium coverage of the precursor gas (θ_A) from equation (3):

$$(2.6)\quad EtchRate \approx \frac{xA_\sigma \Gamma_e g I_A}{\left(gI_A + \frac{Z}{\tau_A}\right)} = x\theta_A A_\sigma \Gamma_e$$

This is a reasonable result, as the impingement of precursor gas keeps the adsorption sites at the equilibrium coverage level and the reaction is limited by the rate of electrons arriving to the surface.

Mass Transport Limited Regime (Type I)

For the opposite case, where the electron flux is much greater than the impingement rate of precursor gas or the maximum precursor desorption rate, the third term in the denominator of equation (5), $A_\sigma \Gamma_e$, dominates. The etch rate is then proportional to the molecular impingement rate and has no further dependence on electron flux. This is consistent with qualitative expectations; as the high flux of electrons consumes the entire adsorbed precursor, the surface concentration of precursor is essentially zero. The etch reaction is then limited by the arrival rate of new precursor to the surface in equation (7).

$$(2.7)\quad EtchRate = \frac{xA_\sigma \Gamma_e g I_A}{\left(gI_A + \frac{Z}{\tau_A} + A_\sigma \Gamma_e\right)} \approx \frac{xA_\sigma \Gamma_e g I_A}{(A_\sigma \Gamma_e)} \approx xgI_A$$

Plotting the relative etching rate versus electron flux for various parameters gives insight into the process kinetics. As a baseline, it is assumed that the substrate has 10^{15} adsorption sites per square cm, that is $Z=10^{15}cm^{-2}$. Contained in the low electron flux region of Figure 13 is a plot of the relative etch rate versus electron flux for various precursor impingement rates (pressures) which illustrates that at low electron flux, the etch rate increases with increasing electron flux (*electron flux limited* regime). The high electron flux behavior is explained later in the Precursor-Product EBIE Model. The analog of this effect in deposition is also seen in the work of Toth *et al*[12] in their Figure 8(a). At higher electron flux, for a fixed precursor flux, the etch rate saturates as the process shifts to a *mass transport limited* regime. Also illustrated in Figure 13 is the fact that as the precursor flux increases, a higher electron flux is required to transition to mass transport limited etching, and the rate at which it saturates is at a proportionately higher level. With regards to the precursor dissociation probability (A_σ), note from Equations 6 and 7 that the etching rate is only affected in the *electron flux limited* regime. The etching rate is not affected by the dissociation probability in the *mass transport limited* regime as there is such an abundance of electrons, effectively all precursor molecules that are adsorbed are dissociated. Figure 14 is a plot of relative etching rate versus electron flux that illustrates the effect of precursor residence time.

As the precursor residence time decreases, the equilibrium coverage (θ_A) decreases. This changes the threshold of the transition from the *electron flux limited* regime to the

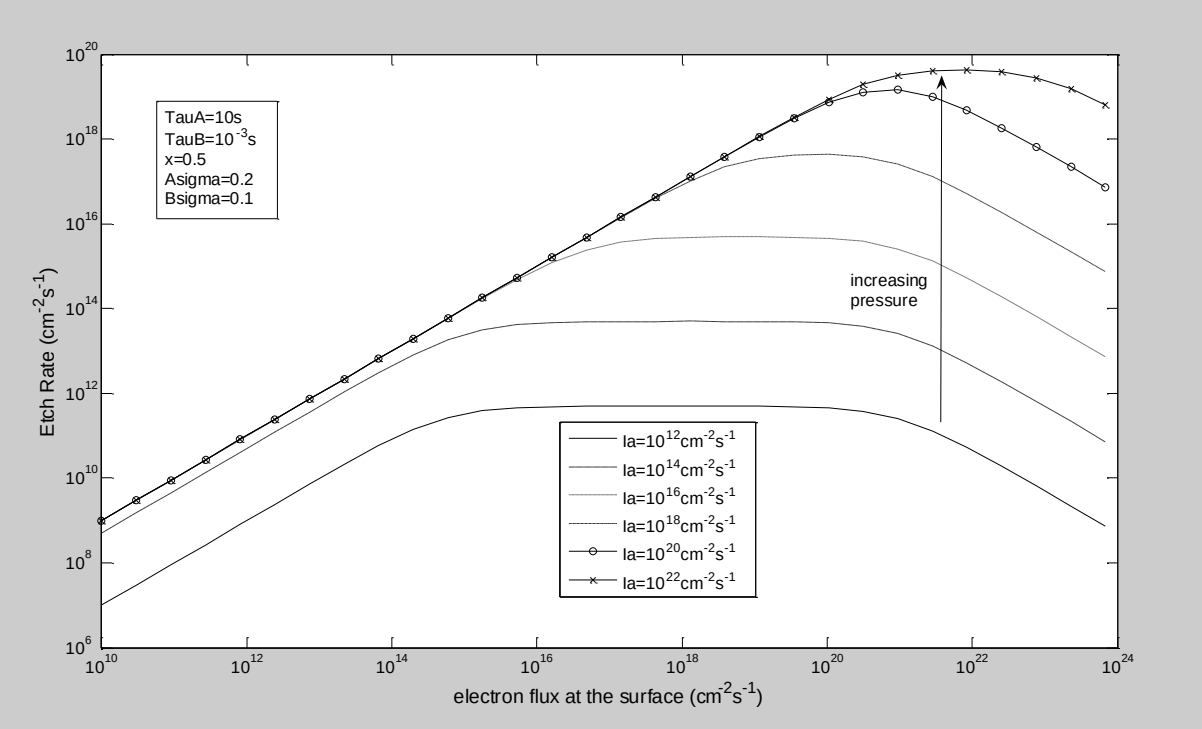

Figure 13: Precursor-Product EBIE Model: Effect of Precursor Impingement Rate with Product Residence/Dissociation

The finite lifetime of the product reduces the etching rate under high electron flux. Under most precursor impingement rates, the *etch product dissociation limited* regime dominates the *mass transport limited* regime and can cover the high end of the *electron flux limited* regime.

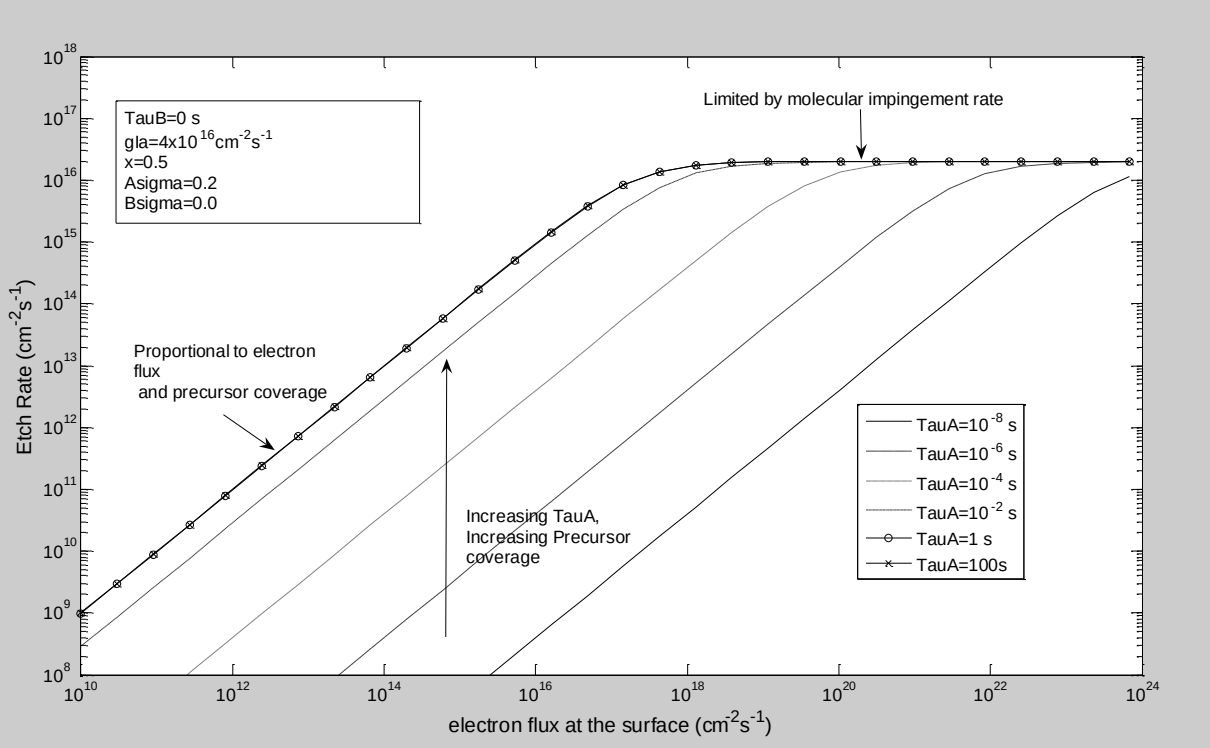

Figure 14: Precursor EBIE Model: Effect of Precursor Residence Time on Etch Rate

If the residence time is sufficiently large, the equilibrium coverage is essentially unity and there is little sensitivity to the precursor residence time. As the residence time decreases, the coverage decreases; and the relative etching rate decreases proportional to the residence time. Observe that the threshold for transitioning from the *electron flux limited* regime to the *mass transport limited* regime increases inversely proportional to the precursor residence time. If the precursor residence time is sufficiently large, the equilibrium coverage is essentially one and there is no further dependence of the etch rate on increasing residence time.

mass transport limited regime. Also, it can be observed that the etching rate in the *electron flux limited* regime is reduced proportional to the reduction in coverage.

Precursor EBIE Model with Surface Diffusion

The electron flux radial profile was calculated as the result of a 2-D convolution of an impinging beam profile of primary electrons and a substrate point spread function to account for backscattered and secondary electrons. The impinging electron beam profile accounts for the shape of the beam spot (usually circular, but not necessarily so with an abberated lens) and the effect of electron diffraction through the limiting aperture. The impinging electron beam profile is the result of a 2-D convolution of the top hat shape from the source focused onto the substrate with the Airy disc from electron diffraction through the circular aperture. The substrate point-spread function is derived from a plural scattering Monte-Carlo based electron-solid interaction simulation[4]. Figure 15 is an example of an electron flux profile using 5keV electrons with a beam current of 300pA impinging on a SiO_2 substrate. The half angle (α) is 3.75 x 10^{-3} radians. Note the full width half maximum of the beam is only about 4nm, which is good for imaging; yet there is a flux of electrons at the surface for hundreds of nanometers away from the beam center from backscattered electrons (BSE) and the resulting secondary electrons (SE).

Using the calculated radial profile for the electron flux at the surface and the addition of a surface diffusion term to the Precursor EBIE model, the ordinary differential equation (ODE) becomes a partial differential equation (PDE).

$$\frac{\partial N_A}{\partial t} = D_A \nabla^2 N_A + g I_A \left[1 - \frac{N_A}{Z}\right] - \frac{N_A}{\tau_A} - \frac{A_\sigma \Gamma_e N_A}{Z} \tag{2.8}$$

D_A is the diffusion coefficient in units of (cm^2/s) that relates the Laplacian of the concentration to the rate of change of concentration from Fick's Second Law of Diffusion. If radial symmetry is assumed, then the PDE in equation (8) becomes:

$$\frac{\partial N_A}{\partial t} = D_A \left[\frac{1}{r}\frac{\partial N_A}{\partial r} + \frac{\partial^2 N_A}{\partial r^2}\right] + g I_A \left[1 - \frac{N_A}{Z}\right] - \frac{N_A}{\tau_A} - \frac{A_\sigma \Gamma_e N_A}{Z} \tag{2.9}$$

Using the simple Precursor EBIE model, one would predict that the fastest etching rate would occur under the beam spot and in the immediate vicinity due to the high electron flux. The etch rate in the periphery of the beam spot could be enhanced by diffusion of precursor gas from the periphery where the precursor concentration is high relative to the center where the precursor concentration is low. A *mass transport limited* etch would have a faster etch rate in the transition region from high to low precursor concentration due to an enhanced surface diffusion flux of precursor beyond the rate of impinging gases to these sites. This would yield a ring of enhanced etch rate about the center analogous to the volcano shaped structures demonstrated by EBID[65,14,12]. However, a precursor diffusion-enhanced etching ring does not explain the near zero

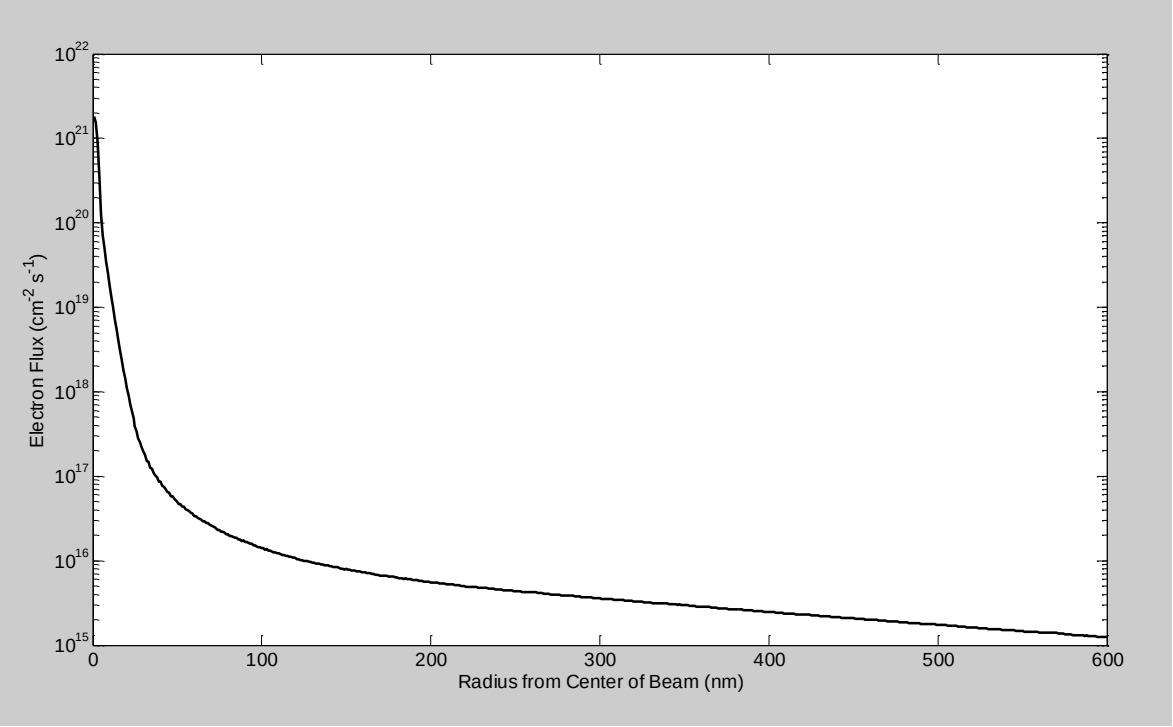

Figure 15: Simulated Electron Flux at the Surface

The radial electron flux profile simulating the effect of electron diffraction through the lens aperture and the effect of electron-solid interaction. The incident electron energy is 5keV using a 100pA beam current.

etch rate observed immediately under the beam spot, as this area would still be etching in a *mass transport limited* regime due to the impinging flux of precursor gas molecules. Figure 16 shows a simulation of a diffusion-enhanced moat structure using the previously described precursor EBIE model with the inclusion of surface diffusion. The electron flux profile of Figure 15 was used as it is the profile expected from the 300pA beam current in Figure 12. As can be seen, depending on the ratio of precursor impingement rate to the diffusion flux from the periphery and the electron flux distribution, different moat profiles can be obtained. If using a precursor only model, the etching rate in the center under *mass transport limited (type I)* is at a minimum: xgI_A, and can only be enhanced by surface diffusion of precursor into the beam center. For the case of XeF_2 at $2x10^{-2}$Pa and a sticking coefficient (g) of 1.0 and stoichiometry factor (x) of 0.5, the result is a minimum etching rate (xgI_A) of $1.17x10^{16}cm^{-2}s^{-1}$ (neglecting the pressure enhancement of the localized pressure realized by the nozzle). For SiO_2, this translates to nearly 15 monolayers per second (or 5.3nm/s). As the film is about 280 layers thick (measured by reflectometry), we would expect the center to etch in ~ 18 seconds. From Figure 12, the center has only etched about ~15nm in 120 seconds (0.125nm/s). This discrepancy in the etching rate cannot be explained by a precursor only model. Instead, we must consider the residence time of the etch product species to explain the slower etch rate under high electron flux.

Precursor-Product EBIE Model

To understand the experimental observations, it is important to consider that EBIE requires that the product formed from the reaction must desorb from the surface. This is actually very different from the well-studied electron beam induced deposition process where the stimulated deposition reaction produces a condensed species. The Precursor EBIE model above assumed that the surface residence time of the etch product was zero; that is, the etch product immediately desorbs from the surface after it is formed. Realistically, there is a finite lifetime for the etch product due to an interaction potential with the surface. In plasma etching for instance, the product lifetime can often rate limit the etch process, and adding ion bombardment (i.e. a reactive ion etch) can facilitate desorption and significantly increase the etch rate. Adding a simultaneous second ordinary differential equation to describe the rate of product formation and desorption to the precursor rate equation yields a Precursor-Product EBIE model:

$$\frac{dN_A}{dt} = gI_A\left[1 - \frac{N_A}{Z} - \frac{N_B}{Z}\right] - \frac{N_A}{\tau_A} - \frac{A_\sigma \Gamma_e N_A}{Z} \tag{2.10}$$

$$\frac{dN_B}{dt} = \frac{xA_\sigma \Gamma_e N_A}{Z} - \frac{N_B}{\tau_B} \tag{2.11}$$

where the first rate equation (10) is similar to the Precursor EBIE model from equation (1), and the second rate equation (11) describes the concentration of etch product on

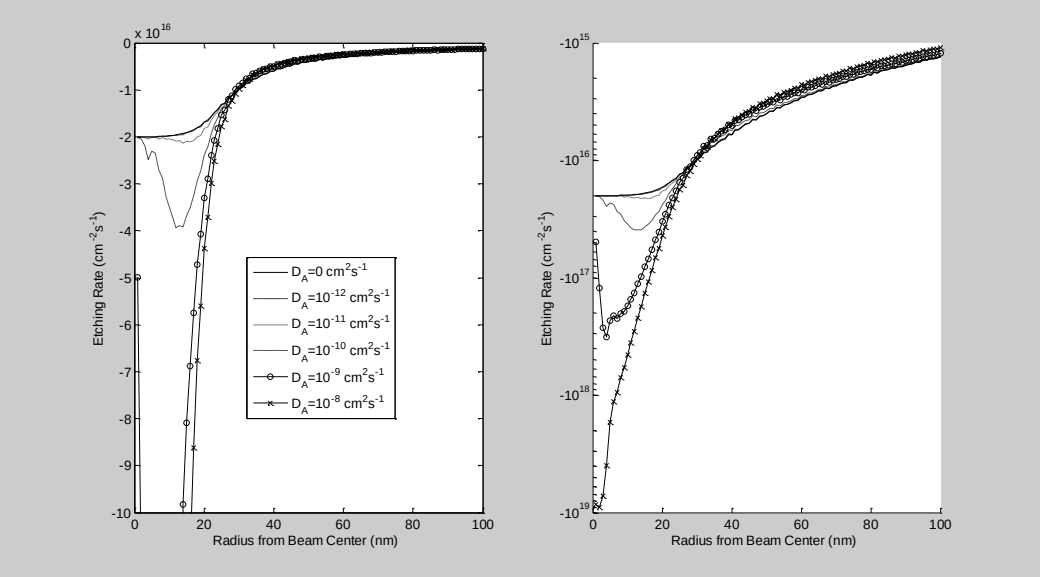

Figure 16: Precursor EBIE Model with Surface Diffusion

Left: Linear vertical scale. Right: Logarithmic vertical scale. The effect of surface diffusion is seen as enhancing the etching rate in regions that would be *mass transport limited* by precursor impingement see extra mass transport by the arrival of precursor by surface diffusion. The rate is then higher as the coverage of precursor is enhanced. For small to moderate surface diffusion coefficients, the enhanced precursor is consumed before it can reach the center and the etching rate is enhanced in the periphery. For higher surface diffusion coefficients, some of the diffusing precursor survives to reach the beam center where it significantly enhances the etching rate due to the magnitude of the electron flux in that region. Modeling only the precursor, only enhancement of etching rate is possible rather than impedance.

the surface. The first term on the right hand side of equation (11) is the rate of formation of the etch product. As discussed earlier, this is proportional by a stoichiometry factor (x) to the dissociation of the precursor molecule. The second term on the right hand side of equation (11) describes desorption of the etch product. N_B is the surface concentration of the etch product and τ_B is the average residence time of the etch product on the surface. Solving for the steady state concentration of precursor and etch product yields:

$$(2.12) \quad N_A = \frac{gI_A\left(\frac{1}{\tau_B}\right)}{\left(\frac{gI_A}{Z}+\frac{1}{\tau_A}+\frac{A_\sigma\Gamma_e}{Z}\right)\left(\frac{1}{\tau_B}\right)+\frac{gI_AxA_\sigma\Gamma_e}{Z^2}}$$

$$(2.13) \quad N_B = \frac{gI_A\left(\frac{xA_\sigma\Gamma_e}{Z}\right)}{\left(\frac{gI_A}{Z}+\frac{1}{\tau_A}+\frac{A_\sigma\Gamma_e}{Z}\right)\left(\frac{1}{\tau_B}\right)+\frac{gI_AxA_\sigma\Gamma_e}{Z^2}}$$

The steady state concentrations of precursor gas and product gas now have a dependence on the residence time of the etch product. Investigating different regimes and simplifying gives insight into the above equations. If the product residence time (τ_B) is very small, then the denominators of both equations (12) and (13) are dominated by the first term and the concentrations of precursor and product reduce respectively to:

$$(2.14) \quad N_A \approx \frac{gI_A}{\left(\frac{gI_A}{Z}+\frac{1}{\tau_A}+\frac{A_\sigma\Gamma_e}{Z}\right)}$$

$$(2.15) \quad N_B \approx N_A\left(\frac{xA_\sigma\Gamma_e}{Z}\tau_B\right)$$

In this case, the precursor concentration is minimally affected by the finite product lifetime and the product concentration is just proportional to the rate of product formation times the surface residence time of the product molecule. This is analogous to Henry adsorption where the surface concentration is proportional to the arrival rate of gas and the surface residence time[66]. Of note here is that the etching rate is not affected by very small product residence time as there is effectively no change in the precursor concentration at the surface from the limiting case of zero product residence time previously discussed in the Precursor EBIE model of equation (1). The etch rate here is essentially the same as the *electron flux limited* regime and *mass transport limited (type I)* regime discussed earlier.

Mass Transport Limited (Type II)

The case of longer product lifetime leads to a much different result. In the case of long product residence times and sufficiently high electron fluxes, the first term in the

denominator of equations (12) and (13) is small compared to the second term. The steady state surface concentrations of precursor and product reduce to:

$$(2.16) \quad N_A \approx \frac{Z^2}{\tau_B x A_\sigma \Gamma_e}$$

$$(2.17) \quad N_B \approx Z$$

The etch product essentially fills all of the sites as it has a long residence time. The concentration of precursor is limited by the availability of adsorption sites rather than the molecular impingement rate. The etch rate is then:

$$(2.18) \quad EtchRate = \frac{x A_\sigma \Gamma_e N_A}{Z} \approx \frac{x A_\sigma \Gamma_e}{Z}\left(\frac{Z^2}{\tau_B x A_\sigma \Gamma_e}\right) = \frac{Z}{\tau_B}$$

The etch rate is limited by the desorption of the etch product from the surface, making new sites available for precursor adsorption. Figure 17 illustrates the effect of increasing the etch product residence time as the *mass transport limited* regime transitions from molecular impingement rate limited (Type I) to etch product desorption limited (Type II).

Electron Beam Induced Product Dissociation

In EBIE, during the product residence time on the surface, it is possible for subsequent energetic electrons to dissociate the etch product before it is able to desorb. The dissociated etch product re-deposits the substrate species, inhibiting the etch process. The electron beam induced etching (EBIE) process can be described by the Precursor-Product EBIE model adding a new term to the etch product rate equation describing the dissociation and subsequent re-deposition of the etch product. These simultaneous equations are now:

$$(2.19) \quad \frac{dN_A}{dt} = g I_A \left[1 - \frac{N_A}{Z} - \frac{N_B}{Z}\right] - \frac{N_A}{\tau_A} - \frac{A_\sigma \Gamma_e N_A}{Z}$$

$$(2.20) \quad \frac{dN_B}{dt} = \frac{x A_\sigma \Gamma_e N_A}{Z} - \frac{N_B}{\tau_B} - \frac{B_\sigma \Gamma_e N_B}{Z}$$

Equation (19) is identical to equation (10), and equation (20) adds the etch product dissociation rate term to equation (11). B_σ is the dissociation probability of the etch product molecule. The third term on the right hand side is the electron beam dissociation of the product before it desorbs from the surface, resulting in a re-deposition of the solid phase. Solving for the steady state behavior of equations (19) and (20), we find the concentration of precursor and etch product on the surface is:

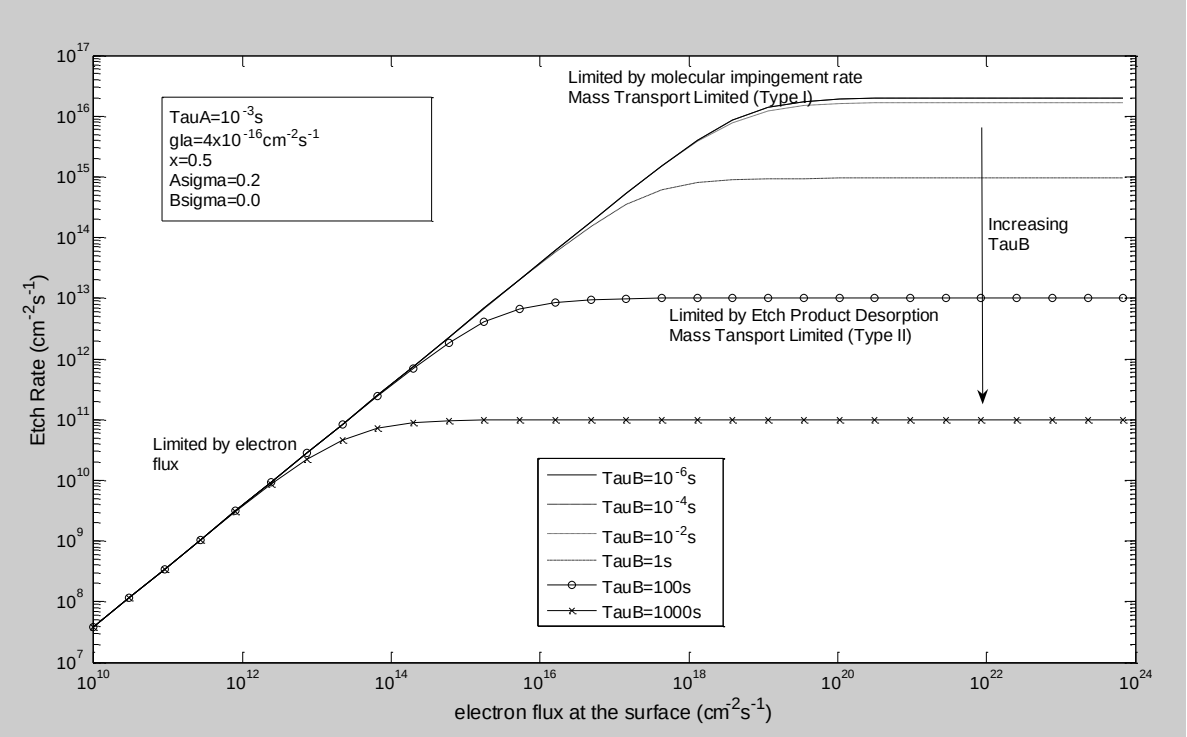

Figure 17: Precursor-Product EBIE Model: Effect of Product Residence Time on the Etching Rate

For small product lifetimes, the *mass transport limited* etching regime is limited by the arrival rate of precursor to the surface (Type I). For sufficiently high product residence times, the *mass transport limited* etching regime is limited by the rate of product leaving the surface (Type II). Essentially, all sites are full of etch product limiting the ability of new precursor to arrive at the surface. The etching rate is limited by the rate of product desorption.

$$(2.21)\quad N_A = \frac{gI_A\left(\frac{1}{\tau_B}+\frac{B_\sigma\Gamma_e}{Z}\right)}{\left(\frac{gI_A}{Z}+\frac{1}{\tau_A}+\frac{A_\sigma\Gamma_e}{Z}\right)\left(\frac{1}{\tau_B}+\frac{B_\sigma\Gamma_e}{Z}\right)+\frac{gI_AxA_\sigma\Gamma_e}{Z^2}}$$

$$(2.22)\quad N_B = \frac{gI_A\left(\frac{xA_\sigma\Gamma_e}{Z}\right)}{\left(\frac{gI_A}{Z}+\frac{1}{\tau_A}+\frac{A_\sigma\Gamma_e}{Z}\right)\left(\frac{1}{\tau_B}+\frac{B_\sigma\Gamma_e}{Z}\right)+\frac{gI_AxA_\sigma\Gamma_e}{Z^2}}$$

The etching rate is now proportional to the rate of etch product formation as before in equation (5) minus the rate of etch product dissociation:

$$(2.23)\quad EtchRate = \frac{xA_\sigma\Gamma_e}{Z}N_A - \frac{B_\sigma\Gamma_e}{Z}N_B$$

After substitution of the steady state values of N_A and N_B from equations (21) and (22), simplification reveals the etch rate is then proportional to:

$$(2.24)\quad EtchRate = \frac{xA_\sigma\Gamma_e gI_A}{\left(gI_A+\frac{Z}{\tau_A}+A_\sigma\Gamma_e\right)\left(1+\frac{\tau_B B_\sigma\Gamma_e}{Z}\right)+\frac{\tau_B gI_AxA_\sigma\Gamma_e}{Z}}$$

Investigating the regimes discussed earlier, we find that for the *Electron Flux Limited* regime equation (24) reduces neatly, just as in the Precursor EBIE model equation (6), to:

$$(2.25)\quad EtchRate \approx \frac{xA_\sigma\Gamma_e gI_A}{\left(gI_A+\frac{Z}{\tau_A}\right)} = x\theta_A A_\sigma\Gamma_e$$

But, for the *Mass Transport Limited* regime where $A_\sigma\Gamma_e >> gI_A$ equation (24) reduces to:

$$(2.26)\quad EtchRate \approx \frac{xgI_A}{\left[1+\frac{\tau_B}{Z}(xgI_A+B_\sigma\Gamma_e)\right]}$$

And for large τ_B, but $A_\sigma\Gamma_e << gI_A$, the *Mass Transport Limited (Type II)* regime, equation (24) reduces to:

$$(2.27)\quad EtchRate \approx \frac{Z}{\tau_B}\left(\frac{xA_\sigma}{xA_\sigma+B_\sigma}\right)$$

It can be seen that when τ_B is zero, the *mass transport limited* regime of equation (26) is the same as the Type I (impingement limited) regime of equation (7). Also, when τ_B is

sufficiently large and B_σ is zero, the Type II (product desorption limited) dominates the etching rate, and equation (27) reduces to equation (18). But consider the scenario when τ_B is finite and there is also a non-zero B_σ, inspection of equation (26) reveals that the etch rate goes inversely proportional to the electron flux. The effect of a finite surface lifetime of etch product and finite probability of etch product dissociation is the reduction of the etching rate at high electron fluxes. The longer the surface lifetime of the etch product, the lower the electron flux threshold where the etch rate is reduced. Figure 13 shows the relative etch rate versus electron flux for various precursor impingement rates with a fixed product lifetime (τ_B) of 10^{-3} sec. The result shows that the etch rate increases with increasing electron flux, reaches a maximum value, turns over, and has a lower etch rate at higher currents. The peak etch rate and range of the transition region are functions of the precursor impingement rate (gI_A) and the product residence time (τ_B). Figure 18 is a plot of the relative etch rate versus electron flux with various etch product lifetimes. This plot illustrates that increasing the product residence time decreases the threshold for the onset of the *etch product dissociation limited* regime. The longer the etch product resides on the surface, the more likely it will be re-dissociated by a subsequent energetic electron. Figure 19 shows the effect of increasing the etch product dissociation probability (B_σ). Increasing the likelihood of dissociating the etch product molecule results in decreasing the threshold for the onset of *etch product dissociation limited* etching. If the B_σ term becomes comparable to the A_σ term then the *mass transport limited (type II)* etching rate is also reduced.

The system of ordinary differential equations (19) and (20) can be converted to a system of partial differential equations (PDE) to solve for etching rate as a function of radius from the beam spot given a radial profile of the electron flux at the surface, that is Γ_e = f(r). Therefore, the effect of surface diffusion of the precursor and product molecules can be simulated.

$$\frac{\partial N_A}{\partial t} = D_A \nabla^2 N_A + g I_A \left[1 - \frac{N_A}{Z} - \frac{N_B}{Z}\right] - \frac{N_A}{\tau_A} - \frac{A_\sigma \Gamma_e N_A}{Z} \quad (2.28)$$

$$\frac{\partial N_B}{\partial t} = D_B \nabla^2 N_B + \frac{x A_\sigma \Gamma_e N_A}{Z} - \frac{N_B}{\tau_B} - \frac{B_\sigma \Gamma_e N_B}{Z} \quad (2.29)$$

D_A and D_B are the surface diffusion coefficients of the precursor and product molecules, respectively. The system of equations was solved using a second order Runge-Kutta algorithm with initial and boundary conditions. The initial condition for all radii of the gas concentrations was set to the equilibrium gas coverage level for the precursor gas considering the beam was off and the gas was flowing, the initial condition for the etch product gas was set to zero for all radii. The boundary conditions for the PDE were set as a Dirichlet boundary condition equal to the initial conditions for the outer radii boundary. That is, far away from the beam spot, it is assumed the precursor gas

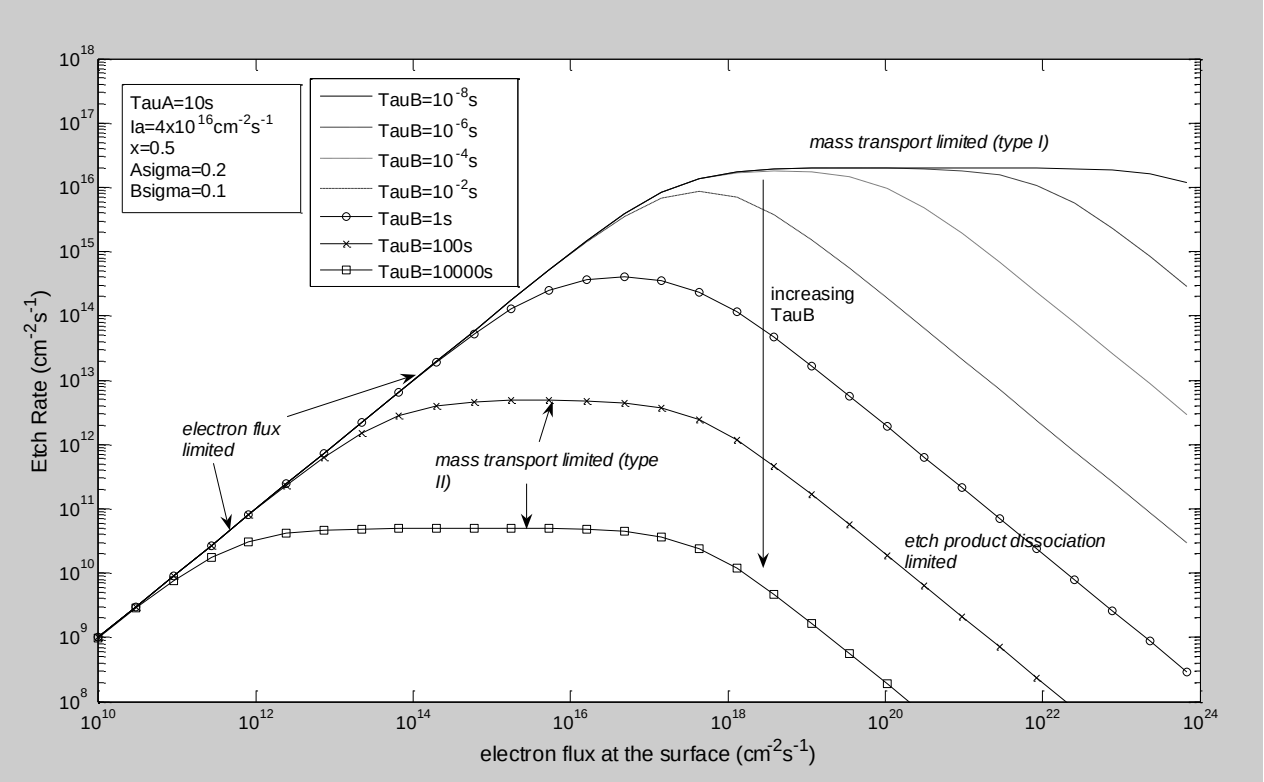

Figure 18: Precursor-Product EBIE Model: Effect of Etch Product Lifetime

Increasing the etch product residence time on the surface reduces the threshold for the onset of the etch product dissociation limited regime. The etching rate is reduced over multiple orders of magnitude as the etch product residence time increases.

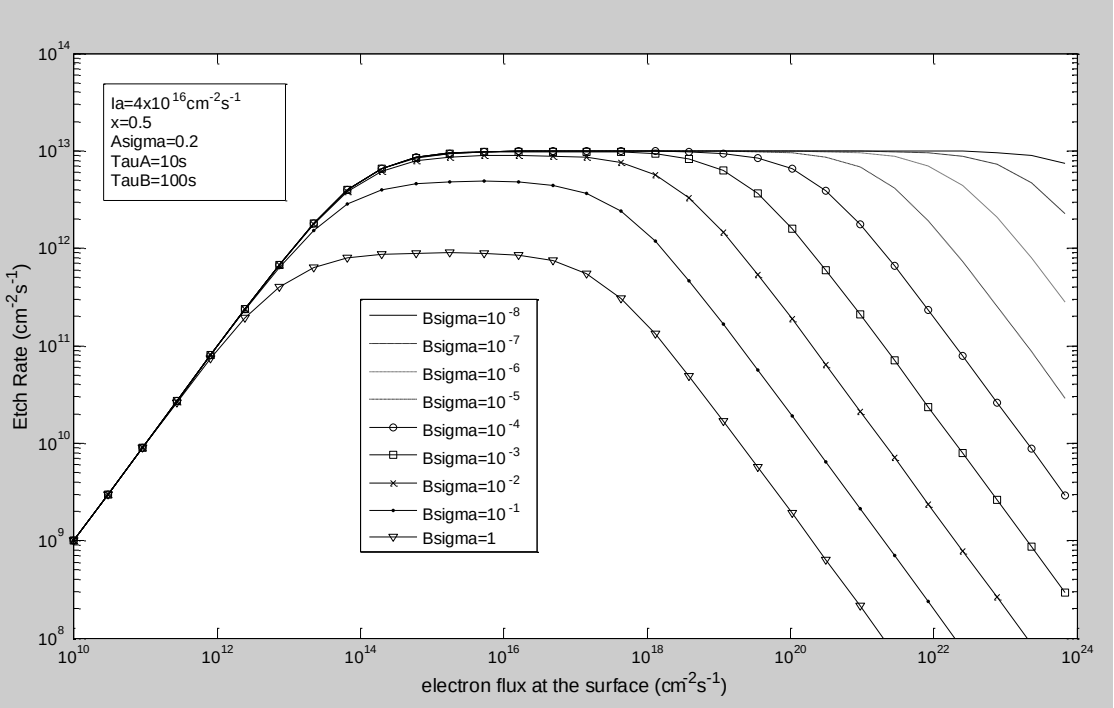

Figure 19: Precursor Product EBIE Model: Effect of Etch Product Dissociation Probability

As the product dissociation probability increases, the electron flux threshold for transitioning from the *mass transport limited* regime to the *etch product dissociation limited* regime is lowered. When B_σ becomes comparable to xA_σ, the etching rate is further reduced in the mass transport limited (type II) regime.

maintains an equilibrium coverage and there is zero coverage of the etch product. For the boundary at r=0, the Neumann boundary condition was used assuming the radial derivative of the concentrations of gas is zero at the center of the beam spot. This maintains continuity at the beam center. Time was then integrated until a steady state of gas concentrations was achieved. Based upon the radial profile of gas concentrations, the expected etching rate is calculated as a function of radius in terms of number of molecules of material etched per unit area per second.

Although all the specific parameters for the SiO_2-XeF_2 system are not known, we have simulated a variety of parameters to illustrate the observed experimental trends in Figure 12. Figure 20 is an example of how the simulated profile can change significantly with changes in beam current. Compared to the Figure 12 experimental results, the same trends are observed. There is a critical beam current (i.e. electron flux) that results in an *etch product dissociation limited* regime. Below that critical beam current, the etch profile takes on the shape of the beam, while above that current a moat effect is observed where the center etches slower than the periphery. Increasing the beam current further has the effect of increasing the radius of the moat in both the simulated and experimental results.

Additional Experimental

The Precursor-Product EBIE model was verified by comparing the etch profiles using a spot mode etch at various levels of defocus. The effect of defocus on the radial profile of the etching is shown in Figure 21. The moat effect has been observed on multiple substrates with xenon difluoride precursor. For this experiment a TaO_x/TaN thin film material was used (a typical extreme ultraviolet masking material)[2], which demonstrated the moat etching profile. The TaO_x film is about 20nm thick and is stable to xenon difluoride in the absence of the electron beam. The underlying TaN film is about 50 nm thick and etches spontaneously on exposure to xenon difluoride[67]. The TaO_x/TaN film sits on a thin Ru etch stop layer that offers a very high etch selectivity. The TaO_x/TaN film stack was chosen because it best illustrates the fact that the etch rate slows significantly in the *etch product dissociation limited* regime. The defocus experiment was performed using a 30keV beam energy, a 100 pA sample current, and an etch time of 60 seconds. Initially, the beam was focused to the best focus and the initial etch was performed. Then the beam was manually de-focused by turning the focus knob 0.5 of a turn which equates to ~ 500 μm defocus and the film was etched again. Etches were then performed after the beam was then de-focused another half of a turn (~ 1mm total defocus) and another whole turn (2mm total defocus), respectively.

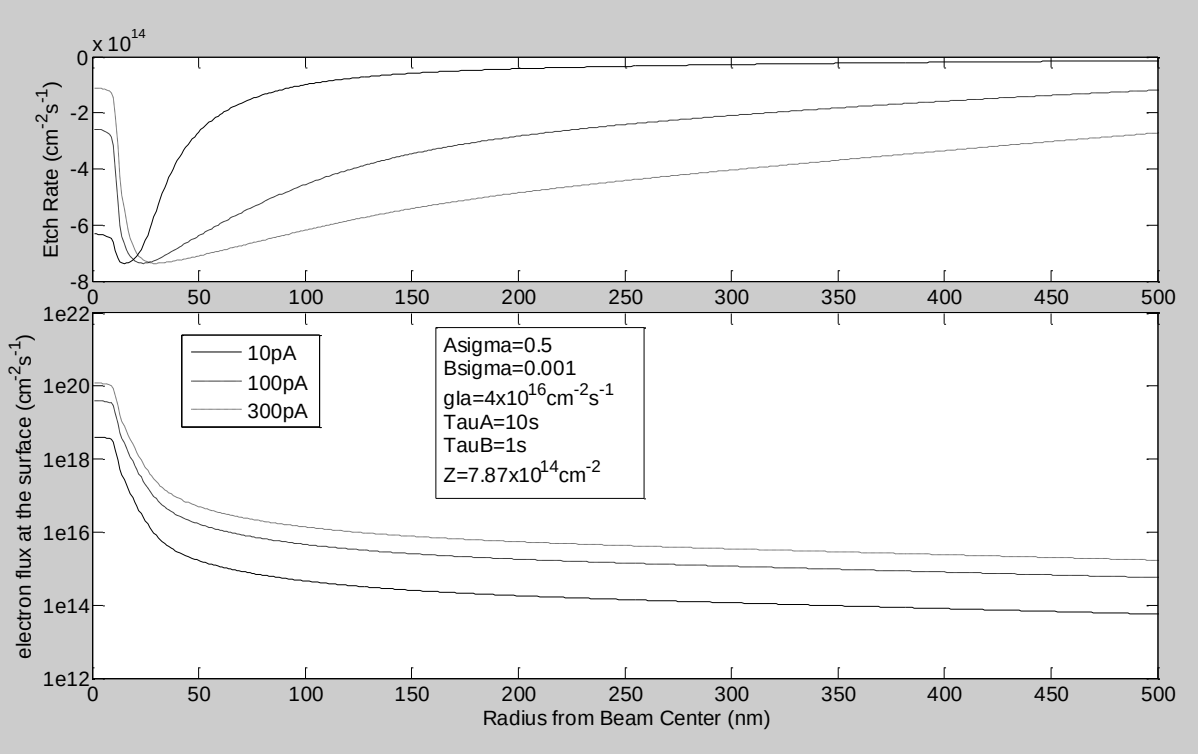

Figure 20: Spatial Resolved Simulation of Experimental Results

The highest beam current results in a "moat" shape and a low etching rate at the center (*etch product dissociation limited*). Lowering the beam current reduces the radius of maximum etch rate. Further lowering of the beam current eliminates the moat shape and leaves the center as the fastest etching in a *mass transport limited (type II)* regime.

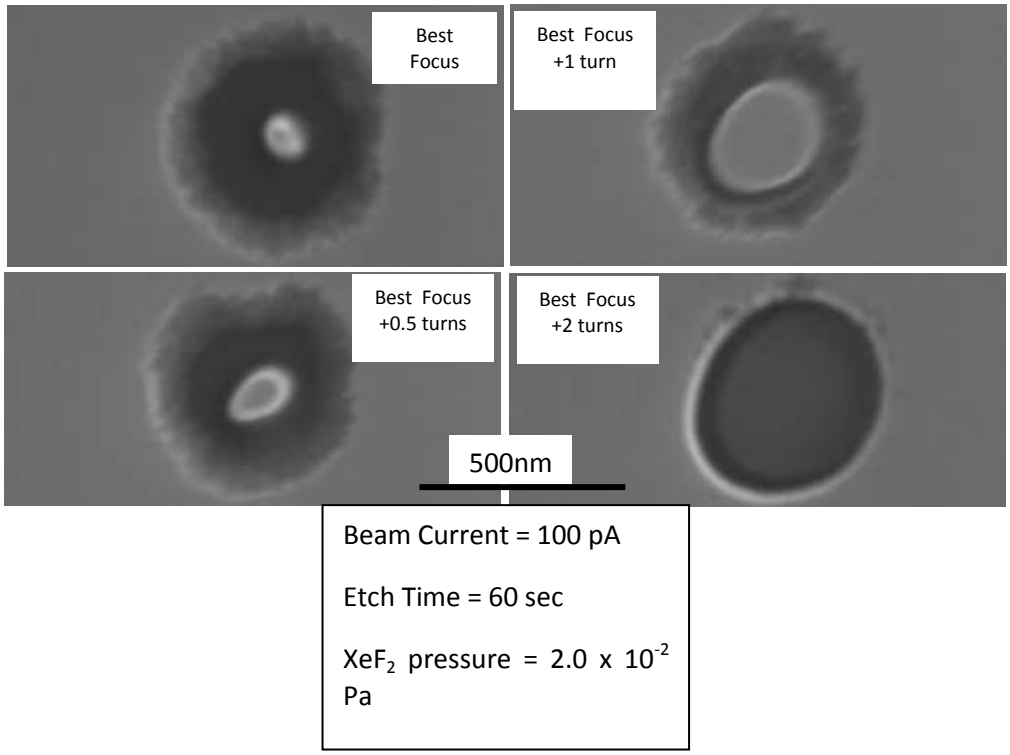

Figure 21: The Effect of Defocus on Etch Shape

At high electron flux under the beam spot at best focus, the etching rate is reduced by the etch product dissociation limited regime. The moat effect is observed as the back-scattered electrons (BSE) and BSE generated secondary electrons (SE_{II}) cause the etching of the substrate at larger radii from the beam spot. Defocus of the e-beam results in a decrease of the electron flux under the beam spot by spreading the beam across a larger area. For the first two levels of defocus, the flux under the beam spot is still high enough to result in an etch product dissociation limited regime under a larger area. Further defocus results in a reduction of the electron flux under the beam spot to a mass transport limited regime that results in a uniform etch rate under the e-beam.

When the beam is defocused, the peak electron flux is reduced and the shape of the profile changes from an Airy disc shape (diffraction limited) to a cylindrical shape with a skirt. Figure 21 shows the effect of defocus on the etch shape for a fixed beam current and gas pressure. In this case, there appear to be two thresholds for the etching regime transitions. In the outer periphery where the electron flux is low, the etch rate increases with decreasing radius according to an *electron flux limited* regime. There appears to be a range of radii, therefore a range of electron fluxes, where the etch rate is uniform and the etching is in a *mass transport limited* regime. Closest to the beam spot, the electron flux is highest, and the etch rate is diminished, in an *etch product dissociation limited* regime. This is consistent with the simulated results of etch rate as a function of electron flux demonstrated in Figures 13, 18, and 19. As the beam is defocused, the radius of the transition from *mass transport limited* to *etch productdissociation limited* regimes increases. This is seen in the first two levels of defocus of Figure 21. As the beam is further defocused, the peak electron flux continues to drop and eventually reaches the case where the entire region under the beam is below the critical electron flux for *etch product dissociation limited* etching. So, a uniform *mass transport limited* etching rate is observed with a more abrupt transition through the *electron flux limited* regime. The defocus experiment was simulated using the Precursor-Product EBIE model and the results are seen in Figure 22. The same trends are observed in the simulation as in the experimental data. Moving from the periphery towards the center, there is clearly a region of radii (thus electron fluxes) at which the etching switches to a uniform *mass transport limited* regime, then the etching rate slows down under the higher electron flux of the impinging beam. As the beam is defocused, the size of the beam increases, while the electron flux under the beam decreases. For the first two levels of defocus, the electron flux under the impinging beam is still high enough to inhibit the etch rate. Under the most severe defocus, the electron flux under the beam is below the threshold for the onset of the *etch product dissociation limited* regime, and thus we observe a uniform *mass transport limited (type II)* etching under the entire impinging beam spot. This behavior cannot be explained using only a Precursor EBIE model with surface diffusion.

Summary

To summarize, Figure 23 shows various etch profiles (normalized etch depth versus radius) to demonstrate the effect that surface diffusion, etch product residence time, and etch product dissociation probability have on EBIE. For increasing surface diffusion coefficients, note that there is little difference between the zero surface diffusion and the $10^{-12}cm^2s^{-1}$. After the diffusion coefficients ($D=D_A=D_B$) increase above $10^{-12}cm^2s^{-1}$, there is a noticeable effect. For small etch product lifetimes, the Precursor-Product EBIE model reduces to the Precursor EBIE model and there is only *etch product dissociation*

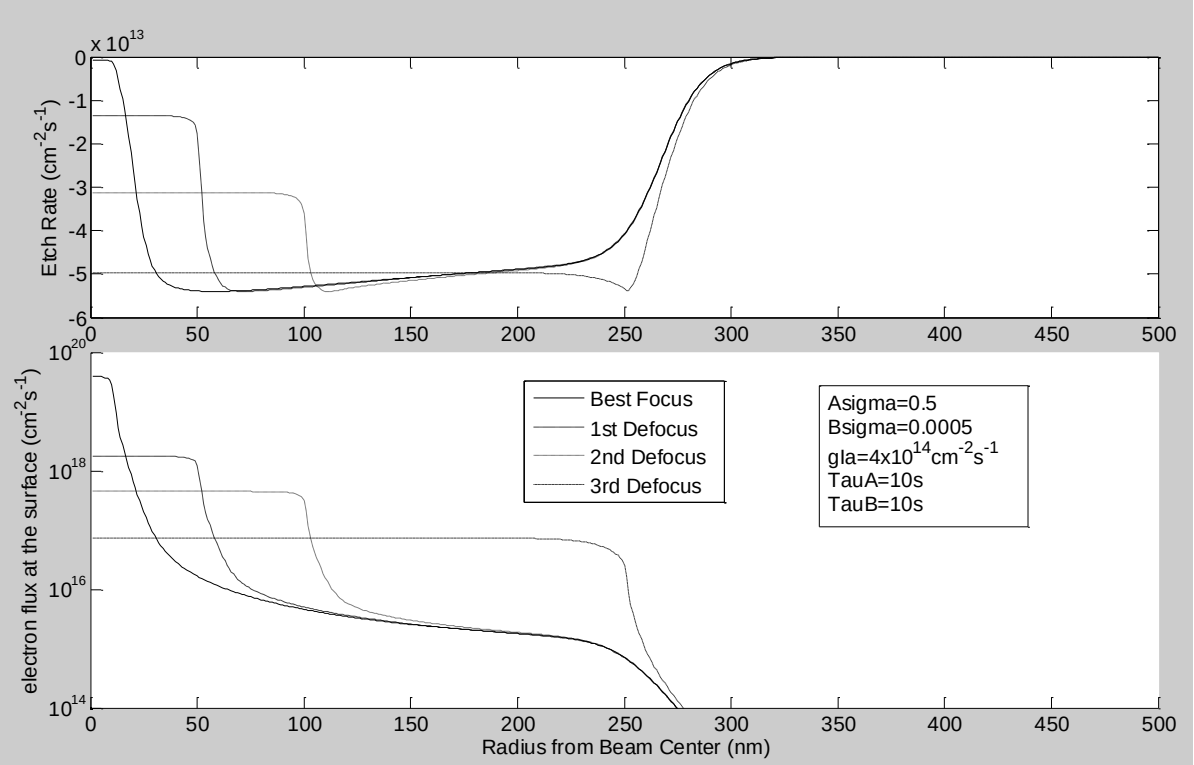

Figure 22: Simulation of Defocus Experiment

A simulation of the radial electron flux profile (bottom) combined with the Precursor-Product EBIE model gives the expected profiles (top). Note that the best focus and the first two levels of defocus exhibit the *etch product dissociation limited* regime, while at the third level of defocus only *mass transport limited* etching is observed in the center region.

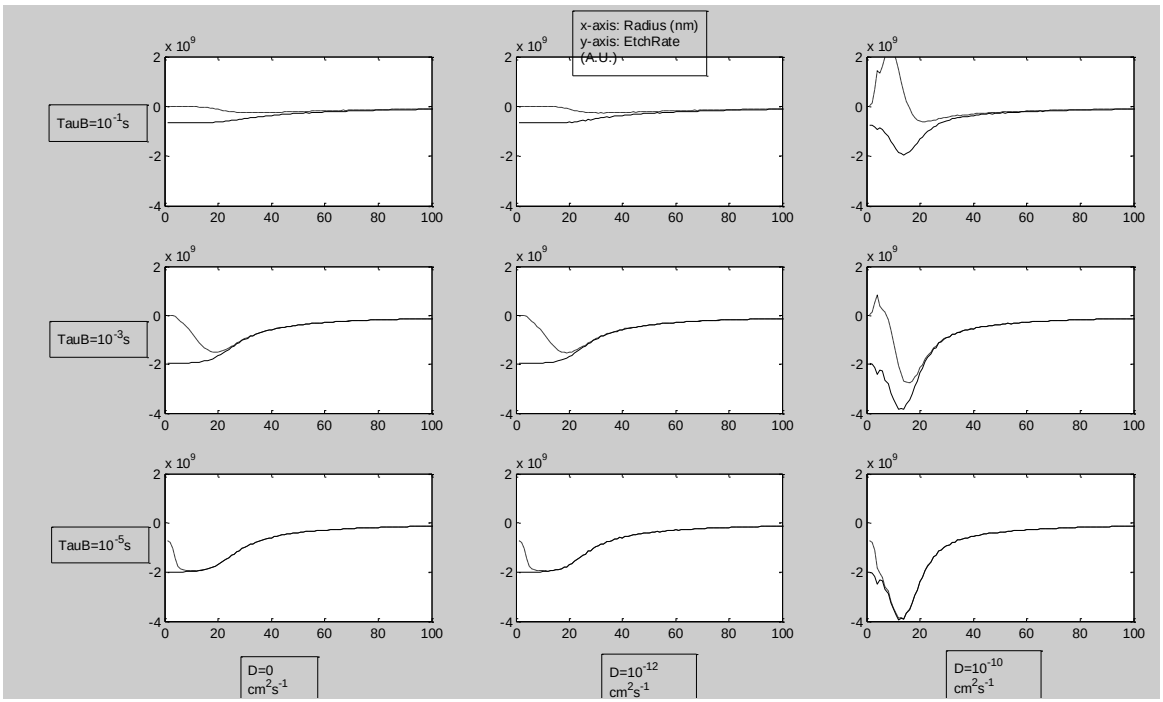

Figure 23: Simulated radial etch profiles

The surface diffusion coefficient ($D=D_A=D_B$), etch product residence time (τ_B), and the etch product dissociation probability (B_σ) were varied to investigate the various effects on the etch shape. The x-axes are radial position in nm, and the y-axes are etch profile in arbitrary units. The solid lines represent a $B_\sigma=0.0$ and the dashed line represent a $B_\sigma=0.1$. The electron flux profile is that of Figure 4. Note that for fast surface diffusion and long etch product residence times, it is possible for the material etched in the periphery to be redeposited closer to the beam center, resulting in a net deposit in some regions.

limited etching at the highest electron flux closest to the beam center. As the etch product residence time increases, the size of the *etch product dissociation limited* regime increases as a lower electron flux is required to enter this regime. Also, the *mass transport limited* etching region transitions from *Type I (impingement rate limited)* to *Type II (etch product desorption limited)*. Note that for fast surface diffusion and long etch product residence times, it is possible for the material etched in the periphery to be redeposited closer to the beam center, resulting in a net deposit in some regions. This is the result of the fact that there is a ring of etch product concentration that results from the dissociation of the etch product near the beam center. The radial gradient in the etch product concentration results in a net surface flux both away from the center and towards the center. The etch product that diffuses away from the center will reach a spatial region with a lower electron flux making it more likely that the etch product can thermally desorb. The etch product that diffuses to the center reaches a region with a much higher electron flux. This makes it more likely to be dissociated and redeposit the original solid material. The net effect is a movement of material from one region of radii to closer radii. Of course, this is only possible when the product residence time is long and the surface diffusion coefficient is high. These are thermodynamically opposing effects. In order to the increase surface diffusion coefficient, the temperature must be increased, but increasing the temperature will also decrease the etch product residence time.

It is worthwhile to discuss the parameter space that would give the optimal resolution in a spot mode etching. The highest resolution can be obtained by keeping the entire area under the beam spot in an *electron flux limited* regime, then the beam shape exactly determines the etch shape. This can be accomplished by several means: increasing the molecular impingement rate, decreasing the beam current, and/or increasing the temperature. Increasing the molecular impingement increases the threshold for transition to the *mass transport limited* regime, ensuring the high electron flux in the center of the beam remains in the *electron flux limited* regime. Ultimately, the pressure could become too high for the electron beam to travel without significant gas phase collisions, resulting in an altered beam shape. Also, if τ_B is too large, the *mass transport limited (type II)* and *etch product dissociation* regimes will dominate and increasing the molecular impingement rate will not help. Decreasing the beam current helps to reduce the peak flux below the regime transition, but also results in poor imaging quality in the microscope. Raising the substrate temperature will result in lowering both τ_A and τ_B. The result of lowering τ_B is the elimination of unwanted *mass transport limited (type II)* and *etch product dissociation limited* regimes. Reducing τ_A lowers the precursor coverage, thus reducing the etch rate in peripheral areas under low electron flux while extending the *electron flux limited* regime to higher electron fluxes (see Figure 14). Increasing the temperature too high could reduce the precursor coverage too much and result in impracticably slow etching rates.

Chapter 3: Time Dependent Behavior

Overview

In order to understand the effects of beam dwell time (τ_{dwell}) and beam refresh time ($\tau_{refresh}$) have on the net amount of material etched, it is necessary to analytically solve the system of simultaneous ordinary differential equations. Once the analytical solution is determined, then the etching and re-deposition rates as functions of time can be determined. Integration of the instantaneous etching rate gives an analytical solution for the material etched as a function of the process parameters and beam scanning parameters.

Analytical Solutions

The system of ordinary differential equations:

$$\frac{dN_A}{dt} = gI_A\left(1 - \frac{N_A}{Z} - \frac{N_B}{Z}\right) - \frac{N_A}{\tau_A} - \frac{A_\sigma \Gamma_e N_A}{Z} - \frac{A_{ESD}\Gamma_e N_A}{Z}$$

$$\frac{dN_B}{dt} = \frac{xA_\sigma \Gamma_e N_A}{Z} - \frac{N_B}{\tau_B} - \frac{B_\sigma \Gamma_e N_B}{Z} - \frac{B_{ESD}\Gamma_e N_B}{Z}$$

can be written in a general form:

$$\frac{d}{dt}\begin{bmatrix} N_A \\ N_B \end{bmatrix} = \begin{bmatrix} a & b \\ c & d \end{bmatrix}\begin{bmatrix} N_A \\ N_B \end{bmatrix} + \begin{bmatrix} e \\ f \end{bmatrix}$$

where:

$$a = -\left(\frac{gI_A}{Z} + \frac{1}{\tau_A} + \frac{(A_\sigma + A_{ESD})\Gamma_e}{Z}\right)$$

$$b = -\frac{gI_A}{Z}$$

$$c = \frac{xA_\sigma \Gamma_e}{Z}$$

$$d = -\left(\frac{1}{\tau_B} + \frac{(B_\sigma + B_{ESD})\Gamma_e}{Z}\right)$$

$$e = gI_A$$

$$f = 0$$

The system has a center point at:

$$\frac{d}{dt}\begin{bmatrix} N_A \\ N_B \end{bmatrix} = 0 = \begin{bmatrix} a & b \\ c & d \end{bmatrix}\begin{bmatrix} N_{A\infty} \\ N_{B\infty} \end{bmatrix} + \begin{bmatrix} e \\ f \end{bmatrix}$$

$$\begin{bmatrix} a & b \\ c & d \end{bmatrix}\begin{bmatrix} N_{A\infty} \\ N_{B\infty} \end{bmatrix} = \begin{bmatrix} -e \\ -f \end{bmatrix}$$

$$\begin{bmatrix} N_{A\infty} \\ N_{B\infty} \end{bmatrix} = \frac{1}{ad - bc}\begin{bmatrix} d & -b \\ -c & a \end{bmatrix}\begin{bmatrix} -e \\ -f \end{bmatrix}$$

$$\begin{bmatrix} N_{A\infty} \\ N_{B\infty} \end{bmatrix} = \begin{bmatrix} bf - de/ad - bc \\ ce - af/ad - bc \end{bmatrix}$$

Finding the eigenvalues of the system from the definition:

$$det\begin{bmatrix} a - \lambda & b \\ c & d - \lambda \end{bmatrix} = 0$$

$$(a - \lambda)(d - \lambda) - bc = 0$$

$$\lambda^2 - (a + d)\lambda + (ad - bc) = 0$$

$$\lambda = \frac{(a + d) \pm \sqrt{(a + d)^2 - 4(ad - bc)}}{2}$$

The corresponding eigenvectors can be derived from:

$$\begin{bmatrix} a - \lambda & b \\ c & d - \lambda \end{bmatrix}\begin{bmatrix} k_1 \\ k_2 \end{bmatrix} = 0$$

Choosing k_1=1 the eigenvectors are:

$$\begin{bmatrix} 1 \\ \frac{\lambda - a}{b} \end{bmatrix} \; or \; \begin{bmatrix} 1 \\ \frac{c}{\lambda - d} \end{bmatrix}$$

Choosing the former definition of the eigenvectors, the general solution to the system of ordinary differential equations is:

$$\begin{bmatrix} N_A \\ N_B \end{bmatrix} = c_1 \begin{bmatrix} 1 \\ \frac{\lambda_1 - a}{b} \end{bmatrix} e^{\lambda_1 t} + c_2 \begin{bmatrix} 1 \\ \frac{\lambda_2 - a}{b} \end{bmatrix} e^{\lambda_2 t} + \begin{bmatrix} N_{A\infty} \\ N_{B\infty} \end{bmatrix}$$

The constants c_1 and c_2 depend upon the initial values of the system. Rearranging the solution at t=0 and solving for the constants:

$$\begin{bmatrix} N_{A0} - N_{A\infty} \\ N_{B0} - N_{B\infty} \end{bmatrix} = \begin{bmatrix} 1 & 1 \\ \frac{\lambda_1 - a}{b} & \frac{\lambda_2 - a}{b} \end{bmatrix} \begin{bmatrix} c_1 \\ c_2 \end{bmatrix}$$

$$\begin{bmatrix} c_1 \\ c_2 \end{bmatrix} = \frac{1}{\frac{\lambda_2 - a}{b} - \frac{\lambda_1 - a}{b}} \begin{bmatrix} \frac{\lambda_2 - a}{b} & -1 \\ \frac{a - \lambda_1}{b} & 1 \end{bmatrix} \begin{bmatrix} N_{A0} - N_{A\infty} \\ N_{B0} - N_{B\infty} \end{bmatrix}$$

$$\begin{bmatrix} c_1 \\ c_2 \end{bmatrix} = \frac{b}{\lambda_2 - \lambda_1} \begin{bmatrix} \frac{\lambda_2 - a}{b} & -1 \\ \frac{a - \lambda_1}{b} & 1 \end{bmatrix} \begin{bmatrix} N_{A0} - N_{A\infty} \\ N_{B0} - N_{B\infty} \end{bmatrix}$$

$$\begin{bmatrix} c_1 \\ c_2 \end{bmatrix} = \begin{bmatrix} \frac{\lambda_2 - a}{\lambda_2 - \lambda_1} & \frac{-b}{\lambda_2 - \lambda_1} \\ \frac{a - \lambda_1}{\lambda_2 - \lambda_1} & \frac{b}{\lambda_2 - \lambda_1} \end{bmatrix} \begin{bmatrix} N_{A0} - N_{A\infty} \\ N_{B0} - N_{B\infty} \end{bmatrix}$$

$$\begin{bmatrix} c_1 \\ c_2 \end{bmatrix} = \begin{bmatrix} \frac{\lambda_2 - a}{\lambda_2 - \lambda_1}(N_{A0} - N_{A\infty}) - \frac{b}{\lambda_2 - \lambda_1}(N_{B0} - N_{B\infty}) \\ \frac{a - \lambda_1}{\lambda_2 - \lambda_1}(N_{A0} - N_{A\infty}) + \frac{b}{\lambda_2 - \lambda_1}(N_{B0} - N_{B\infty}) \end{bmatrix}$$

This leads to the general solution for the system:

$$\begin{bmatrix} N_A \\ N_B \end{bmatrix}$$
$$= \begin{bmatrix} \dfrac{\lambda_2 - a}{\lambda_2 - \lambda_1}(N_{A0} - N_{A\infty}) - \dfrac{b}{\lambda_2 - \lambda_1}(N_{B0} - N_{B\infty}) \\ \left(\dfrac{\lambda_1 - a}{b}\right)\dfrac{\lambda_2 - a}{\lambda_2 - \lambda_1}(N_{A0} - N_{A\infty}) - \dfrac{\lambda_1 - a}{\lambda_2 - \lambda_1}(N_{B0} - N_{B\infty}) \end{bmatrix} e^{\lambda_1 t}$$
$$+ \begin{bmatrix} \dfrac{a - \lambda_1}{\lambda_2 - \lambda_1}(N_{A0} - N_{A\infty}) + \dfrac{b}{\lambda_2 - \lambda_1}(N_{B0} - N_{B\infty}) \\ \left(\dfrac{\lambda_2 - a}{b}\right)\dfrac{a - \lambda_1}{\lambda_2 - \lambda_1}(N_{A0} - N_{A\infty}) + \dfrac{\lambda_2 - a}{\lambda_2 - \lambda_1}(N_{B0} - N_{B\infty}) \end{bmatrix} e^{\lambda_2 t} + \begin{bmatrix} N_{A\infty} \\ N_{B\infty} \end{bmatrix}$$

Substitution of the expressions of the eigenvalues and subsequently the parameters a through f gives an exact expression for the surface concentrations as a function of the process parameters. This expression is cumbersome and is not readily intuitive for understanding the impact of each process parameter. It is best to consider different process regimes as in the case of the static electron beam and reduce the exact equation to a simpler approximate form.

It was discussed in the prior chapter the net etch rate (expressed as a negative quantity) is the rate of re-deposition due to etch product dissociation minus the rate of etch product creation. That is:

$$\frac{d(Etched)}{dt} = \frac{B_\sigma \Gamma_e N_B}{Z} - \frac{x A_\sigma \Gamma_e N_A}{Z}$$

Definite integration of this expression gives the amount of material etched as a function of the beam dwell time.

$$Etched = \int_{t=0}^{t=\tau_{dwell}} \left(\frac{B_\sigma \Gamma_e N_B}{Z} - \frac{x A_\sigma \Gamma_e N_A}{Z}\right) dt$$

$$Etched = \frac{\Gamma_e}{Z}\left[B_\sigma \int_{t=0}^{t=\tau_{dwell}} N_B \, dt - x A_\sigma \int_{t=0}^{t=\tau_{dwell}} N_A \, dt\right]$$

Substitution of the exact solution for the precursor and etch product concentrations leaves an onerous equation, but many of the terms are negligible. For each process regime, a reduced approximation for $N_A(t)$ and $N_B(t)$ can be used inside the integrals making the ultimate expression compact.

Small Product Residence Time, Electron Flux Limited Regime

In this regime, the electron flux is much less than the molecular impingement rate and the average surface residence time of the etch product is small (<10^{-6}seconds). That is the product thermally desorbs before either another electron or another precursor molecule impinges on the surface. The substitution parameters a-f reduce as follows:

$$a \approx -\left(\frac{gI_A}{Z} + \frac{1}{\tau_A}\right)$$

$$b = -\frac{gI_A}{Z}$$

$$c = \frac{xA_\sigma \Gamma_e}{Z}$$

$$d \approx -\frac{1}{\tau_B}$$

$$e = gI_A$$

$$f = 0$$

Substitution a-f into the form for the eigenvalues:

$$\lambda = \frac{(a+d) \pm \sqrt{(a+d)^2 - 4(ad-bc)}}{2}$$

$$\lambda \approx \frac{-\left(\frac{gI_A}{Z} + \frac{1}{\tau_A} + \frac{1}{\tau_B}\right) \pm \sqrt{\left(\frac{gI_A}{Z} + \frac{1}{\tau_A} + \frac{1}{\tau_B}\right)^2 - 4\left(\left(\frac{gI_A}{Z} + \frac{1}{\tau_A}\right)\frac{1}{\tau_B} + \frac{gI_A}{Z}\frac{xA_\sigma \Gamma_e}{Z}\right)}}{2}$$

When considering the relative sizes of molecular impingement, electron flux, and product residence time, the expression simplifies to:

$$\lambda \approx \frac{-\left(\frac{1}{\tau_B}\right) \pm \sqrt{\left(\frac{1}{\tau_B}\right)^2 - 4\left(\left(\frac{gI_A}{Z} + \frac{1}{\tau_A}\right)\frac{1}{\tau_B}\right)}}{2}$$

Taking advantage of the first order Taylor series expansion:

$$\sqrt{\alpha^2+\beta} \approx \alpha + \frac{\beta}{2\alpha} \; for \; \alpha^2 \gg \beta$$

$$\lambda \approx \frac{-\left(\frac{1}{\tau_B}\right) \pm \left(\frac{1}{\tau_B} - 2\left(\frac{gI_A}{Z} + \frac{1}{\tau_A}\right)\right)}{2}$$

$$\lambda_1 \approx -\frac{1}{\tau_B}$$

$$\lambda_2 \approx -\left(\frac{gI_A}{Z} + \frac{1}{\tau_A}\right)$$

Substitution into the exact equation for $N_A(t)$ and $N_B(t)$ results in:

$$\begin{bmatrix} N_A \\ N_B \end{bmatrix} = \begin{bmatrix} \frac{gI_A}{Z}\tau_B(N_{B0} - xA_\sigma\Gamma_e\theta_A\tau_B) \\ (N_{B0} - xA_\sigma\Gamma_e\theta_A\tau_B) \end{bmatrix} e^{-\frac{t}{\tau_B}} + \begin{bmatrix} (N_{A0} - \theta_A Z) - \frac{gI_A}{Z}\tau_B(N_{B0} - xA_\sigma\Gamma_e\theta_A\tau_B) \\ 0 \end{bmatrix} e^{-\left(\frac{gI_A}{Z}+\frac{1}{\tau_A}\right)t} + \begin{bmatrix} \theta_A Z \\ xA_\sigma\Gamma_e\theta_A\tau_B \end{bmatrix}$$

Where θ_A is the equilibrium coverage of precursor gas in the absence of the electron beam:

$$\theta_A = \frac{gI_A}{\left(gI_A + \frac{Z}{\tau_A}\right)}$$

Recognizing that the steady state coverage of etch product is very small when τ_B is small, further simplification gives us:

$$\begin{bmatrix} N_A \\ N_B \end{bmatrix} = \begin{bmatrix} \frac{gI_A}{Z}\tau_B(N_{B0}) \\ (N_{B0}) \end{bmatrix} e^{-\frac{t}{\tau_B}} + \begin{bmatrix} (N_{A0} - \theta_A Z) - \frac{gI_A}{Z}\tau_B(N_{B0}) \\ 0 \end{bmatrix} e^{-\left(\frac{gI_A}{Z}+\frac{1}{\tau_A}\right)t} + \begin{bmatrix} \theta_A Z \\ 0 \end{bmatrix}$$

Now using this approximation for integrating the amount of etched material:

$$Etched = \frac{\Gamma_e}{Z}\left[B_\sigma \int_{t=0}^{t=\tau_{dwell}} N_B\, dt - xA_\sigma \int_{t=0}^{t=\tau_{dwell}} N_A\, dt\right]$$

$$Etched = \frac{\Gamma_e}{Z}\left[B_\sigma \int_{t=0}^{t=\tau_{dwell}} \left(N_{B0} e^{-\frac{t}{\tau_B}}\right) dt - xA_\sigma \int_{t=0}^{t=\tau_{dwell}} \left(\frac{gI_A}{Z}\tau_B (Ni_{B0}) e^{-\frac{t}{\tau_B}} + \left((N_{A0} - \theta_A Z) - \frac{gI_A}{Z}\tau_B (N_{B0})\right) e^{-\left(\frac{gI_A}{Z}+\frac{1}{\tau_A}\right)t} + \theta_A Z\right) dt\right]$$

$$Etched = \frac{\Gamma_e}{Z}\left[B_\sigma N_{B0}\tau_B \left(1 - e^{-\frac{\tau_{dwell}}{\tau_B}}\right) - xA_\sigma \frac{gI_A}{Z}{\tau_B}^2 N_{B0}\left(1 - e^{-\frac{\tau_{dwell}}{\tau_B}}\right) - xA_\sigma \left(\frac{(N_{A0} - \theta_A Z) - \frac{gI_A}{Z}\tau_B (N_{B0})}{\left(\frac{gI_A}{Z} + \frac{1}{\tau_A}\right)}\right)\left(1 - e^{-\left(\frac{gI_A}{Z}+\frac{1}{\tau_A}\right)\tau_{dwell}}\right) - xA_\sigma \theta_A Z \tau_{dwell}\right]$$

$$Etched = B_\sigma \frac{\Gamma_e}{Z} N_{B0}\tau_B \left(1 - e^{-\frac{\tau_{dwell}}{\tau_B}}\right) - xA_\sigma \frac{\Gamma_e}{Z}\frac{gI_A}{Z}{\tau_B}^2 N_{B0}\left(1 - e^{-\frac{\tau_{dwell}}{\tau_B}}\right) - xA_\sigma \frac{\Gamma_e}{Z}\left(\frac{(N_{A0} - \theta_A Z) - \frac{gI_A}{Z}\tau_B N_{B0}}{\left(\frac{gI_A}{Z} + \frac{1}{\tau_A}\right)}\right)\left(1 - e^{-\left(\frac{gI_A}{Z}+\frac{1}{\tau_A}\right)\tau_{dwell}}\right) - xA_\sigma \Gamma_e \theta_A \tau_{dwell}$$

The first term and second term relate to deposition events from existing product on the surface at the beginning of the beam dwell time. In this regime we are assuming a small product residence time (τ_B) and a small electron flux (Γ_e), so these terms are insignificant even in the worst case of N_{B0}=Z. That is, nearly all of any surplus of etch

product on the surface will desorb from the surface before being dissociated and leaving a re-deposit. The third term accounts for any depletion in the initial precursor coverage from the equilibrium coverage, this can be significant for small dwell times. If the initial coverage is depleted, then the etching rate is slower as it waits for the sites to be filled by impinging precursor molecules. In this case there is an initial mass transport limit to the etch rate until the equilibrium coverage is approached, then the rate is limited by the electron flux. If the sites are initially at the equilibrium coverage level, or the dwell time is sufficiently long, then the only term of significance is the fourth term which is identical to the steady state etching rate discussed in Chapter 2.

Removing the insignificant terms due to a small product residence time leaves:

$$Etched = -xA_\sigma \frac{\Gamma_e}{Z}\left(\frac{(N_{A0}-\theta_A Z)}{\left(\frac{gI_A}{Z}+\frac{1}{\tau_A}\right)}\right)\left(1-e^{-\left(\frac{gI_A}{Z}+\frac{1}{\tau_A}\right)\tau_{dwell}}\right) - xA_\sigma \Gamma_e \theta_A \tau_{dwell}$$

The dwell time in this regime could be broken down into two regions: the *precursor accumulation region* and the *steady state region*. The *precursor accumulation region* is only relevant if the precursor started in a depleted state. The time scale for this region is determined by the molecular impingement rate.

The process variables used consistently through this section for the purpose of illustrating the time dependent effects in these equations are: gI_A=4.0x10^{17}cm^{-2}s^{-1}, Z=1x10^{15}cm^{-2}, τ_A=1.0s, A_σ=0.1, B_σ=0.05 and stoichiometry factor x=0.5. For simplicity, the probabilities of electron stimulated desorption are kept at zero for both precursor and etch product. For the consideration of small etch product residence time, τ_B=10^{-7}s; and for large etch product residence time, τ_B=10s.

Figure 24 illustrates the effect of electron flux on the gas surface concentrations for this regime. Starting under the initial conditions of N_{A0}=Z and N_{B0}=0, it is seen that the precursor concentration remains mostly unaffected by the relatively small amount of electron flux. The etch product concentration reaches a steady state on the time scale of the fast eigenvalue (τ_B=10^{-7}s). The steady state level that the etch product reaches depends upon the electron flux.

Figure 25 illustrates the etching as a function of the dwell time for the conditions of Figure 24. The etching is linear in time and proportional to electron flux. There is no re-dissociation and re-deposition because of the short residence time of the etch product and the small electron flux.

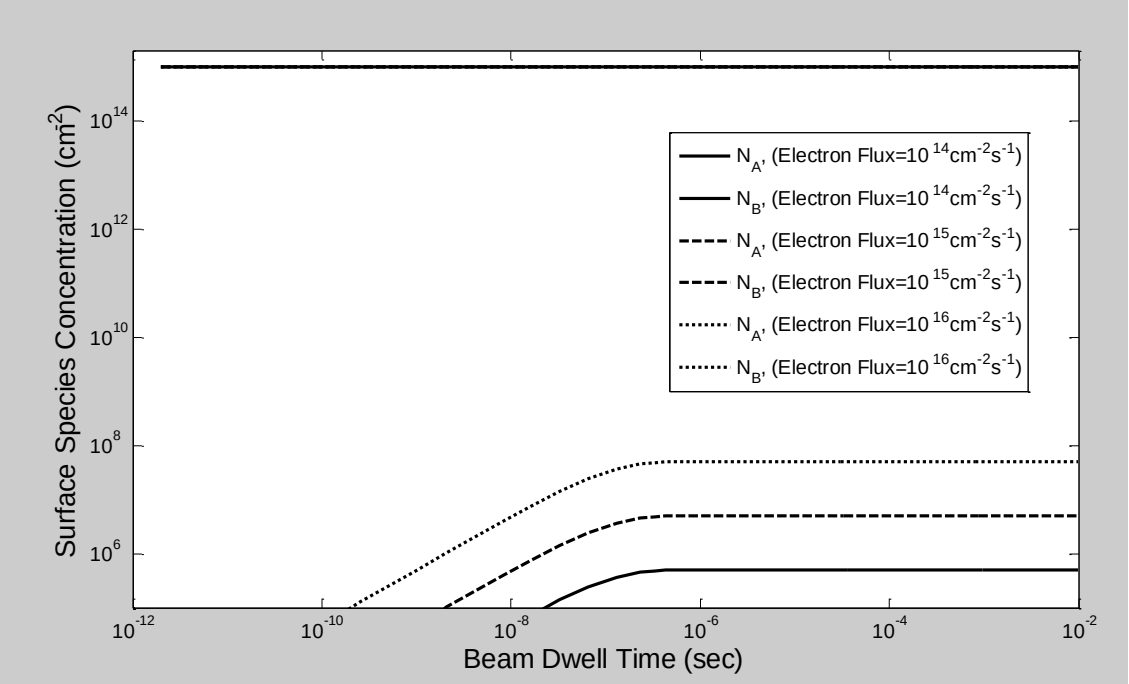

Figure 24: *Small Product Residence Time, Electron Flux Limited Regime*: Time dependence of Precursor and Etch Product Surface Concentration versus Electron Flux.

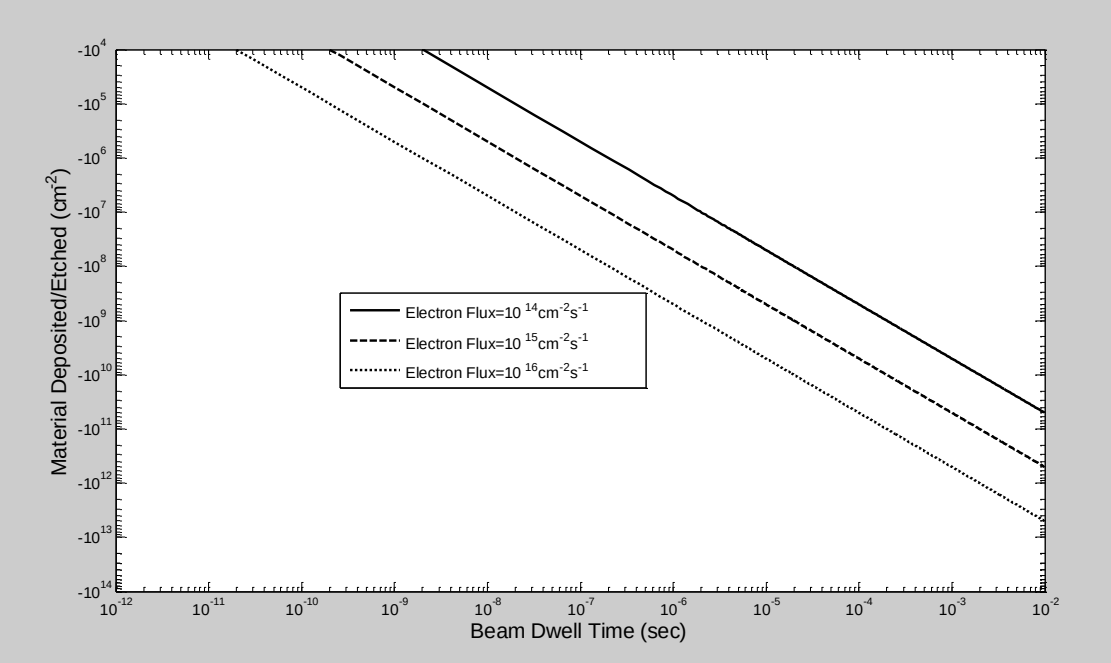

Figure 25: ***Small Product Residence Time, Electron Flux Limited Regime*****: Time Dependence of Etching versus Electron Flux**

The effects of differing initial conditions are potted in Figure 26 using an electron flux of $10^{15}cm^{-2}s^{-1}$. Of note, is the fact that no matter the initial conditions, the gases come to the same steady state levels. For the cases where the precursor concentration starts low, the system is waiting for the gas sites to fill with impinging precursor molecules; and the etch product concentration is limited by the precursor concentration. For cases where the etch product concentration starts high, the system first relaxes along the fast eigenvector at a time scale of the fast eigenvalue of (τ_B=10^{-7}s). Then the etch product concentration follows its precursor concentration limited path to steady state.

The results of differing the initial conditions on the time dependent behavior of etching in this regime are plotted in Figure 27. Just as the equation suggests, there is no impact on the etching by the initial condition of etch product, but if the initial condition of precursor is depleted, then the etching rate will be slowed until the precursor reaches the equilibrium concentration.

Small Product Residence Time, Mass Transport Limited Regime

In this regime, the electron flux is much higher than the molecular impingement rate and the average surface residence time of the etch product is small (<10^{-6}seconds). The etch product thermally desorbs before interacting with another electron or impinging precursor molecule. The substitution parameters a-f reduce as follows:

$$a \approx -\frac{(A_\sigma + A_{ESD})\Gamma_e}{Z}$$

$$b = -\frac{gI_A}{Z}$$

$$c = \frac{xA_\sigma\Gamma_e}{Z}$$

$$d \approx -\frac{1}{\tau_B}$$

$$e = gI_A$$

$$f = 0$$

Substitution a-f into the form for the eigenvalues:

$$\lambda = \frac{(a+d) \pm \sqrt{(a+d)^2 - 4(ad-bc)}}{2}$$

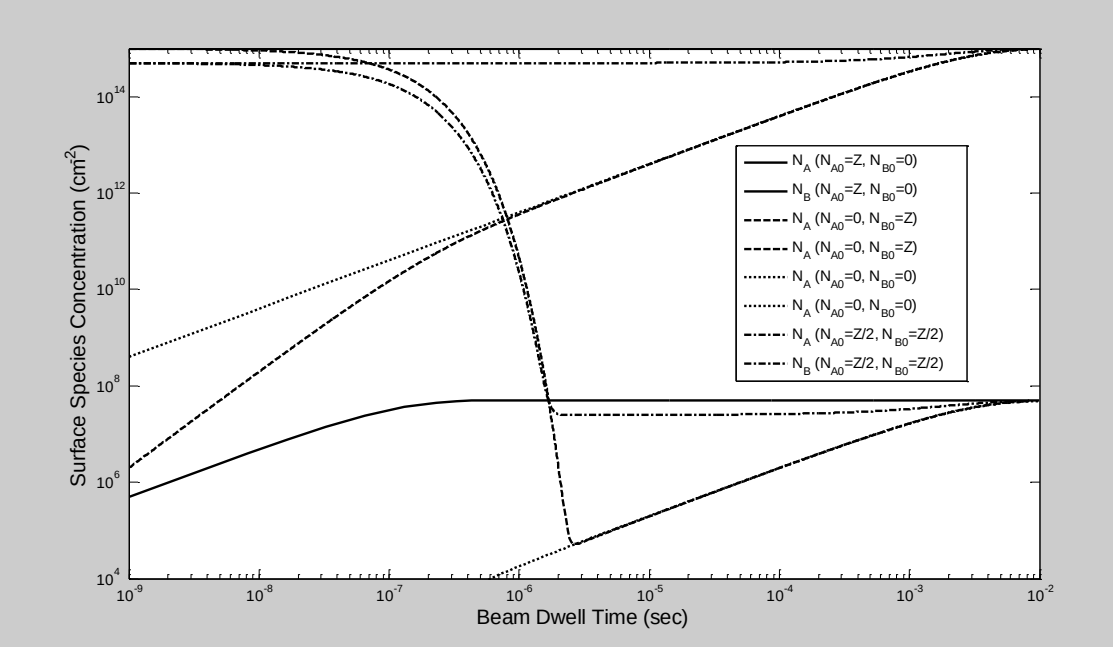

Figure 26: ***Small Product Residence Time, Electron Flux Limited Regime*****: Time Dependence of Precursor and Etch Product Surface Concentrations versus Initial Conditions**

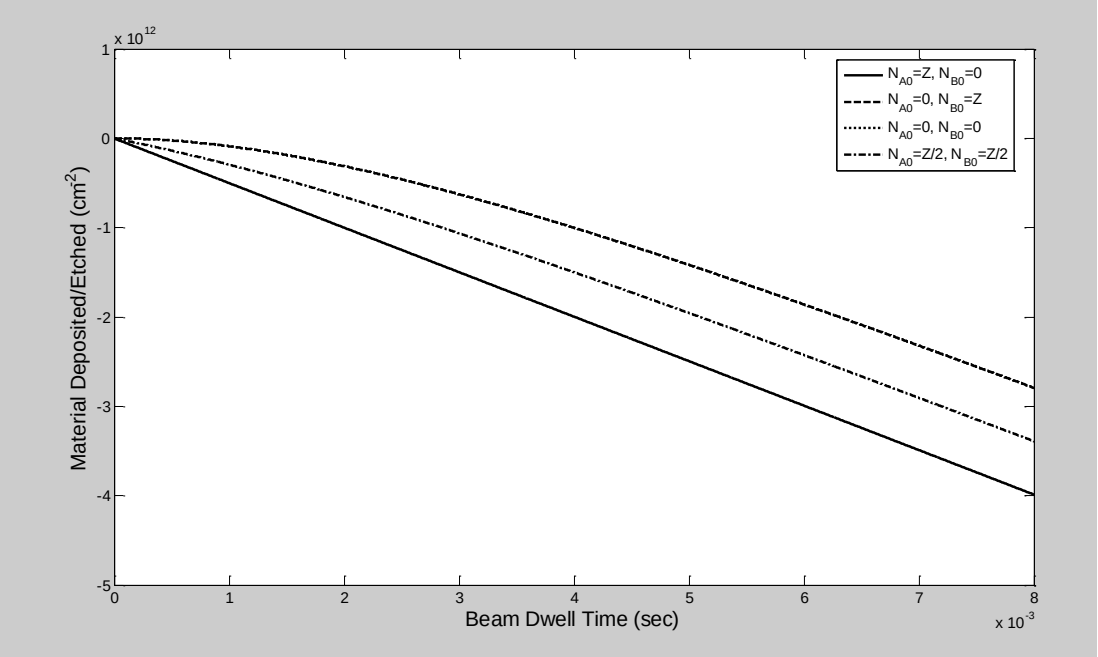

Figure 27: *Small Product Residence Time, Electron Flux Limited Regime*: Time Dependence of Etching versus Initial Conditions

$$\lambda \approx \frac{-\left(\frac{(A_\sigma + A_{ESD})\Gamma_e}{Z} + \frac{1}{\tau_B}\right) \pm \sqrt{\left(\frac{(A_\sigma + A_{ESD})\Gamma_e}{Z} + \frac{1}{\tau_B}\right)^2 - 4\left(\left(\frac{(A_\sigma + A_{ESD})\Gamma_e}{Z}\right)\frac{1}{\tau_B} + \frac{gI_A}{Z}\frac{xA_\sigma\Gamma_e}{Z}\right)}}{2}$$

This simplifies to:

$$\lambda \approx \frac{-\left(\frac{(A_\sigma + A_{ESD})\Gamma_e}{Z} + \frac{1}{\tau_B}\right) \pm \sqrt{\left(\frac{(A_\sigma + A_{ESD})\Gamma_e}{Z}\right)^2 + \left(\frac{1}{\tau_B}\right)^2 - 2\left(\left(\frac{(A_\sigma + A_{ESD})\Gamma_e}{Z}\right)\frac{1}{\tau_B}\right)}}{2}$$

$$\lambda \approx \frac{-\left(\frac{(A_\sigma + A_{ESD})\Gamma_e}{Z} + \frac{1}{\tau_B}\right) \pm \sqrt{\left(\frac{(A_\sigma + A_{ESD})\Gamma_e}{Z} - \frac{1}{\tau_B}\right)^2}}{2}$$

$$\lambda \approx \frac{-\left(\frac{(A_\sigma + A_{ESD})\Gamma_e}{Z} + \frac{1}{\tau_B}\right) \pm \left|\frac{(A_\sigma + A_{ESD})\Gamma_e}{Z} - \frac{1}{\tau_B}\right|}{2}$$

$$\lambda \approx \frac{-\left(\frac{(A_\sigma + A_{ESD})\Gamma_e}{Z} + \frac{1}{\tau_B}\right) \pm \left|\frac{(A_\sigma + A_{ESD})\Gamma_e}{Z} - \frac{1}{\tau_B}\right|}{2}$$

$$\lambda_1 \approx -\frac{(A_\sigma + A_{ESD})\Gamma_e}{Z}$$

$$\lambda_2 \approx -\frac{1}{\tau_B}$$

Or vice versa depending upon which has the larger absolute value. This results in a solution for the precursor and product concentrations.

$$\begin{bmatrix} N_A \\ N_B \end{bmatrix} = \begin{bmatrix} (N_{A0} - N_{A\infty}) + \dfrac{\dfrac{gI_A}{Z}}{\dfrac{(A_\sigma + A_{ESD})\Gamma_e}{Z} - \dfrac{1}{\tau_B}} (N_{B0} - N_{B\infty}) \\ 0 \end{bmatrix} e^{-\frac{(A_\sigma + A_{ESD})\Gamma_e}{Z} t}$$

$$+ \begin{bmatrix} -\dfrac{\dfrac{gI_A}{Z}}{\dfrac{(A_\sigma + A_{ESD})\Gamma_e}{Z} - \dfrac{1}{\tau_B}} (N_{B0} - N_{B\infty}) \\ (N_{B0} - N_{B\infty}) \end{bmatrix} e^{-\frac{1}{\tau_B} t} + \begin{bmatrix} N_{A\infty} \\ N_{B\infty} \end{bmatrix}$$

$$\begin{bmatrix} N_A \\ N_B \end{bmatrix}$$

$$= \begin{bmatrix} \left(N_{A0} - \dfrac{gI_A Z}{(A_\sigma + A_{ESD})\Gamma_e}\right) + \dfrac{\dfrac{gI_A}{Z}}{\dfrac{(A_\sigma + A_{ESD})\Gamma_e}{Z} - \dfrac{1}{\tau_B}} \left(N_{B0} - \dfrac{xA_\sigma gI_A \tau_B}{A_\sigma + A_{ESD}}\right) \\ 0 \end{bmatrix} e^{-\frac{(A_\sigma + A_{ESD})\Gamma_e}{Z} t}$$

$$+ \begin{bmatrix} -\dfrac{\dfrac{gI_A}{Z}}{\dfrac{(A_\sigma + A_{ESD})\Gamma_e}{Z} - \dfrac{1}{\tau_B}} \left(N_{B0} - \dfrac{xA_\sigma gI_A \tau_B}{A_\sigma + A_{ESD}}\right) \\ \left(N_{B0} - \dfrac{xA_\sigma gI_A \tau_B}{A_\sigma + A_{ESD}}\right) \end{bmatrix} e^{-\frac{1}{\tau_B} t} + \begin{bmatrix} \dfrac{gI_A Z}{(A_\sigma + A_{ESD})\Gamma_e} \\ \dfrac{xA_\sigma gI_A \tau_B}{A_\sigma + A_{ESD}} \end{bmatrix}$$

Further simplification can be made by recognizing steady state coverage of product is extremely small with small product residence times. The approximate solution becomes:

$$\begin{bmatrix} N_A \\ N_B \end{bmatrix} \approx \begin{bmatrix} N_{A0} - \dfrac{gI_A Z}{(A_\sigma + A_{ESD})\Gamma_e} \\ 0 \end{bmatrix} e^{\frac{-(A_\sigma + A_{ESD})\Gamma_e}{Z} t} + \begin{bmatrix} 0 \\ N_{B0} \end{bmatrix} e^{-\frac{1}{\tau_B} t} + \begin{bmatrix} \dfrac{gI_A Z}{(A_\sigma + A_{ESD})\Gamma_e} \\ 0 \end{bmatrix}$$

It can be seen from the above equation that in this regime, the steady state coverage of precursor is inversely proportional to the electron flux, and directly proportional to the molecular impingement rate. The initial coverage of precursor will exponentially approach the steady state at a rate dependent upon the electron flux. The higher the electron flux, the faster the rate. Any initial coverage of etch product will rapidly desorb due to the small τ_B. Integrating this approximation to get the amount of material etched as a function of dwell time, process conditions, and initial conditions:

$$Etched = \frac{\Gamma_e}{Z}\left[B_\sigma \int_{t=0}^{t=\tau_{dwell}} N_B\, dt - xA_\sigma \int_{t=0}^{t=\tau_{dwell}} N_A\, dt\right]$$

$$Etched = \frac{\Gamma_e}{Z}\left[B_\sigma \int_{t=0}^{t=\tau_{dwell}} N_{B0} e^{-\frac{1}{\tau_B}t}\, dt - xA_\sigma \int_{t=0}^{t=\tau_{dwell}} \left[\left(N_{A0} - \frac{gI_A Z}{(A_\sigma + A_{ESD})\Gamma_e}\right) e^{\frac{-(A_\sigma + A_{ESD})\Gamma_e}{Z}t} + \frac{gI_A Z}{(A_\sigma + A_{ESD})\Gamma_e}\right] dt\right]$$

$$Etched = \frac{\Gamma_e}{Z}\left[B_\sigma N_{B0}\tau_B\left(1 - e^{-\frac{\tau_{dwell}}{\tau_B}}\right) - xA_\sigma\left(N_{A0} - \frac{gI_A Z}{(A_\sigma + A_{ESD})\Gamma_e}\right)\frac{Z}{(A_\sigma + A_{ESD})\Gamma_e}\left(1 - e^{\frac{-(A_\sigma + A_{ESD})\Gamma_e}{Z}\tau_{dwell}}\right) - xA_\sigma \frac{gI_A Z\tau_{dwell}}{(A_\sigma + A_{ESD})\Gamma_e}\right]$$

$$Etched = B_\sigma N_{B0}\frac{\Gamma_e}{Z}\tau_B\left(1 - e^{-\frac{\tau_{dwell}}{\tau_B}}\right) - \frac{xA_\sigma}{A_\sigma + A_{ESD}}\left(N_{A0} - \frac{gI_A Z}{(A_\sigma + A_{ESD})\Gamma_e}\right)\left(1 - e^{\frac{-(A_\sigma + A_{ESD})\Gamma_e}{Z}\tau_{dwell}}\right) - \frac{xA_\sigma}{A_\sigma + A_{ESD}} gI_A\tau_{dwell}$$

The first term is positive and describes the amount of the initial product coverage that is re-deposited before it could desorb from the surface. This requires an initially high coverage of etch product, which is not likely considering that in this regime the etch product residence time is short. Also, the amount of re-deposit is proportional to the product residence time. The shorter this time, the less likely to be re-deposited and the more likely to desorb.

The second term above describes the etching due to the initial coverage of precursor. Since the electron flux is higher than the molecular impingement rate, once the initial coverage is consumed, the rate is limited by the arrival of new precursor to the surface (third term above). The *mass transport limited* regime is modified by the fractional probability of dissociation versus electron induced desorption.

In this case there is no *precursor accumulation region* because the precursor is headed toward a depleted state. The temporal behavior during the beam dwell is best described by a *precursor depletion region* and a *steady state region*. The *precursor depletion region* has a time scale dependent upon the electron flux and the respective probabilities of dissociation and electron stimulated desorption.

The time dependence on the gas surface concentrations for differing electron flux is plotted in Figure 28. Using initial conditions of N_{A0}=Z and N_{B0}=0, it is seen that the etch product rapidly accumulates along the fast eigenvector on the timescale of the fast eigenvalue (τ_B=10^{-7}s). The etch product concentration reaches its precursor concentration limited level. Now, as the electron flux is higher than the molecular impingement rate, the precursor concentration will deplete to a level much lower than the beam off equilibrium level. This happens on the time scale of the slower eigenvalue, which is dependent upon the electron flux. So, higher electron flux means shorter time to reach steady state precursor concentration, as illustrated in Figure 28. As the precursor concentration falls, so does the etch product concentration. In the *steady state region*, the etch product concentration comes to the same level regardless of electron flux. Once the initial precursor coverage is depleted, the rate of etch product formation is constant and limited by the arrival rate of new precursor to the surface, independent of the electron flux for this regime.

Plotting the resulting etching as functions of beam dwell time in Figure 29, we find that the etch rate is initially dependent upon the electron flux, then decreases until the initial coverage of precursor is depleted, from that point on, the etching rate is *mass transport limited* and independent of the electron flux.

Figure 30 plots the results of a fixed electron flux of 10^{22}cm^{-2}s^{-1} with different initial conditions. The precursor concentration goes from its initial condition towards its steady state value along a time scale of the first eigenvalue ($e^{-\frac{(A_\sigma+A_{ESD})\Gamma_e}{Z}t}$), while the etch product concentration approaches a value that is limited by the precursor concentration at a rate determined by the second eigenvalue ($e^{-\frac{1}{\tau_B}t}$). In this regime, the etch product residence time (τ_B) is small, so the etch product reaches a level limited by the time-dependent concentration of precursor before the precursor reaches its steady state concentration. So, for cases where the precursor starts high (N_{A0}=Z, N_{B0}=0), the etch product will accumulate until it reaches a precursor concentration limited state, then it will fall as the precursor depletes to its steady state concentration. When the precursor starts low (N_{A0}=0, N_{B0}=0 or N_{A0}=0, N_{B0}=Z), the etch product still follows the fast eigenvector, accumulating or depleting, towards a precursor limited state. The precursor concentration increases towards the steady state, while the etch product then increases with it. The case of mixed initial conditions (N_{A0}=Z/2, N_{B0}=Z/2) shows that the

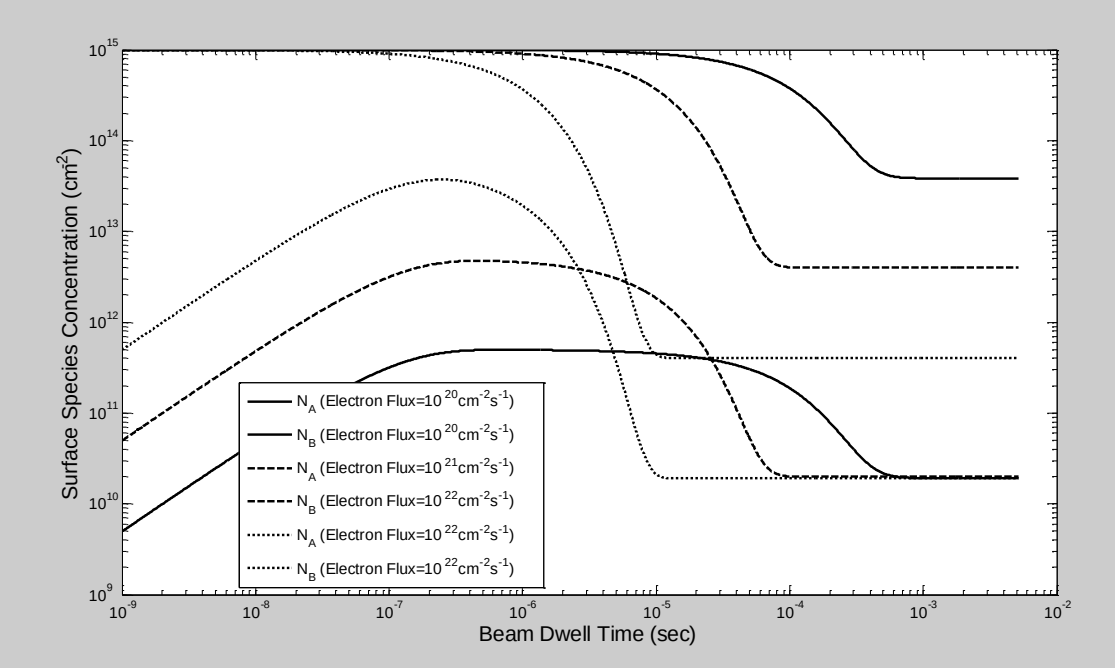

Figure 28: ***Small Product Residence Time, Mass Transport Limited Regime*****: Time Dependence of Precursor and Etch Product Surface Concentration versus Electron Flux**

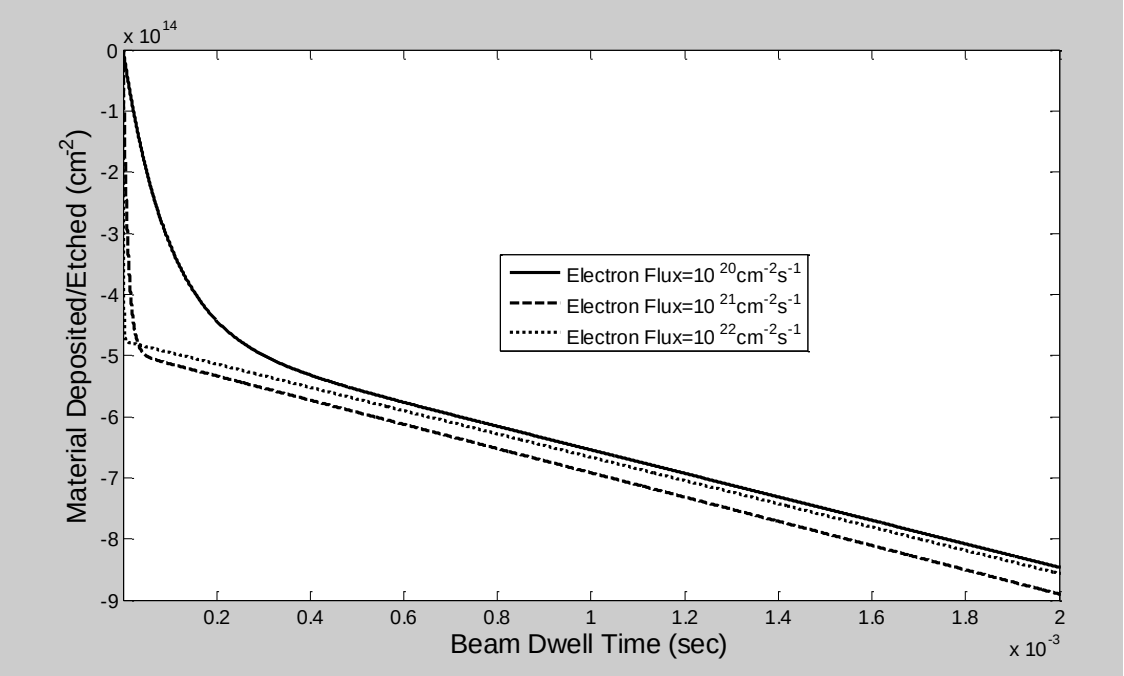

Figure 29: ***Small Product Residence Time, Mass Transport Limited Regime*****: Time Dependence of Etching versus Electron Flux**

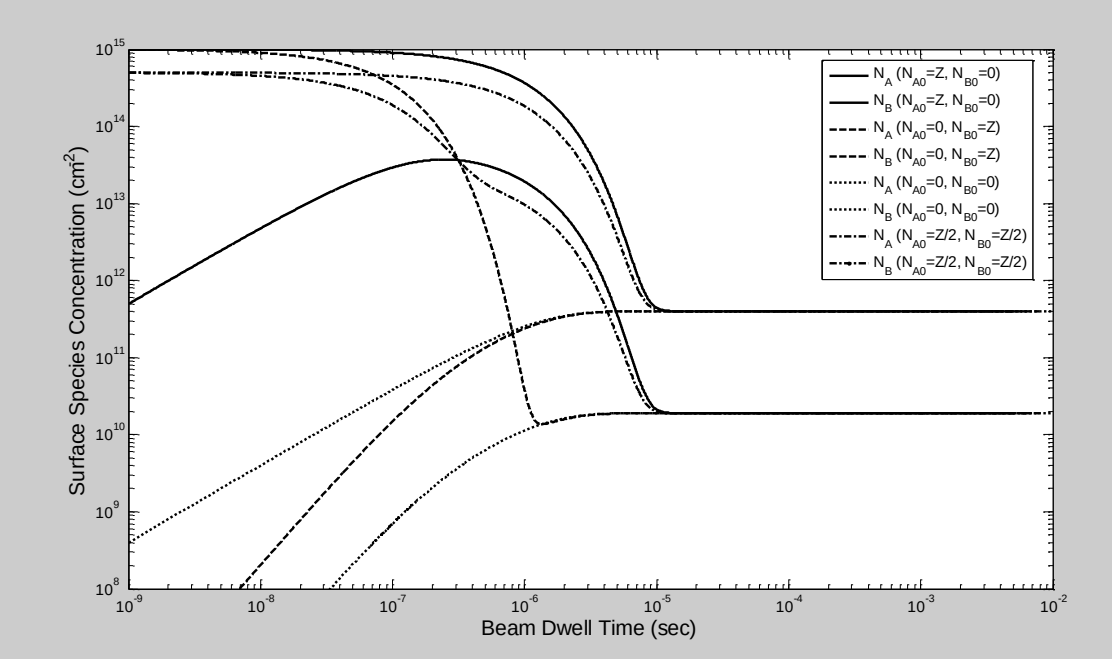

Figure 30: ***Small Product Residence Time, Mass Transport Limited Regime*****: Time Dependence of Precursor and Etch Product Surface Concentrations versus Initial Conditions**

etch product will desorb until it reaches the precursor limited state, and then it follows the precursor down to the steady state.

The impact of the various initial conditions on the material etched is seen in Figure 31 (logarithmic time scale) and Figure 32 (linear time scale). Even though the etch product has a short residence time, the electron flux is high enough to cause some of the initial etch product to re-deposit. So, cases with high initial condition of etch product show a net deposit for small beam dwell times, before the steady state etching rate is achieved. For cases where there is little initial etch product on the surface, the etch rate depends upon the excess coverage (or lack thereof) of precursor until the steady state is achieved.

Large Product Residence Time, Electron Flux Limited Regime

This regime involves an electron flux less than the molecular impingement rate, but a large product residence time. The regime behaves the same as the *small product residence time, electron flux limited regime*; but the first terms are now relevant as the etch product residence time is long.

Starting with the solution for the precursor and etch product concentrations:

$$\begin{bmatrix} N_A \\ N_B \end{bmatrix} = \begin{bmatrix} \frac{gI_A}{Z}\tau_B(N_{B0} - xA_\sigma\Gamma_e\theta_A\tau_B) \\ (N_{B0} - xA_\sigma\Gamma_e\theta_A\tau_B) \end{bmatrix} e^{-\frac{t}{\tau_B}} + \begin{bmatrix} (N_{A0} - \theta_A Z) - \frac{gI_A}{Z}\tau_B(N_{B0} - xA_\sigma\Gamma_e\theta_A\tau_B) \\ 0 \end{bmatrix} e^{-\left(\frac{gI_A}{Z}+\frac{1}{\tau_A}\right)t} + \begin{bmatrix} \theta_A Z \\ xA_\sigma\Gamma_e\theta_A\tau_B \end{bmatrix}$$

Due to large etch product residence time (τ_B), the simplifications made earlier cannot be ignored. Integration gives the material etched:

$$Etched = \frac{\Gamma_e}{Z}\left[B_\sigma \int_{t=0}^{t=\tau_{dwell}} N_B\, dt - xA_\sigma \int_{t=0}^{t=\tau_{dwell}} N_A\, dt\right]$$

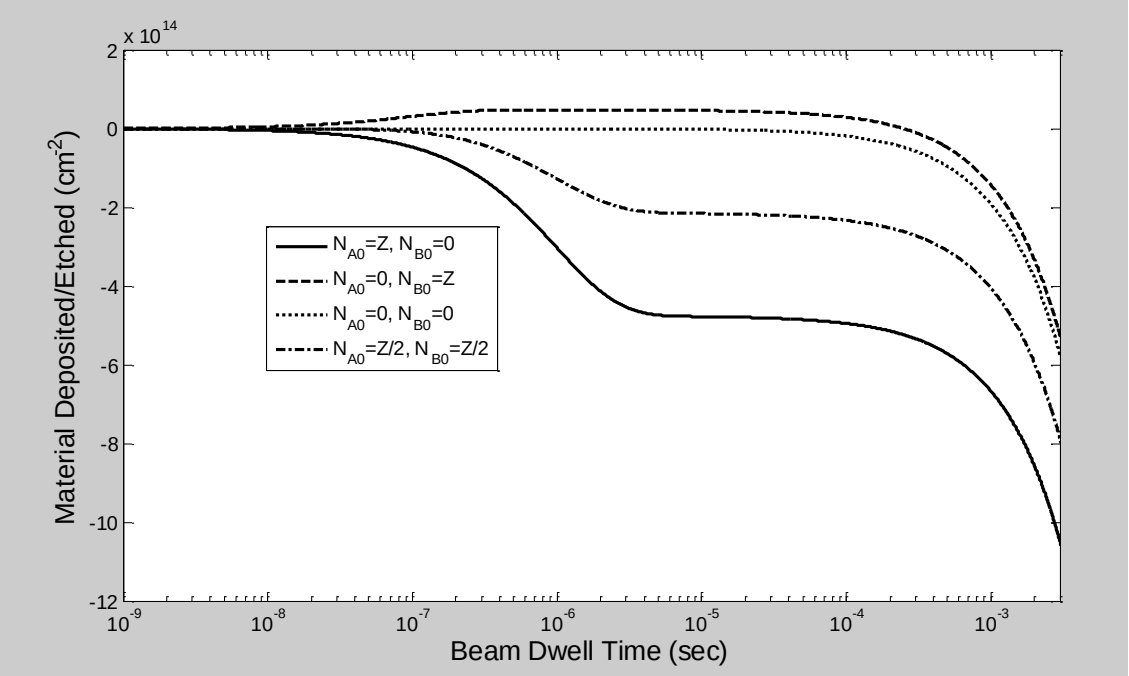

Figure 31: ***Small Product Residence Time, Mass Transport Limited Regime*****: Time Dependence of Etching versus Initial Conditions**

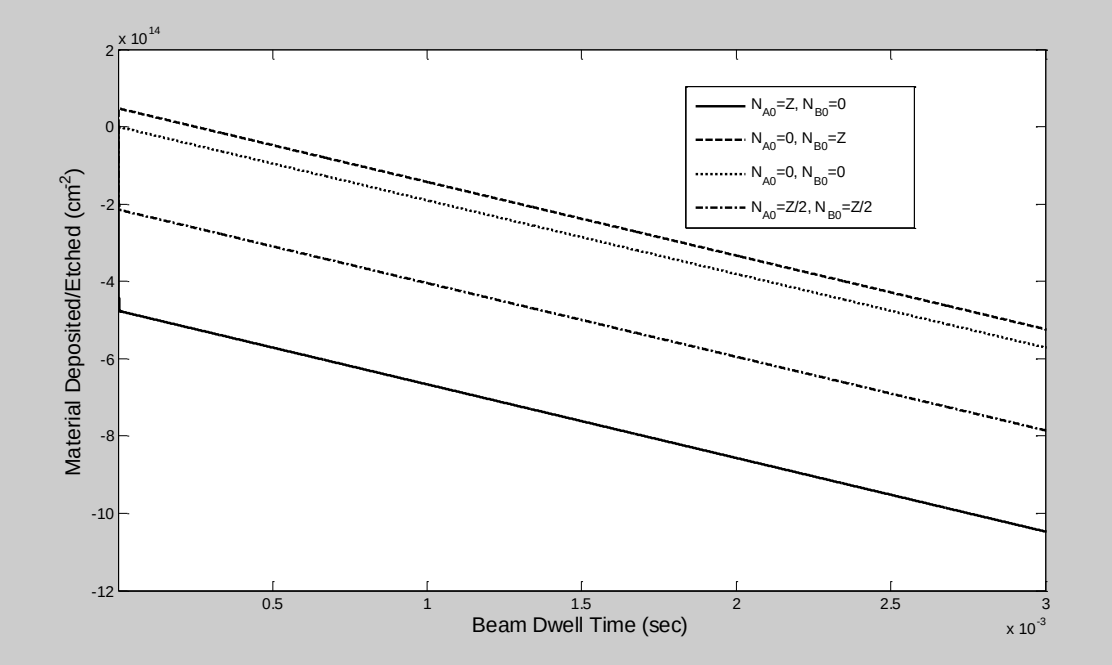

Figure 32: ***Small Product Residence Time, Mass Transport Limited Regime*****: Time Dependence of Etching versus Initial Conditions**

$$Etched = \frac{\Gamma_e}{Z}\left[B_\sigma \int_{t=0}^{t=\tau_{dwell}} \left[(N_{B0} - xA_\sigma\Gamma_e\theta_A\tau_B)e^{-\frac{t}{\tau_B}} + xA_\sigma\Gamma_e\theta_A\tau_B\right]dt \right.$$
$$- xA_\sigma \int_{t=0}^{t=\tau_{dwell}} \left[\frac{gI_A}{Z}\tau_B(N_{B0} - xA_\sigma\Gamma_e\theta_A\tau_B)e^{-\frac{t}{\tau_B}}\right.$$
$$\left. + \left((N_{A0} - \theta_A Z) - \frac{gI_A}{Z}\tau_B(N_{B0} - xA_\sigma\Gamma_e\theta_A\tau_B)\right)e^{-\left(\frac{gI_A}{Z}+\frac{1}{\tau_A}\right)t}\right.$$
$$\left. \left. + \theta_A Z\right]dt\right]$$

$$Etched = \frac{\Gamma_e}{Z}\left[B_\sigma\tau_B(N_{B0} - xA_\sigma\Gamma_e\theta_A\tau_B)\left(1 - e^{-\frac{\tau_{dwell}}{\tau_B}}\right)\right.$$
$$+ B_\sigma\tau_B xA_\sigma\Gamma_e\theta_A\tau_{dwell}$$
$$- xA_\sigma\frac{gI_A}{Z}{\tau_B}^2(N_{B0} - xA_\sigma\Gamma_e\theta_A\tau_B)\left(1 - e^{-\frac{\tau_{dwell}}{\tau_B}}\right)$$
$$- xA_\sigma\left((N_{A0} - \theta_A Z) - \frac{gI_A}{Z}\tau_B(N_{B0} - xA_\sigma\Gamma_e\theta_A\tau_B)\right)\left(1\right.$$
$$\left. \left. - e^{-\left(\frac{gI_A}{Z}+\frac{1}{\tau_A}\right)\tau_{dwell}}\right) - xA_\sigma\theta_A Z\tau_{dwell}\right]$$

$$Etched = \left(B_\sigma\tau_B - xA_\sigma\frac{gI_A}{Z}{\tau_B}^2\right)\frac{\Gamma_e}{Z}(N_{B0} - xA_\sigma\Gamma_e\theta_A\tau_B)\left(1 - e^{-\frac{\tau_{dwell}}{\tau_B}}\right)$$
$$- xA_\sigma\frac{\Gamma_e}{Z}\left((N_{A0} - \theta_A Z) - \frac{gI_A}{Z}\tau_B(N_{B0} - xA_\sigma\Gamma_e\theta_A\tau_B)\right)\left(1\right.$$
$$\left. - e^{-\left(\frac{gI_A}{Z}+\frac{1}{\tau_A}\right)\tau_{dwell}}\right) + \left(\frac{B_\sigma\tau_B\Gamma_e}{Z} - 1\right)xA_\sigma\Gamma_e\theta_A\tau_{dwell}$$

The first term and second term describe the effect of starting with non-equilibrium concentrations of precursor and etch product on the surface. If the initial condition has an abundance of the sites full of etch product, the etch rate will be inhibited until the excess etch product desorbs from the surface. This is due to the fact that impinging precursor is blocked from adsorbing on the surface and the initial coverage is lower than the equilibrium level. The rate at which the sites can fill with precursor gas is limited by the slower process (molecular impingement or product desorption). If the initial

condition of the precursor concentration is close to the equilibrium condition and the etch product initial condition is small, then these terms diminish in significance. The third term describes the steady state etching. Note that If either the etch product dissociation probability or the etch product residence time is small, then the above equation reduces to the case of the *Small Product Residence Time, Electron Flux Limited Regime* discussed earlier. This regime can be best described by a possible *product desorption/precursor accumulation region* and a *steady state region*.

Figure 33 shows the effect of electron flux on the gas surface concentrations with from an initial condition of N_{A0}=Z and N_{B0}=0. The etch product increases at an initial rate proportional to electron flux and reaches a steady state level proportionate to the electron flux on a time scale of the first eigenvalue ($e^{-\frac{t}{\tau_B}}$), in this case τ_B=10s. The precursor concentration remains mostly unchanged except for the case where the steady state etch product concentration is high enough to fill enough sites to effect the steady state concentration of precursor.

For the case of initial condition of N_{A0}=Z and N_{B0}=0, the etching rate is proportional to electron flux as the first two terms of the etched equation are insignificant. The material etched for the conditions of Figure 33 are plotted in Figure 34.

Figures 35 and 36 give the time dependence of the gas concentrations for differing initial conditions and the corresponding deposit/etching, respectively. Of interest here is the fact that the long residence time of the etch product brings the first two time dependent terms into relevance. So, due to the long residence time of the etch product, if the adsorption sites start full of etch product, there is no place for precursor to adsorb. During this time, some fraction of the etch product will be dissociated and re-deposited, despite the small electron flux. Eventually, after a dwell time approaching the residence time of the etch product, the electron flux limited etching rate is achieved. Compare this to the case of short etch product residence time in Figure 27, noting the time scales are quite different. If the etch product desorbs rapidly, then there is no chance for the small electron flux to dissociate and cause re-deposition.

Large Product Residence Time, Mass Transport Limited Regime

In the case of large product residence time, the etch product remains on the surface long enough to interact with another electron or an impinging precursor molecule. The parameters a-f reduce to:

$$a = -\frac{(A_\sigma + A_{ESD})\Gamma_e}{Z}$$

$$b = -\frac{gI_A}{Z}$$

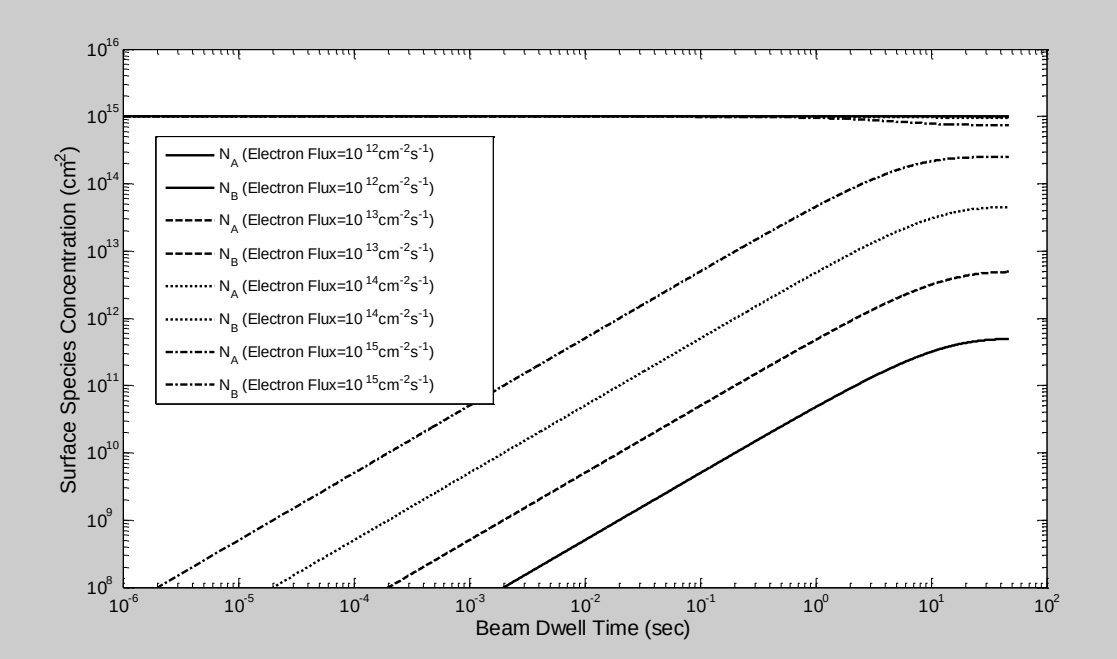

Figure 33: ***Large Product Residence Time, Electron Flux Limited Regime*****: Time Dependence of Precursor and Etch Product Surface Concentration versus Electron Flux**

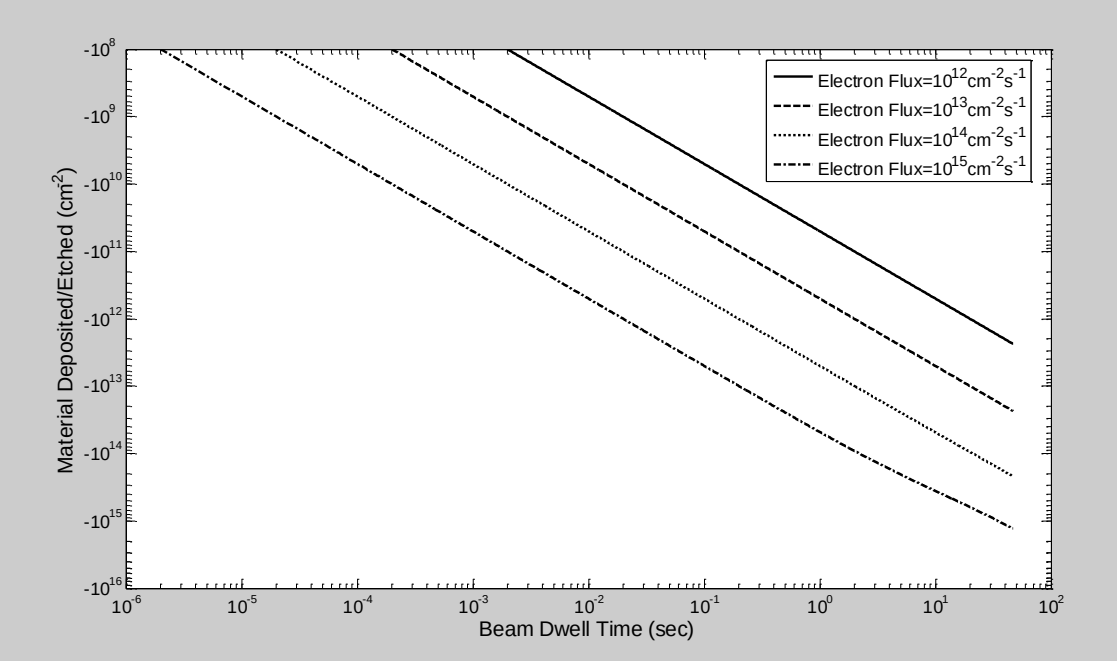

Figure 34: ***Large Product Residence Time, Electron Flux Limited Regime*****: Time Dependence of Etching versus Electron Flux**

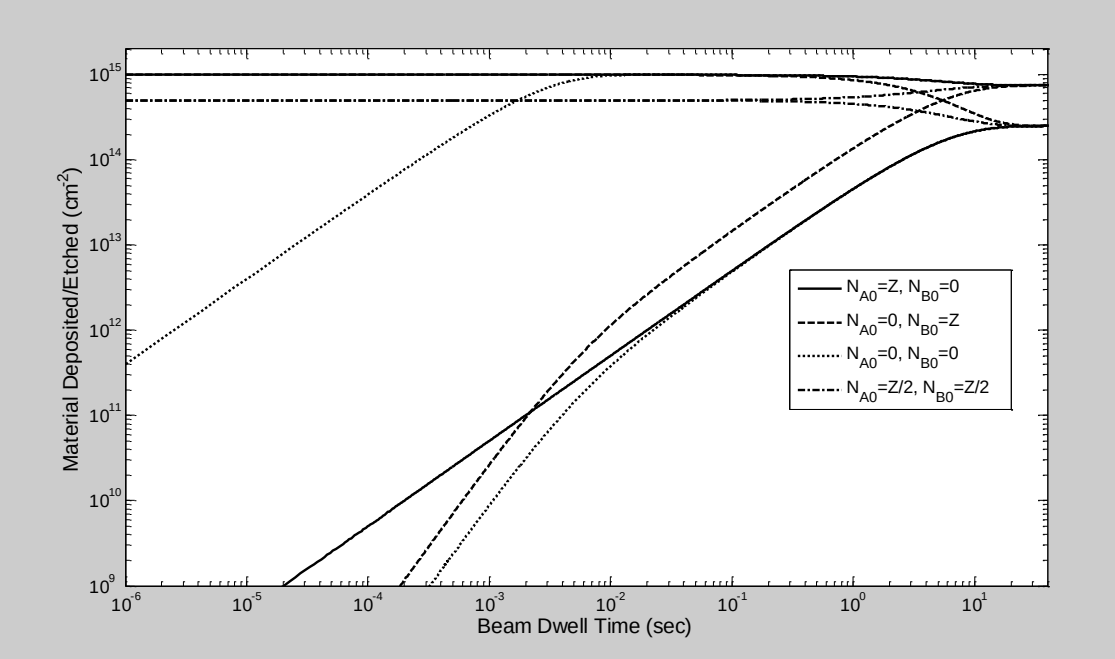

Figure 35: ***Large Product Residence Time, Electron Flux Limited Regime*****: Time Dependence of Precursor and Etch Product Surface Concentration versus Initial Conditions**

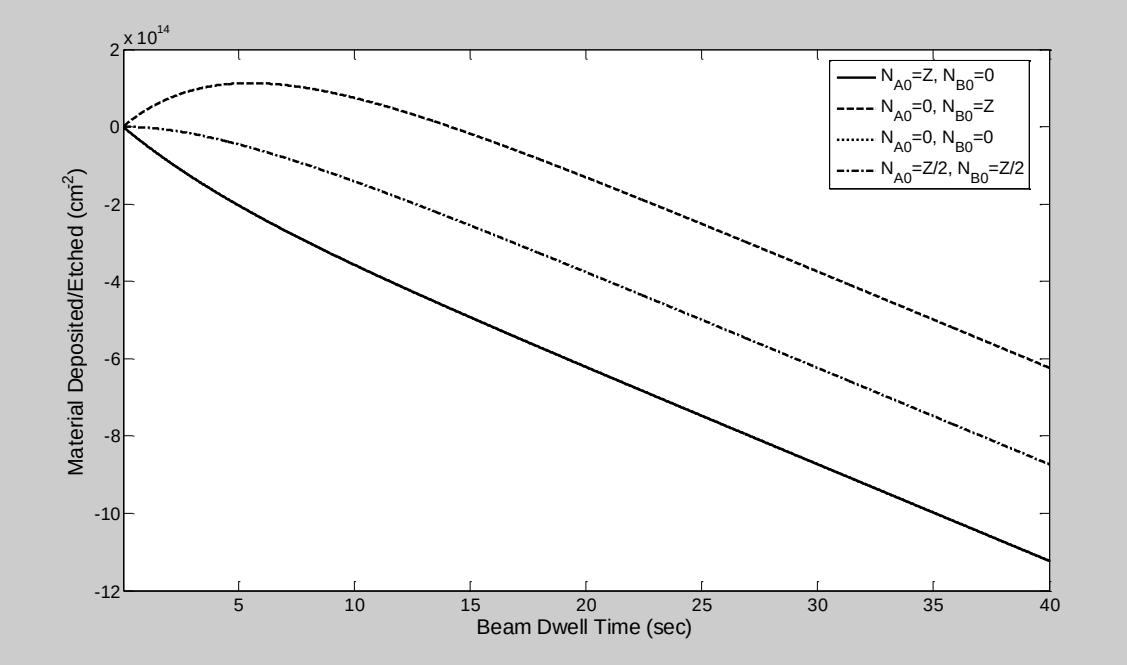

Figure 36: ***Large Product Residence Time, Electron Flux Limited Regime*****: Time Dependence of Etching versus Initial Conditions**

$$c = \frac{xA_\sigma \Gamma_e}{Z}$$

$$d = -\frac{(B_\sigma + B_{ESD})\Gamma_e}{Z}$$

$$e = gI_A$$

$$f = 0$$

This makes the eigenvalues:

$$\lambda = \frac{(a+d) \pm \sqrt{(a+d)^2 - 4(ad-bc)}}{2}$$

$$\lambda = \frac{(a+d) \pm \sqrt{(a-d)^2 + 4bc}}{2}$$

$$\lambda \approx \frac{\left(-\frac{(A_\sigma + A_{ESD})\Gamma_e}{Z} - \frac{(B_\sigma + B_{ESD})\Gamma_e}{Z}\right) \pm \sqrt{\left(-\frac{(A_\sigma + A_{ESD})\Gamma_e}{Z} + \frac{(B_\sigma + B_{ESD})\Gamma_e}{Z}\right)^2 - 4\frac{gI_A}{Z}\left(\frac{xA_\sigma \Gamma_e}{Z}\right)}}{2}$$

$$\lambda \approx \frac{\left(-\frac{(A_\sigma + A_{ESD})\Gamma_e}{Z} - \frac{(B_\sigma + B_{ESD})\Gamma_e}{Z}\right) \pm \left|-\frac{(A_\sigma + A_{ESD})\Gamma_e}{Z} + \frac{(B_\sigma + B_{ESD})\Gamma_e}{Z}\right|}{2}$$

$$\lambda_1 \approx -\frac{(A_\sigma + A_{ESD})\Gamma_e}{Z}$$

$$\lambda_2 \approx -\frac{(B_\sigma + B_{ESD})\Gamma_e}{Z}$$

The solution for the surface concentrations becomes approximately:

$$\begin{bmatrix} N_A \\ N_B \end{bmatrix}$$

$$\approx \begin{bmatrix} (N_{A0} - N_{A\infty}) + \dfrac{gI_A}{\big((A_\sigma + A_{ESD}) - (B_\sigma + B_{ESD})\big)\Gamma_e}(N_{B0} - N_{B\infty}) \\ \dfrac{-xA_\sigma}{\big((A_\sigma + A_{ESD}) - (B_\sigma + B_{ESD})\big)}(N_{A0} - N_{A\infty}) \end{bmatrix} e^{-\frac{(A_\sigma + A_{ESD})\Gamma_e}{Z}t}$$

$$+ \begin{bmatrix} -\dfrac{gI_A}{\big((A_\sigma + A_{ESD}) - (B_\sigma + B_{ESD})\big)\Gamma_e}(N_{B0} - N_{B\infty}) \\ \dfrac{xA_\sigma}{\big((A_\sigma + A_{ESD}) - (B_\sigma + B_{ESD})\big)}(N_{A0} - N_{A\infty}) + (N_{B0} - N_{B\infty}) \end{bmatrix} e^{-\frac{(B_\sigma + B_{ESD})\Gamma_e}{Z}t}$$

$$+ \begin{bmatrix} N_{A\infty} \\ N_{B\infty} \end{bmatrix}$$

Integration gives:

$$Etched = \frac{\Gamma_e}{Z}\left[B_\sigma \int_{t=0}^{t=\tau_{dwell}} N_B\, dt - xA_\sigma \int_{t=0}^{t=\tau_{dwell}} N_A\, dt\right]$$

$$Etched = \frac{\Gamma_e}{Z}\Bigg[B_\sigma \int_{t=0}^{t=\tau_{dwell}} \Bigg(\frac{-xA_\sigma}{\big((A_\sigma + A_{ESD}) - (B_\sigma + B_{ESD})\big)}(N_{A0} - N_{A\infty})e^{-\frac{(A_\sigma + A_{ESD})\Gamma_e}{Z}t}$$
$$+ \left(\frac{xA_\sigma}{\big((A_\sigma + A_{ESD}) - (B_\sigma + B_{ESD})\big)}(N_{A0} - N_{A\infty}) + (N_{B0} - N_{B\infty})\right)e^{-\frac{(B_\sigma + B_{ESD})\Gamma_e}{Z}t}$$
$$+ N_{B\infty}\Bigg)dt$$
$$- xA_\sigma \int_{t=0}^{t=\tau_{dwell}} \Bigg(\Bigg((N_{A0} - N_{A\infty})$$
$$+ \frac{gI_A}{\big((A_\sigma + A_{ESD}) - (B_\sigma + B_{ESD})\big)\Gamma_e}(N_{B0} - N_{B\infty})\Bigg)e^{-\frac{(A_\sigma + A_{ESD})\Gamma_e}{Z}t}$$
$$- \frac{gI_A}{\big((A_\sigma + A_{ESD}) - (B_\sigma + B_{ESD})\big)\Gamma_e}(N_{B0} - N_{B\infty})e^{-\frac{(B_\sigma + B_{ESD})\Gamma_e}{Z}t} + N_{A\infty}\Bigg)dt\Bigg]$$

$$Etched = \frac{\Gamma_e}{Z}\Bigg[\frac{-xA_\sigma Z B_\sigma}{\big((A_\sigma + A_{ESD}) - (B_\sigma + B_{ESD})\big)(A_\sigma + A_{ESD})\Gamma_e}(N_{A0} - N_{A\infty})\left(1 - e^{-\frac{(A_\sigma + A_{ESD})\Gamma_e}{Z}\tau_{dwell}}\right)$$
$$+\left(\frac{xA_\sigma Z B_\sigma}{\big((A_\sigma + A_{ESD}) - (B_\sigma + B_{ESD})\big)(B_\sigma + B_{ESD})\Gamma_e}(N_{A0} - N_{A\infty})\right.$$
$$\left.+\frac{ZB_\sigma}{(B_\sigma + B_{ESD})\Gamma_e}(N_{B0} - N_{B\infty})\right)\left(1 - e^{-\frac{(B_\sigma + B_{ESD})\Gamma_e}{Z}\tau_{dwell}}\right) + B_\sigma N_{B\infty}\tau_{dwell}$$
$$- xA_\sigma\left(\frac{Z(N_{A0} - N_{A\infty})}{(A_\sigma + A_{ESD})\Gamma_e}\right.$$
$$\left.+\frac{gI_A Z}{\big((A_\sigma + A_{ESD}) - (B_\sigma + B_{ESD})\big)(A_\sigma + A_{ESD})\Gamma_e^{\,2}}(N_{B0} - N_{B\infty})\right)\Big(1$$
$$- e^{-\frac{(A_\sigma + A_{ESD})\Gamma_e}{Z}\tau_{dwell}}\Big)$$
$$+\frac{xA_\sigma gI_A Z}{\big((A_\sigma + A_{ESD}) - (B_\sigma + B_{ESD})\big)(A_\sigma + A_{ESD})\Gamma_e^{\,2}}(N_{B0} - N_{B\infty})\Big(1$$
$$\left.- e^{-\frac{(B_\sigma + B_{ESD})\Gamma_e}{Z}\tau_{dwell}}\Big) - xA_\sigma N_{A\infty}\tau_{dwell}\right]$$

$$Etched = \frac{-xA_\sigma B_\sigma}{\big((A_\sigma + A_{ESD}) - (B_\sigma + B_{ESD})\big)(A_\sigma + A_{ESD})}(N_{A0} - N_{A\infty})\left(1 - e^{-\frac{(A_\sigma + A_{ESD})\Gamma_e}{Z}\tau_{dwell}}\right)$$
$$+\left(\frac{xA_\sigma B_\sigma}{\big((A_\sigma + A_{ESD}) - (B_\sigma + B_{ESD})\big)(B_\sigma + B_{ESD})}(N_{A0} - N_{A\infty})\right.$$
$$\left.+\frac{B_\sigma}{(B_\sigma + B_{ESD})}(N_{B0} - N_{B\infty})\right)\left(1 - e^{-\frac{(B_\sigma + B_{ESD})\Gamma_e}{Z}\tau_{dwell}}\right) + B_\sigma\frac{\Gamma_e}{Z}N_{B\infty}\tau_{dwell}$$
$$- xA_\sigma\left(\frac{(N_{A0} - N_{A\infty})}{(A_\sigma + A_{ESD})} + \frac{gI_A}{\big((A_\sigma + A_{ESD}) - (B_\sigma + B_{ESD})\big)(A_\sigma + A_{ESD})\Gamma_e}(N_{B0} - N_{B\infty})\right)\Big(1$$
$$- e^{-\frac{(A_\sigma + A_{ESD})\Gamma_e}{Z}\tau_{dwell}}\Big)$$
$$+\frac{xA_\sigma gI_A}{\big((A_\sigma + A_{ESD}) - (B_\sigma + B_{ESD})\big)(A_\sigma + A_{ESD})\Gamma_e}(N_{B0} - N_{B\infty})\left(1 - e^{-\frac{(B_\sigma + B_{ESD})\Gamma_e}{Z}\tau_{dwell}}\right)$$
$$- xA_\sigma\frac{\Gamma_e}{Z}N_{A\infty}\tau_{dwell}$$

$$Etched = \left(\frac{-xA_\sigma}{A_\sigma + A_{ESD}}\right)\left[\left(1 + \frac{B_\sigma}{(A_\sigma + A_{ESD}) - (B_\sigma + B_{ESD})}\right)(N_{A0} - N_{A\infty}) + \frac{gI_A}{\left((A_\sigma + A_{ESD}) - (B_\sigma + B_{ESD})\right)\Gamma_e}(N_{B0} - N_{B\infty})\right]\left(1 - e^{-\frac{(A_\sigma + A_{ESD})\Gamma_e}{Z}\tau_{dwell}}\right) + \left(\frac{xA_\sigma B_\sigma}{\left((A_\sigma + A_{ESD}) - (B_\sigma + B_{ESD})\right)(B_\sigma + B_{ESD})}(N_{A0} - N_{A\infty}) + \left[\frac{B_\sigma}{(B_\sigma + B_{ESD})} + \frac{xA_\sigma gI_A}{\left((A_\sigma + A_{ESD}) - (B_\sigma + B_{ESD})\right)(A_\sigma + A_{ESD})\Gamma_e}\right](N_{B0} - N_{B\infty})\right)\left(1 - e^{-\frac{(B_\sigma + B_{ESD})\Gamma_e}{Z}\tau_{dwell}}\right) + B_\sigma\frac{\Gamma_e}{Z}\frac{xA_\sigma gI_A Z}{(A_\sigma + A_{ESD})(B_\sigma + B_{ESD})\Gamma_e}\tau_{dwell} - xA_\sigma\frac{\Gamma_e}{Z}\frac{gI_A Z}{(A_\sigma + A_{ESD})\Gamma_e}\tau_{dwell}$$

$$Etched = \left(\frac{-xA_\sigma}{A_\sigma + A_{ESD}}\right)\left[\left(1 + \frac{B_\sigma}{(A_\sigma + A_{ESD}) - (B_\sigma + B_{ESD})}\right)(N_{A0} - N_{A\infty}) + \frac{gI_A}{\left((A_\sigma + A_{ESD}) - (B_\sigma + B_{ESD})\right)\Gamma_e}(N_{B0} - N_{B\infty})\right]\left(1 - e^{-\frac{(A_\sigma + A_{ESD})\Gamma_e}{Z}\tau_{dwell}}\right) + \left(\frac{xA_\sigma B_\sigma}{\left((A_\sigma + A_{ESD}) - (B_\sigma + B_{ESD})\right)(B_\sigma + B_{ESD})}(N_{A0} - N_{A\infty}) + \left[\frac{B_\sigma}{(B_\sigma + B_{ESD})} + \frac{xA_\sigma gI_A}{\left((A_\sigma + A_{ESD}) - (B_\sigma + B_{ESD})\right)(A_\sigma + A_{ESD})\Gamma_e}\right](N_{B0} - N_{B\infty})\right)\left(1 - e^{-\frac{(B_\sigma + B_{ESD})\Gamma_e}{Z}\tau_{dwell}}\right) - \left(\frac{B_{ESD}}{B_\sigma + B_{ESD}}\right)\left(\frac{A_\sigma}{A_\sigma + A_{ESD}}\right)xgI_A\tau_{dwell}$$

While the above equation is workable, it can be simplified somewhat by understanding that the electron flux is much higher than the molecular impingement rate, so the terms with the form (gI_A/Γ_e) are less significant. Also, recognizing that the steady state coverage of precursor and product are both small; that is, $N_{A\infty}$ and $N_{B\infty}$ are both approximately zero when compared in significance to N_{A0} and N_{B0}. Therefore the material etched is:

$$Etched = \left(\frac{-xA_\sigma}{A_\sigma + A_{ESD}}\right)\left(1 + \frac{B_\sigma}{(A_\sigma + A_{ESD}) - (B_\sigma + B_{ESD})}\right) N_{A0}\left(1 - e^{-\frac{(A_\sigma + A_{ESD})\Gamma_e}{Z}\tau_{dwell}}\right) + \left(\frac{xA_\sigma B_\sigma}{\big((A_\sigma + A_{ESD}) - (B_\sigma + B_{ESD})\big)(B_\sigma + B_{ESD})} N_{A0} + \frac{B_\sigma}{(B_\sigma + B_{ESD})} N_{B0}\right)\left(1 - e^{-\frac{(B_\sigma + B_{ESD})\Gamma_e}{Z}\tau_{dwell}}\right) - \left(\frac{B_{ESD}}{B_\sigma + B_{ESD}}\right)\left(\frac{A_\sigma}{A_\sigma + A_{ESD}}\right) xgI_A\tau_{dwell}$$

The first term describes the conversion of the initial coverage of precursor into etch product. This is the *precursor depletion/product accumulation region*. The second term describes the re-dissociation of etch product, both any initial coverage of etch product and any etch product created by dissociation of the initial precursor coverage. This describes the *etch product depletion region.* The third term describes the *steady state region* of etching. In this case, the etch product interacts with another electron moments before it can spontaneously desorb. Only the fraction of etch product that undergoes electron stimulated desorption contributes to net etching in the steady state. In the case that there is no electron stimulated desorption mechanism for the etch product molecule, the steady state etching rate goes to zero.

Note that once the residence time is sufficiently large, both the spontaneous thermal desorption of precursor and etch product do not factor into this regime. The surface residence time of the etch product is too long compared to the time to interact with subsequent electrons. Also for the time dependent regions, it can be seen that both dissociation and electron stimulated desorption contribute to depletion of the precursor and etch product on the surface, but only the fraction of interactions that are dissociative contribute to the net amount of material etched or deposited. Electron stimulated desorption of the precursor serves only to reduce the amount of etching, while electron stimulated desorption of the etch product contributes to net etching.

Figure 37 illustrates the effect of electron flux on the time dependence of precursor and etch product concentrations. Each case starts with the conditions (N_{A0}=Z, N_{B0}=0). Note that for each electron flux, initially, the etch product is formed as the precursor is depleted. Then the etch product concentration is depleted as the beam re-dissociates and re-deposits this material. As the eigenvalues suggest, the time scale behavior for this process ($e^{-\frac{(A_\sigma + A_{ESD})\Gamma_e}{Z}t}$ and $e^{-\frac{(B_\sigma + B_{ESD})\Gamma_e}{Z}t}$) is dependent upon the electron flux. Higher electron flux gives a faster accumulation and subsequent depletion of the etch product.

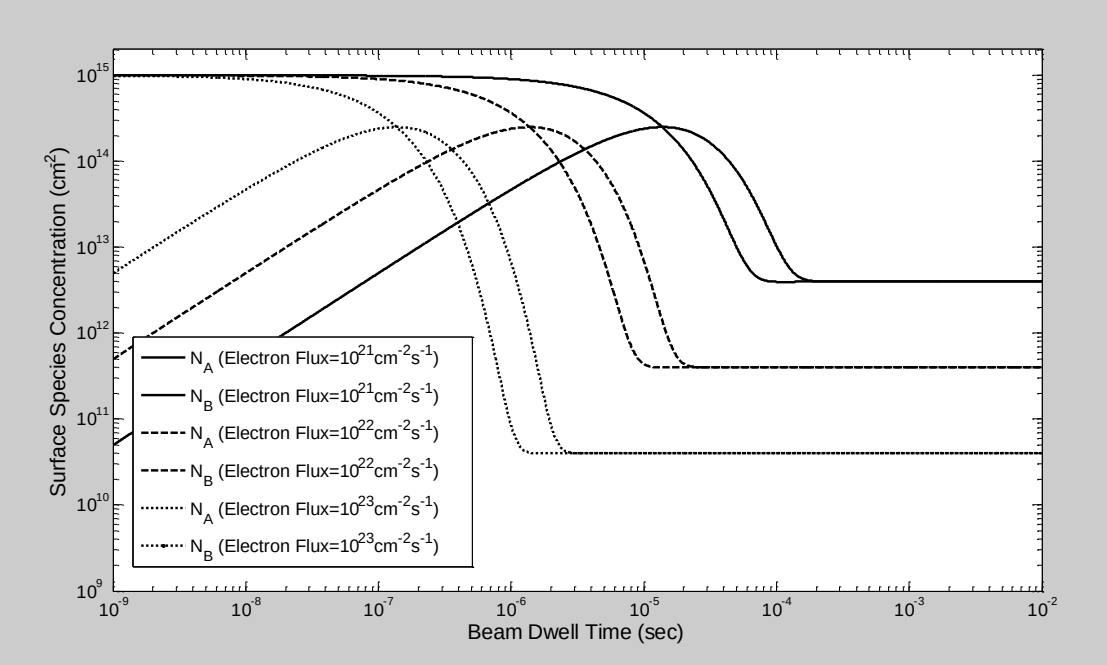

Figure 37: ***Large Product Residence Time, Mass Transport Limited Regime*****: Time Dependence of Precursor and Etch Product Surface Concentration versus Electron Flux**

Integrating and plotting in Figure 38 the time dependence of the etching, we find that the amount of material etched during the pulse increases rapidly reaches a peak, then rapidly returns toward zero. That is, a fraction of the surface is converted into etch product, but then re-dissociated and re-deposited for longer beam dwell times. The key to effective etching in this regime is to use a beam dwell time that is short enough to dissociate the precursor, create a maximum amount of etch product, then refresh with zero electron flux while the etch product desorbs or diffuses away while new precursor gas impinges or diffuses onto the newly exposed surface.

Figure 39 shows the time dependence of the precursor and etch product gases for a fixed electron flux of $10^{22}cm^{-2}s^{-1}$ and varying the initial conditions. As in all of the cases, the steady state concentrations of each gas are independent of the initial conditions, but the path to steady state is considerably different. For all cases of any initial precursor, the etch product accumulates then depletes. Any initial etch product depletes toward the steady state by re-dissociating and re-depositing on the surface. If both precursor and etch product start low, then neither will accumulate beyond the steady state.

The results of different initial conditions on the time dependence of the deposition/etching are plotted in Figure 40. If the initial condition is a high amount of etch product on the surface and a low amount of precursor gas the result is a net deposition of the initial coverage of etch product that increases with increasing beam dwell time. New precursor that arrives at the surface will create new etch product after being dissociated by the electron beam, but will only result in re-deposition of that product by a subsequent electron. Starting depleted in both precursor and etch product, there is no etching or deposit for any amount of beam dwell time. Only in cases where the etch product starts low and the precursor starts high is a net etching possible. This means that the refresh is vitally important to etching as we must allow the etch product to leave and precursor to refresh to accomplish etching in this regime.

Zero Electron Flux, Refresh Region

The beam off condition is necessary to study in order to understand the effect of the beam refresh time. While the beam is scanning other pixels far away from the pixel of interest, any etch product on the surface will spontaneously desorb from the surface, and new precursor molecules will arrive at the surface by molecular impingement. The system of ordinary differential equations gives us factors a-f:

$$a = -\left(\frac{gI_A}{Z} + \frac{1}{\tau_A}\right)$$

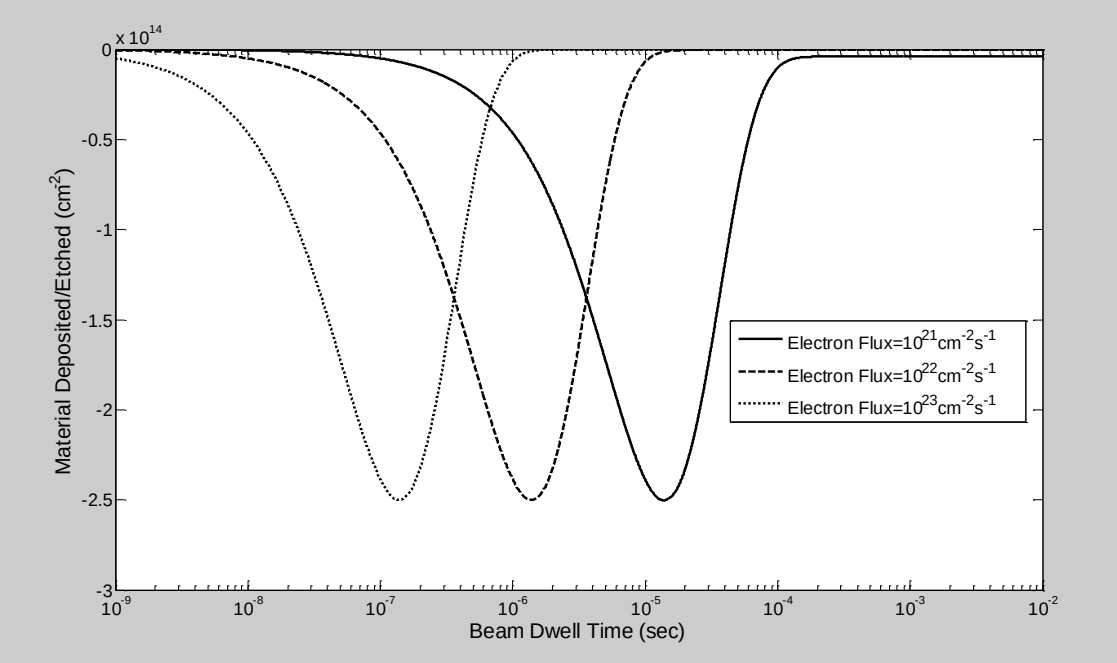

Figure 38: ***Large Product Residence Time, Mass Transport Limited Regime*****: Time Dependence of Etching versus Electron Flux**

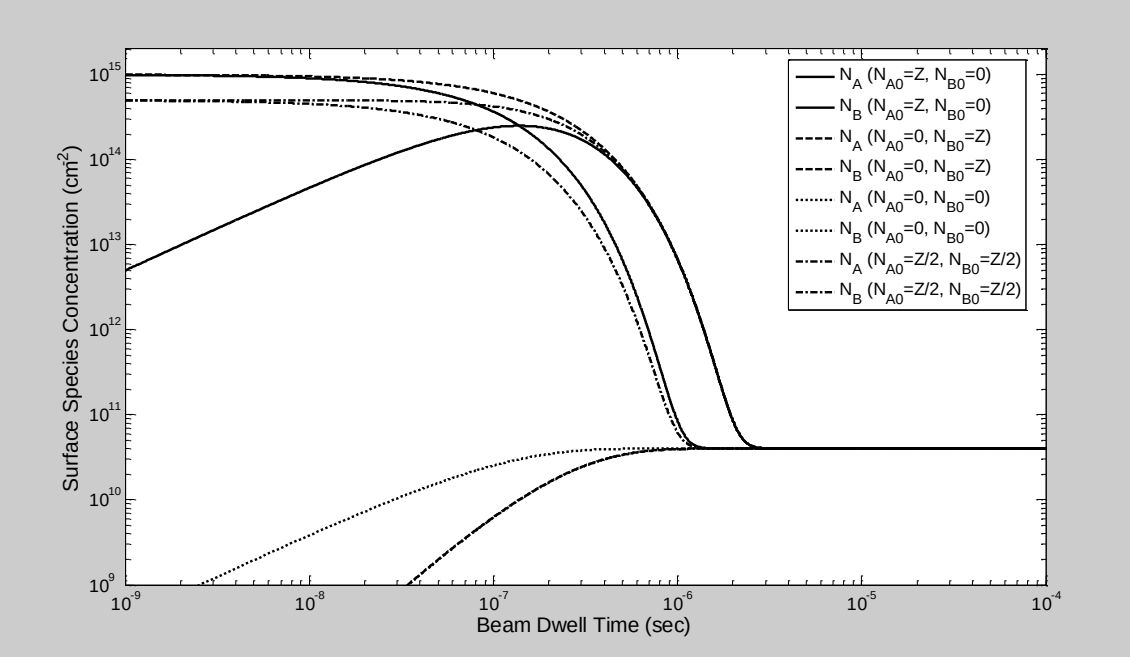

Figure 39: ***Large Product Residence Time, Mass Transport Limited Regime*****: Time Dependence of Precursor and Etch Product Surface Concentration versus Initial Conditions**

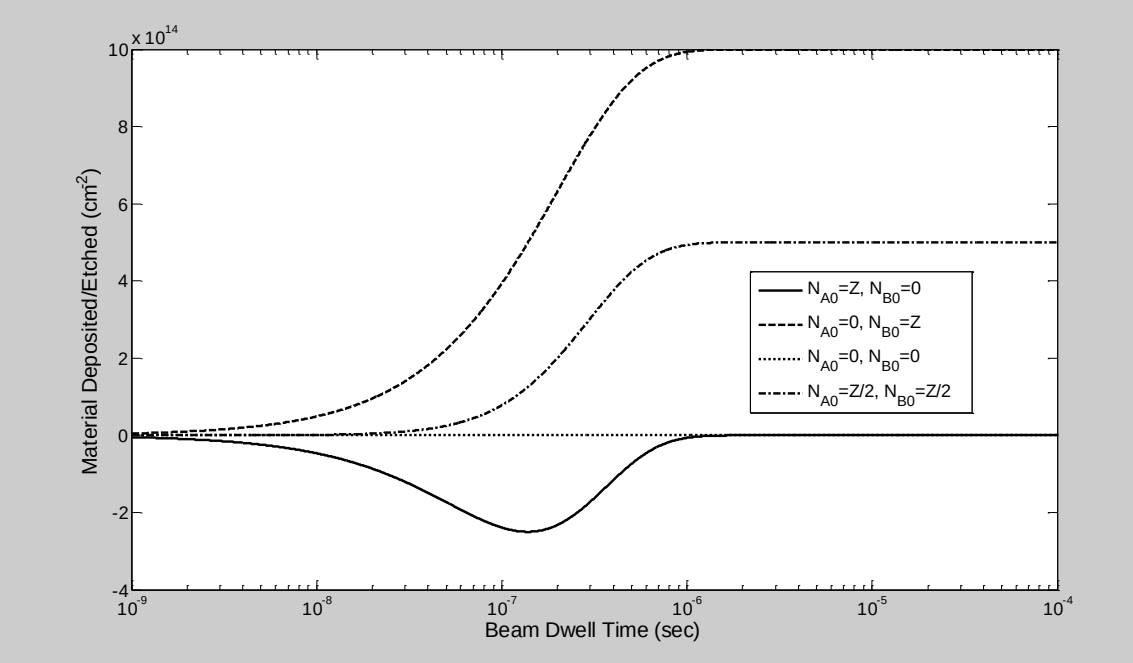

Figure 40: ***Large Product Residence Time, Mass Transport Limited Regime*****: Time Dependence of Etching versus Initial Conditions**

$$b = -\frac{gI_A}{Z}$$

$$c = 0$$

$$d = -\frac{1}{\tau_B}$$

$$e = gI_A$$

$$f = 0$$

The eigenvalues are:

$$\lambda = \frac{(a+d) \pm \sqrt{(a+d)^2 - 4(ad-bc)}}{2}$$

$$\lambda = \frac{-\left(\frac{gI_A}{Z} + \frac{1}{\tau_A} + \frac{1}{\tau_B}\right) \pm \sqrt{\left(\frac{gI_A}{Z} + \frac{1}{\tau_A} + \frac{1}{\tau_B}\right)^2 - 4\left(\left(\frac{gI_A}{Z} + \frac{1}{\tau_A}\right)\frac{1}{\tau_B} - 0\right)}}{2}$$

$$\lambda = \frac{-\left(\frac{gI_A}{Z} + \frac{1}{\tau_A} + \frac{1}{\tau_B}\right) \pm \sqrt{\left(\frac{gI_A}{Z} + \frac{1}{\tau_A} - \frac{1}{\tau_B}\right)^2}}{2}$$

$$\lambda_1 = -\left(\frac{gI_A}{Z} + \frac{1}{\tau_A}\right)$$

$$\lambda_2 = -\frac{1}{\tau_B}$$

The solution for the differential equations becomes:

$$\begin{bmatrix} N_A \\ N_B \end{bmatrix} = \begin{bmatrix} \left(N_{A0} - \frac{gI_A}{\frac{gI_A}{Z} + \frac{1}{\tau_A}} \right) + \frac{gI_A}{gI_A + \frac{Z}{\tau_A} - \frac{Z}{\tau_B}} N_{B0} \\ 0 \end{bmatrix} e^{-\left(\frac{gI_A}{Z} + \frac{1}{\tau_A}\right)t} + \begin{bmatrix} -\frac{gI_A}{gI_A + \frac{Z}{\tau_A} - \frac{Z}{\tau_B}} N_{B0} \\ N_{B0} \end{bmatrix} e^{-\frac{t}{\tau_B}} + \begin{bmatrix} \frac{gI_A}{\frac{gI_A}{Z} + \frac{1}{\tau_A}} \\ 0 \end{bmatrix}$$

It is seen that any initial coverage of etch product will desorb from the surface at an exponential rate governed by the average residence time of the etch product. Any initial depletion in the precursor will fill towards the equilibrium coverage at a rate governed by the molecular impingement rate or the surface residence time of the precursor whichever is faster. The rate of precursor refresh can also be limited by desorption of the etch product. If the etch product residence time is long, the impinging precursor cannot adsorb onto sites that are still full of etch product.

Numerical Differentiation Methods

Discrete Derivatives

Parabolic Partial Differential Equations are approximated numerically by discretizing and replacing the derivatives with respect to space by numerical approximations. The most common use is the three point central difference formulas for the first and second derivatives:

$$f'(x) = \frac{f(x+h) - f(x-h)}{2h} + O(h^2)$$

$$f''(x) = \frac{f(x+h) - 2f(x) + f(x-h)}{h^2} + O(h^2)$$

The derivatives are described in terms of the original functions and the spacing between sampling of the function. The final term describes the error in the approximations. In the case of the three point formulas, the error is on the order of the square of the discretization spacing. In order to achieve sufficient accuracy, the discretization may be required to be very small and thus increases the computation time and memory requirements. There are five point formulas for example the central difference first derivative:

$$f'(x) = \frac{-f(x+2h) + 8f(x+h) - 8f(x-h) + f(x-2h)}{12h} + O(h^4)$$

These five-point formulas have error on the order of the fourth power of h. These formulas can be used to achieve greater accuracy for the same discretization step size, or can be used to increase the discretization step size and achieve the same accuracy level. Often, the increased computation required to calculate the five point derivatives can be offset by the decrease in discrete steps.

The first few terms of the Taylor Series expansion of a function f(x) are expressed as:

$$f(x) = \frac{f(x_0)}{0!}(x-x_0)^0 + \frac{f'(x_0)}{1!}(x-x_0)^1 + \frac{f''(x_0)}{2!}(x-x_0)^2 + \frac{f'''(x_0)}{3!}(x-x_0)^3 + \frac{f^{[4]}(x_0)}{4!}(x-x_0)^4 + \frac{f^{[5]}(x_0)}{5!}(x-x_0)^5 + \cdots$$

Therefore substitution reveals:

$$f(x_0+h) = f(x_0) + \frac{f'(x_0)}{1!}h + \frac{f''(x_0)}{2!}h^2 + \frac{f'''(x_0)}{3!}h^3 + \frac{f^{[4]}(x_0)}{4!}h^4 + \frac{f^{[5]}(x_0)}{5!}h^5 + \cdots$$

$$f(x_0+2h) = f(x_0) + \frac{f'(x_0)}{1!}2h + \frac{f''(x_0)}{2!}4h^2 + \frac{f'''(x_0)}{3!}8h^3 + \frac{f^{[4]}(x_0)}{4!}16h^4 + \frac{f^{[5]}(x_0)}{5!}32h^5 + \cdots$$

The goal is to add these two equations using linear operators to solve for $f'(x_0)$ or $f''(x_0)$ and eliminate the lowest order term. Rearranging and adding linear multipliers:

$$a[f(x_0+h) - f(x_0)] \approx a\left[\frac{f'(x_0)}{1!}h + \frac{f''(x_0)}{2!}h^2\right]$$

$$b[f(x_0+2h) - f(x_0)] \approx b\left[\frac{f'(x_0)}{1!}2h + \frac{f''(x_0)}{2!}4h^2\right]$$

In order to eliminate the second derivative and solve for the first derivative, the right hand side columns can be written in the form:

$$ax + 2bx = 1$$

$$ay + 4by = 0$$

where:

$$x = \frac{f'(x_0)}{1!}h$$

$$y = \frac{f''(x_0)}{2!}h^2$$

Solving for a and b using matrix algebra:

$$\begin{bmatrix}1 & 2\\ 1 & 4\end{bmatrix}\begin{bmatrix}a\\ b\end{bmatrix} = \begin{bmatrix}1\\ 0\end{bmatrix}$$

$$\begin{bmatrix}a\\ b\end{bmatrix} = \begin{bmatrix}2\\ -0.5\end{bmatrix}$$

Now, using the solved values of a and b, look at the sum of the linear equations:

$$2[f(x_0 + h) - f(x_0)] - 0.5[f(x_0 + 2h) - f(x_0)]$$
$$\approx 2\left[\frac{f'(x_0)}{1!}h + \frac{f''(x_0)}{2!}h^2\right] - 0.5\left[\frac{f'(x_0)}{1!}2h + \frac{f''(x_0)}{2!}4h^2\right]$$

Rearranging and isolating f'(x_0):

$$\frac{-1.5f(x_0) + 2f(x_0 + h) - 0.5f(x_0 + 2h)}{h} \approx f'(x_0)$$

Multiplying by 2 in numerator and denominator to get integer coefficients gives the final form:

$$f'(x_0) \approx \frac{-3f(x_0) + 4f(x_0 + h) - f(x_0 + 2h)}{2h}$$

This is the three-point forward difference algorithm for the first derivative. If the next higher order term is included:

$$f'(x_0) \approx \frac{-3f(x_0) + 4f(x_0 + h) - f(x_0 + 2h)}{2h} + h^2\frac{f'''(x_0)}{3}$$

The error in using this formula scales with the square of h and the third derivative. The same method can be used to calculate the central difference and backward difference formulas:

$$f'(x_0) \approx \frac{f(x_0+h)-f(x_0-h)}{2h} - h^2\frac{f'''(x_0)}{6}$$

$$f'(x_0) \approx \frac{f(x_0-2h)-4f(x_0-h)+3f(x_0)}{2h} + h^2\frac{f'''(x_0)}{3}$$

In a similar fashion, the five point formulas can be calculated by using the first through fourth order terms of the Taylor expansion and four equations. The example of the five-point center difference equation for the second derivative is below:

$$\begin{bmatrix} -2 & -1 & 1 & 2 \\ 4 & 1 & 1 & 4 \\ -8 & -1 & 1 & 8 \\ 16 & 1 & 1 & 16 \end{bmatrix} \begin{bmatrix} a \\ b \\ c \\ d \end{bmatrix} = \begin{bmatrix} 0 \\ 1 \\ 0 \\ 0 \end{bmatrix}$$

$$\begin{bmatrix} a \\ b \\ c \\ d \end{bmatrix} = \begin{bmatrix} -1/24 \\ 2/3 \\ 2/3 \\ -1/24 \end{bmatrix}$$

$$24\begin{bmatrix} a \\ b \\ c \\ d \end{bmatrix} = \begin{bmatrix} -1 \\ 16 \\ 16 \\ -1 \end{bmatrix}$$

$$f''(x_0) \approx \frac{-f(x_0-2h)+16f(x_0-h)-30f(x_0)+16f(x_0+h)-f(x_0+2h)}{12h^2} + h^4\frac{f^{[6]}(x_0)}{120}$$

Note that the five-point formula is more accurate with error on h^4 and the 6^{th} derivative. Using this method, all the possible combinations of 2, 3, 4, and 5 point methods are listed below for the first and second derivative as well as the first error term.

2-point Formulas

$$f'(x_0) \approx \frac{-f(x_0) + f(x_0 + h)}{h} - h\frac{f''(x_0)}{2}$$

$$f'(x_0) \approx \frac{-f(x_0 - h) + f(x_0)}{h} + h\frac{f''(x_0)}{2}$$

3-point Formulas

$$f'(x_0) \approx \frac{f(x_0 - 2h) - 4f(x_0 - h) + 3f(x_0)}{2h} + h^2\frac{f'''(x_0)}{3}$$

$$f'(x_0) \approx \frac{-f(x_0 - h) + f(x_0 + h)}{2h} - h^2\frac{f'''(x_0)}{6}$$

$$f'(x_0) \approx \frac{-3f(x_0) + 4f(x_0 + h) - f(x_0 + 2h)}{2h} + h^2\frac{f'''(x_0)}{3}$$

$$f''(x_0) \approx \frac{f(x_0 - 2h) - 2f(x_0 - h) + f(x_0)}{h^2} - hf'''(x_0)$$

$$f''(x_0) \approx \frac{f(x_0 - h) - 2f(x_0) + f(x_0 + h)}{h^2} - h^2\frac{f^{[4]}(x_0)}{12}$$

$$f''(x_0) \approx \frac{f(x_0) - 2f(x_0 + h) + f(x_0 + 2h)}{h^2} - hf'''(x_0)$$

4-point Formulas

$$f'(x_0) \approx \frac{-2f(x_0 - 3h) + 9f(x_0 - 2h) - 18f(x_0 - h) + 11f(x_0)}{6h} + h^3\frac{f^{[4]}(x_0)}{72}$$

$$f'(x_0) \approx \frac{f(x_0 - 2h) - 6f(x_0 - h) + 3f(x_0) + 2f(x_0 + h)}{6h} - h^3\frac{f^{[4]}(x_0)}{12}$$

$$f'(x_0) \approx \frac{-2f(x_0-h)-3f(x_0)+6f(x_0+h)-f(x_0+2h)}{6h} + h^3\frac{f^{[4]}(x_0)}{12}$$

$$f'(x_0) \approx \frac{-11f(x_0)+18f(x_0+h)-9f(x_0+2h)+2f(x_0+3h)}{6h} - h^3\frac{f^{[4]}(x_0)}{72}$$

$$f''(x_0) \approx \frac{f(x_0-3h)-4f(x_0-2h)+5f(x_0-h)-2f(x_0)}{h^2} + h^2\frac{5f^{[4]}(x_0)}{24}$$

$$f''(x_0) \approx \frac{2f(x_0)-5f(x_0+h)+4f(x_0+2h)-f(x_0+3h)}{h^2} - h^2\frac{5f^{[4]}(x_0)}{24}$$

Note: The other two 4-point formulas for the second derivative are identical to the 3-point center difference formula.

5-point Formulas

$$f'(x_0) \approx \frac{-25f(x_0)+48f(x_0+h)-36f(x_0+2h)+16f(x_0+3h)-3f(x_0+4h)}{12h} + h^4\frac{f^{[5]}(x_0)}{5}$$

$$f'(x_0) \approx \frac{-3f(x_0-h)-10f(x_0)+18f(x_0+h)-6f(x_0+2h)+f(x_0+3h)}{12h} - h^4\frac{f^{[5]}(x_0)}{20}$$

$$f'(x_0) \approx \frac{f(x_0-2h)-8f(x_0-h)+8f(x_0+h)-f(x_0+2h)}{12h} + h^4\frac{f^{[5]}(x_0)}{30}$$

$$f'(x_0) \approx \frac{-f(x_0-3h)+6f(x_0-2h)-18f(x_0-h)+10f(x_0)+3f(x_0+h)}{12h} + h^4\frac{f^{[5]}(x_0)}{20}$$

$$f'(x_0) \approx \frac{3f(x_0-4h)-16f(x_0-3h)+36f(x_0-2h)-48f(x_0-h)+25f(x_0)}{12h} - h^4\frac{f^{[5]}(x_0)}{5}$$

$$f''(x_0) \approx \frac{35f(x_0)-104f(x_0+h)+114f(x_0+2h)-56f(x_0+3h)+11f(x_0+4h)}{12h^2} - h^3\frac{5f^{[5]}(x_0)}{6}$$

$$f''(x_0) \approx \frac{11f(x_0-h)-20f(x_0)+6f(x_0+h)+4f(x_0+2h)-f(x_0+3h)}{12h^2} - h^3\frac{f^{[5]}(x_0)}{24}$$

$$f''(x_0) \approx \frac{-f(x_0-2h)+16f(x_0-h)-30f(x_0)+16f(x_0+h)-f(x_0+2h)}{12h^2} + h^4\frac{f^{[6]}(x_0)}{90}$$

$$f''(x_0) \approx \frac{-f(x_0-3h)+4f(x_0-2h)+6f(x_0-h)-20f(x_0)+11f(x_0+h)}{12h^2} - h^3\frac{f^{[5]}(x_0)}{24}$$

$$f''(x_0) \approx \frac{11f(x_0-4h)-56f(x_0-3h)+114f(x_0-2h)-104f(x_0-h)+35f(x_0)}{12h^2} - h^3\frac{5f^{[5]}(x_0)}{6}$$

Note: The error term is smallest for the centered difference approximations. If fact, symmetry allows the error in the second derivative to be on the order of h^4 versus h^3 for the other second derivative terms.

As an example, let's compare the use of the 3-point central difference versus the 5-point central difference to estimate the value of the second derivative of:

$$f(x) = \cos x$$

at x=0. Since the analytical solution is known:

$$f''(x=0) = -\cos 0 = -1$$

then the accuracy can be compare for various values of h in Table 1.

The accuracy increases with decreasing h for both methods, but the 5-point method is more accurate for all h above 10^{-3}. Below this value of h and the formula error is no longer the dominant error as the computer software floating point precision begins to add errors. Use of a higher precision software package greatly improves this issue.

Application to PDE Numerical Solutions

The 3-point center finite difference formulas are commonly used to approximate the first and second derivatives in numerical solutions to partial differential equations. If the 5-point finite difference formulas are used, then the accuracy could be improved or the number of discrete steps in the spatial dimensions can be reduced without sacrificing the accuracy of the solution. In order to investigate the usefulness of using the 5-point formulas over the 3-point formulas, a PDE with a known analytical solution will be solved using both 5-point and 3-point formulas. The parabolic PDE:

$$\frac{\partial c}{\partial t} = \frac{1}{\pi^2}\frac{\partial^2 c}{\partial x^2}$$

With boundary conditions:

$$c(0,t) = 0$$

$$c(1,t) = 0$$

And initial condition:

$$c(x,0) = \sin(\pi x)$$

Has the analytical solution:

$$c(x,t) = \sin(\pi x)\, e^{-t}$$

Using the 3-point formulas and dt=10^{-4}sec and dl=0.01, the numerical solution is plotted in Figure 41. The absolute error from the analytical solution is plotted in Figure 42. The maximum error from the true analytical solution is 3.03 x 10^{-5}. If the 5-point method is used for the same spatial and temporal resolution, the maximum error is 3.49 x 10^{-9}. A plot of absolute error is included in Figure 43. The spatial step size using 5-point formulas can be increased to 1/15 and still have comparable absolute error (<2.2 x 10^{-5}) to the 1/100 step size using 3-point formulas.

Table 1: Comparison of 3-point and 5-point Accuracy

h	3-point	5-point
1.0000	-0.9193953883	-0.9898360449
0.1000	-0.9991669444	-0.9999988899
0.0100	-0.9999916667	-0.9999999999
0.0010	-0.9999999167	-0.9999999999
0.0001	-0.9999999939	-0.9999999939

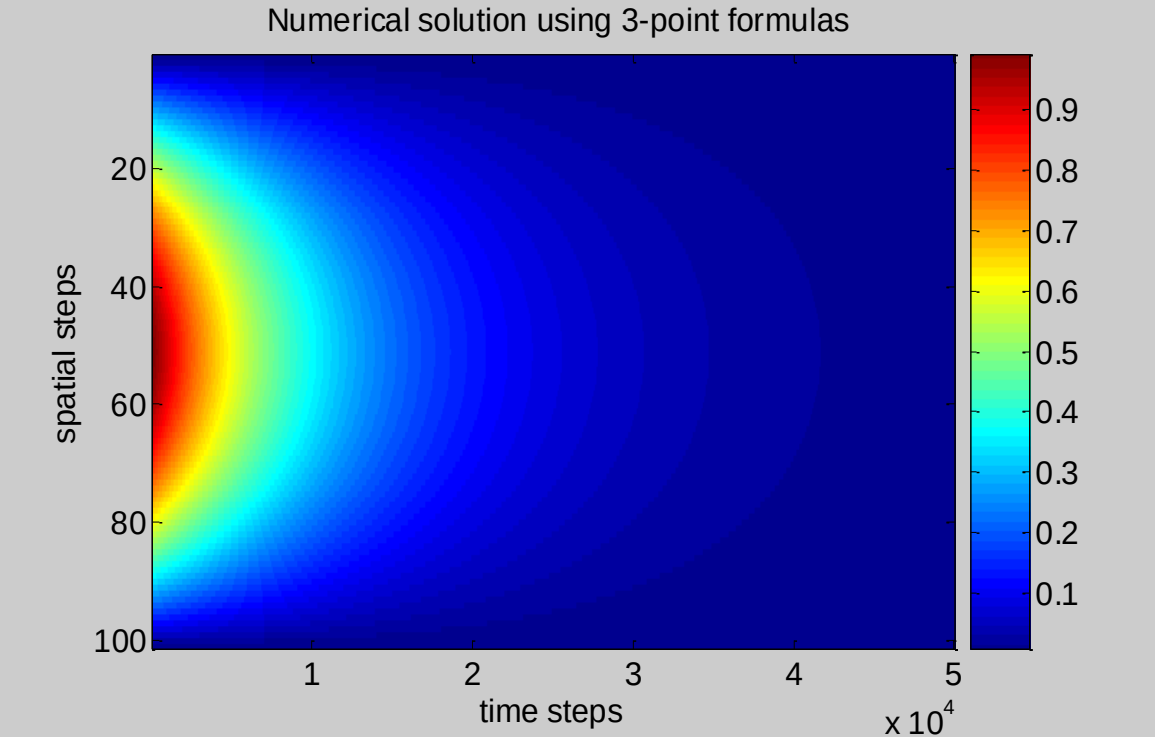
Numerical solution using 3-point formulas
spatial steps
20
40
60
80
100
1
2
3
4
5
time steps
x 10^4
0.9
0.8
0.7
0.6
0.5
0.4
0.3
0.2
0.1

Figure 41

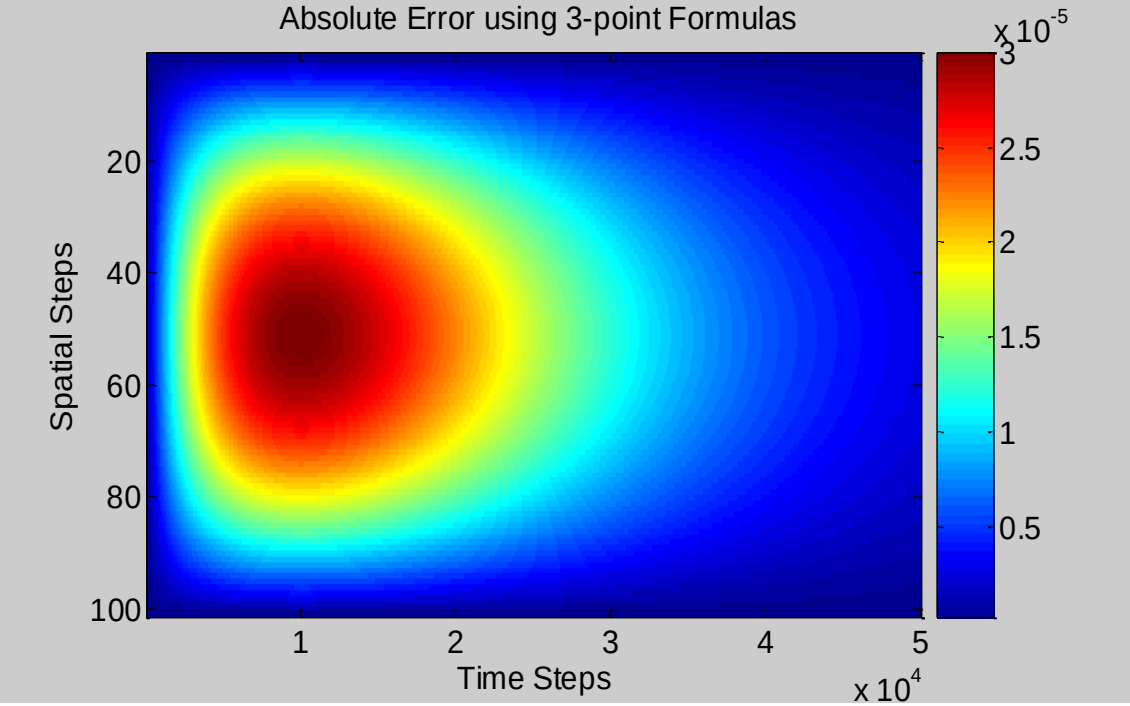
Absolute Error using 3-point Formulas
x 10^-5
3
2.5
2
1.5
1
0.5
Spatial Steps
20
40
60
80
100
1
2
3
4
5
Time Steps
x 10^4

Figure 42

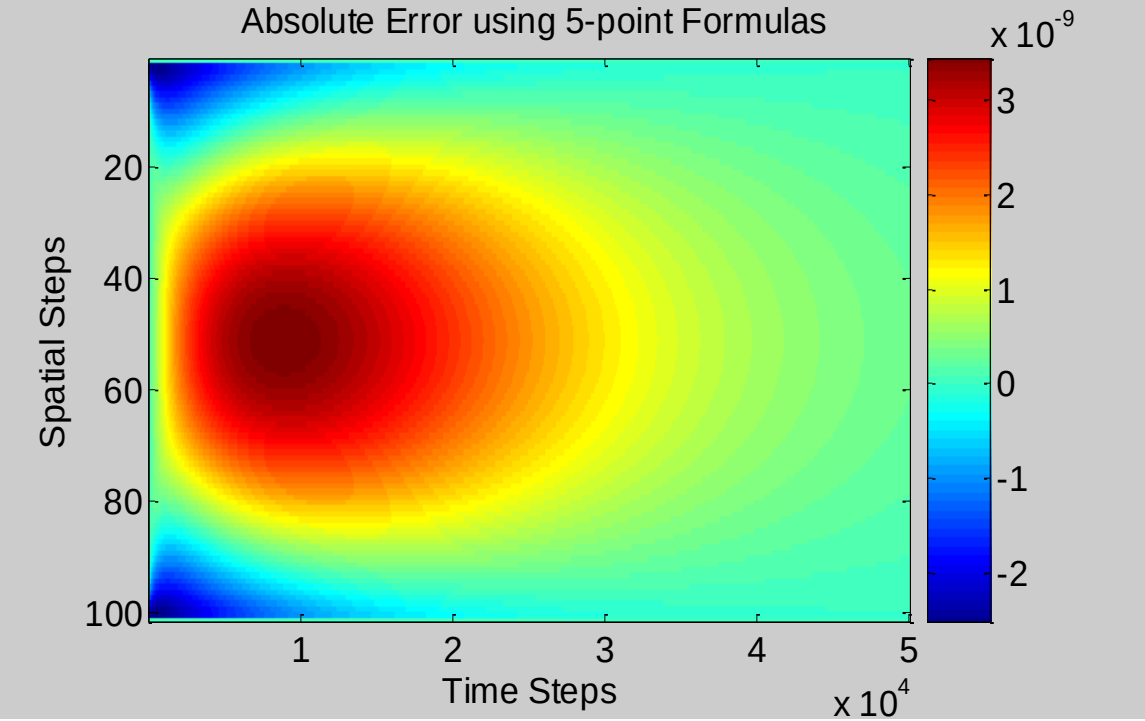
Absolute Error using 5-point Formulas
x 10^-9
3
2
1
0
-1
-2
Spatial Steps
20
40
60
80
100
1
2
3
4
5
Time Steps
x 10^4

Figure 43

General Solution to n-point Numerical Derivatives

The method can be generalized to create formulae for n-point numerical derivatives with asymmetrical spacing. Starting with the three points and their Taylor Series expansions:

$$f(x_0), f(x_0+\alpha), and\ \ f(x_0+\beta)$$

$$f(x_0+\alpha)-f(x_0) = f'(x_0)\alpha + \frac{f''(x_0)}{2}\alpha^2 + \frac{f'''(x_0)}{6}\alpha^3 + \frac{f^{[4]}(x_0)}{24}\alpha^4 + \frac{f^{[5]}(x_0)}{120}\alpha^5 + \cdots$$

$$f(x_0+\beta)-f(x_0) = f'(x_0)\beta + \frac{f''(x_0)}{2}\beta^2 + \frac{f'''(x_0)}{6}\beta^3 + \frac{f^{[4]}(x_0)}{24}\beta^4 + \frac{f^{[5]}(x_0)}{120}\beta^5 + \cdots$$

Adding linear operators as before:

$$a[f(x_0+\alpha)-f(x_0)] = a\left[f'(x_0)\alpha + \frac{f''(x_0)}{2}\alpha^2 + \frac{f'''(x_0)}{6}\alpha^3 + \frac{f^{[4]}(x_0)}{24}\alpha^4 + \frac{f^{[5]}(x_0)}{120}\alpha^5 + \cdots\right]$$

$$b[f(x_0+\beta)-f(x_0)] = b\left[f'(x_0)\beta + \frac{f''(x_0)}{2}\beta^2 + \frac{f'''(x_0)}{6}\beta^3 + \frac{f^{[4]}(x_0)}{24}\beta^4 + \frac{f^{[5]}(x_0)}{120}\beta^5 + \cdots\right]$$

Arranging the first two terms of the right hand side of each equation and solving for the first derivative while eliminating the second order terms:

$$\begin{bmatrix}\alpha & \beta\\ \alpha^2 & \beta^2\end{bmatrix}\begin{bmatrix}a\\ b\end{bmatrix} = \begin{bmatrix}1\\ 0\end{bmatrix}$$

$$\begin{bmatrix}a\\ b\end{bmatrix} = \frac{1}{\alpha\beta^2-\alpha^2\beta}\begin{bmatrix}\beta^2 & -\beta\\ -\alpha^2 & \alpha\end{bmatrix}\begin{bmatrix}1\\ 0\end{bmatrix}$$

$$\begin{bmatrix}a\\ b\end{bmatrix} = \begin{bmatrix}\frac{\beta^2}{\alpha\beta^2-\alpha^2\beta}\\ \frac{-\alpha^2}{\alpha\beta^2-\alpha^2\beta}\end{bmatrix}$$

Now using the linear operators a and b to add the two equations together we find that:

$$\frac{\beta^2}{\alpha\beta^2-\alpha^2\beta}[f(x_0+\alpha)-f(x_0)]+\frac{-\alpha^2}{\alpha\beta^2-\alpha^2\beta}[f(x_0+\beta)-f(x_0)]$$
$$=\frac{\beta^2}{\alpha\beta^2-\alpha^2\beta}\left[f'(x_0)\alpha+\frac{f''(x_0)}{2}\alpha^2+\frac{f'''(x_0)}{6}\alpha^3+\cdots\right]$$
$$+\frac{-\alpha^2}{\alpha\beta^2-\alpha^2\beta}\left[f'(x_0)\beta+\frac{f''(x_0)}{2}\beta^2+\frac{f'''(x_0)}{6}\beta^3+\cdots\right]$$

$$\frac{\beta^2}{\alpha\beta^2-\alpha^2\beta}f(x_0+\alpha)+\frac{-\alpha^2}{\alpha\beta^2-\alpha^2\beta}f(x_0+\beta)+\frac{\alpha^2-\beta^2}{\alpha\beta^2-\alpha^2\beta}f(x_0)$$
$$=f'(x_0)-\alpha\beta\left(\frac{f'''(x_0)}{6}\right)+\cdots$$

We now have a generalized approximation for the first derivative using the point of interest and any two other points. The three points change in weighting depending upon the values of α and β. The formula error is scaled by the third derivative and the product ($\alpha\beta$). It should be noted that substitution of α=h and β=-h gives the familiar three point central difference equation or substitution of α=h and β=2h gives the three point forward difference equation discussed earlier. Using the above derived equation gives the flexibility to use variable spatial step sizes. This allows for high spatial resolution to be used in the regions of interest while larger spatial steps are used in regions where the dependent variable changes slowly (that is, has a small third derivative). The method can be extended to the second derivative as:

$$\begin{bmatrix}a\\b\end{bmatrix}=\frac{1}{\alpha\beta^2-\alpha^2\beta}\begin{bmatrix}\beta^2 & -\beta\\ -\alpha^2 & \alpha\end{bmatrix}\begin{bmatrix}0\\1\end{bmatrix}$$

$$\begin{bmatrix}a\\b\end{bmatrix}=\begin{bmatrix}\frac{-\beta}{\alpha\beta^2-\alpha^2\beta}\\ \frac{\alpha}{\alpha\beta^2-\alpha^2\beta}\end{bmatrix}$$

$$\frac{-\beta}{\alpha\beta^2-\alpha^2\beta}[f(x_0+\alpha)-f(x_0)]+\frac{\alpha}{\alpha\beta^2-\alpha^2\beta}[f(x_0+\beta)-f(x_0)]$$
$$=\frac{-\beta}{\alpha\beta^2-\alpha^2\beta}\left[f'(x_0)\alpha+\frac{f''(x_0)}{2}\alpha^2+\frac{f'''(x_0)}{6}\alpha^3+\cdots\right]$$
$$+\frac{\alpha}{\alpha\beta^2-\alpha^2\beta}\left[f'(x_0)\beta+\frac{f''(x_0)}{2}\beta^2+\frac{f'''(x_0)}{6}\beta^3+\cdots\right]$$

$$\frac{-2\beta}{\alpha\beta^2-\alpha^2\beta}f(x_0+\alpha)+\frac{2\alpha}{\alpha\beta^2-\alpha^2\beta}f(x_0+\beta)+\frac{2(\beta-\alpha)}{\alpha\beta^2-\alpha^2\beta}f(x_0)$$
$$=f''(x_0)-(\alpha+\beta)\left(\frac{f'''(x_0)}{6}\right)+\cdots$$

Note that if α=h and β=-h for the central difference formula, the error term drops to zero and so the next higher order term dominates the formula error.

Using more points to evaluate the derivatives offers higher order accuracy in the formulae. Writing the analytical form of the four point and five point derivatives is tedious due to the complexity of the inverse 3x3 and 4x4 matrices, and so left out for the sake of brevity. But the inverse of an n-by-n matrix is easily calculated numerically by MATLAB™. So, the numerical approximation to the first derivative is easily done by:

$$\begin{bmatrix}a\\b\\c\\d\end{bmatrix}=\begin{bmatrix}\alpha & \beta & \gamma & \delta\\ \alpha^2 & \beta^2 & \gamma^2 & \delta^2\\ \alpha^3 & \beta^3 & \gamma^3 & \delta^3\\ \alpha^4 & \beta^4 & \gamma^4 & \delta^4\end{bmatrix}^{-1}\begin{bmatrix}1\\0\\0\\0\end{bmatrix}$$

$$f'(x_0)\cong af(x_0+\alpha)+\ bf(x_0+\beta)+cf(x_0+\gamma)+df(x_0+\delta)$$
$$-(a+b+c+d)f(x_0)$$

And the second derivative by:

$$\begin{bmatrix}a\\b\\c\\d\end{bmatrix}=\begin{bmatrix}\alpha & \beta & \gamma & \delta\\ \alpha^2 & \beta^2 & \gamma^2 & \delta^2\\ \alpha^3 & \beta^3 & \gamma^3 & \delta^3\\ \alpha^4 & \beta^4 & \gamma^4 & \delta^4\end{bmatrix}^{-1}\begin{bmatrix}0\\1\\0\\0\end{bmatrix}$$

$$f''(x_0)\cong 2[af(x_0+\alpha)+\ bf(x_0+\beta)+cf(x_0+\gamma)+df(x_0+\delta)$$
$$-(a+b+c+d)f(x_0)]$$

In these cases the formulae have error that is scaled by the fifth derivative and is on the order of the product ($\alpha\beta\gamma\delta$) for the first derivative approximation and on the order of the product of the three largest (by absolute values) terms for the second derivative approximation.

Numerical Solution to Electron Beam Induced Etching Partial Differential Equations

Parabolic Partial Differential Equation Solver

The system of simultaneous ordinary differential equations for electron beam induced etching (EBIE) become partial differential equations when considering the surface diffusion of the precursor and etch product. The equations are parabolic and can be solved numerically as initial value problems with boundary conditions.

$$\frac{\partial N_A}{\partial t} = \nabla(D_A \nabla \mathrm{N_A}) + gI_A\left(1 - \frac{N_A}{Z} - \frac{N_B}{Z}\right) - \frac{N_A}{\tau_A} - \frac{A_\sigma \Gamma_e N_A}{Z} - \frac{A_{ESD}\Gamma_e N_A}{Z}$$

$$\frac{\partial N_B}{\partial t} = \nabla(D_B \nabla \mathrm{N_B}) + \frac{xA_\sigma \Gamma_e N_A}{Z} - \frac{N_B}{\tau_B} - \frac{B_\sigma \Gamma_e N_B}{Z} - \frac{B_{ESD}\Gamma_e N_B}{Z}$$

If the diffusion coefficient has no dependence on position, that is, no dependence on concentration, then the diffusion coefficient is a constant value and the diffusion components simplify to:

$$\frac{\partial N_A}{\partial t} = D_A \nabla^2 \mathrm{N_A} + gI_A\left(1 - \frac{N_A}{Z} - \frac{N_B}{Z}\right) - \frac{N_A}{\tau_A} - \frac{A_\sigma \Gamma_e N_A}{Z} - \frac{A_{ESD}\Gamma_e N_A}{Z}$$

$$\frac{\partial N_B}{\partial t} = D_B \nabla^2 \mathrm{N_B} + \frac{xA_\sigma \Gamma_e N_A}{Z} - \frac{N_B}{\tau_B} - \frac{B_\sigma \Gamma_e N_B}{Z} - \frac{B_{ESD}\Gamma_e N_B}{Z}$$

As before, the assumption of radial symmetry is made, so the system becomes:

$$\frac{\partial N_A}{\partial t} = D_A\left[\frac{1}{\mathrm{r}}\frac{\partial N_A}{\partial r} + \frac{\partial^2 N_A}{\partial r^2}\right] + gI_A\left(1 - \frac{N_A}{Z} - \frac{N_B}{Z}\right) - \frac{N_A}{\tau_A} - \frac{A_\sigma \Gamma_e N_A}{Z} - \frac{A_{ESD}\Gamma_e N_A}{Z}$$

$$\frac{\partial N_B}{\partial t} = D_B\left[\frac{1}{\mathrm{r}}\frac{\partial N_B}{\partial r} + \frac{\partial^2 N_B}{\partial r^2}\right] + \frac{xA_\sigma \Gamma_e N_A}{Z} - \frac{N_B}{\tau_B} - \frac{B_\sigma \Gamma_e N_B}{Z} - \frac{B_{ESD}\Gamma_e N_B}{Z}$$

This system solution can be approximated numerically using the Runge-Kutta 4th order algorithm. First, the spatial derivatives are replaced by discrete formulae to approximate the first and second derivatives, in this case the three-point central difference formulae (but any n-point derivative approximation could be used):

$$\frac{\partial N_A}{\partial t} = f\left(t, \begin{bmatrix} N_A \\ N_B \end{bmatrix}\right) = D_A\left[\frac{1}{\mathrm{r_i}}\left(\frac{N_{Ai+1} - N_{Ai-1}}{\Delta r}\right) + \left(\frac{N_{Ai+1} - 2N_{Ai} + N_{Ai-1}}{(\Delta r)^2}\right)\right] + gI_A\left(1 - \frac{N_{Ai}}{Z} - \frac{N_{Bi}}{Z}\right) - \frac{N_{Ai}}{\tau_A} - \frac{A_\sigma \Gamma_{ei} N_{Ai}}{Z} - \frac{A_{ESD}\Gamma_{ei}N_{Ai}}{Z}$$

$$\frac{\partial N_B}{\partial t} = g\left(t, \begin{bmatrix} N_A \\ N_B \end{bmatrix}\right) = D_B\left[\frac{1}{\mathrm{r_i}}\left(\frac{N_{Bi+1} - N_{Bi-1}}{\Delta r}\right) + \left(\frac{N_{Bi+1} - 2N_{Bi} + N_{Bi-1}}{(\Delta r)^2}\right)\right] + \frac{xA_\sigma \Gamma_{ei} N_{Ai}}{Z} - \frac{N_{Bi}}{\tau_B} - \frac{B_\sigma \Gamma_{ei} N_{Bi}}{Z} - \frac{B_{ESD}\Gamma_{ei}N_{Bi}}{Z}$$

The Runge-Kutta 4th-order algorithm (RK4) gives an approximation to the next time step by:

$$k_1 = \Delta t \begin{bmatrix} f\left(t, \begin{bmatrix} N_A \\ N_B \end{bmatrix}\right) \\ g\left(t, \begin{bmatrix} N_A \\ N_B \end{bmatrix}\right) \end{bmatrix}$$

$$k_2 = \Delta t \begin{bmatrix} f\left(t + \frac{1}{2}\Delta t, \begin{bmatrix} N_A \\ N_B \end{bmatrix} + \frac{1}{2}k_1\right) \\ g\left(t + \frac{1}{2}\Delta t, \begin{bmatrix} N_A \\ N_B \end{bmatrix} + \frac{1}{2}k_1\right) \end{bmatrix}$$

$$k_3 = \Delta t \begin{bmatrix} f\left(t + \frac{1}{2}\Delta t, \begin{bmatrix} N_A \\ N_B \end{bmatrix} + \frac{1}{2}k_2\right) \\ g\left(t + \frac{1}{2}\Delta t, \begin{bmatrix} N_A \\ N_B \end{bmatrix} + \frac{1}{2}k_2\right) \end{bmatrix}$$

$$k_4 = \Delta t \begin{bmatrix} f\left(t + \Delta t, \begin{bmatrix} N_A \\ N_B \end{bmatrix} + k_3\right) \\ g\left(t + \Delta t, \begin{bmatrix} N_A \\ N_B \end{bmatrix} + k_3\right) \end{bmatrix}$$

$$\begin{bmatrix} N_A \\ N_B \end{bmatrix}_{j+1} = \begin{bmatrix} N_A \\ N_B \end{bmatrix}_j + \frac{1}{6}(k_1 + 2k_2 + 2k_3 + k_4) + O[(\Delta t)^5]$$

The error in the formula is on the order of the time increment to the 5th power. It is helpful to observe that a 2nd order Runge-Kutta formula (RK2) is calculated exactly the same way, except that the calculation need only go to k_2. The approximation is then:

$$\begin{bmatrix} N_A \\ N_B \end{bmatrix}_{j+1} = \begin{bmatrix} N_A \\ N_B \end{bmatrix}_j + k_2 + O[(\Delta t)^3]$$

The error in this formula scales with time increment to the 3rd power. The partial differential equations of interest have widely varying time scales. Initially, a very small time step is necessary in order to maintain stability in the approximation, but the time range of interest can extend several orders of magnitude higher than the initial time step. In order to make the computation time and computer memory requirement reasonable, it is necessary to build an adaptive step size algorithm to reduce the total number of calculations required. This is commonly accomplished by using a 5th order Runge-Kutta algorithm and a 4th order Runge-Kutta algorithm and comparing the results. The difference in the results should scale with the time increment when using 4th and 5th order algorithms. If the difference is too small, then the step size can be increased. Likewise, if the difference is large, then the step size should be decreased to reduce the formula error. The new step size is determined based on the difference in the formulae and the predetermined acceptable error:

$$\Delta t_{new} = \Delta t_{old} \left| \frac{maxerror}{error} \right|$$

Using the new step size, the integration is performed using the higher order algorithm. This strategy can be greatly improved by recognizing that the calculation of the Runge-Kutta 4th order algorithm requires the calculation of the Runge-Kutta 2nd order algorithm. Simply put, the 4th order algorithm already contains all the necessary information to calculate an adaptive step size. Subtracting the 4th order from the 2nd order approximations we find that:

$$k_2 - \frac{1}{6}(k_1 + 2k_2 + 2k_3 + k_4) = (O[(\Delta t)^3] - O[(\Delta t)^5]) \approx O[(\Delta t)^3]$$

Now, the difference between the 2nd order algorithm and 4th order algorithm scales as the time increment to the 3rd power, so the new time step becomes:

$$\Delta t_{new} = \Delta t_{old} \left| \frac{maxerror}{error} \right|^{\frac{1}{3}}$$

To ensure that the integration remains inside the maximum error limit, a 10% safety margin is used:

$$\Delta t_{new} = (0.9)\Delta t_{old} \left| \frac{maxerror}{error} \right|^{\frac{1}{3}}$$

For each time step, the 4th order algorithm is calculated, the error in the calculation is determined. If the existing error is too large, then the new time step is reduced to a level that brings the error in line; likewise, if the existing error is small, then the new time step is increased as large as possible while maintaining the minimum accuracy required.

It is best to start with a very small time step to ensure accuracy of the Runge-Kutta algorithm. But, if the initial time step is greatly different than the optimal time step for the desired maximum error, then the subsequent time step can differ greatly. That is, if the first time step is very small and results in a very small error compared to the maximum desirable error, the new time step could be too large and cause the PDE to lose stability. In order to avoid this problem, the maximum incremental increase in time step allowed is double the existing time step. This allows the algorithm to start with a very small time step then for each subsequent time step doubling the size until the error is comparable in size to the maximum allowable error. After that point the existing error determines the next step size. The time steps typically increase in size as the PDE system relaxes toward the steady state.

The outer boundary (large radius) is handled by setting the precursor and etch product surface concentrations to their zero electron flux equilibrium conditions. That is:

$$\begin{bmatrix} N_A \\ N_B \end{bmatrix}_{Boundary} = \begin{bmatrix} \dfrac{gI_A}{\left(\dfrac{gI_A}{Z} + \dfrac{1}{\tau_A}\right)} \\ 0 \end{bmatrix}$$

The inner boundary at r=0 is treated as a special case by using the forward difference equations for the derivatives. Specifically, the 5-point forward difference algorithms were used at the inner boundary for the first and second derivatives. In order to maintain continuity, the derivative of the gas surface concentrations at the center is zero, and this could be considered a boundary condition. If the true center at r=0 is excluded and the boundary in the approximation is set at $r_1=\Delta r$, then the PDE system forces itself to the boundary condition of:

$$\frac{\partial}{\partial r}\begin{bmatrix} N_A \\ N_B \end{bmatrix}_{Center} = \begin{bmatrix} 0 \\ 0 \end{bmatrix}$$

because of the term:

$$\frac{\partial N_A}{\partial t} = D_A\left[\frac{1}{\mathrm{r}}\frac{\partial N_A}{\partial r} + \frac{\partial^2 N_A}{\partial r^2}\right] + \cdots$$

for radii approaching zero and a non-zero diffusion coefficient, the spatial derivative is forced to zero by the temporal derivative. If the surface diffusion coefficient is zero, then the partial differential equations system is actually an ordinary differential equations system, and it is no longer a boundary value problem.

The initial condition is set to the same value as the outer boundary condition. The precursor concentration is at its equilibrium level assuming the gas has been on and the beam has been off. The etch product concentration is initially zero. The beam on simulation proceeds until the beam dwell time setting is reached after (count) time steps. Because the time steps are adaptive in size, the value of (count) is not fixed. At this point, the ending values of precursor and etch product concentrations at each radii are stored.

Etched Material Integration

The material etched for each radii is calculated by integrating in time the precursor and etch product concentrations. As before:

$$Etched = \frac{\Gamma_e}{Z}\left[B_\sigma \int_{t=0}^{t=\tau_{dwell}} N_B\, dt - xA_\sigma \int_{t=0}^{t=\tau_{dwell}} N_A\, dt\right]$$

The integration is done by the trapezoidal method, where a line is fit from one data point to the next and the area of the resulting trapezoid formed by the line and the time axis:

$$\int_{t=0}^{t=\tau_{dwell}} N_A\, dt \approx \sum_{i=1}^{i=(count-1)} \frac{(N_{Ai} + N_{Ai+1})(t_{i+1} - t_i)}{2}$$

The solver is then reset and the final conditions from the previous run are loaded in as the initial conditions for the subsequent run. The electron flux is set to zero, and the system of partial differential equations is solved for the refresh time. The end conditions of the gas concentrations are then used as the initial conditions for the second beam pulse. This process is repeated until the desired number of beam pulses are completed or the initial conditions for each pulse change within a minimum increment, indicating that a “steady state” of cycling has been achieved.

Beam Shape Calculation

The shape of the electron flux profile is highly influential in the impact of dwell time on the shape of the etch. While a Gaussian shape is often used to emulate the electron flux density it is not able to describe the effect of defocusing the beam or the effect of backscattered and secondary electron emissions.

If the effect of brightness, spherical and chromatic aberrations, as well as defocusing of the beam can be considered as a cylindrical disc of uniform flux, then the shape of the impinging beam can be modeled as the two dimensional convolution of the cylinder with the appropriate Airy disc shape for the aperture size and De Broglie wavelength for the impinging electrons.

$$\Gamma_{\mathrm{defocus}} = \frac{4\mathrm{i}_{\mathrm{beam}}}{e\pi\mathrm{d}_0{}^2}\,\mathrm{cyl}\left(\frac{\mathrm{r}}{\mathrm{d}_0}\right)$$

Where i_{beam} is the beam current, *e* is the fundamental charge of the electron, and d_0 is the diameter of the cylindrical shape. The cylinder function (cyl) is defined as 1 for all values of r less than one half of d_0 and 0 for values of r greater than one half of d_0.

$$cyl\left(\frac{r}{d}\right) = \begin{cases} 1, 0 \le r < \dfrac{d}{2} \\ \dfrac{1}{2}, r = \dfrac{d}{2} \\ 0, r > \dfrac{d}{2} \end{cases}$$

The Airy disc, also known as the sombrero function, gives the diffraction pattern of an electron passing through the limiting aperture of the objective lens. This shape can be thought of as the probability distribution of locating an electron at the focal plane that has passed through the aperture at the pupil plane of the lens. The simplest way of determining this shape is to consider the aperture as a low pass filter in the pupil plane and take an Inverse Fourier Transform of the pupil filter to arrive at the point spread function of the lens. Considering the pupil filter as:

$$D[\rho] = cyl\left(\frac{\rho}{\left(2\sin\alpha/\lambda\right)}\right) \approx cyl\left(\frac{\rho\lambda}{2\alpha}\right)$$

Where ρ is the radial spatial frequency, λ is the De Broglie wavelength of the electron, and α is the maximum arrival angle of electrons at the sample due to the lens aperture. The Zeroth Order Hankel Transform is the radially symmetric 2-D Fourier Transform. It is useful for developing analytical equations using the Bessel function, which is difficult to evaluate, but fortunately MATLAB™ is able to perform operations in two dimensions easily. The radial spatial frequency can be converted to ξ and η, the x and y directional spatial frequencies by the relationship:

$$\rho = \sqrt{\xi^2 + \eta^2}$$

The diffraction effect in the sample plane is determined by taking the square magnitude of the Two-Dimensional Inverse Fourier Transform of the pupil filter.

$$d[x,y] = \left| \iint_{-\infty}^{\infty} D[\xi,\eta] e^{2\pi i(\xi x + \eta y)} d\xi d\eta \right|^2$$

MATLAB™ can handle this by use of the 2-D FFT algorithm to form a discrete approximation to the Fourier Transform. The result is the appropriate Airy disc probability distribution for the likelihood of locating a single electron diffracting through the lens aperture. When this shape is convolved with the beam flux defocus cylinder, the actual impinging beam flux shape is determined.

$$\Gamma_{\text{beam}} = \Gamma_{\text{defocus}}[\text{x},\text{y}] ** \text{d}[\text{x},\text{y}]$$

This gives the shape of the impinging beam at the surface of the sample. In order to get the full electron flux at the surface, consideration must be made for the secondary and back-scattered electrons that are emitted from the surface some distance away from where the primary electron entered the surface.

A double-scattering Monte Carlo simulation was run at the wavelength of interest to determine a backscattered/secondary emission probability distribution. The Monte Carlo simulation was run for 10^7 primary electrons entering the surface at r=0. Every time a secondary electron or back-scattered electron was emitted from the surface, the radius from the center was recorded and a histogram of emissions per unit area versus radius is generated. When the histogram is divided by the number density of primary electrons at the origin, the result is a radial probability distribution of an emission per primary electron. An analytical function is fit to the probability distribution of the form:

$$\text{Emission}(r) = \frac{a_0 e^{-\frac{r}{r_0}} + a_1 e^{-\frac{r}{r_1}}}{1 + e^{-\frac{(r-r_2)}{r_3}} + e^{-\frac{(r-r_4)}{r_5}}}$$

The first term in the numerator describes the secondary electrons emitted by the primary beam as it first passes into the surface of the sample. These are the so-called SE_I. The second term in the numerator describes the emission of the back-scattered electrons and secondary electrons generated by the backscattered electrons (BSE and SE_{II}). The denominator, inspired by the form of the Fermi function, provides a drop off toward zero in the emissions at the perimeter. The parameters r_2 and r_4 are governed by the Bethe range.

The emission probability function is transformed into rectangular coordinate then convolved in two dimensions with the impinging beam flux profile to get the shape of the emitted electron flux. This is added back to the impinging electron beam flux profile (by convolving with the Dirac-delta function) to arrive at the total electron flux at the surface. It is this shape that is used in the PDE approximation solver.

$$\Gamma_{\text{emission}} = (\Gamma_{\text{defocus}}[x, y] ** d[x, y]) ** \text{Emission}[x, y]$$

$$\Gamma_{\text{total}} = (\Gamma_{\text{defocus}}[x, y] ** d[x, y]) ** (\delta[x, y] + \text{Emission}[x, y])$$

Two-dimensional convolution is computationally cumbersome, so it is more efficient to take advantage of the fact that the convolution operation in real space is multiplication in frequency space. So, each component of the convolution is transformed into frequency space by the Fast Fourier Transform; and complex multiplication of all three transforms gives the frequency space equivalent of the total electron flux. An Inverse Fast Fourier Transform gives the total electron flux shape at the surface. In this way, the effects of defocusing the beam, aperture diffraction, and electron-solid interaction on the electron flux profile and ultimately the etch or deposit shape can be appropriately considered.

Figure 44 illustrates the different cylinders for different levels of defocus for the same beam current. Note that the flux decreases with increasing spot size. The effect of the electron diffraction is convolved onto the defocus cylinders for a 5keV electron beam and a 5.4×10^{-3} convergence angle (α) is seen in Figure 45. The emission of the backscattered and secondary electrons for 5keV electrons in silica is seen in Figure 46. The total effect of the primary electrons and the emitted electrons is seen on a logarithmic scale in Figure 47.

Simulated Factor Effects

It is worthwhile to explore some of the various process parameters and determine the various effects of these parameters on the expected etch shape. In each case the effects of varying a single parameter are displayed to convey a general sense of the effect of that parameter on the gas surface concentrations and etch shape profile. Table 2 gives the "center" value for each of the parameters, so that they need not be repeated for each plot. The corresponding figures for each factor effect are listed in the table. The first figure using the low etch product residence time, the second figure using the middle etch product residence time, and the third figure using the high etch product residence time.

The effect of the first ten pulses is accounted for in these simulations. It should be noted that for some cases of high diffusion and/or small molecular impingement rates, it takes a large number of pulses to reach "steady pulsing". This topic is discussed in greater detail later in this chapter.

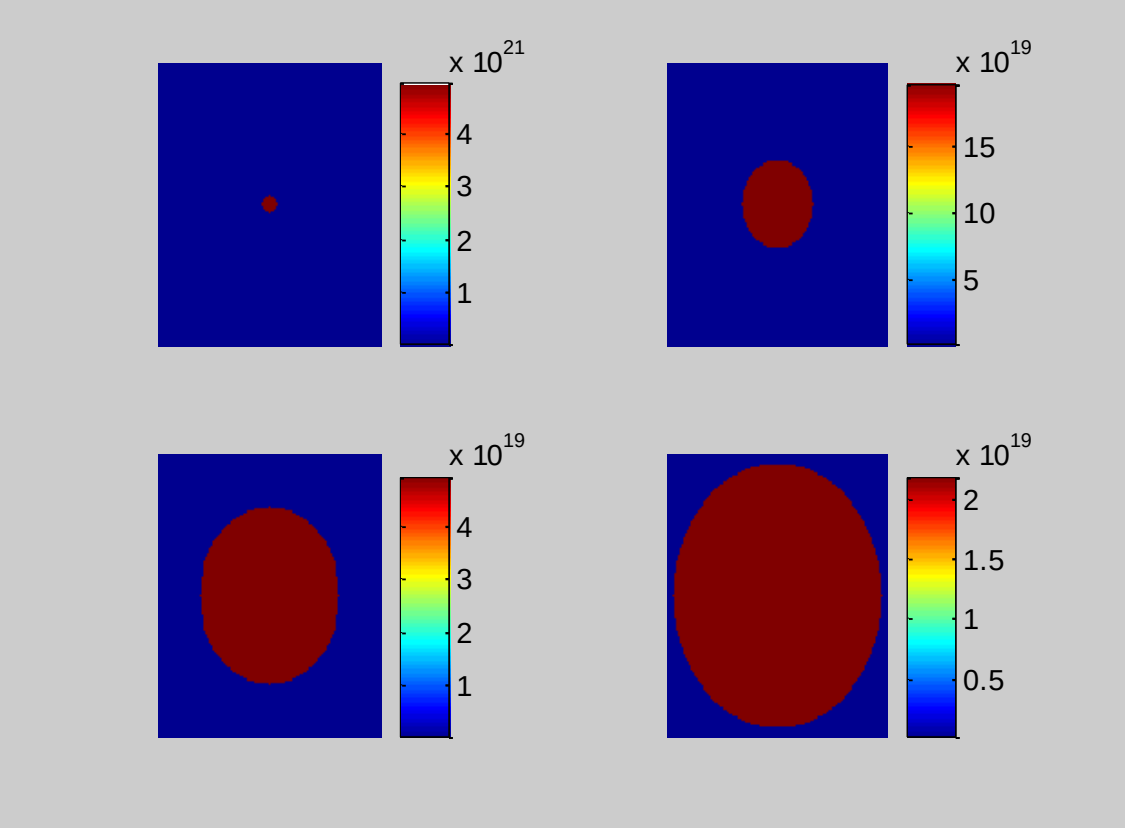

Figure 44: Defocus Cylinders

The horizontal and vertical scales are 128nm, and the electron flux scale varies for each sub-plot.

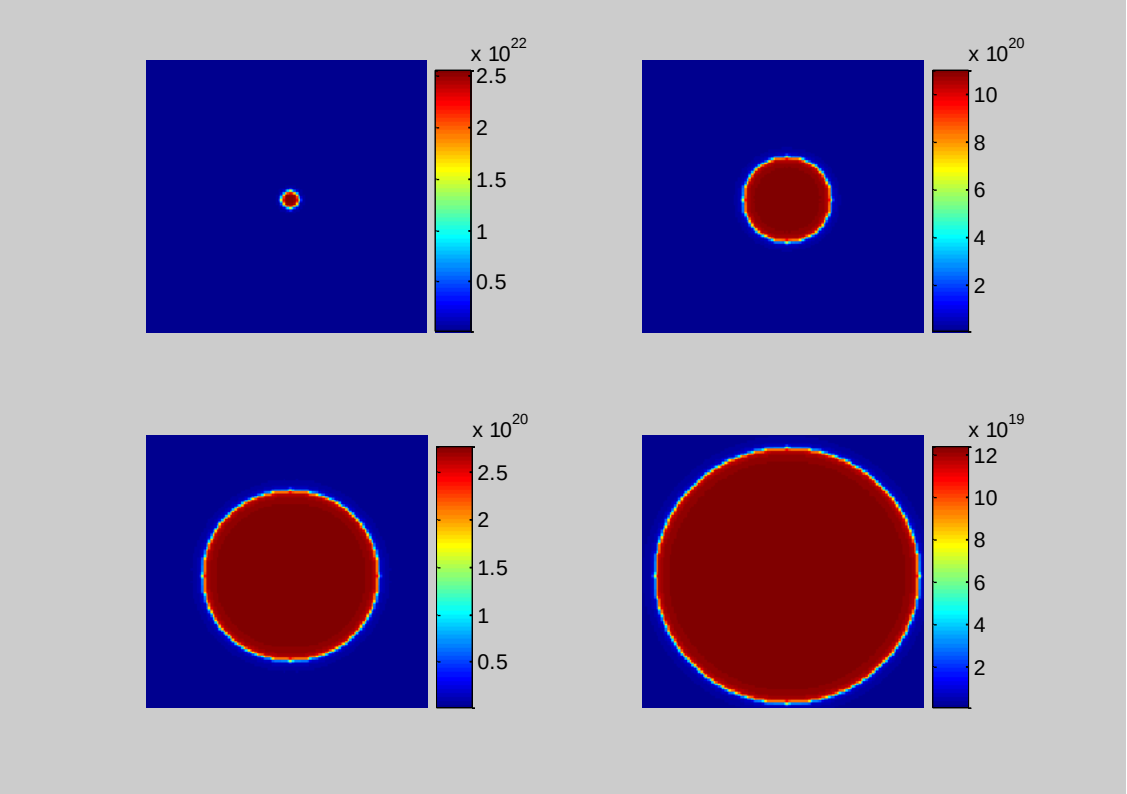

Figure 45: Defocus Cylinders with Electron Diffraction

The horizontal and vertical scales are 128nm, and the electron flux scale varies for each sub-plot.

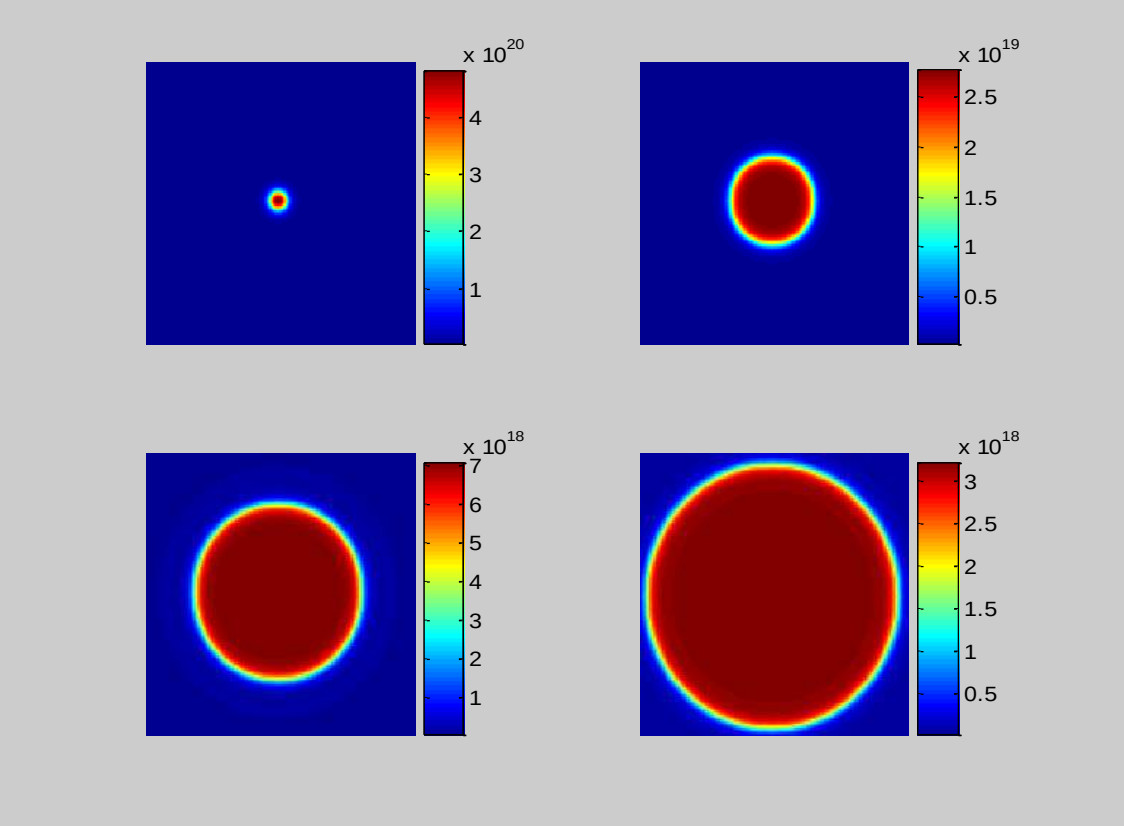

Figure 46: Backscattered and Secondary Electron Emissions

The horizontal and vertical scales are 128nm, and the electron flux scale varies for each sub-plot.

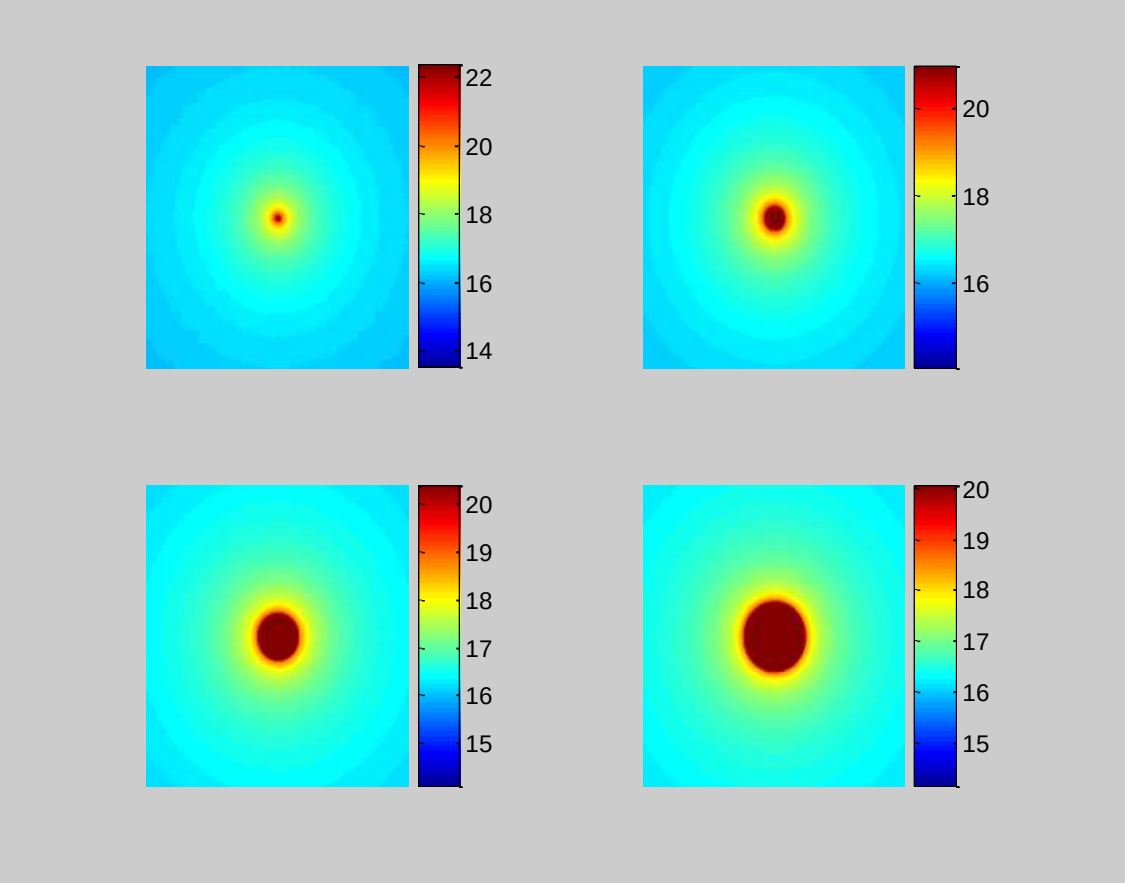

Figure 47: Combined Effect of Primary, Backscattered, and Secondary Electrons

The horizontal and vertical scales are 512nm each and the electron flux is scaled on a base-10 logarithm.

Table 2: Center Conditions for Simulated Experimental Factor Effects

Name	Symbol	Value	Units	Figures
Effective Molecular Impingement Rate	gI_A	1.0×10^{16}	$cm^{-2}s^{-1}$	48, 49, 50
Precursor Residence Time	τ_A	1.0	s	51, 52, 53
Surface Adsorption Site Density	Z	1.0×10^{15}	cm^{-2}	none
Precursor Dissociation Probability	A_σ	0.5	unitless	54, 55, 56
Precursor Electron Stimulated Desorption Probability	A_{ESD}	0.0	unitless	57, 58, 59
Precursor Surface Diffusion Coefficient	D_A	1.0×10^{-10}	cm^2s^{-1}	60, 61, 62
Stoichiometry Factor	x	0.5	unitless	none
Etch Product Residence Time	τ_B	10^{-6} (Short) 10^{-3} (Medium) 1 (Long)	s	all
Etch Product Dissociation Probability	B_σ	0.1	unitless	63, 64, 65
Etch Product Electron Stimulated Desorption Probability	B_{ESD}	0.0	unitless	66, 67, 68
Etch Product Surface Diffusion Coefficient	D_B	1.0×10^{-10}	cm^2s^{-1}	69, 70, 71
Beam Dwell Time	τ_{Dwell}	5.0×10^{-5}	s	72, 73, 74
Beam Refresh Time	$\tau_{Refresh}$	1.0×10^{-3}	s	75, 76, 77

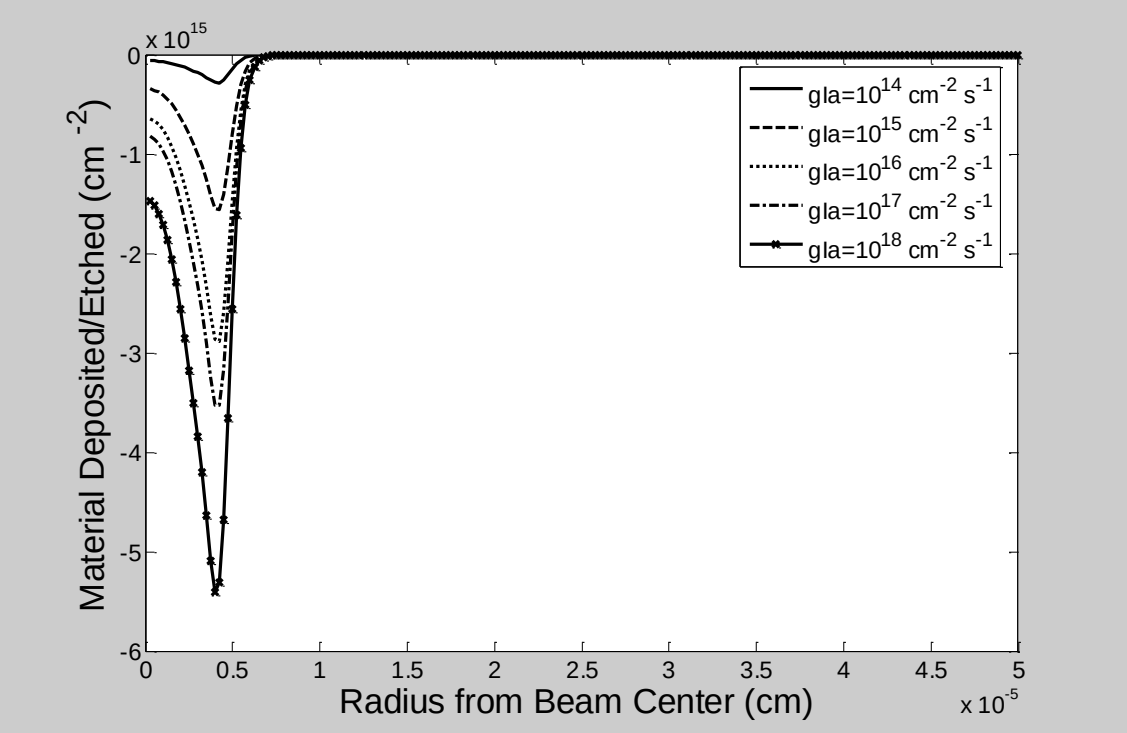

Figure 48: ***Effect of Molecular Impingement Rate with a Short Etch Product Residence Time***

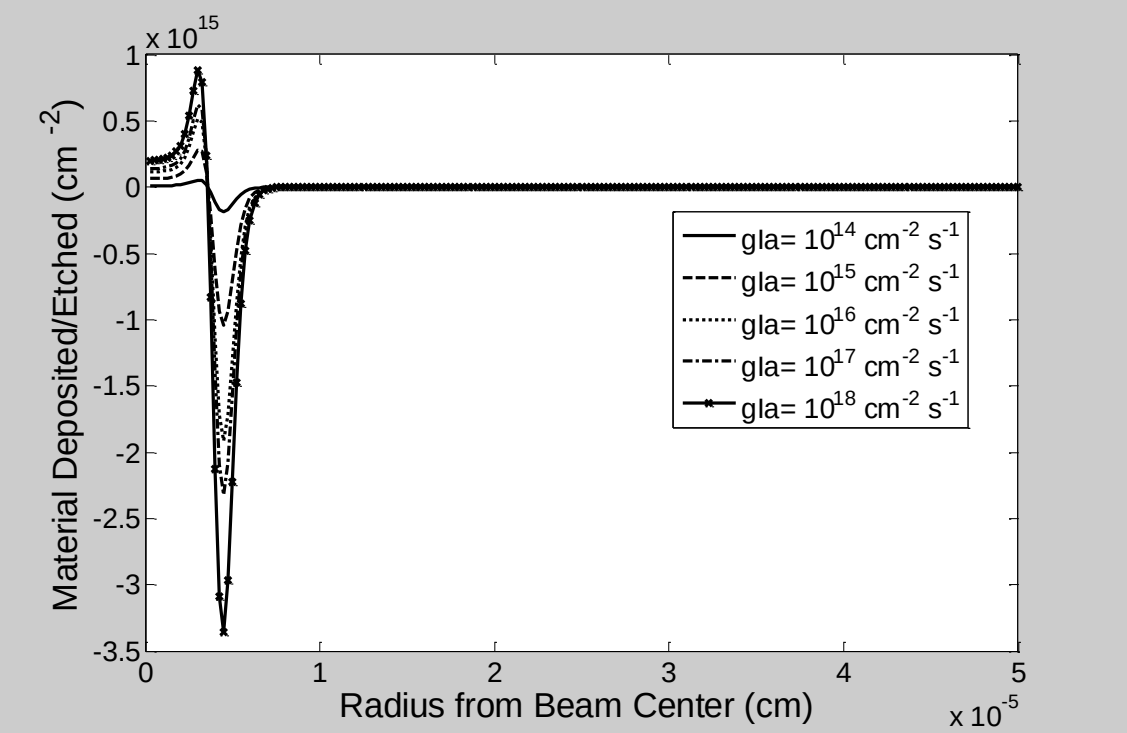

Figure 49: ***Effect of Molecular Impingement Rate with a Medium Etch Product Residence Time***

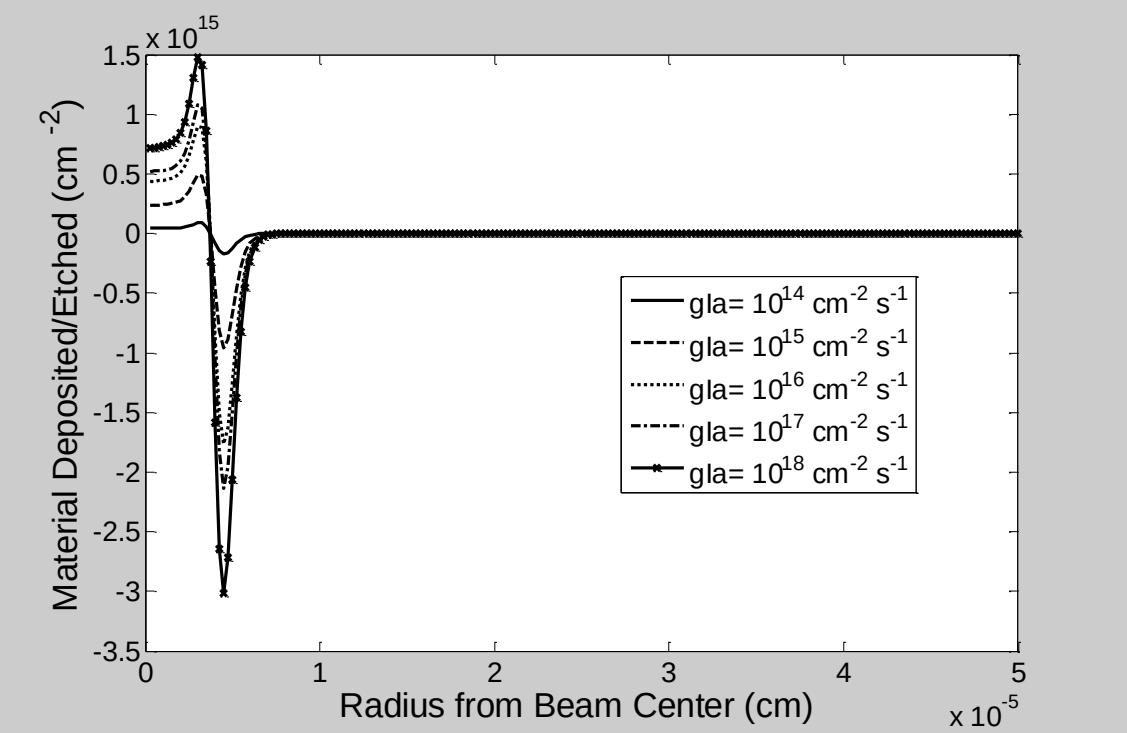

Figure 50: ***Effect of Molecular Impingement Rate with a Long Etch Product Residence Time***

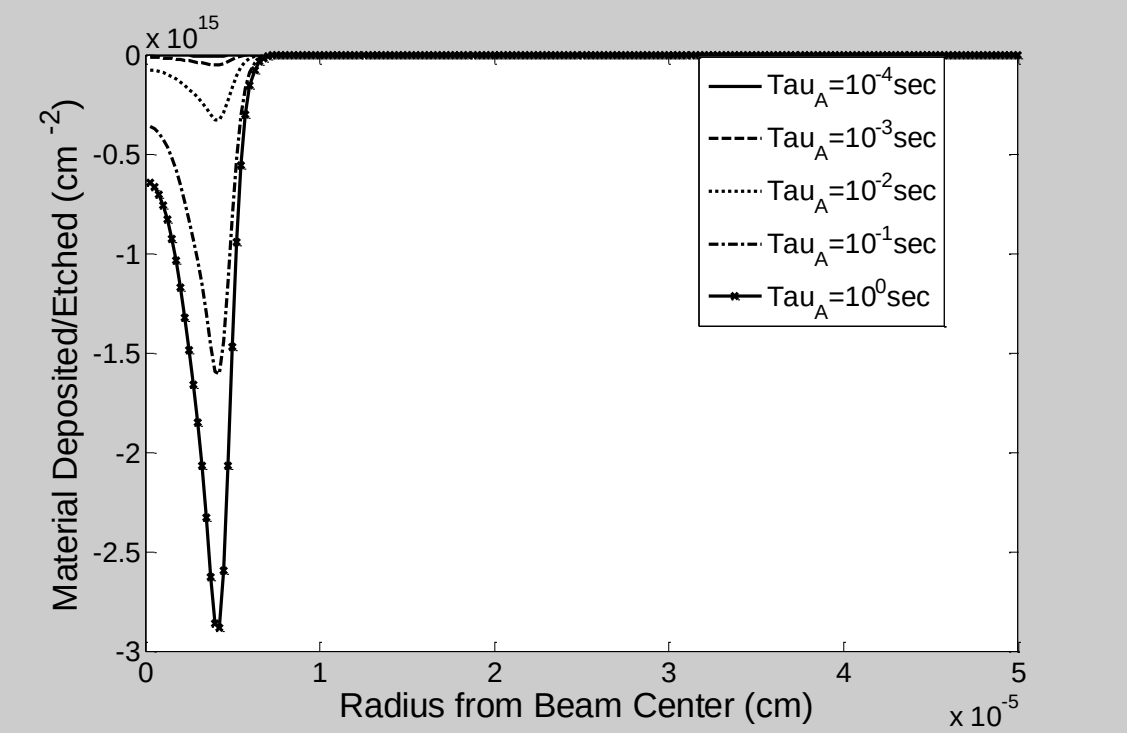

Figure 51: ***Effect of Precursor Residence Time with a Short Etch Product Residence Time***

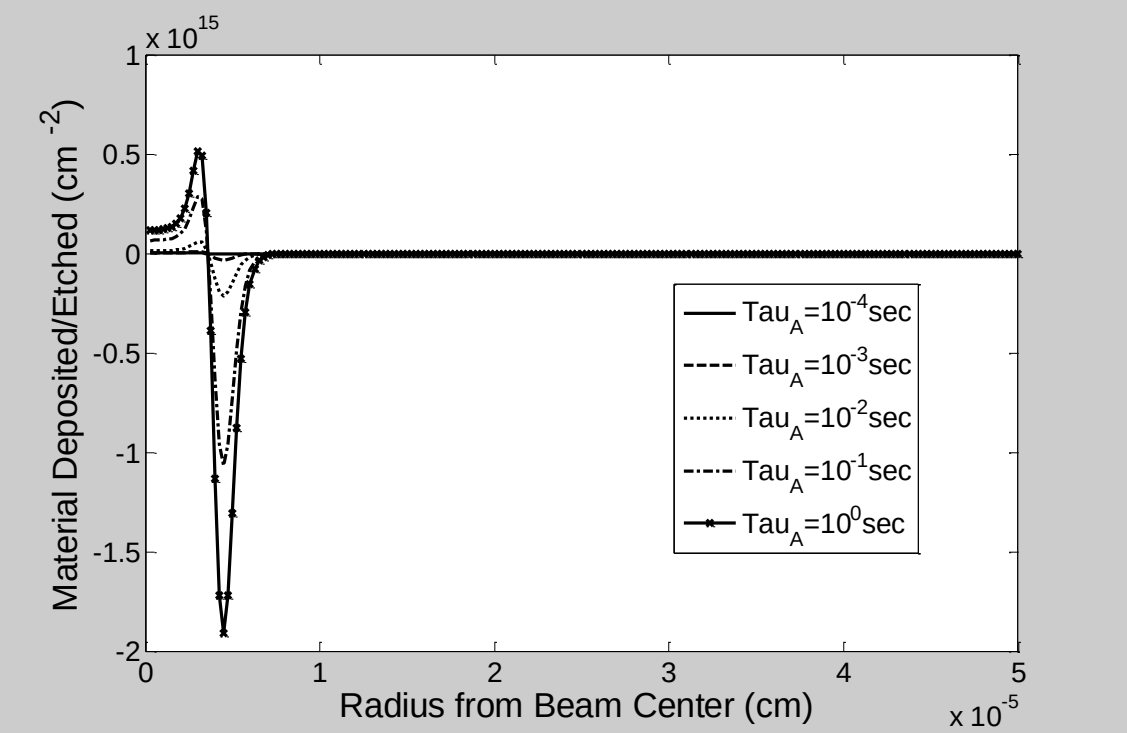

Figure 52: ***Effect of Precursor Residence Time with a Medium Etch Product Residence Time***

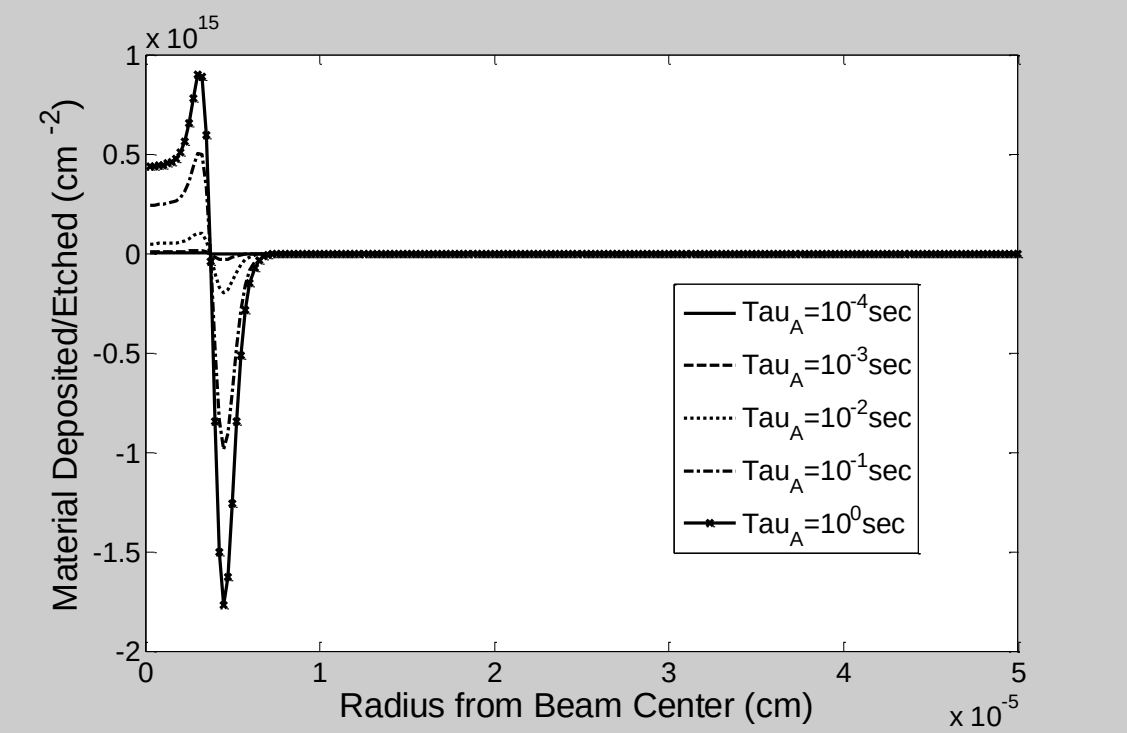

Figure 53: ***Effect of Precursor Residence Time with a Long Etch Product Residence Time***

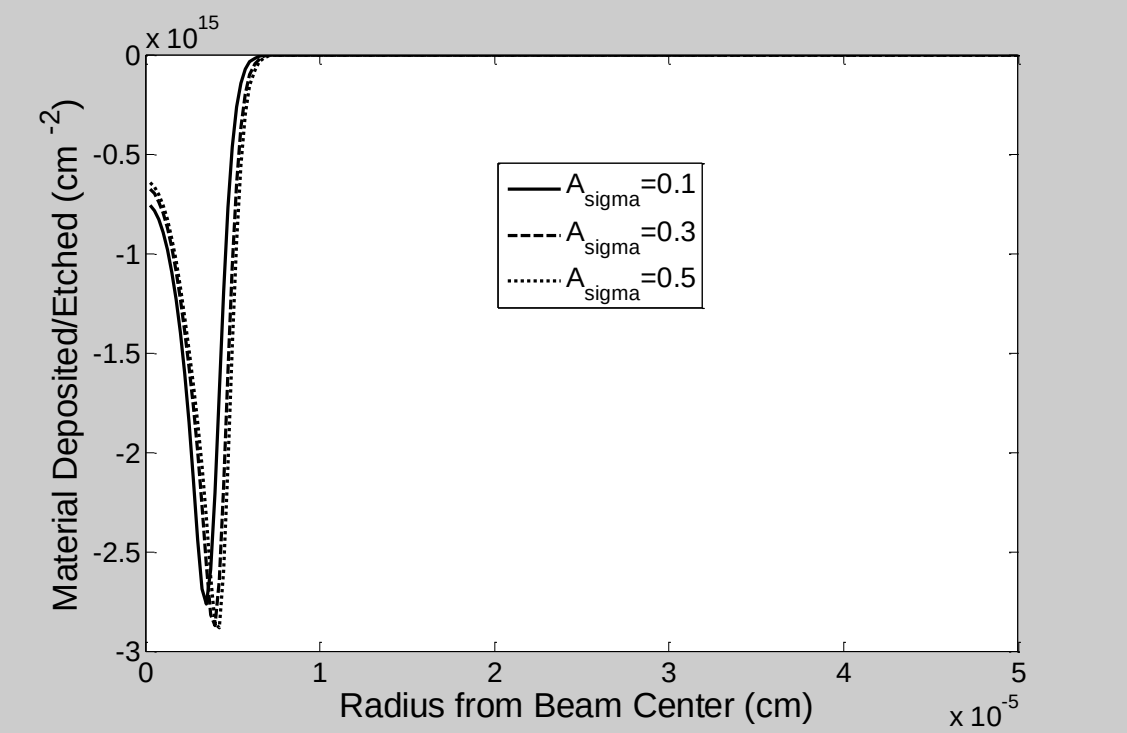

Figure 54: ***Effect of Precursor Dissociation Probability with a Short Etch Product Residence Time***

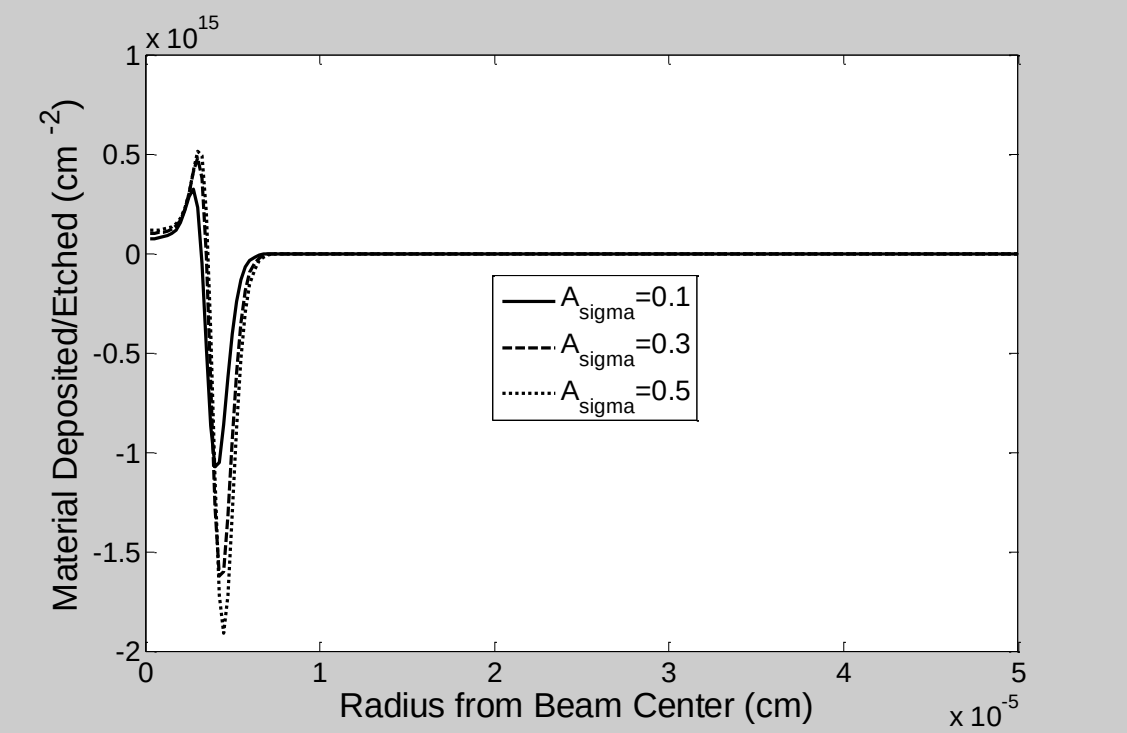

Figure 55: ***Effect of Precursor Dissociation Probability with a Medium Etch Product Residence Time***

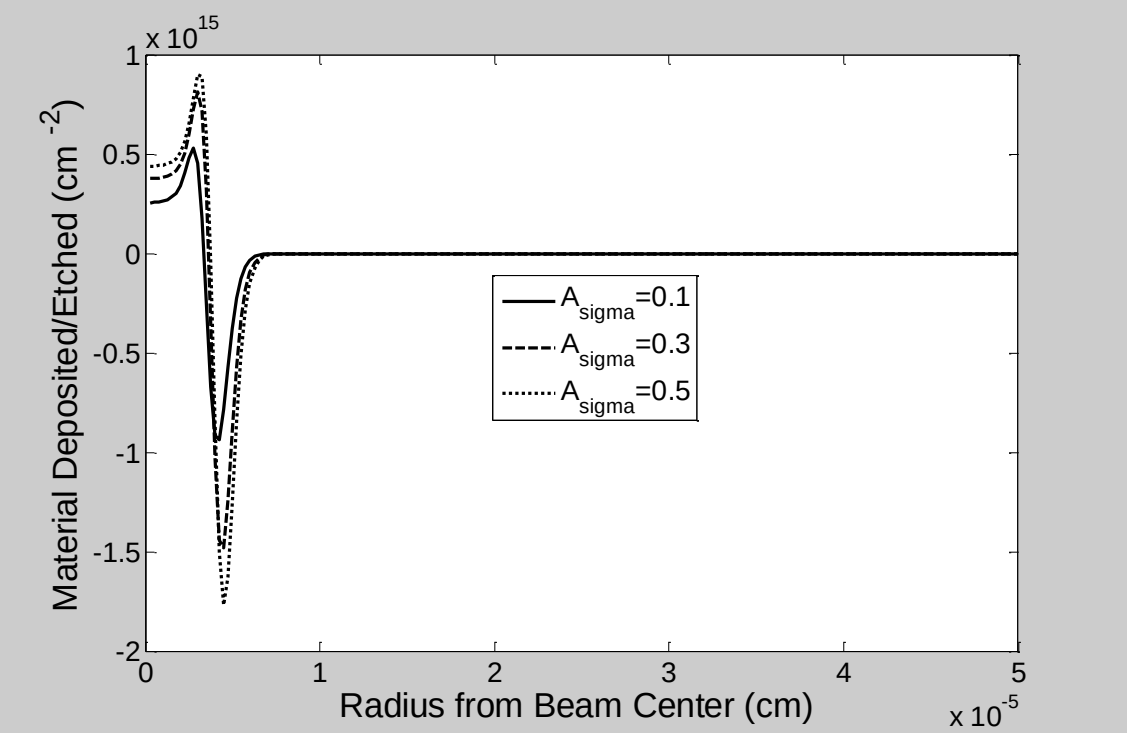

Figure 56: ***Effect of Precursor Dissociation Probability with a Long Etch Product Residence Time***

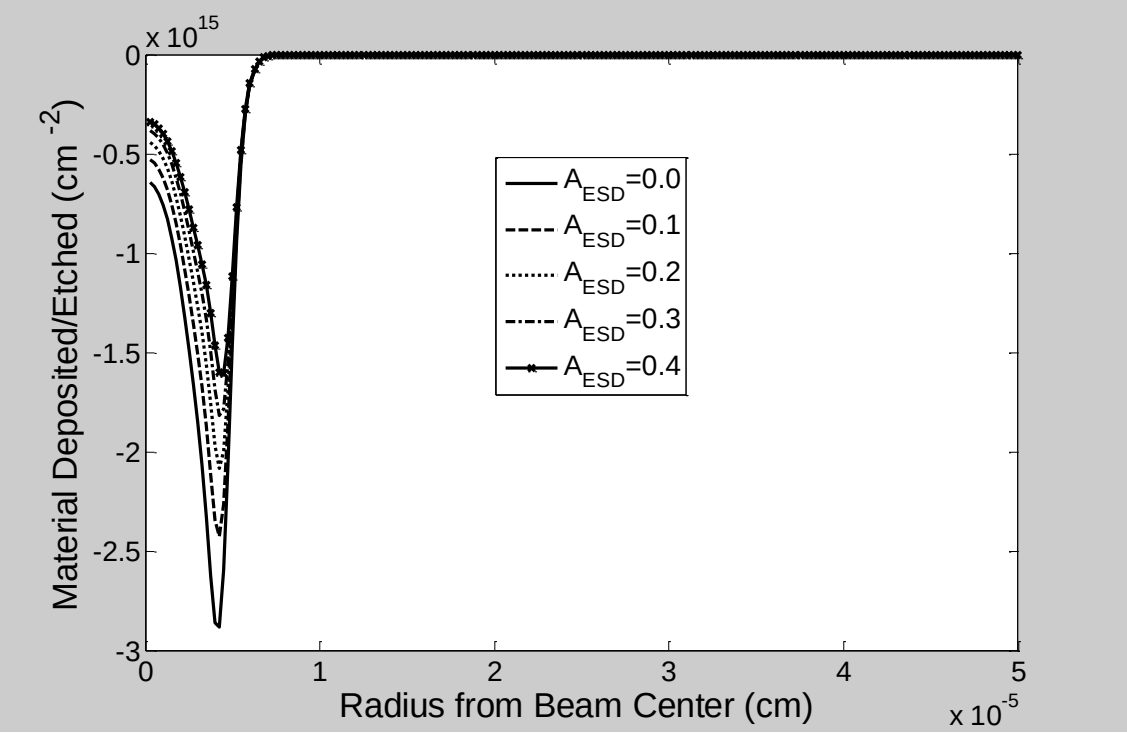

Figure 57: ***Effect of Precursor Electron Stimulated Desorption with a Short Etch Product Residence Time***

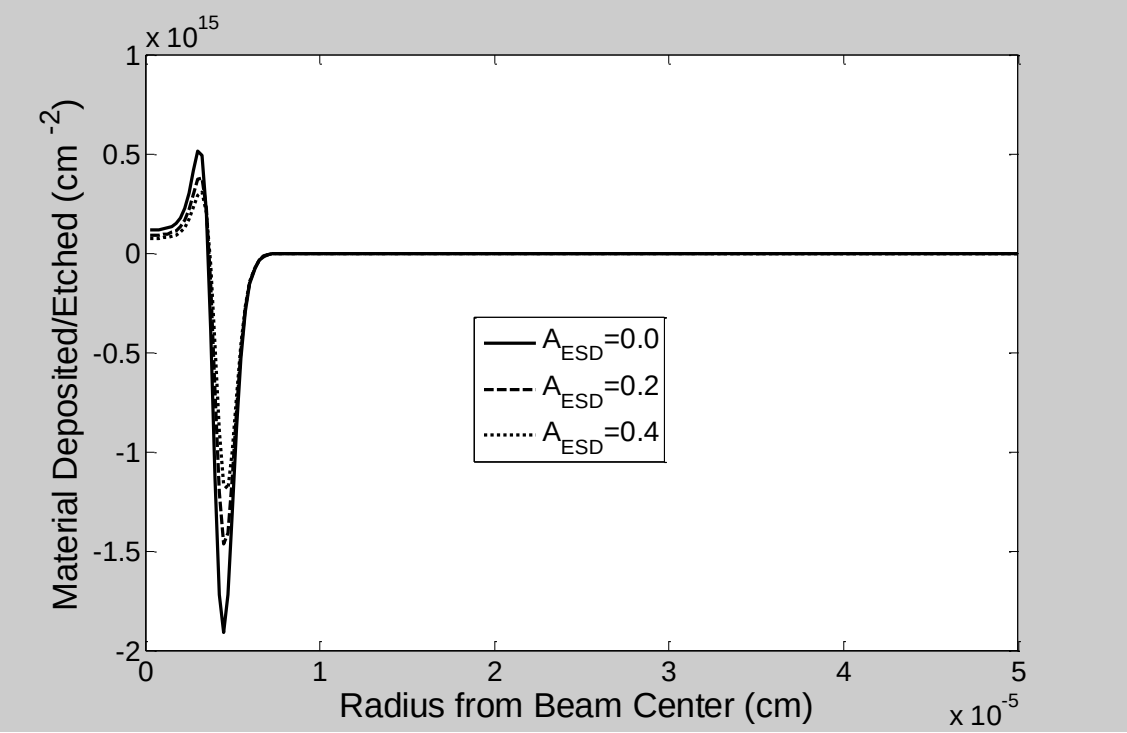

Figure 58: ***Effect of Precursor Electron Stimulated Desorption with a Medium Etch Product Residence Time***

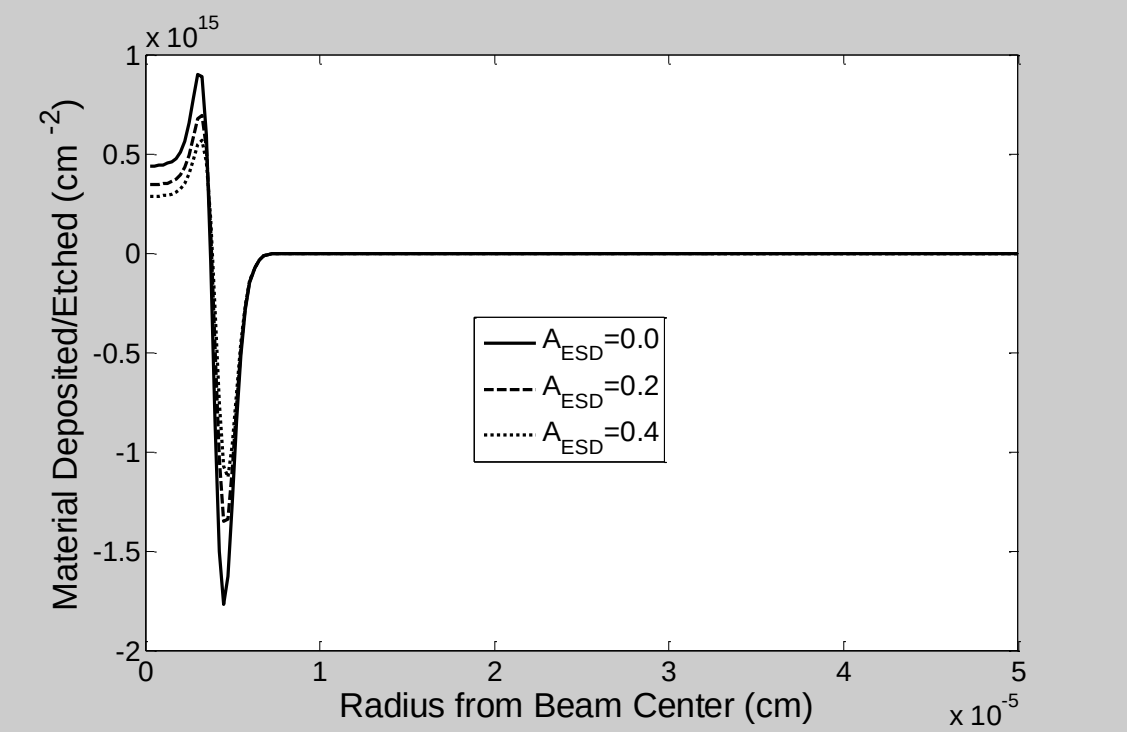

Figure 59: ***Effect of Precursor Electron Stimulated Desorption with a Long Etch Product Residence Time***

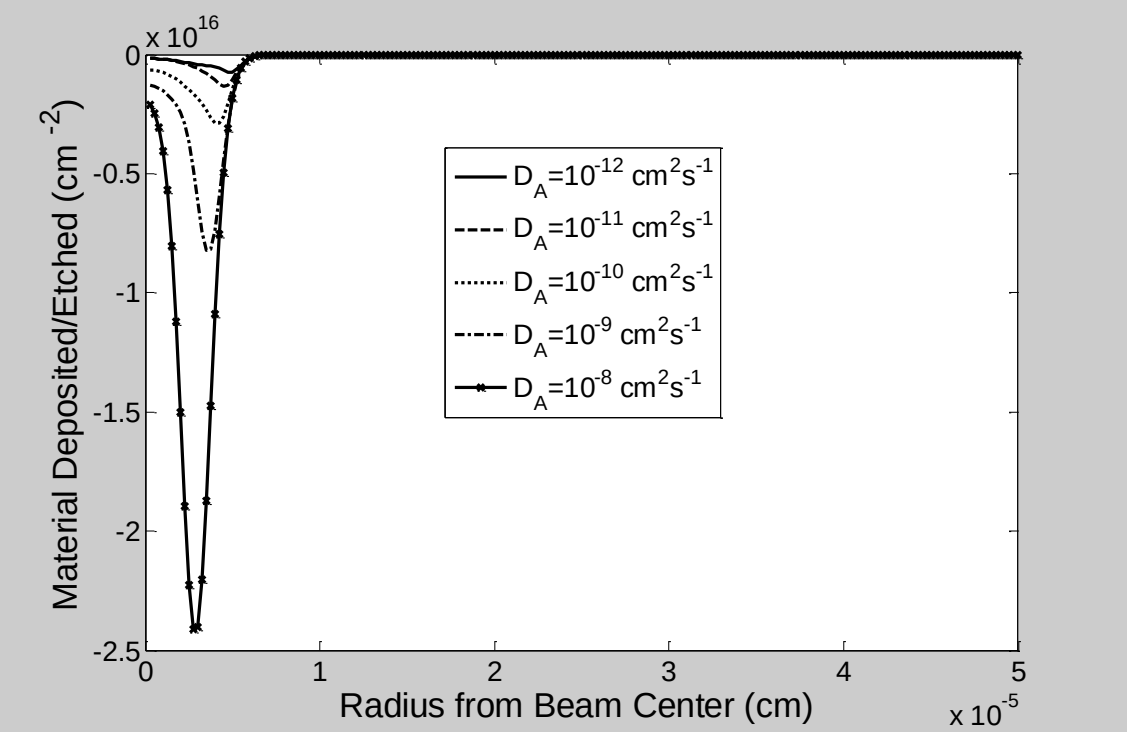

Figure 60: ***Effect of Precursor Surface Diffusion Coefficient with a Short Etch Product Residence Time***

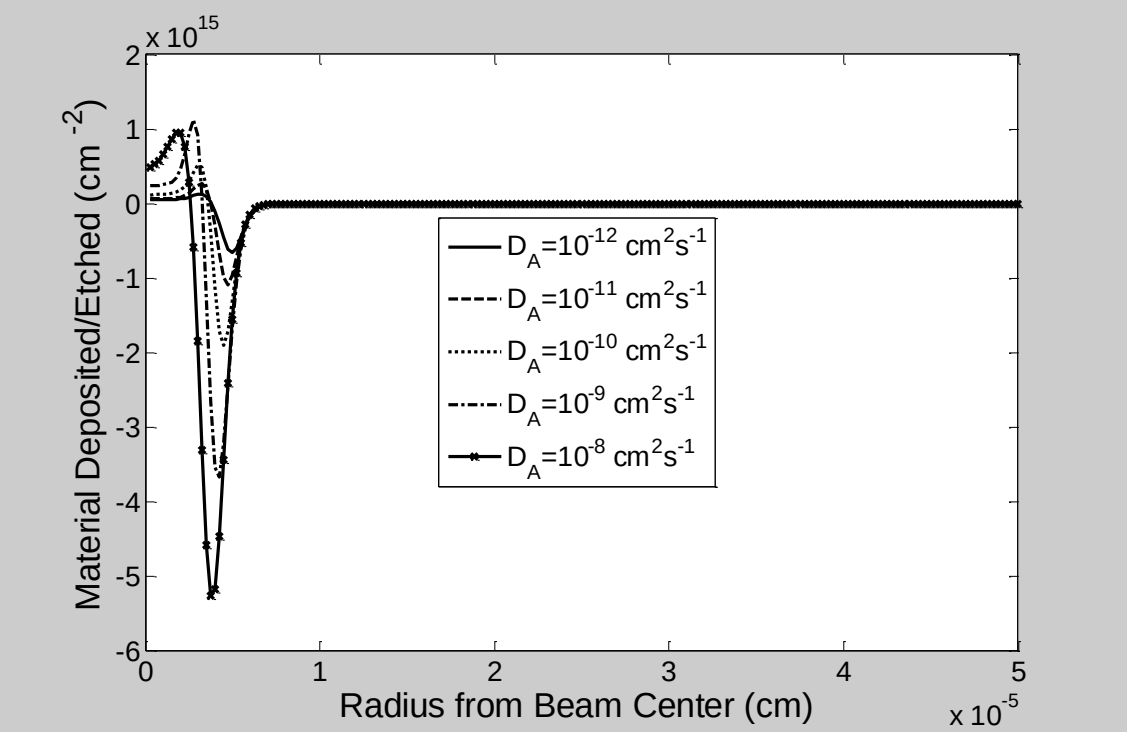

Figure 61: ***Effect of Precursor Surface Diffusion Coefficient with a Medium Etch Product Residence Time***

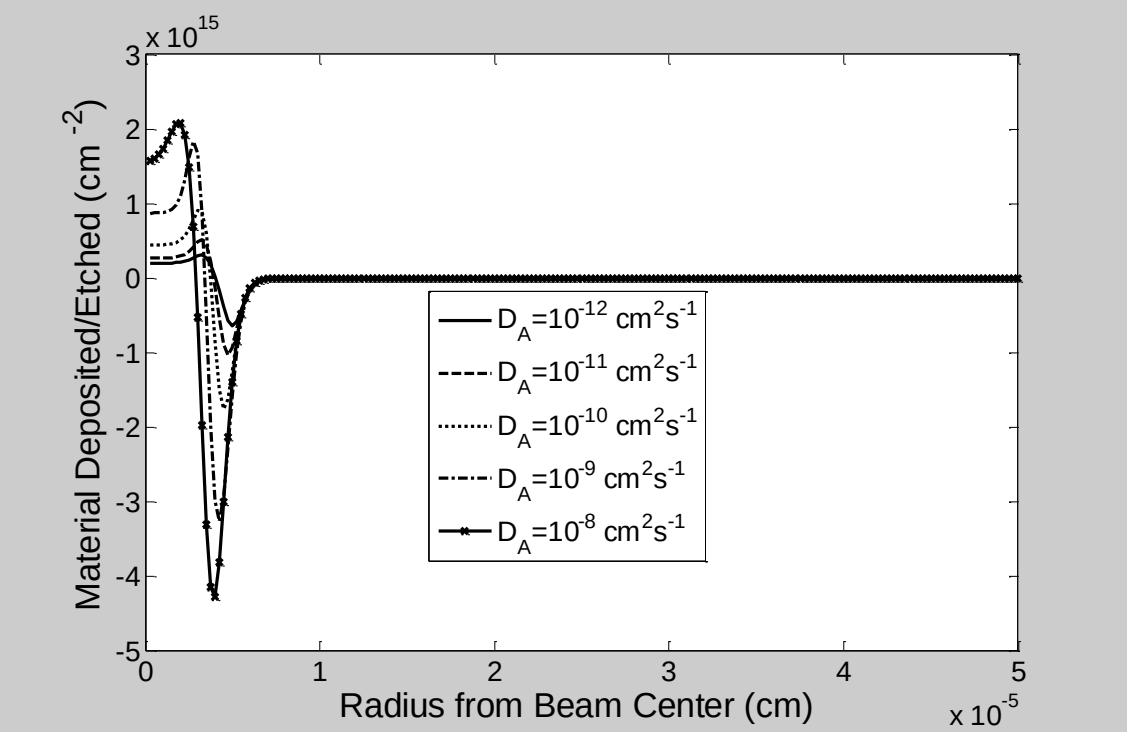

Figure 62: ***Effect of Precursor Surface Diffusion Coefficient with a Long Etch Product Residence Time***

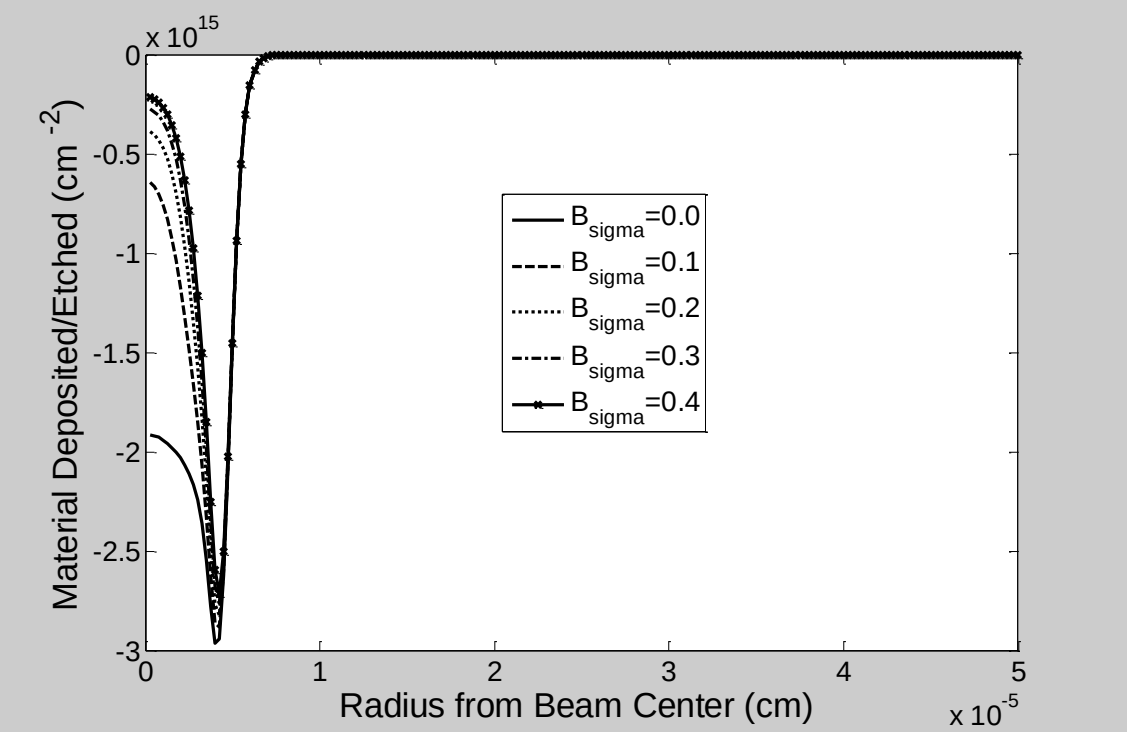

Figure 63: ***Effect of Etch Product Dissociation Probability with a Short Etch Product Residence Time***

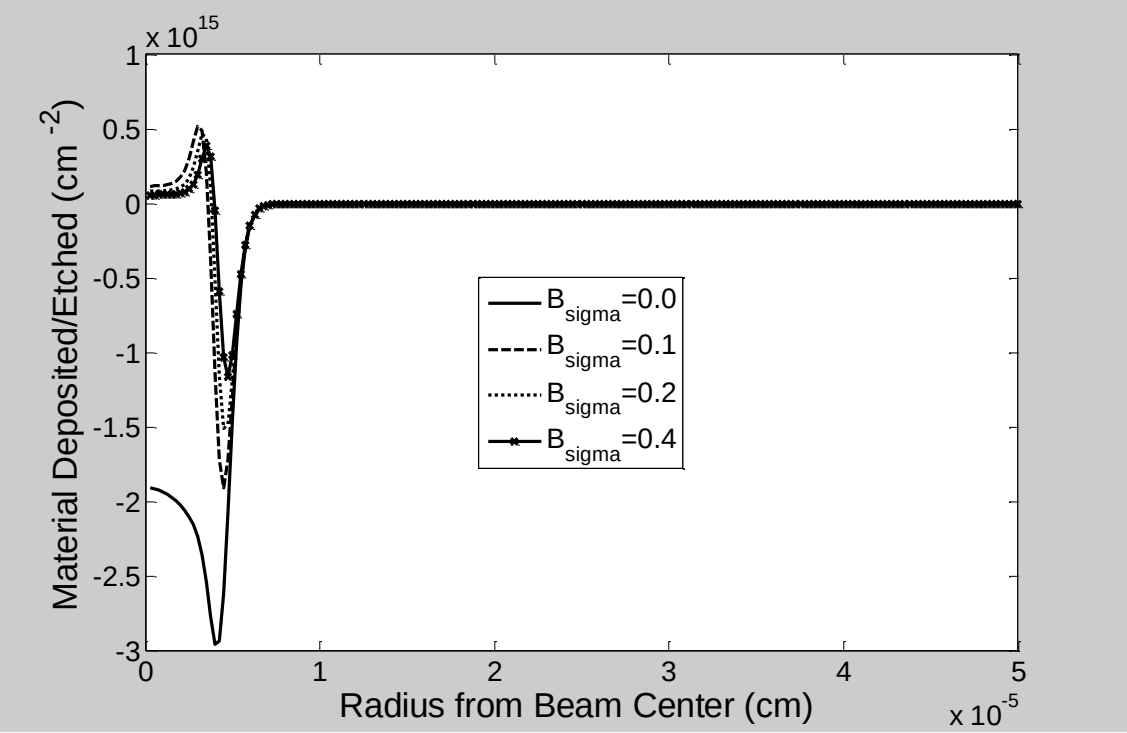

Figure 64: ***Effect of Etch Product Dissociation Probability with a Medium Etch Product Residence Time***

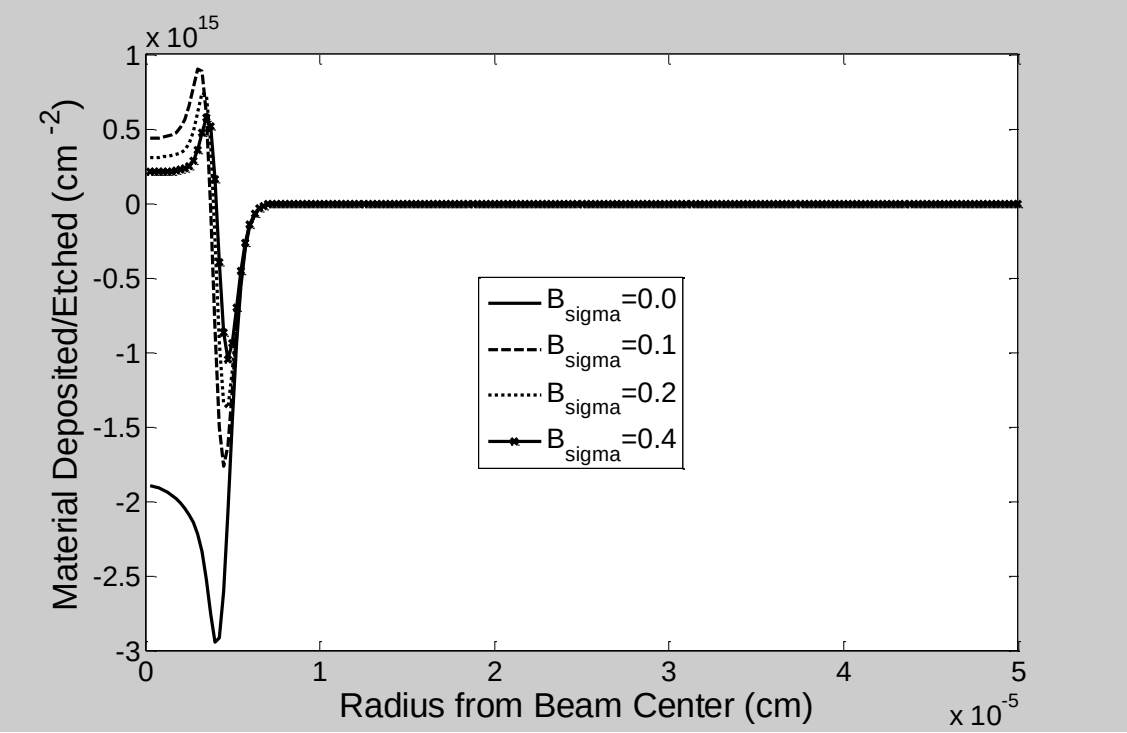

Figure 65: ***Effect of Etch Product Dissociation Probability with a Long Etch Product Residence Time***

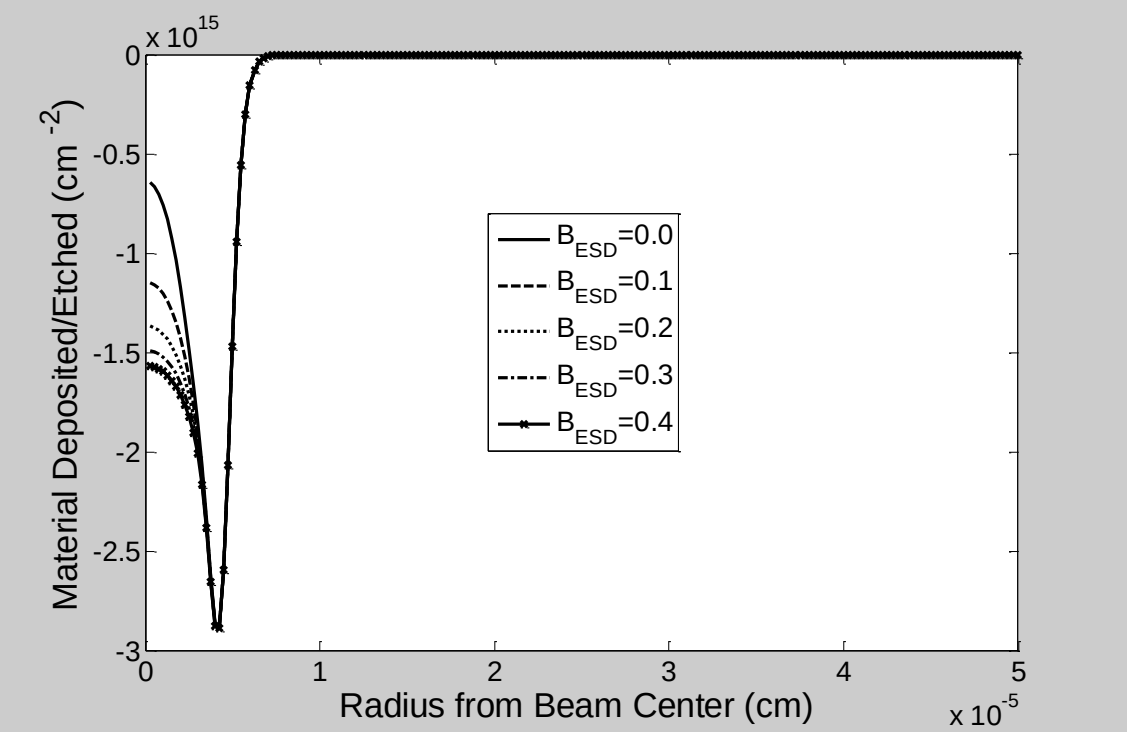

Figure 66: ***Effect of Etch Product Electron Stimulated Desorption with a Short Etch Product Residence Time***

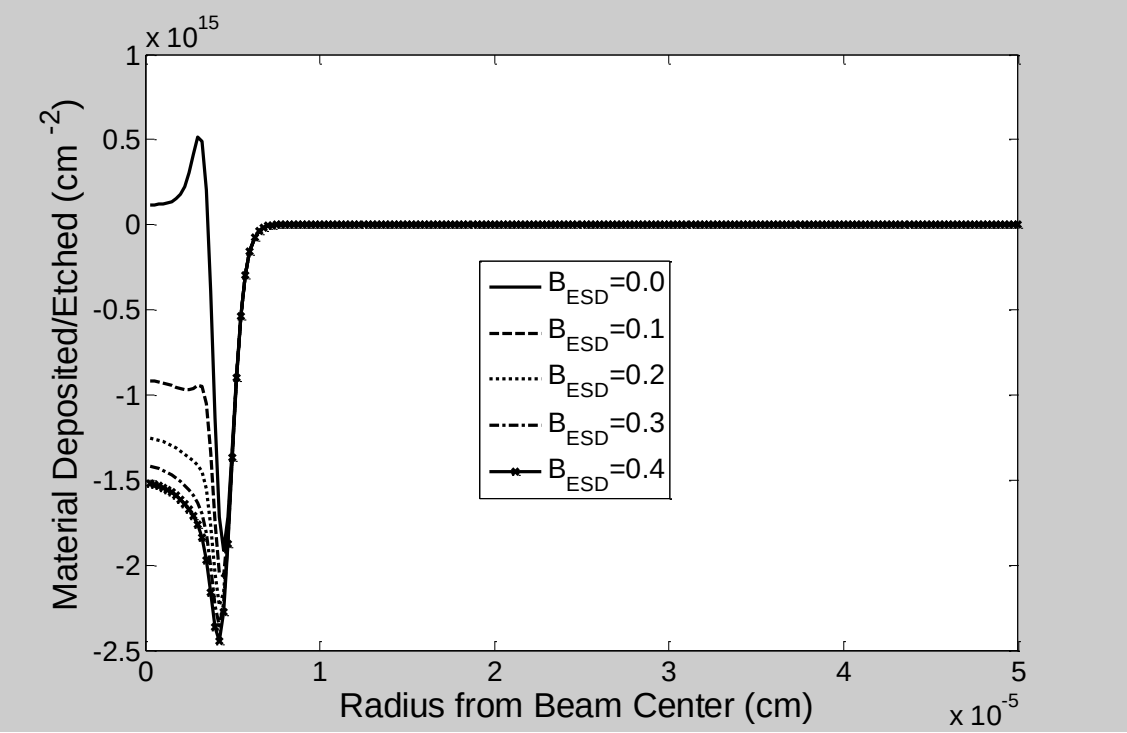

Figure 67: ***Effect of Etch Product Electron Stimulated Desorption with a Medium Etch Product Residence Time***

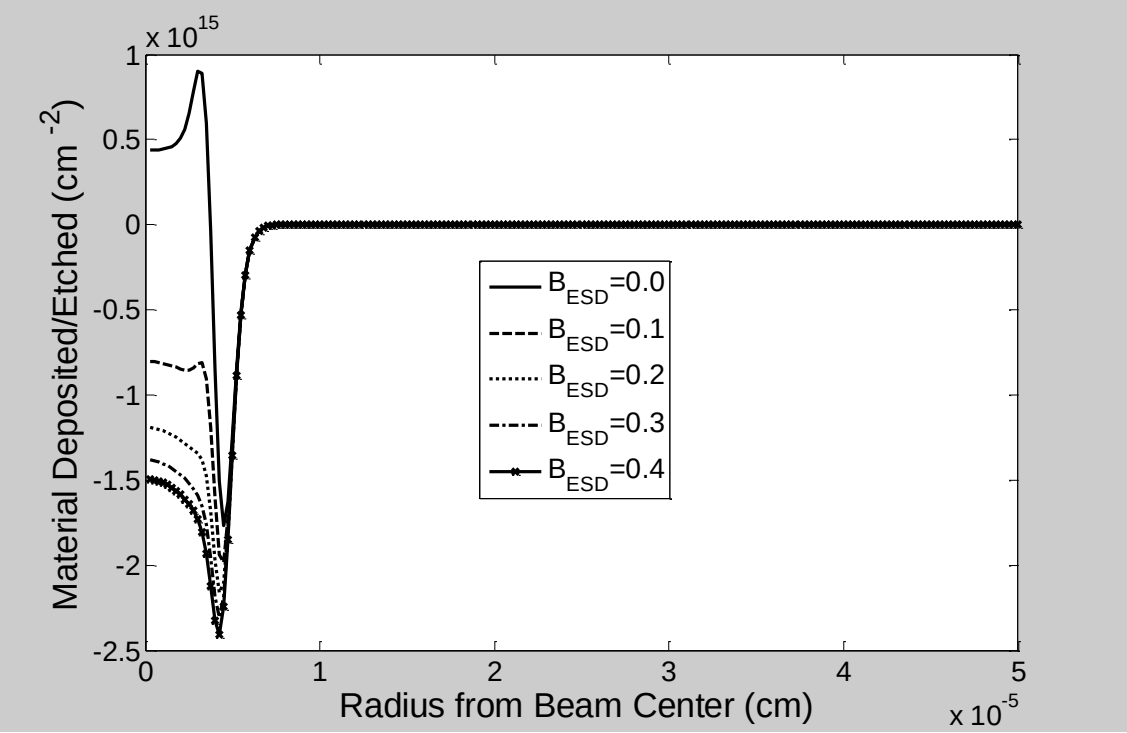

Figure 68: ***Effect of Etch Product Electron Stimulated Desorption with a Long Etch Product Residence Time***

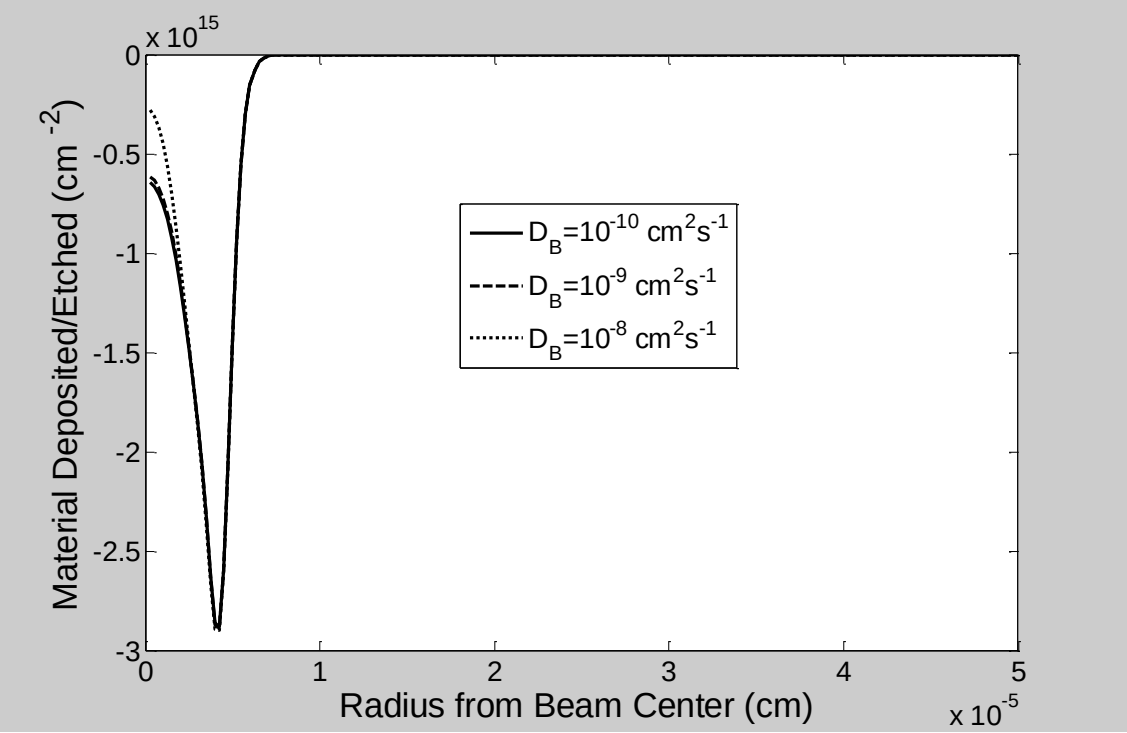

Figure 69: ***Effect of Etch Product Surface Diffusion Coefficient with a Short Etch Product Residence Time***

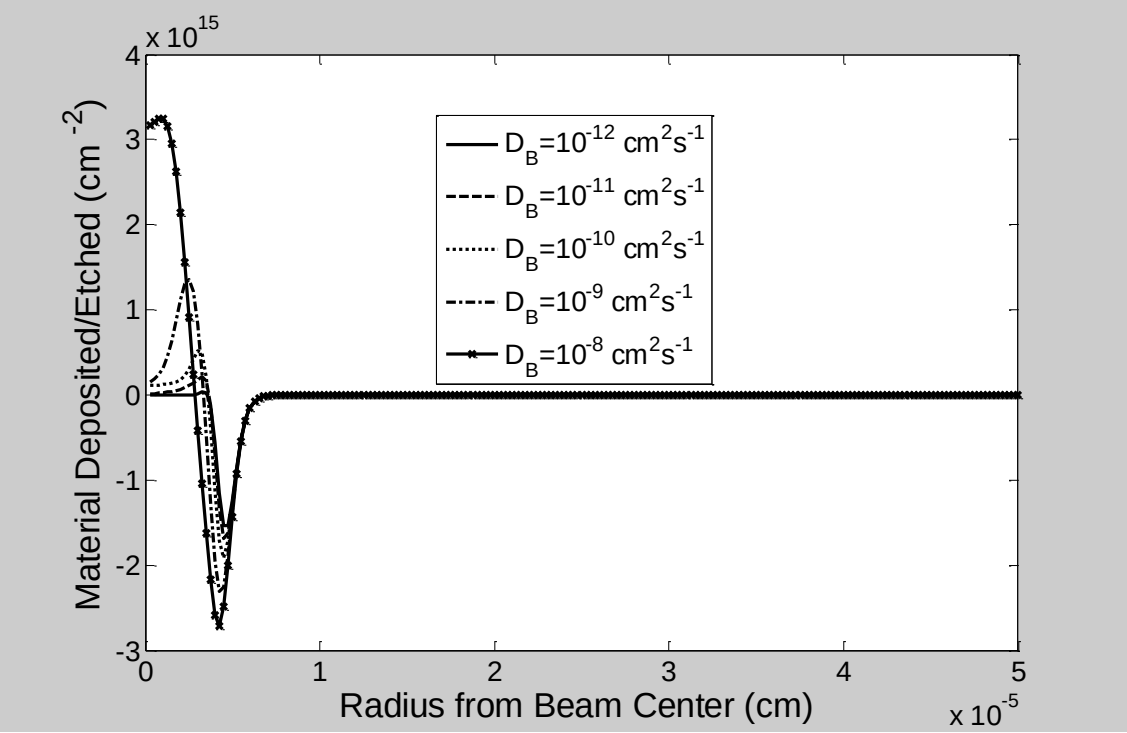

Figure 70: ***Effect of Etch Product Surface Diffusion Coefficient with a Medium Etch Product Residence Time***

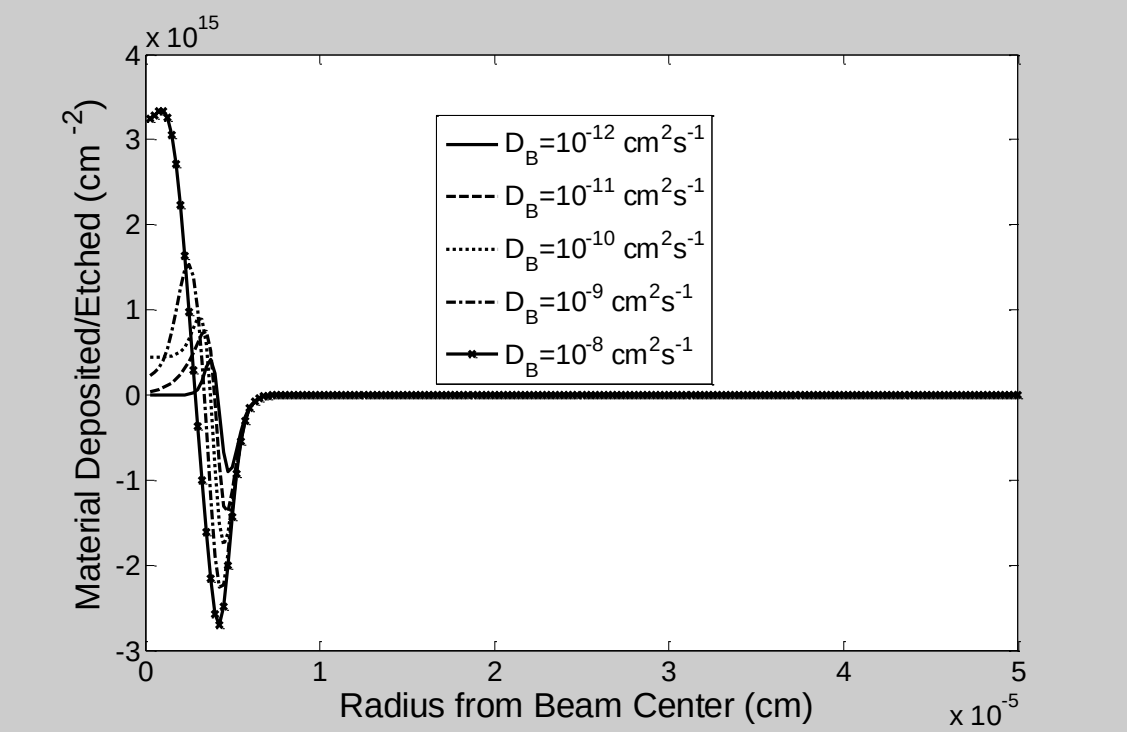

Figure 71: ***Effect of Etch Product Surface Diffusion Coefficient with a Long Etch Product Residence Time***

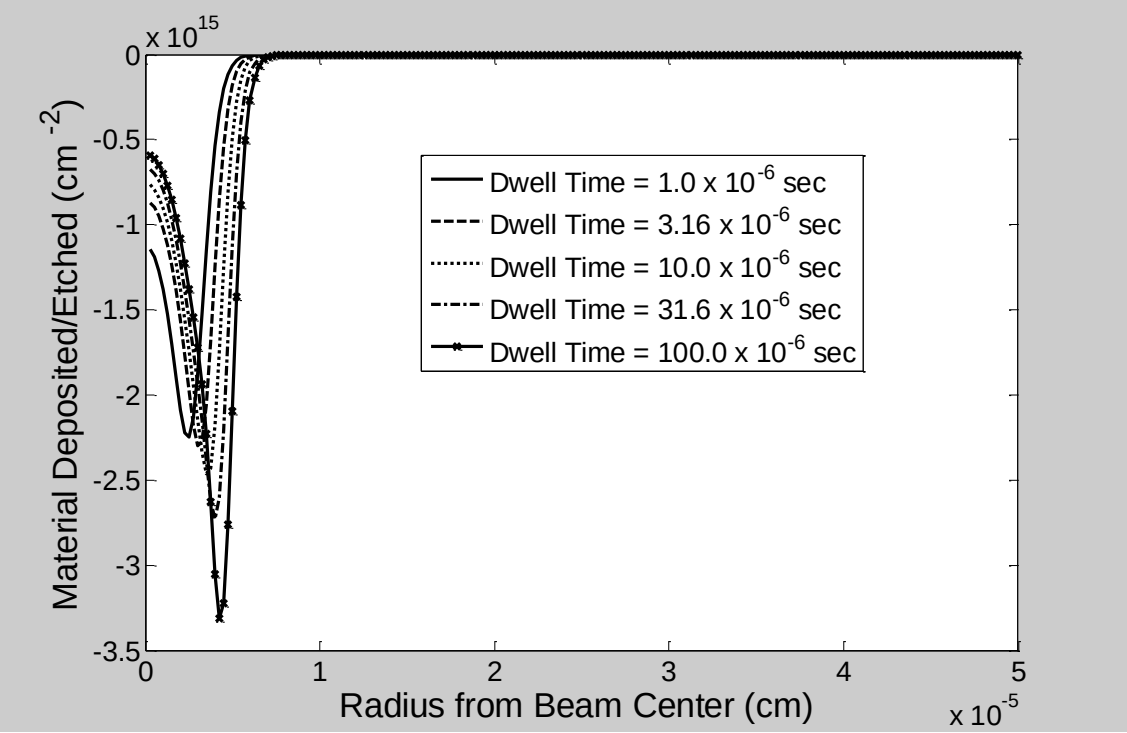

Figure 72: ***Effect of Beam Dwell Time with a Short Etch Product Residence Time***

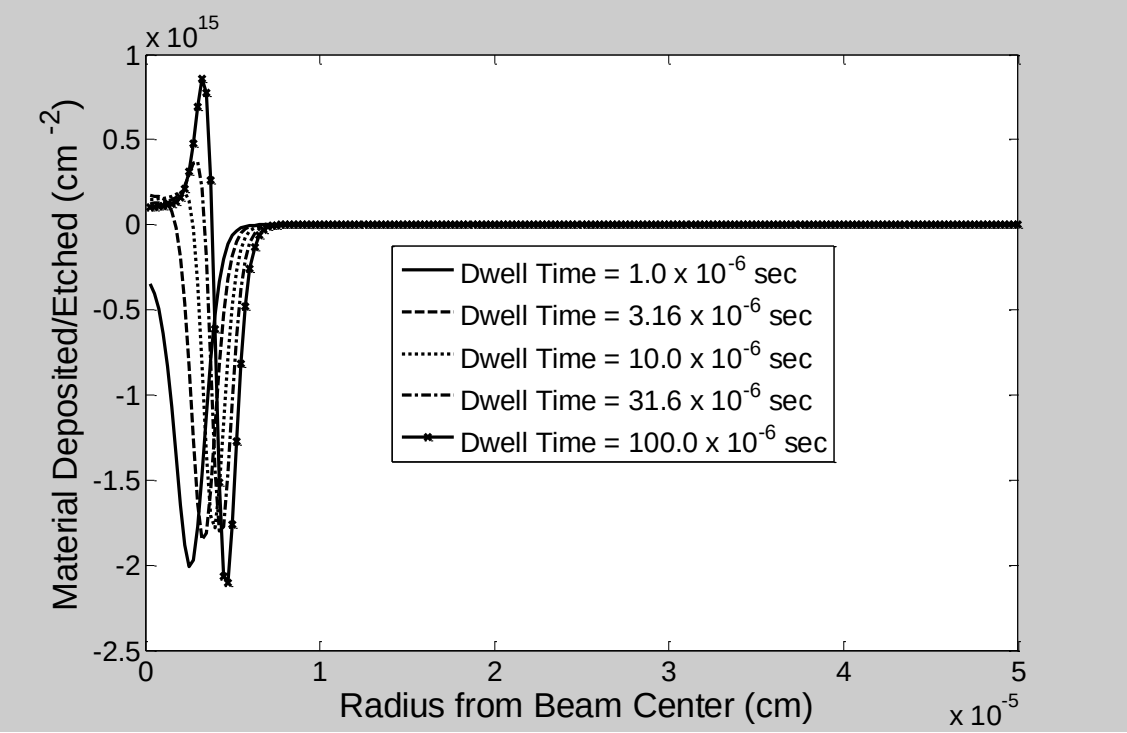

Figure 73: ***Effect of Beam Dwell Time with a Medium Etch Product Residence Time***

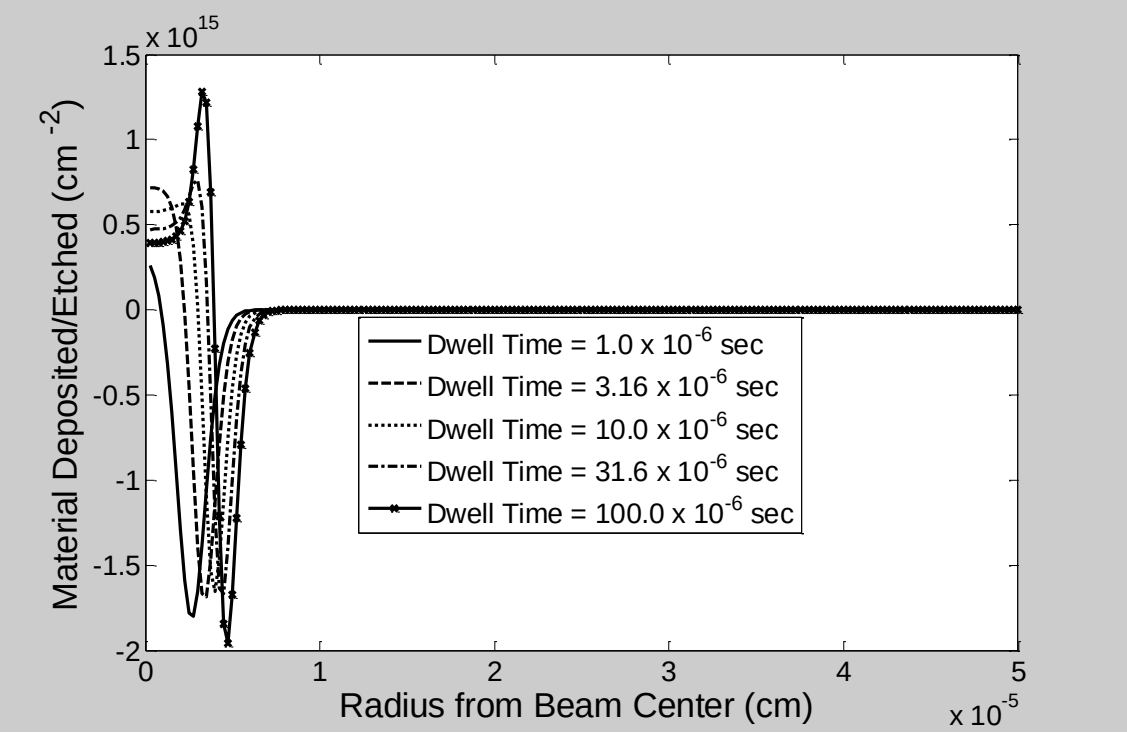

Figure 74: ***Effect of Beam Dwell Time with a Long Etch Product Residence Time***

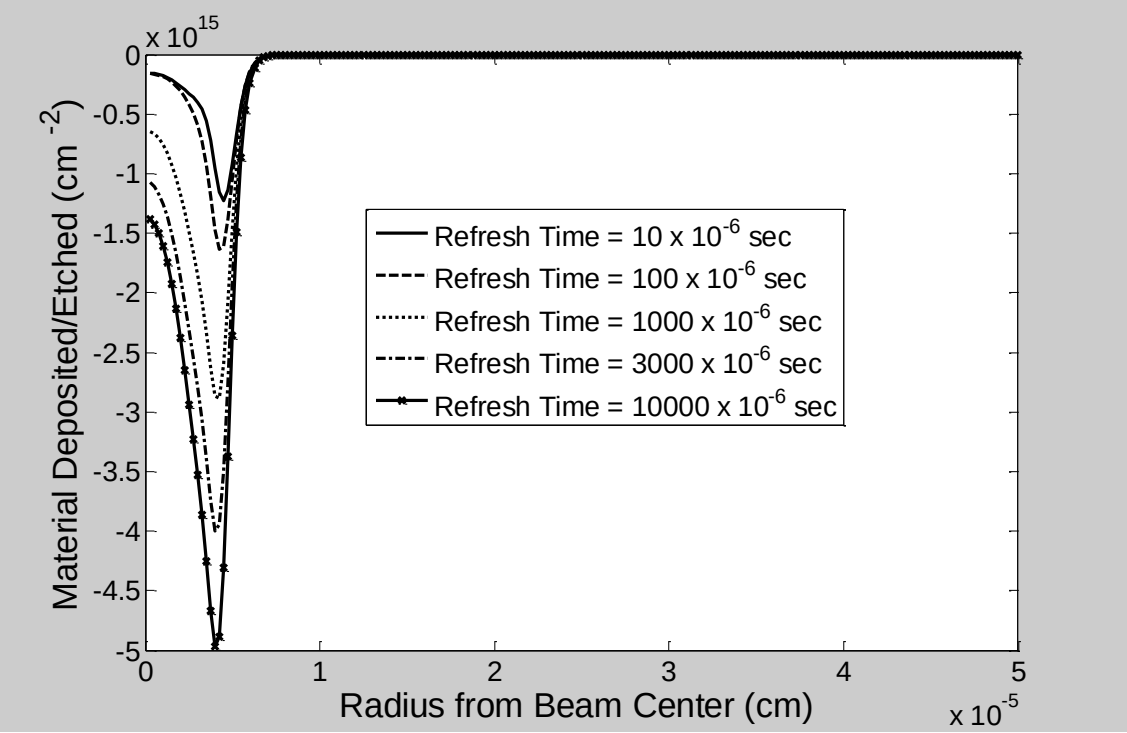

Figure 75: ***Effect of Beam Refresh Time with a Short Etch Product Residence Time***

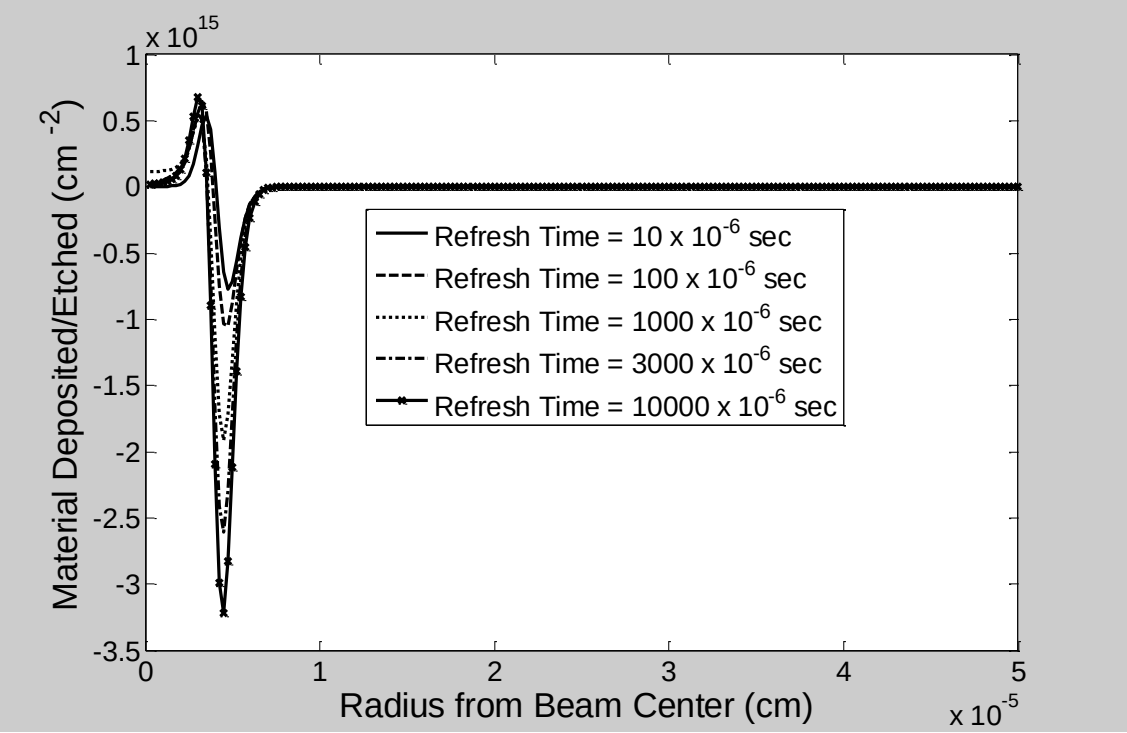

Figure 76: ***Effect of Beam Refresh Time with a Medium Etch Product Residence Time***

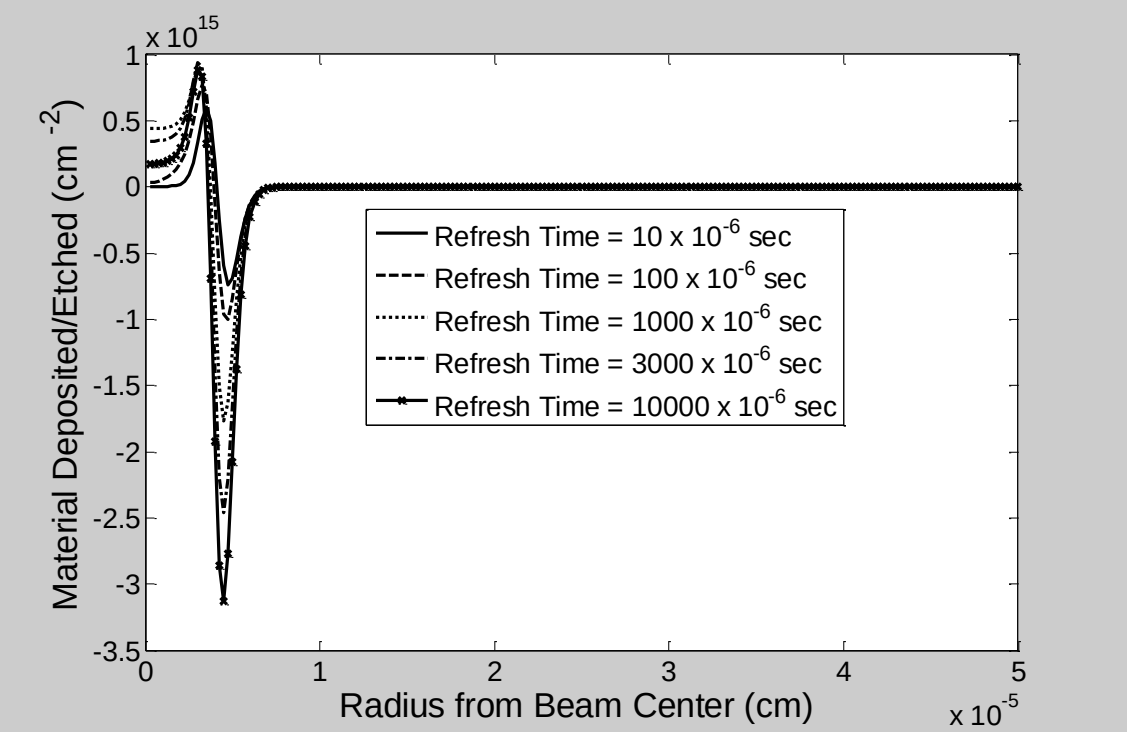

Figure 77: ***Effect of Beam Refresh Time with a Long Etch Product Residence Time***

The effect of molecular impingement rate (i.e. pressure) is to increase the equilibrium coverage of precursor gas on the surface. This means more etching and likewise increased re-deposition with higher impingement rates. Note that the response to impingement rate is not linear, as the impingement rate increases, the coverage asymptotically approaches unity. Further increases in impingement rate affect the periphery less than the center because the mass transport limited etching in the center is sensitive to impingement rate while the electron flux limited etching in the periphery is sensitive to gas coverage. The refresh of the sites can be dominated by surface diffusion, as in the case of low impingement rates; or by molecular impingement rate, in the case of high impingement rates. This is seen in the rate at the center of Figure 48. For small impingement rates, the refresh is dominated by surface diffusion of the product from the periphery and increases with increasing impingement rate due to a higher coverage of precursor in the periphery. As the impingement rate reaches sufficient magnitude to ensure near unity coverage of precursor gas, but is still too small to refresh of the sites in the beam refresh time, the effect of increasing the molecular impingement rate is diminished. Then, as the impingement rate increases, the refresh of precursor is dominated by impingement and the result is a further increase in the etching rate due to higher initial coverage for the beam dwell time and a higher steady state rate during mass transport limited etching. As seen in the cases where the etch product has a longer residence time (Figure 49 and Figure 50), the etch product created in the periphery as a long enough residence time to reach the center during the beam refresh. This results in a relatively large initial condition of etch product for the subsequent beam dwell, and the result is re-deposition of material in the center.

Increasing the precursor residence time (τ_A) increases the equilibrium precursor coverage. This has much the same effect as increasing the molecular impingement rate. For time scales in which the refresh is diffusion limited, the etch shape is governed by the precursor gas coverage in the periphery. The impact of the precursor dissociation probability (A_σ) is to increase the amount of material etched in the periphery where the etching is electron flux limited. This increases the radius at which the mass transport limited etching occurs. For cases where the etch product lifetime is long enough to result in re-deposition in the center, the re-deposition rate is increased with increasing A_σ due to the large amount of etch product generated in the periphery.

The effect of increasing the electron stimulated desorption of the precursor (A_{ESD}) is to decrease the overall rates of etching and re-deposition by lowering the concentration of precursor under the beam. The effect is larger under higher electron flux conditions.

The surface diffusion coefficient of the precursor (D_A) plays a very large role in the final etch shape. For the case of a short etch product residence time, the shape of the etch is dominated by the precursor phenomena. In this case, small precursor diffusion results in molecular impingement rate dominating during the beam refresh, where high

precursor diffusion results in a greater amount of precursor refreshing. For mass transport limited etching, starting with a high coverage of precursor gives an initially higher etching rate than the steady state rate while the initial coverage of precursor is depleted. High surface diffusion gives an enhanced etching at the radial transition from mass transport limited etching to electron flux limited etching.

Increasing the dissociation probability of the etch product (B_σ) increases the amount of re-deposition in the high electron flux regions. For the higher levels of B_σ, the etch product that is formed in the periphery does not diffuse far into the center before being re-deposited due to the higher probability of dissociation. This leads to lower re-deposition in the center and higher amounts around the edges of the high electron flux region. The effect of etch product electron stimulated desorption (B_{ESD}) has the opposite effect as that of dissociation of the etch product. Under high electron flux, rather than re-deposition dominating, the electron stimulated desorption of the etch product dominates with increasing B_{ESD}. These result in improved net etching rather than net deposit or reduced etching rates.

Diffusion of the etch product on the surface gives the most interesting impact on the etch shape of all of the factors. During the beam dwell, the etch product forms a ring where the peak concentration is away from the center due to the dissociation of the etch product under the high electron flux under the beam center. Etch product formed near the beam center has very little effective lifetime, as it is quickly re-deposited under the high electron flux, so only etch product formed in the periphery under a smaller electron flux has opportunity to diffuse on the surface. Diffusion of the etch product during the beam dwell results in one of two things. Etch product that diffuses toward the center is re-deposited by the subsequent electrons under the high electron flux, but etch product that diffuses away from the beam will eventually desorb spontaneously, as it reaches space with low or no electron flux.

The moment the beam is off during the beginning of the refresh period, there exists a gradient of etch product that results in an initially increasing product concentration in the center. If the beam dwell returns while the etch concentration is still high (before either spontaneous desorption or diffusion away from the center), then the result is a net deposit in the center. That is, some of the etch product formed in the periphery during the beam dwell diffuses to the center during the beam refresh. Then this material is re-deposited during the subsequent beam dwell. This etch product would not have the opportunity to diffuse into the center during the beam dwell time due to the high electron flux. The higher the diffusion coefficient, the larger the distance the etch product can diffuse on the surface during the beam refresh time.

For the case of the short etch product residence time, the refresh period is 1000 times the residence time, so there is no etch product remaining on the surface and the end of

the refresh. This means that the reduction in etching rate seen at the highest etch product diffusion coefficient is the result of re-deposition during the beam dwell, not from any initial condition of etch product at the beginning of the beam dwell. For the case of higher etch product residence time (comparable or greater than the refresh time), higher diffusion rates of the product result in higher initial conditions for the beam dwell time of etch product in the center, resulting in higher net deposition in the center. Conceivably, the diffusion coefficient could become high enough that all of the etch product could diffuse away during the refresh, but that level is well above those simulated in this study.

The beam dwell time and refresh time have big impacts on the etch shape. The length of the beam dwell time has a large impact on determining how much material is etched per pulse in the mass transport limited etching regime. The amount of material available to etch in that regime is largely dependent upon the initial conditions of precursor and etch product. The initial conditions of precursor and etch product are dependent greatly on the length of the refresh time.

For short etch product residence times, the effect of the dwell time and refresh time on the etch shape is mostly concerning the precursor concentration profile at the beginning of each pulse. During the first moments of the beam dwell time, the etching rate is linear with electron flux and precursor concentration. So, for the shortest dwell times, the highest etching rates are achieved as long as the initial condition of precursor is high. If the beam dwell time is long enough to significantly deplete the center region, and the refresh time is not long enough to significantly re-accumulate much precursor; then subsequent etching during the next and subsequent dwell times will be reduced. This is due to the lower concentration of the precursor at the beginning of the beam dwell. Increasing the beam dwell time for a fixed refresh time has the effect of widening the etch shape and slowing the rate at the center. Increasing the beam refresh time improves the etching per pulse as the initial precursor concentration is higher for each pulse, and the initial etch product concentration is lower at the beginning of each pulse.

Experimental Work

In order to solve for the process factors such as effective molecular impingement rate (gI_A) and electron dissociation probability (A_σ), it is necessary to determine the etch/re-deposit rates under various beam dwell times. An experiment was designed to vary the beam dwell time for pulsed mode etching. The Xenon Difluoride gas injector on the FEI Nova 600 Dual Beam system, when inserted into the field of view of the SEM, sits between 5mm and 6mm working distance from the electron lens. When the substrate

is placed immediately below the injector needle, the gas flux at the surface is highest and reasonably high etching rates of areas are possible using the fastest scanning rates available on the SEM. A 500nm thick film of silica can be removed in a few minutes (depending upon the size of the scanning box) by a visual end point detection method. In order to be more consistent with day to day experimentation and to reduce the etching rate to a level that can be easily measured by an AFM, all experiments were carried out at a substrate working distance of 6mm. This reduces the molecular impingement at the surface, and gives more sensitivity to dwell time and refresh time experimentation. While the gas flow is on, the background pressure in the system comes to about 1.5×10^{-6} Torr as compared to a background pressure around 7×10^{-7} Torr with the gas flow off. Under the needle, a significant enhancement of the precursor gas pressure is expected.

Using the FEI electron beam patterning system, a six micron "line" of pixel pitch one micron was used with a variable dwell time and a minimum refresh time. Using the immersion lens on the system, the estimated beam spot size is less than 2 nm in diameter. Due to the large spacing between each pixel on the line, the result is there is effectively a pulsed spot mode etching at each pixel. Each line contains 7 pixels, so the system goes for the set dwell time on each pixel, and then maintains the minimum dwell time setting by sitting on the last pixel for long enough to reach the minimum refresh time on the earlier pixels in the line. Table 3 gives the combinations of dwell times and refresh times in the experimental setup. For each run, the beam energy was 5keV, the beam current was 400pA, and the 100k loops were exposed.

An initial series of experiments was run at best focus of the electron beam and some of the results are seen in Figures 78 and 79. As the dwell time increases, the shape of the etch changes significantly. Note that the beam is not blanked as it moves from pixel to pixel, in this case we see the most efficient etching of the silica occurs when the beam is moving across the substrate from one pixel to the next (*id est* very short dwell times). This is consistent with the analytical model discussed earlier where the eigenvalues of the system are dependent upon the electron flux and the dissociation probabilities of precursor and etch product. Under the focused electron beam, the electron flux is as high as $10^{23} cm^{-2} s^{-1}$. Assuming an adsorption site density (Z) of $10^{15} cm^{-2}$, the depletion of the precursor and subsequent re-deposition of the solid by dissociation of the etch product happens in a few tens of nanoseconds. This is faster than the dwell times available for a pulsing experiment, so a reduction in the electron flux was necessary.

Defocusing the electron beam allows one to overcome three major hurdles. First, the electron flux is reduced as the beam current is spread across a larger area. This enable use of dwell times that the scanning system can handle. Second, the size of the pulsed etch feature is larger, allowing for depth profiling by the atomic force microscope probe. Third, the shape of the electron flux can be modeled easier for the defocused beam

Table 3: Experimental Dwell Times and Refresh Times

Run	Dwell Time (10^{-6} sec)	Refresh Time (10^{-6} sec)	Last Pixel Dwell Time (10^{-6} sec)	Last Pixel Refresh Time (10^{-6} sec)
1	10	1000	950	60
2	20	1000	900	120
3	30	1000	850	180
4	40	1000	800	240
5	50	1000	750	300
6	100	1000	500	600
7	200	1200	200	1200
8	500	3000	500	3000

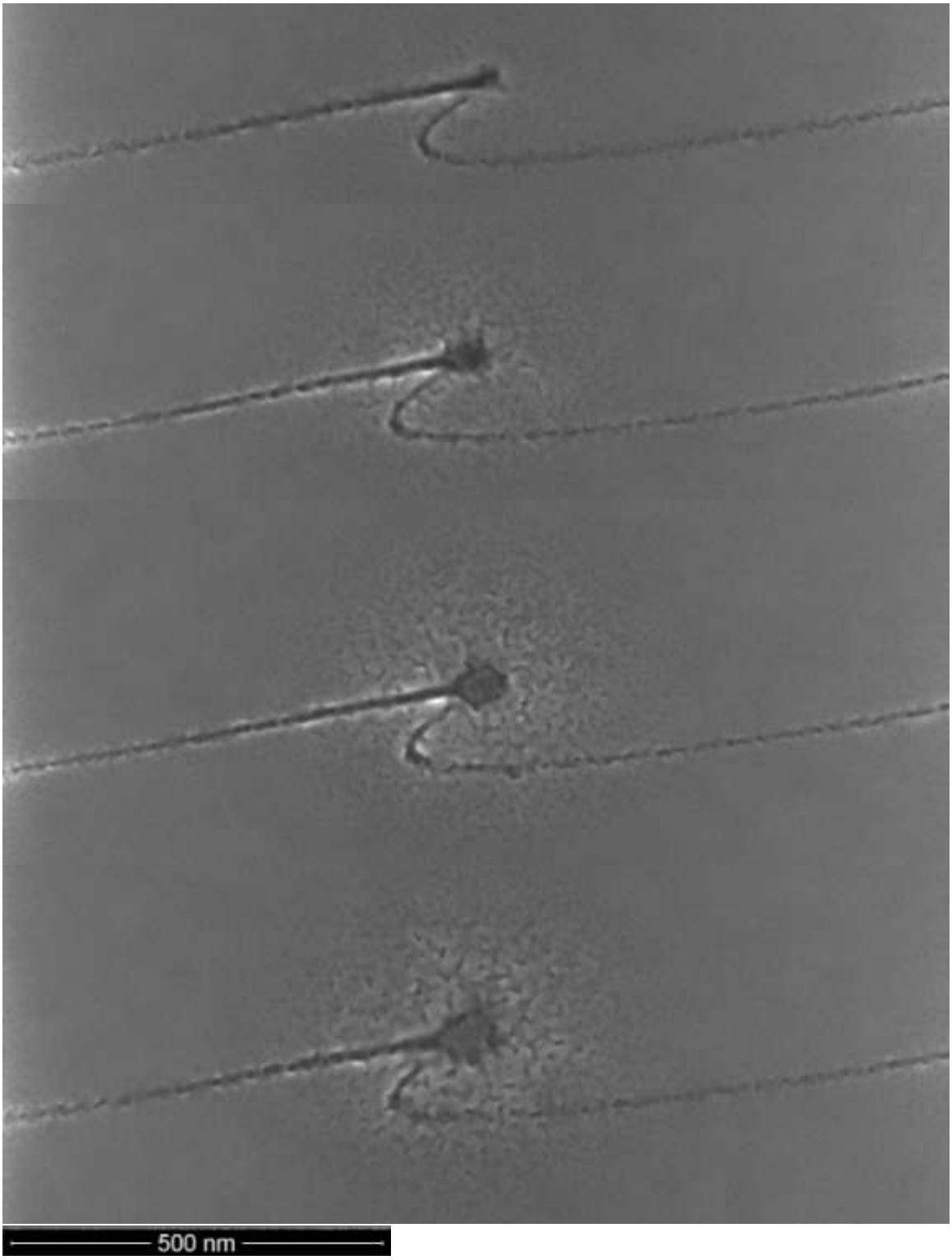

Figure 78: Best Focus Pulsed Beam Etching from the top to the bottom, the 10-, 20-, 30-, and 40-microsecond dwell times.

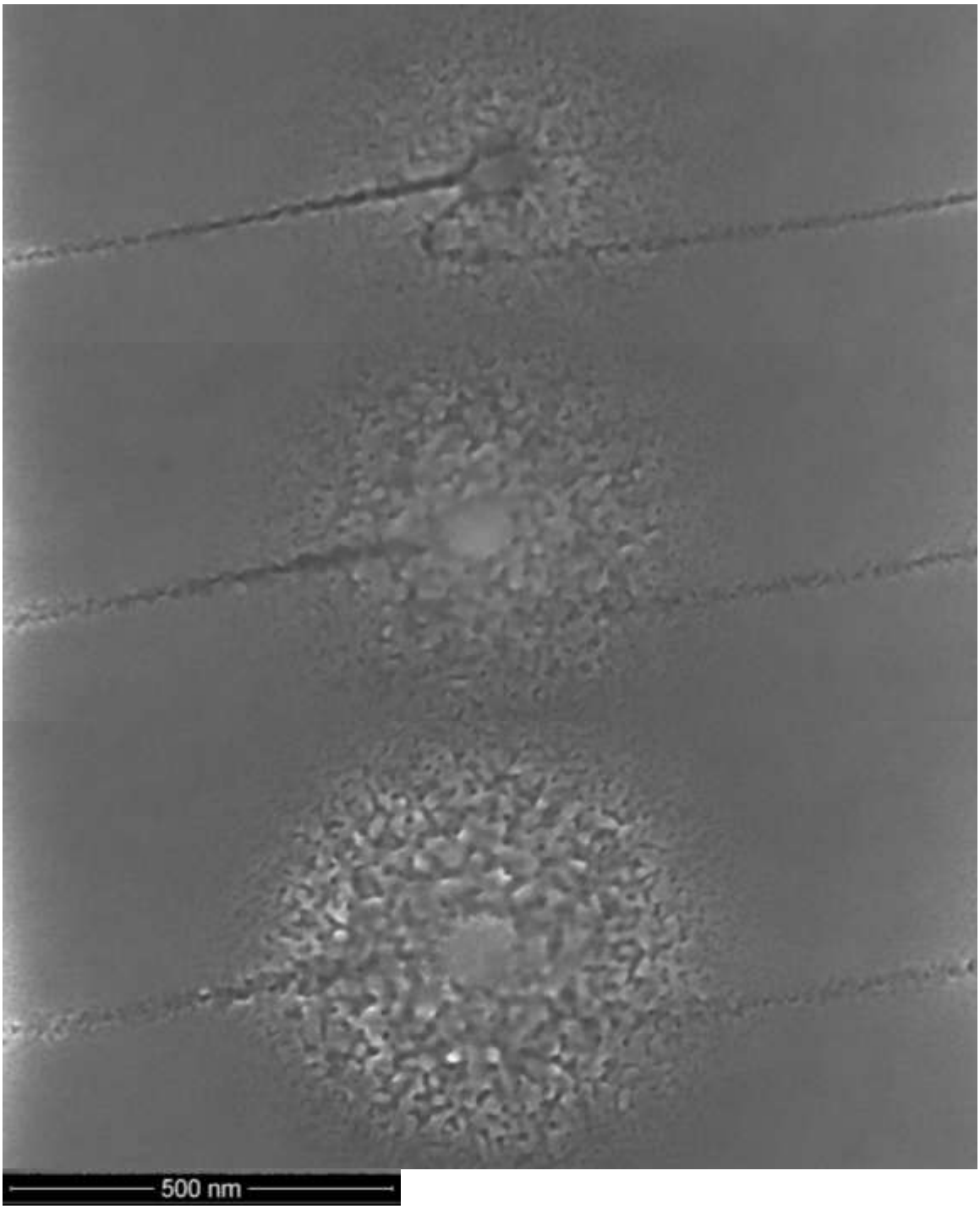

Figure 79: Best Focus Pulsed Beam Etching

From the top to the bottom, the 50-, 100-, and 200-microsecond dwell times.

than the focused electron beam. The effects of lens aberrations on the focused electron beam can cause great variation in the actual peak electron flux. These aberrations, while still present in the defocused beam, are insignificant when determining the electron flux profile of the defocused beam. Because there is such a large parameter space to consider in these etching problems, it is helpful to fix as many unknowns as possible.

The dwell time experiment was repeated for 40-, 20-, 10-, 5-, 2-, and 1-micron defocusing of the beam. The etches were profiled using the Veeco Dimension 3100 Atomic Force Microscope in tapping mode. The center etch depth/height was collected for each condition and plotted for the 0-, 10-, 20-, and 40-micron defocuses (Figure 80). The 5-, 2-, 1-, and 0-micron defocus feature sizes are difficult for the AFM tip to fit into, so the entire data set cannot be used for parameter fitting.

Parameter Fitting

The 40-, 20-, and 10-micron defocused data set was simulated in an effort to determine the experimental process parameters. For each dwell time-refresh time combination, the numerical simulation was run for a set of parameters. Then the center height/depth was determined for each combination and compared to the experimental value. A sum of square error was calculated. One parameter at a time was varied on a logarithmic scale and the sum of square error was calculated for each variation in the parameter. When the minimum was determined along that parametric axis, then the next parameter was varied seeking a new minimum in the sum of square error. This process was repeated multiple times in an attempt to find the minimum sum of square error with the goal of determining the experimental process parameters.

The first few rounds gave the gross changes in the parameters to arrive at the fit seen in Figure 81. The first rounds of fitting were based on using the net etch or deposit from the second beam pulse and multiplying this effect over the 100k pulses in the actual experiment. Unfortunately, for the process parameters the system was approaching (high surface diffusion coefficients, low net molecular impingement rates, and long etch product residence times), the second pulse is not a good representation of the steady pulsing. In some cases, it takes tens or even hundreds of pulses to reach a steady pulsing of surface concentrations. So, the code was adapted to allow the system to continue until the initial condition in concentration of the precursor and etch product at the beginning of the beam on did not change above a small threshold from pulse to pulse. This increased the simulation time by a couple of orders of magnitude due to the high number of pulses required to reach “steady pulsing”.

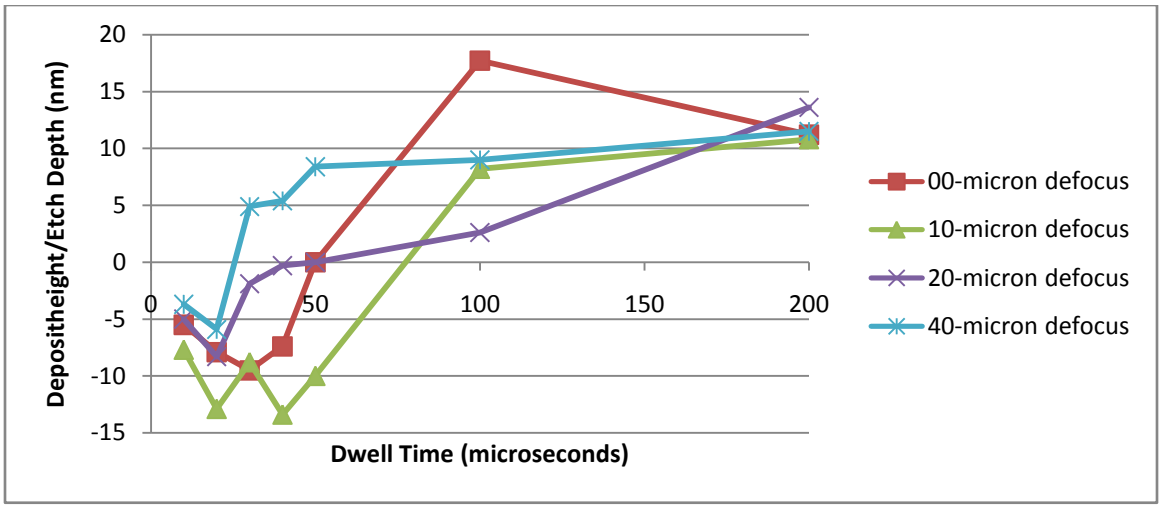

Figure 80: AFM Center Depth/Height Measurements

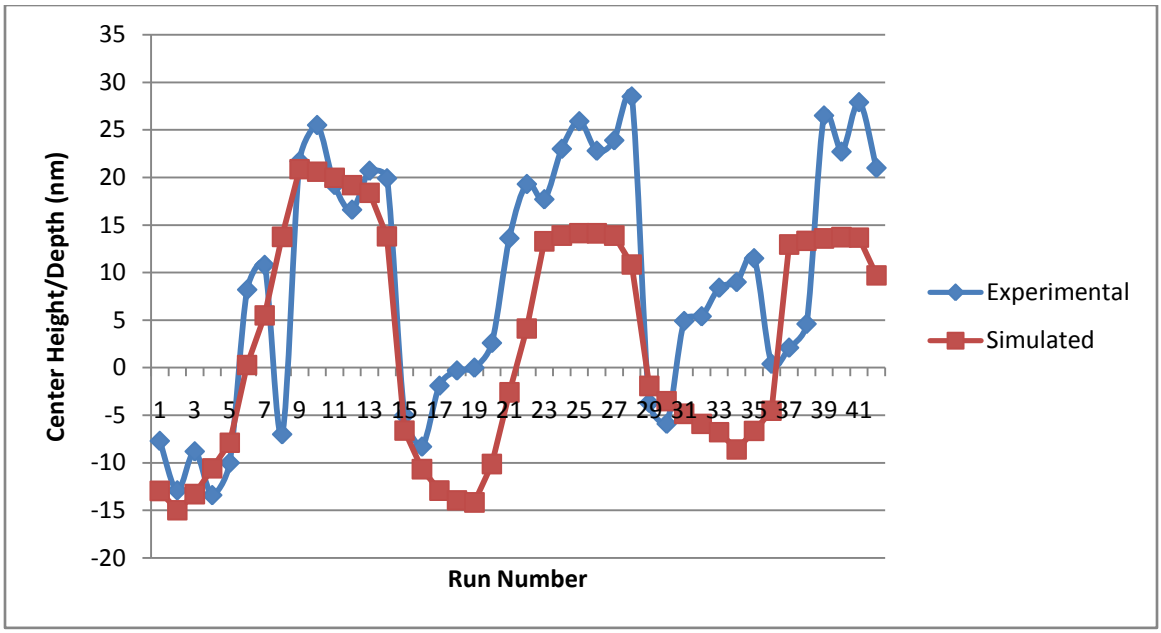

Figure 81: Fitting of the Larger Data Set

In order to accommodate the greatly increased simulation time, the number of dwell time/refresh time combinations were reduced to the twelve with the best confidence in the AFM profile image. This included depths that appeared to be probe size limited or runs that were very noisy and had a large uncertainty in the center height or depth value. Increasing the simulation time until the pulse to pulse concentration profiles changed by less that $10^{10}cm^{-2}$ absolute value at any radius, the sum of square errors was minimized one factor at a time. The latest results for the minimum are plotted in Figure 82 and the factor values are summarized in Table 4. The fit is not yet perfect, but the general trends are observable, and given sufficient simulation time, I believe that the fit will improve.

It is worthwhile to look at the simulated profile versus the AFM profiles and SEM images for each of the runs in the fitting. Figures 83-94 show each run in the smaller experimental data set along with the corresponding profile at the best yet parameters. The naming conventions in the figure captions (XX/YYYY) refer to the dwell time and refresh time in microseconds.

In most cases the center height or depth prediction is relatively close to the experimental value. An item of notice is the simulations show a very narrow moat trench compared to the experimentally observed trenches. In the simulation this is due to the enhanced precursor flux due to diffusion at the transition from equilibrium coverage to depleted coverage. In the simulation this edge is sharply at the edge of the defocused beam and is completely stationary. In reality, the defocus edge may not be as sharp as simulated, and certainly there are vibrations and beam placement variations from pulse to pulse that would amount to a smearing out of this edge and result in a broader less deep moat trench that we observe experimentally.

Another potential source of the simulation error comes from the constant dissociation probability assumption. It is know that the dissociation cross section is a function of energy, and so the effective dissociative electron flux under the beam (consisting of high energy primary electrons may be smaller in proportion to the effective dissociative electron flux in the periphery due to the fact that lower energy secondary electrons are more efficient at dissociation of the precursor molecule. If the dissociation cross sections of the precursor and the etch product were known as functions of electron energy, then the electron flux profile could be modified into effective dissociative electron flux profiles (one for each species), and these could be used to improved the quality (and complexity) of the simulation.

The biggest difficulty in accuracy of the simulation comes from reaching the “steady pulsing”. At high surface diffusion rates the initial gas surface profile changes with each pulse, and can require hundreds of pulses to reach a steady pulsing cycle. If too few pulses are simulated and the effects of the last pulse simulated are assumed to be the steady pulsing effect, then the results can be off by large amounts. There is a trade-off

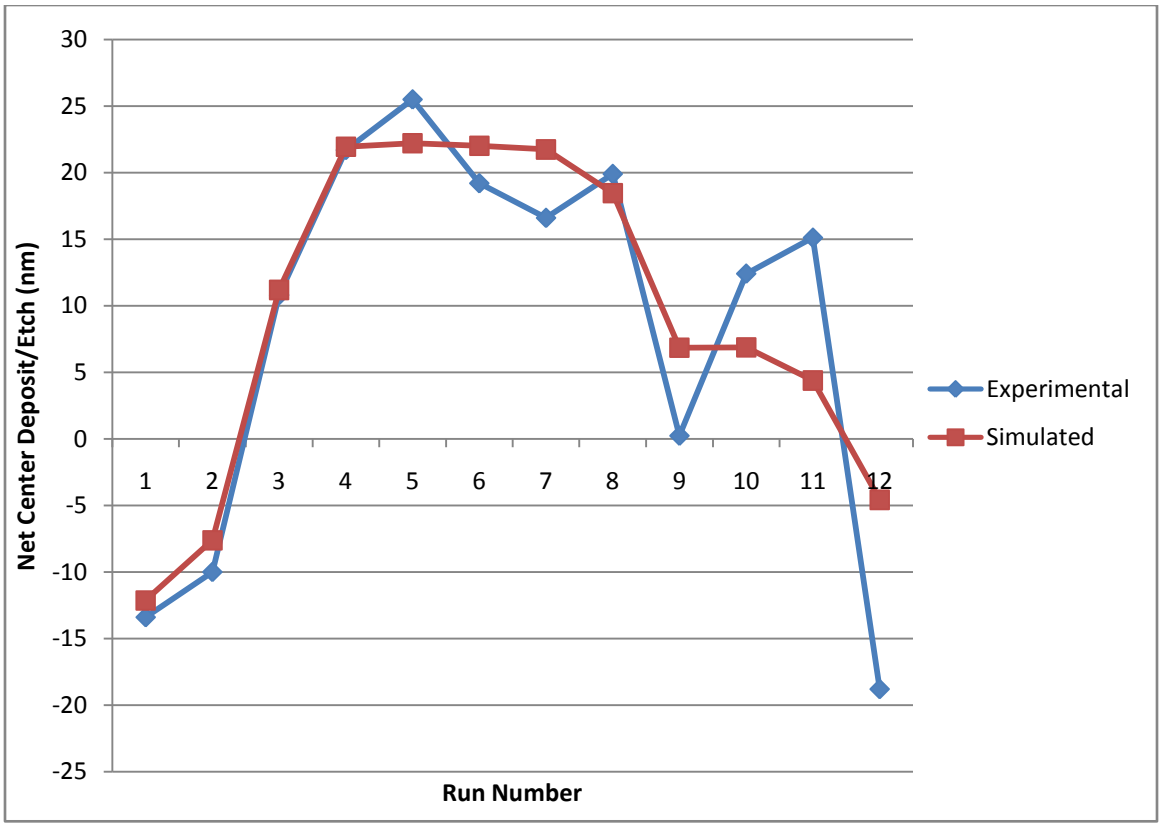

Figure 82: Fit of Reduced Set of Experimental Data

Table 4: Best Fit Values of the Process Parameters for XeF_2-SiO_2 System

Process Parameter	Value
gI_A	$6.56 \times 10^{13} cm^{-2} s^{-1}$
τ_A	$7.82 \times 10^{-2} s$
τ_B	$3.89 \times 10^{-2} s$
A_σ	0.403
B_σ	0.198
D_A	$4.92 \times 10^{-8} cm^2 s^{-1}$
D_B	$5.72 \times 10^{-8} cm^2 s^{-1}$

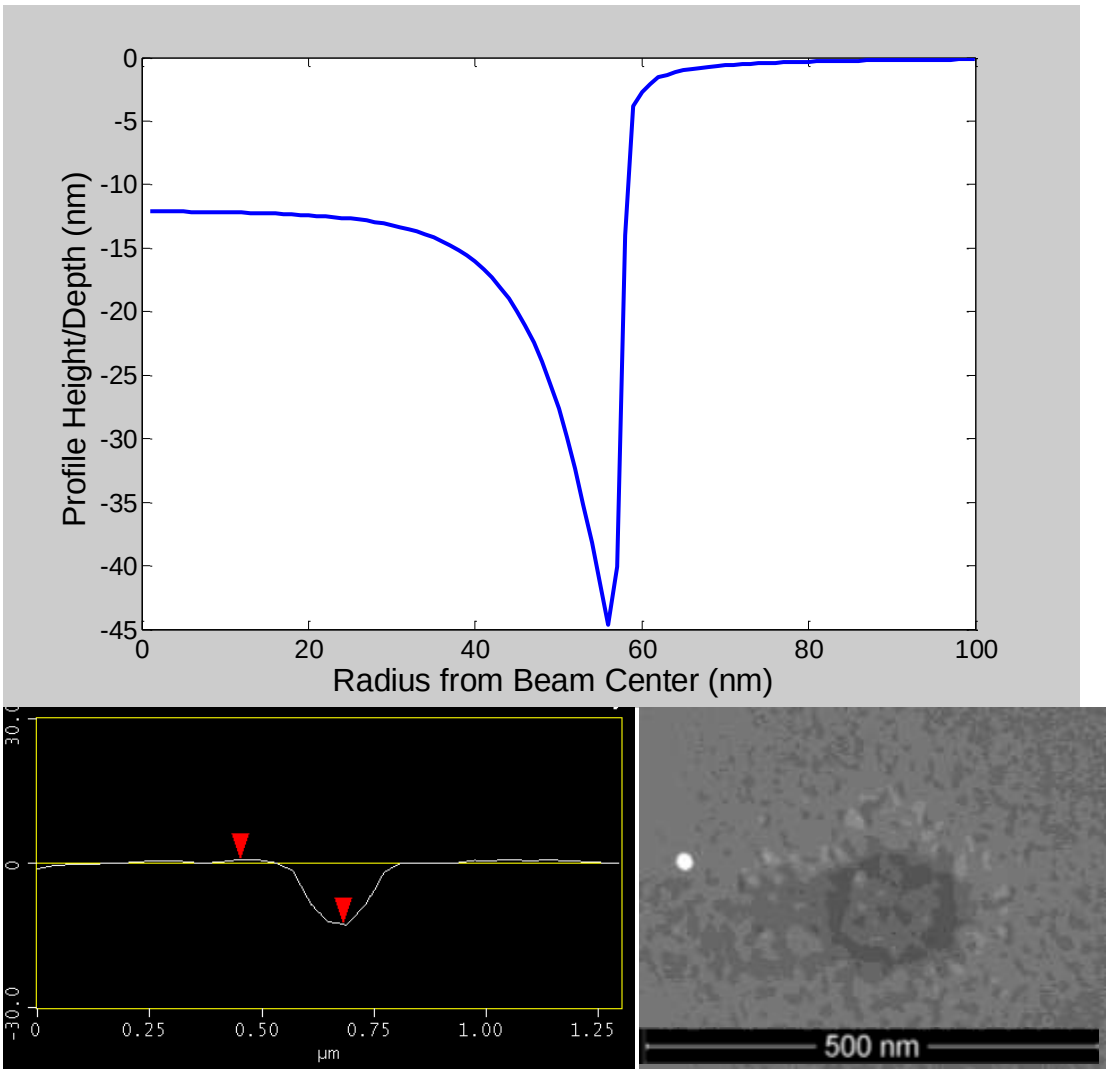

Figure 83: 40/1000 Simulated versus Experimental

(top) Simulated Profile (bottom left) AFM profile – some etch features are not resolved due to tip shape effects. (bottom right) SEM image

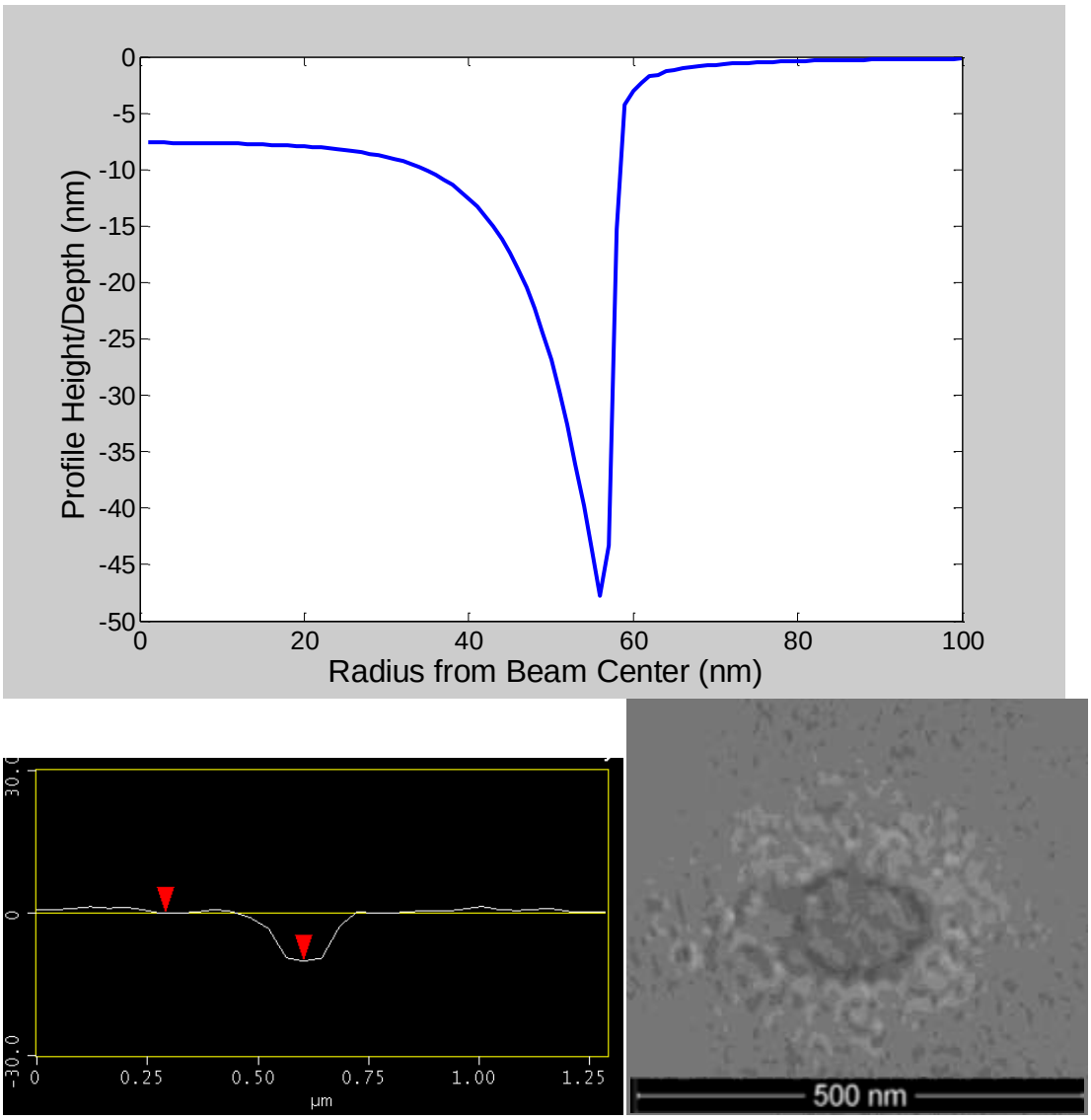

Figure 84: 50/1000 Simulated versus Experimental

(top) Simulated Profile (bottom left) AFM profile – some etch features are not resolved due to tip shape effects. (bottom right) SEM image

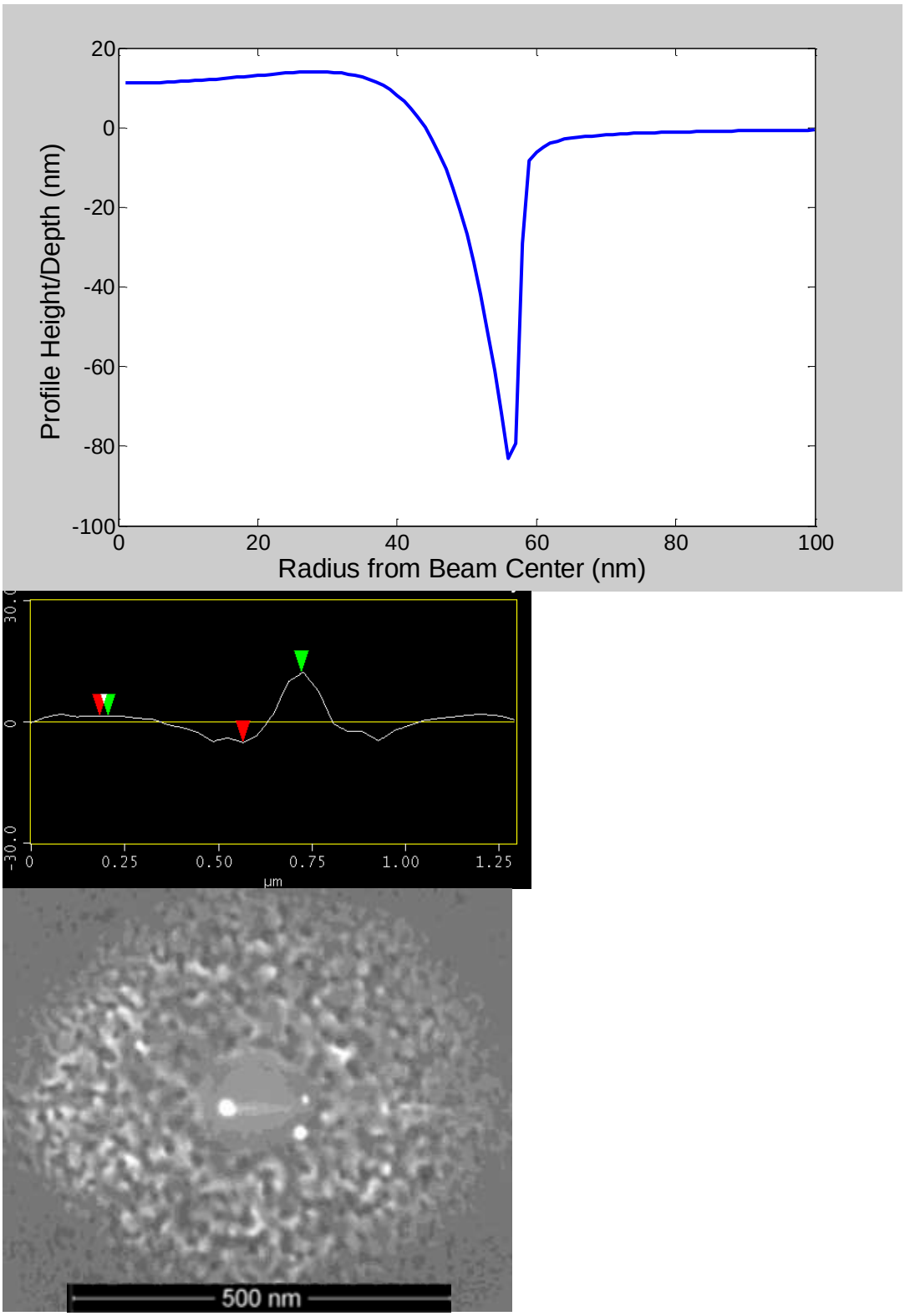

Figure 85: 200/1200 Simulated versus Experimental

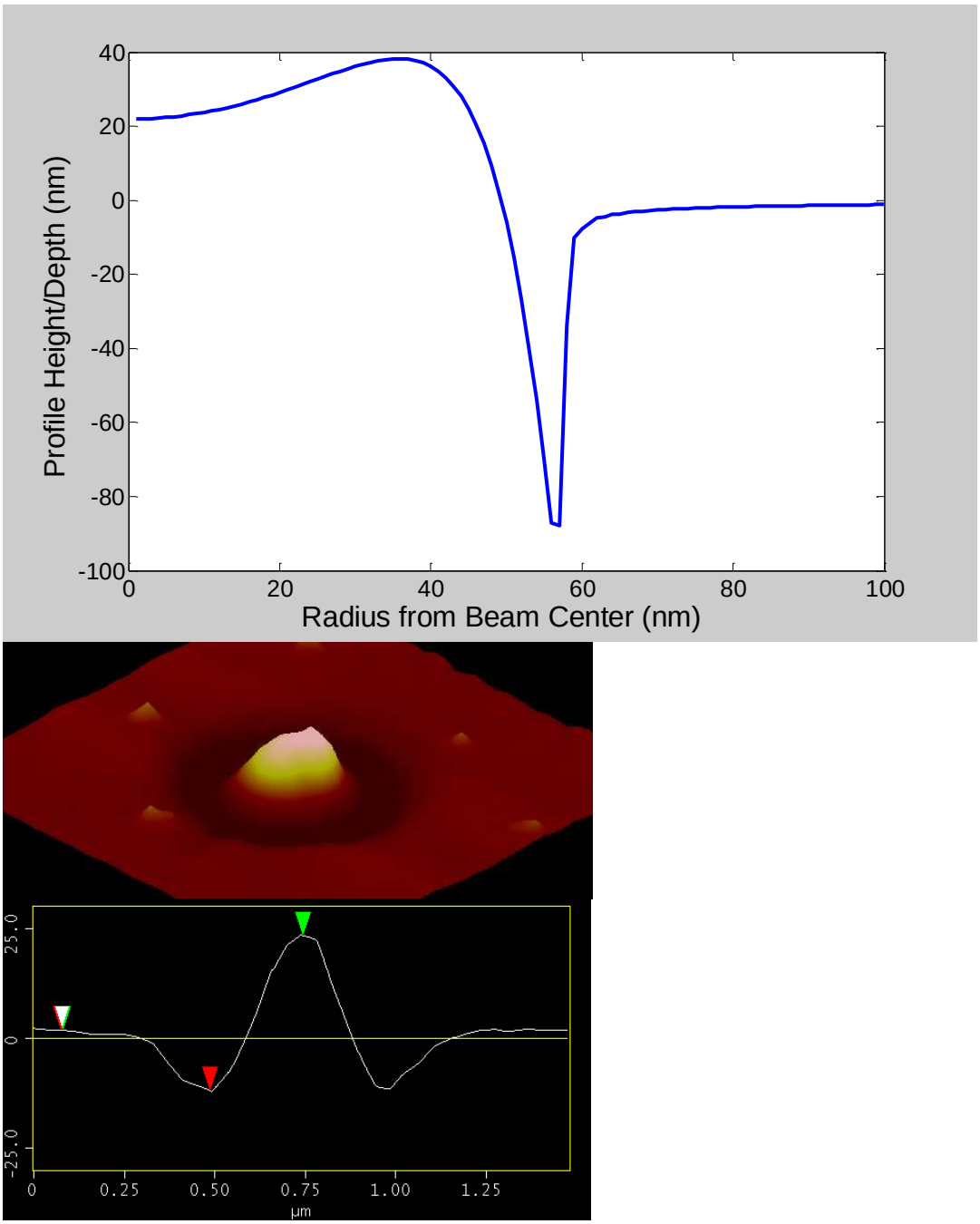

Figure 86: 950/60 Simulated versus Experimental

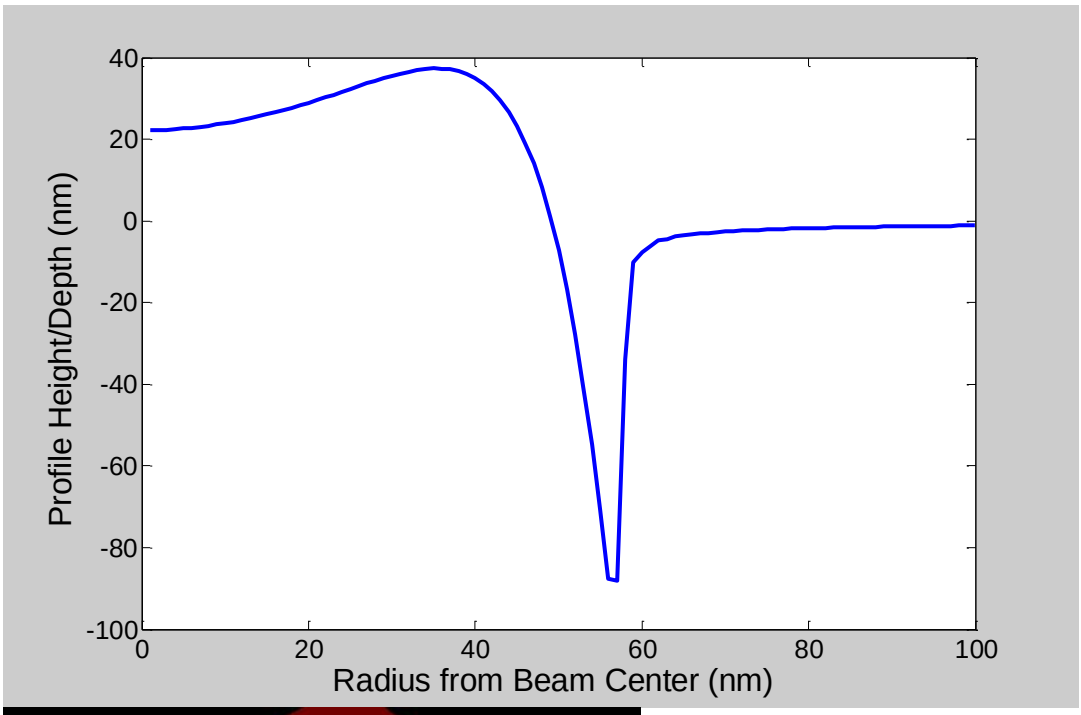

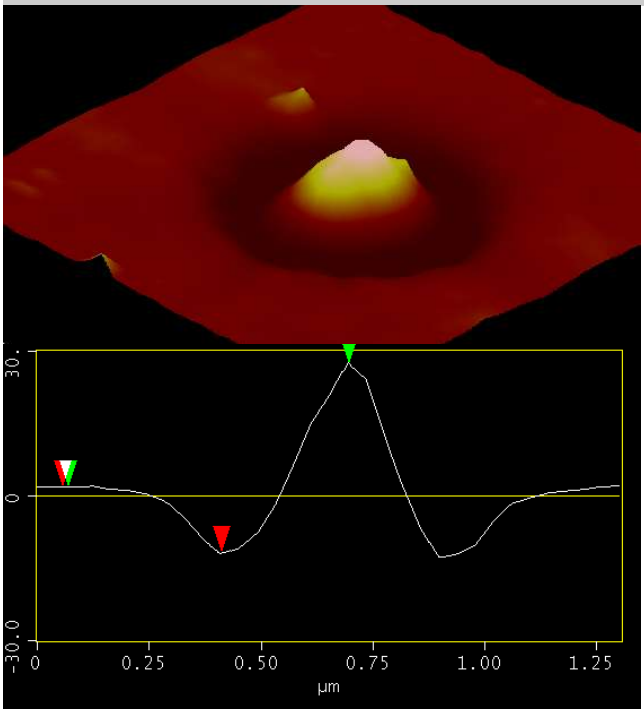

Figure 87: 900/120 Simulated versus Experimental

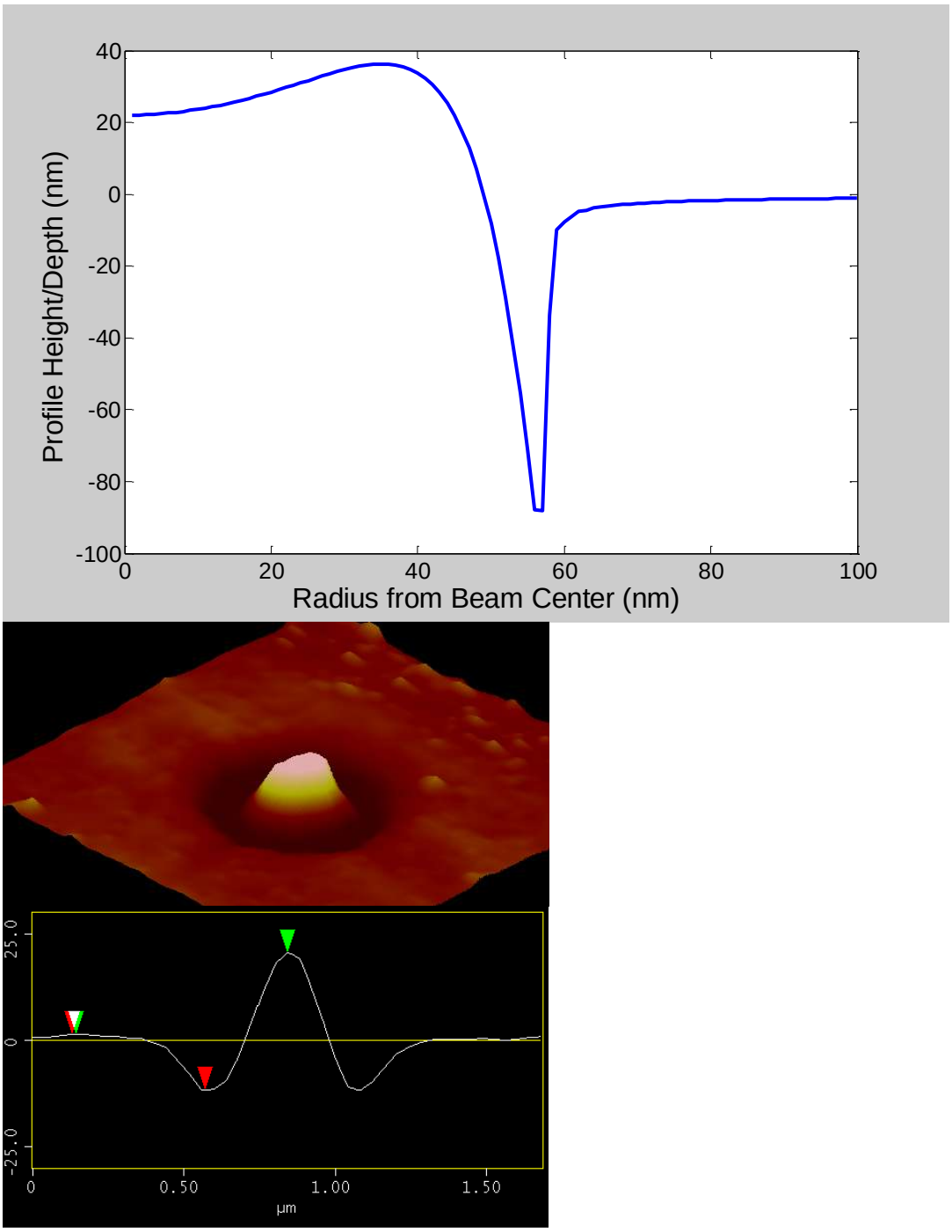

Figure 88: 850/180 Simulated versus Experimental

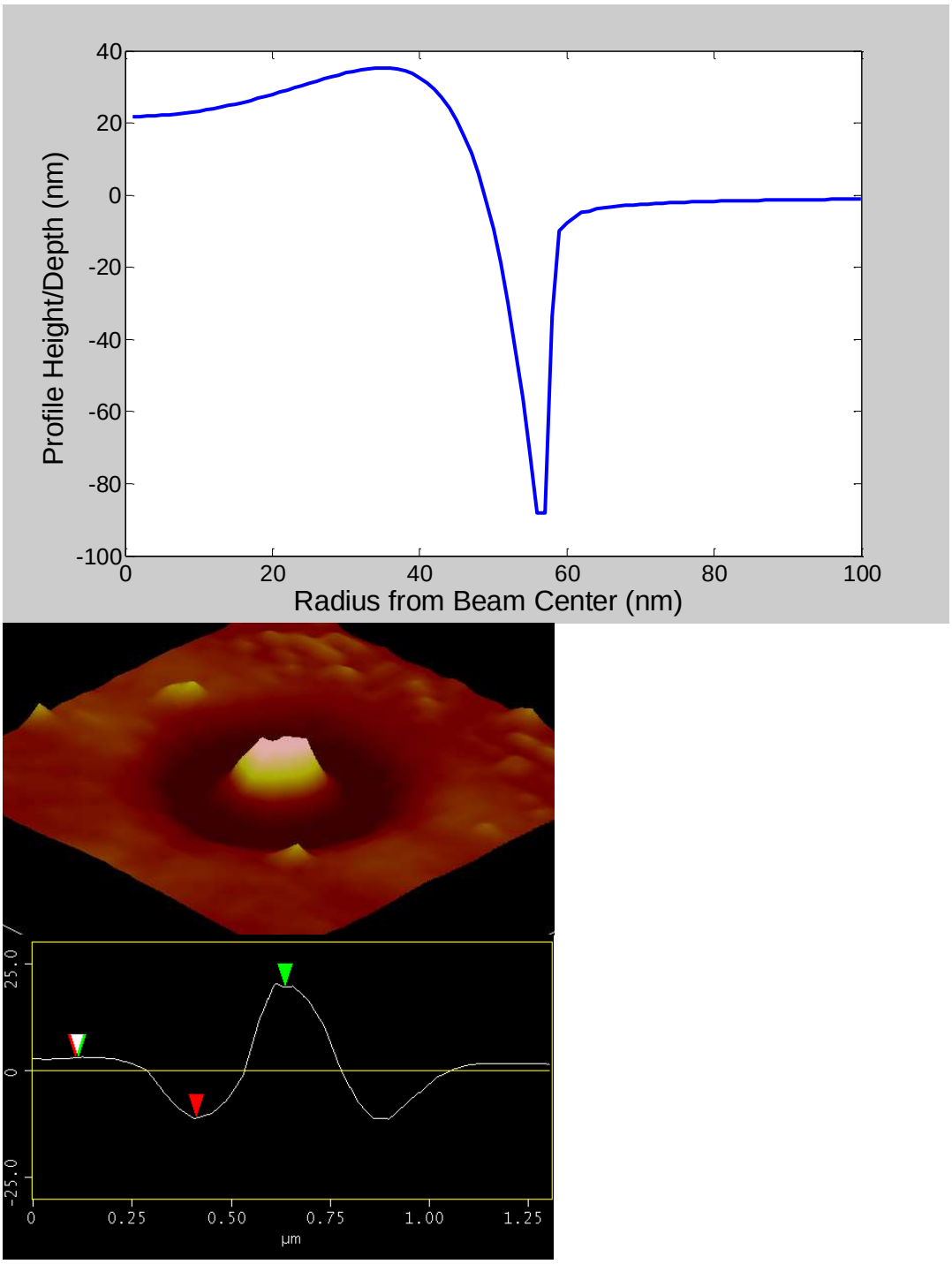

Figure 89: 800/240 Simulated versus Experimental

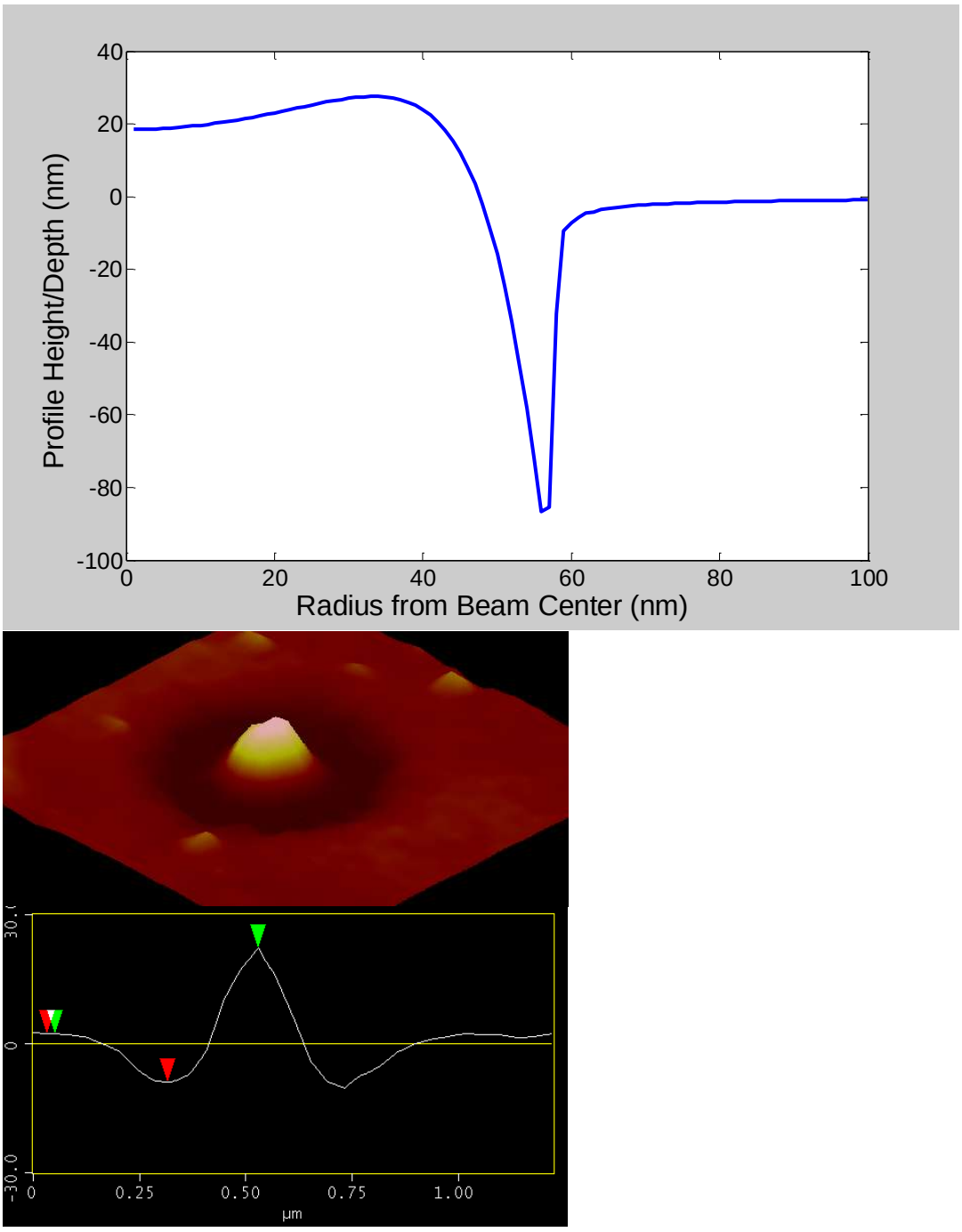

Figure 90: 500/600 Simulated versus Experimental

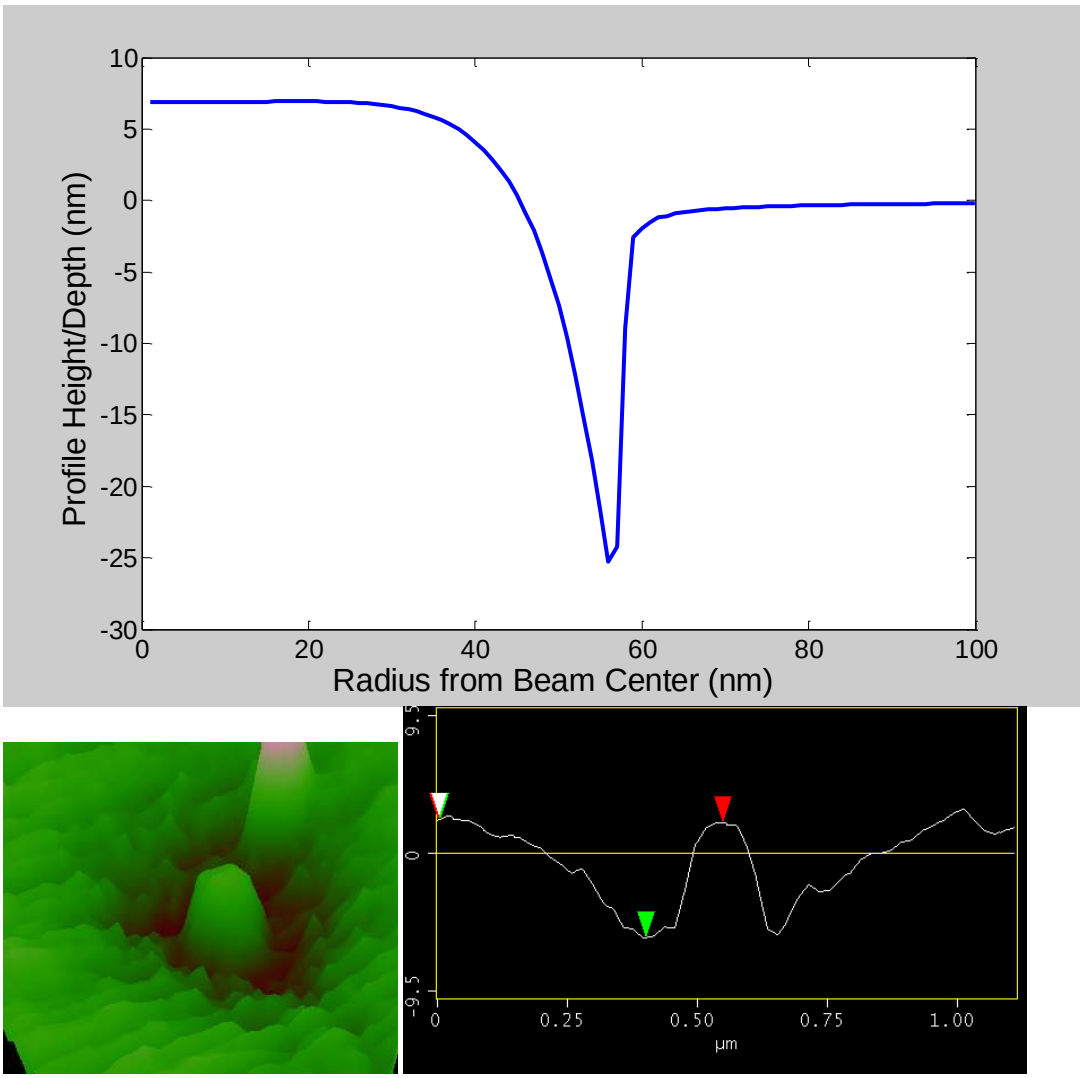

Figure 91: 100/200 Simulated versus Experimental

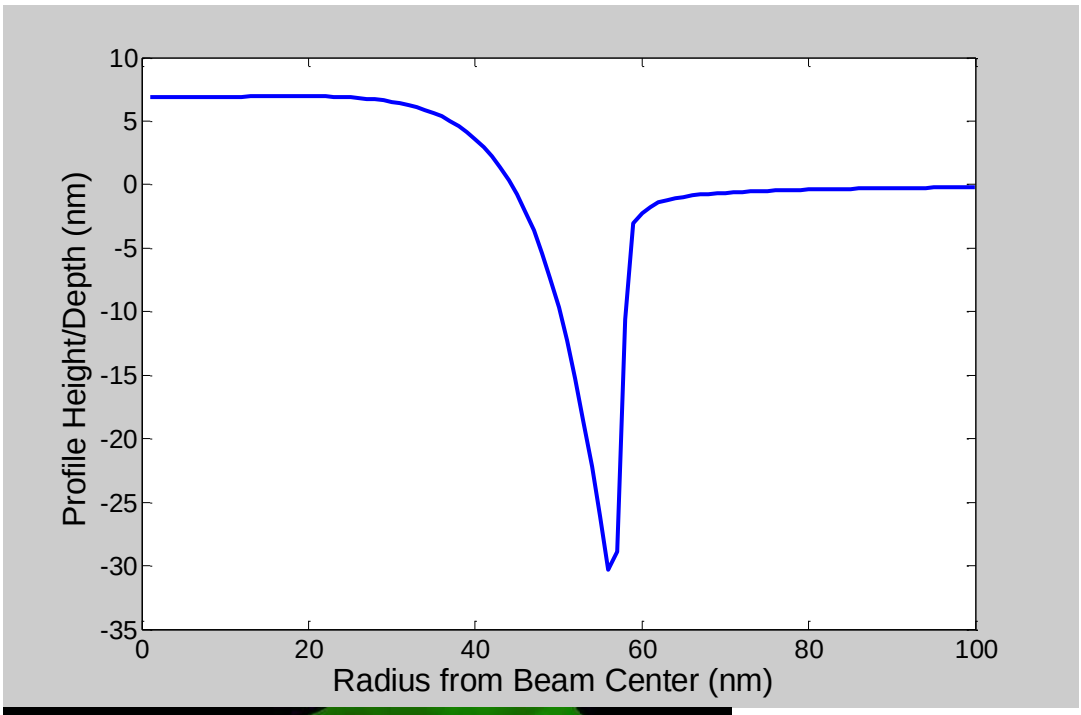

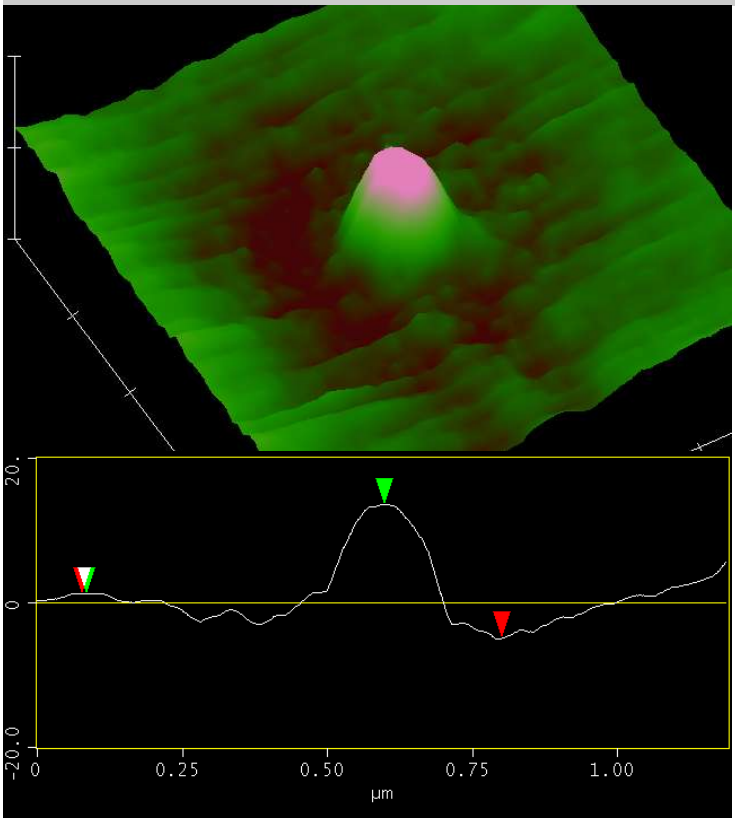

Figure 92: 100/300 Simulated versus Experimental

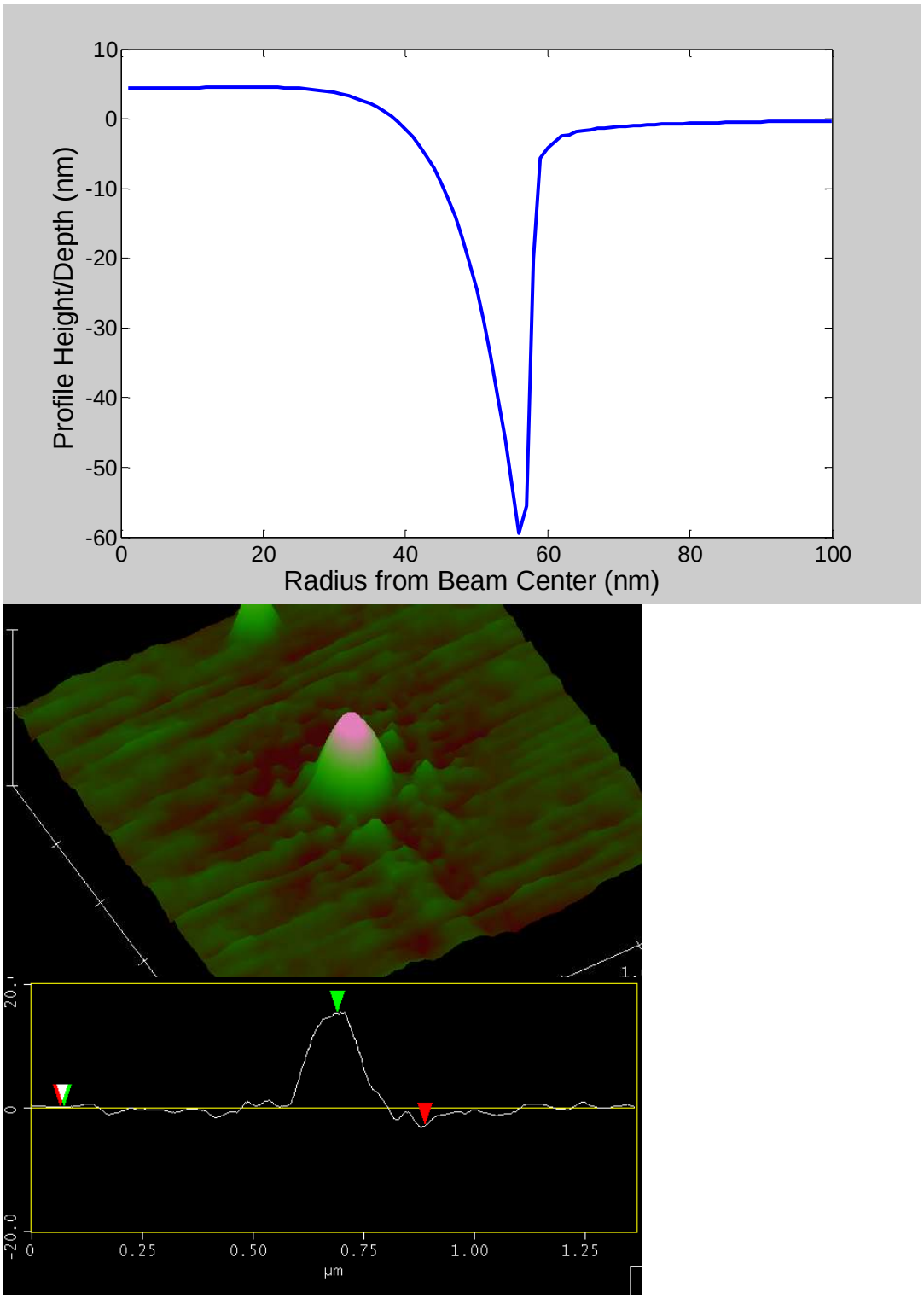

Figure 93: 100/1000 Simulated versus Experimental

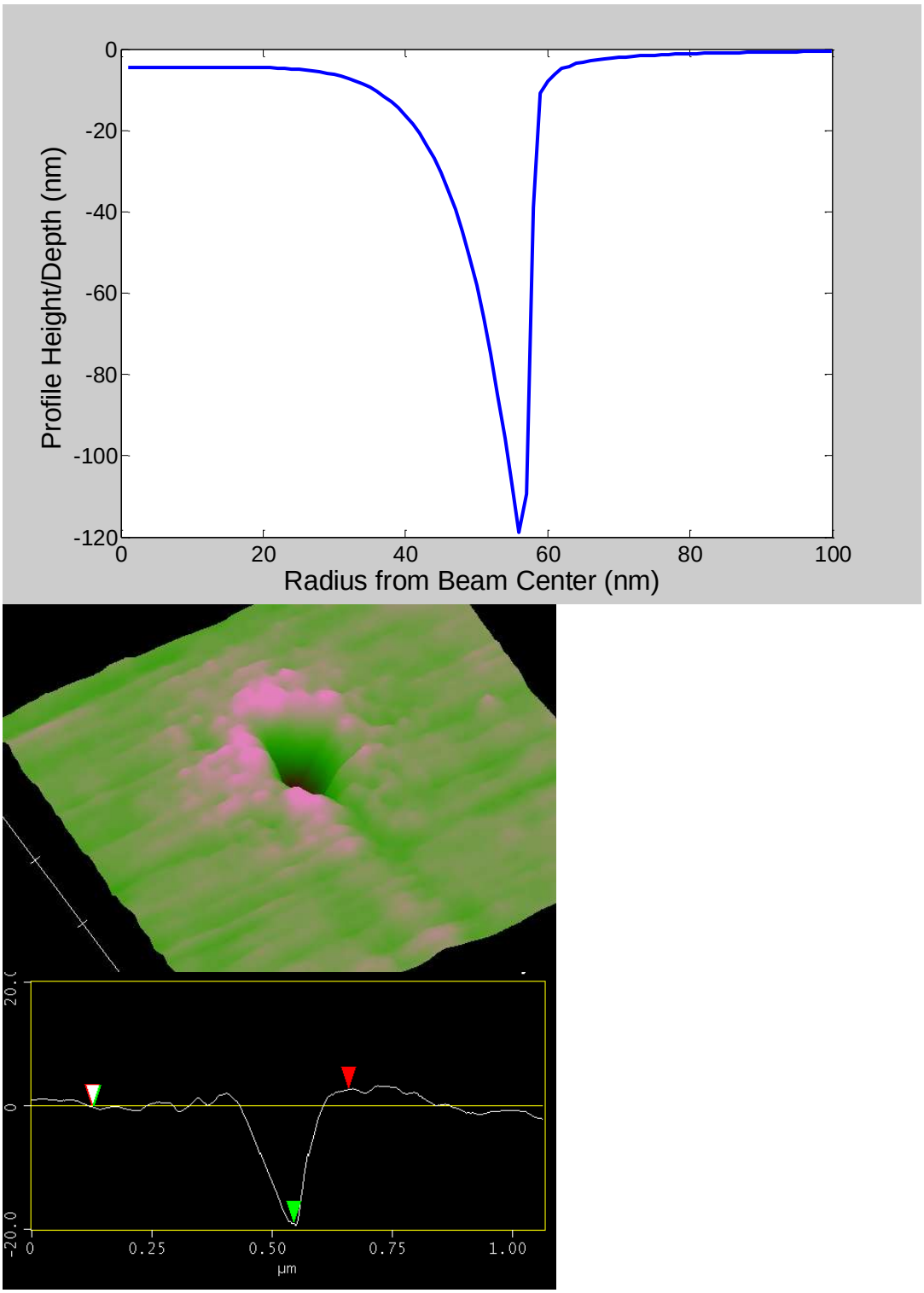

Figure 94: 100/10000 Simulated versus Experimental

required here. Simulating the required number of pulses to reach steady pulsing requires much more computation time and so the best compromise between accuracy and computation time must be determined. Future efforts on this front must forgo the initial pulse simulation and include a fast convergence numerical method on the initial species concentrations in steady pulsing, such as a Newton-Raphson root finding method or a Gauss-Seidel iterative technique for finding the steady pulsing initial conditions.

Engineering Discussion

The performance of the time dependent behavior depends heavily on the interactions between the molecular impingement of precursor, the surface diffusion of precursor and etch product, and the residence time of precursor and etch product. It is seen that high surface diffusion leads to enhanced etching rate trenches when the precursor diffusion dominates the refresh process. Also, long residence time of the etch product leads to re-deposition in the center high electron flux regions. In order to avoid all of these effects it is necessary to operate the system in a "pseudo" electron flux limited regime. In order for this to happen, the dwell time must be reduced to a length that is short enough that the etched material is linear with exposure time. From the analytical discussion earlier in this chapter a reduced form of the high electron flux equations, it is seen that this is dependent upon the electron flux and the initial conditions.

$$\begin{aligned} Etched = & \left(\frac{-xA_\sigma}{A_\sigma + A_{ESD}}\right)\left(1 + \frac{B_\sigma}{(A_\sigma + A_{ESD}) - (B_\sigma + B_{ESD})}\right) N_{A0}\left(1\right. \\ & \left. - e^{-\frac{(A_\sigma + A_{ESD})\Gamma_e}{Z}\tau_{dwell}}\right) \\ & + \left(\frac{xA_\sigma B_\sigma}{\big((A_\sigma + A_{ESD}) - (B_\sigma + B_{ESD})\big)(B_\sigma + B_{ESD})} N_{A0}\right. \\ & \left. + \frac{B_\sigma}{(B_\sigma + B_{ESD})} N_{B0}\right)\left(1 - e^{-\frac{(B_\sigma + B_{ESD})\Gamma_e}{Z}\tau_{dwell}}\right) \\ & - \left(\frac{B_{ESD}}{B_\sigma + B_{ESD}}\right)\left(\frac{A_\sigma}{A_\sigma + A_{ESD}}\right) xgI_A\tau_{dwell} \end{aligned}$$

For short dwell times where:

$$\frac{(A_\sigma + A_{ESD})\Gamma_e}{Z}\tau_{dwell} \ll 1$$

The etched equation reduces neatly to:

$$Etched \approx \left(-xA_{\sigma}\frac{N_{A0}}{Z} + B_{\sigma}\frac{N_{B0}}{Z}\right)\Gamma_e\tau_{dwell}$$

In this case, the short dwell time results in an etch shape that is governed by the electron flux shape rather than other factors. This is the ideal case, because it offers the highest spatial resolution potential.

If a reasonable etching rate is to be accomplished, then the initial condition of precursor must be as high as possible and the initial precursor coverage must be as low as possible. The precursor coverage is replenished by molecular impingement and by diffusion, and so a sufficiently long refresh time will allow for complete refresh of the precursor to the equilibrium concentration. If the precursor refresh is impingement rate limited, then increasing the local pressure will improve the impingement rate and reduce the refresh time required to reach the equilibrium. For minimization of the etch product at the beginning of the dwell time, the engineer has a few options. The first option is to use a refresh time that is at least three or four times the residence time of the etch product. In this case, nearly all of the etch product on the surface has the opportunity to spontaneously desorb. But if that residence time is long, it may be impracticable to wait for such a long time in the refresh, and so an effort must be made to reduce the etch product residence time. Heating the sample offers the reduction in the etch product residence time needed to reduce the required refresh time. The drawback here is the reduction in the precursor residence time as well. There is likely an optimum substrate temperature that allows the etch product residence time to be short enough for significant desorption during a reasonable refresh time, but still allows for a reasonably long precursor residence time combined with a sufficiently high impingement rate to maximize the initial coverage of precursor for each pulse.

Chapter 4: Lithography Mask Repair by Electron Beam Induced Etching: Inhibiting Spontaneous Etching

This chapter is a slightly revised version of a 2008 journal article published in *JVST B* by myself, Ted Liang, and Philip Rack.

Matthew G. Lassiter, Ted Liang, and Philip D. Rack, "Inhibiting Spontaneous Etching of Nanoscale Electron Beam Induced Etching Features: Solutions for Nanoscale Repair of Extreme Ultraviolet Lithography Masks," *JVST B*, **26**, 3, 2008

The use of "we" refers to my co-authors and me. My contributions to the work include: (1) Experimental setup and data collection, (2) literature searching, (3) almost all of the writing, and (4) interaction with journal editor and referees. My co-authors provided direction and funding on the scope of the research, insight into the processes observed in the experimental data, several rounds of helpful editing of the paper, general advice, and motivation.

Abstract

Electron Beam Induced Etching (EBIE) is an important technique for repairing nanoscale defects on extreme ultraviolet (EUV) lithography masks as it provides excellent spatial resolution and etch selectivity while minimizing collateral damage to the mask. While EBIE itself is a complex process, a current problem with EBIE of the TaN EUV mask absorber layer using XeF_2 is the spontaneous etching of repaired features during subsequent edits of the mask. This work explores three passivation techniques for controlling the spontaneous etching after an EBIE repair is made. An oxygen plasma was used to attempt to oxidize the TaN sidewalls, but it was not successful at stopping the spontaneous etching. An active electron-beam induced passivation using water was successful at stopping the spontaneous etching. Also, simple adsorption of water molecules on the TaN sidewalls was successful at inhibiting spontaneous etching. The successful passivation strategies are affected by subsequent scanning electron beam imaging. It was determined that the electron beam activated passivation can be damaged by electron beam imaging in the presence of residual XeF_2 on the surface. Also, the adsorbed water passivation strategy is susceptible to electron induced desorption of the water.

Introduction

Electron beam induced processing has been developed as an alternative to focused ion beam (FIB) processing as a repair process of nanoscale defects on lithography masks (for a review of electron beam induced processing see Randolph *et al*[68]). The electron beam induces the dissociation of a precursor gas to cause a reaction at the surface of the substrate. This reaction either deposits material or causes the etching of the substrate material, depending on the precursor/substrate material combination. The details of the EBIE process are complex; as there are many steps that can be rate limiting. The intricate EBIE process details are beyond the scope of this work, as this work focuses on post EBIE passivation of the etched feature to make it resistant to damage during further exposure to the EBIE precursor gas. The electron beam provides superior spatial resolution than that of the FIB and minimizes damage to the mask materials due of the relatively small mass of the electron versus the gallium ion. Extreme ultraviolet (EUV) lithography masks use a patterned tantalum oxide/tantalum nitride film stack as the absorber layer which is deposited onto a ruthenium etch stop layer that protects the underlying multi-layer Mo-Si mirror[69] (Figure 95). EBIE using a xenon difluoride precursor gas will etch the EUV absorber film stack and has good selectivity to the underlying ruthenium layer[70]. However, while the tantalum oxide layer is stable, the

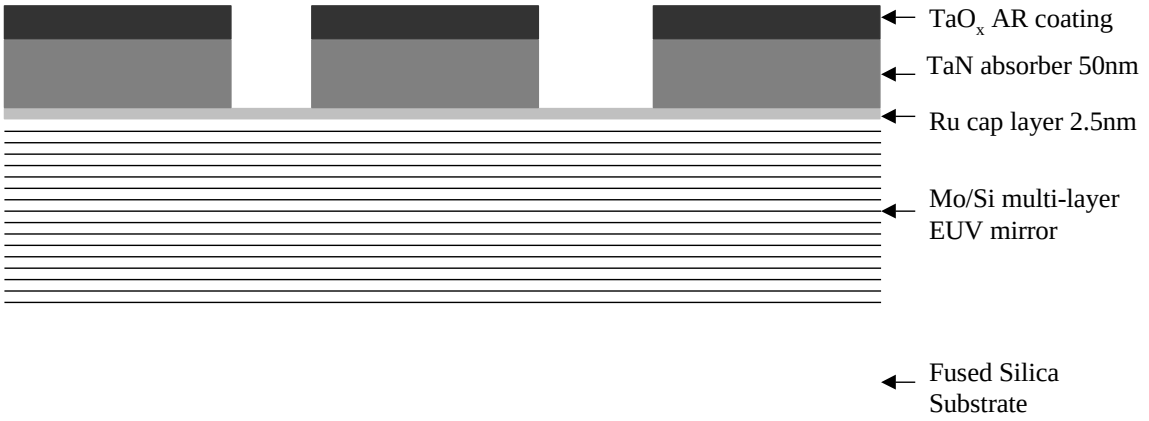

Figure 95: Schematic illustrating an EUV Mask Cross-section.

The Si/Mo multi-layer acts as a mirror to the EUV exposure wavelength. The Ru capping layer protects the multi-layer mirror during mask fabrication and also serves as an etch stop layer for the etching of the TaN film above it. The patterned TaN/TaON film absorbs EUV radiation resulting in a binary reflective mask.

tantalum nitride film spontaneously etches in the xenon difluoride environment, and subsequently compromises the repaired features.

Spontaneous etching of silicon in XeF_2 is a well-known phenomenon and has been studied in detail by Vugts *et al*[71]. Little is known about the exact nature of the spontaneous etching of TaN in XeF_2, but TaO_x is observed to be resistant to spontaneous etching in XeF_2, and we assume this to be analogous to Si/SiO_2 in XeF_2. Ibbottson et al. suggest that the XeF_2 molecule physisorbs at low temperatures (<450K) and undergoes direct impact dissociation at higher temperatures on Si and SiO_2[72]. Below 450K, the physisorbed molecule subsequently reacts with the Si to form a SiF_2 intermediate reaction product, and ultimately a SiF_4 product that has a small desorption energy. Below 450K the etching rate at lower temperatures is limited by the concentration of XeF_2 on the surface, because the XeF_2 residence time increases with decreasing temperature. As the temperature increases, etch rate decreases to a minimum and then begins increasing along a positive activation energy slope. Above 450K, Vugts et al attributed the positive activation energy to the desorption of the intermediate reaction product SiF_2. At room temperature, SiO_2 does not spontaneously etch because of the non-dissociative physisorption of the XeF_2 molecule. Dissociative chemisorption results in F* radicals, which readily etch SiO_2. While detailed studies of Ta, TaN, and TaO_x in XeF_2 have not been previously reported, the Ta and TaN appear to etch spontaneously (analogous to Si) and TaO_x appears to be resistant (analogous to SiO_2).

If an absorber film has been etched using EBIE, the sidewalls of the tantalum nitride sidewalls become exposed. Further exposure to xenon difluoride spontaneously etches the nitride layer, undercutting the tantalum oxide layer and compromising the original EBIE feature. To enable the use of EBIE on EUV masks, it is necessary to protect the sidewalls from spontaneous etching so that multiple edits can be made on the same mask.

During EBIE, the precursor gas adsorbs on to the surface of the film and the electron beam dissociates the xenon difluoride. The fluorine radicals react with the tantalum oxide and nitride film to form volatile species of tantalum fluoride (or oxyfluorides) that desorb from the surface along with the other by-products of xenon, nitrogen, and oxygen. The result is the etching of the tantalum oxide-tantalum nitride film. A simplified view of the EBIE process, neglecting intermediate reaction products, of the TaO_x/TaN film is given below:

$$TaO_x/TaN(s) + XeF_2(g) + e^- \rightarrow TaF_x(g) + Xe(g) + N_2(g) + O_2(g)$$

Ideally, the etching of the Ta-based film in XeF_2 would occur only in the presence of the electron-beam and would otherwise be stable to the XeF_2 gas. Fortunately, the tantalum oxide surface does not spontaneously react with xenon difluoride. This is evidenced by the fact that the absorber film capped with the TaO_x is stable to the XeF_2

before the editing process. However, the tantalum nitride layer does spontaneously react with xenon difluoride without the presence of the electron beam. Therefore, the following reaction (again neglecting intermediate reactions) likely occurs:

$TaN(s) + XeF_2(g) \rightarrow TaF_x(g) + Xe(g) + N_2(g)$

Consequently, once an etch repair is made and the TaN sidewalls of the etched feature are exposed (Figure 96a) the TaN subsequently etches when exposed to XeF_2 (96b). In order for the repaired feature to remain uncompromised, the sidewalls must be protected or passivated (96c) from future exposure to the XeF_2 gas (96d).

Several possibilities for protecting the exposed TaN sidewall were investigated. The most obvious choice is to convert the tantalum nitride surface into a tantalum oxide passivation layer that will not spontaneously etch when exposed to xenon difluoride. It was speculated that this could be accomplished by exposing the surface to oxygen containing species after an EBIE repair. The oxidation of Ta at room temperature has been studied in detail by Sewell et al, and their results indicated that Ta oxidation occurrs faster when exposed to H_2O compared to O_2, and that oxidation rates were greatly enhanced by electron beam exposure[73]. The kinetics of TaN oxidation are of course different from Ta, as they likely require the reduction of the TaN to Ta before the oxidation can occur. Alternatively, TaN could transform to TaO_xN_y. Multiple strategies were attempted to oxidize the TaN sidewalls of an EBIE feature to prevent further spontaneous etching during exposure to XeF_2.

Experimental Procedure

EBIE requires the hydrocarbon contamination on the chamber and the substrate to be removed to eliminate competitive deposition processes to the etching process. If the carbon deposition processes are significant, a net deposition or a very slow etching rate will result as the etching process is competing against the unwanted carbon deposition[74]. The XEI Scientific Inc. EVACTRON® C Decontaminator was used immediately before EBIE to remove residual carbon species in the chamber and on the substrate. The EVACTRON® system creates oxygen radicals from atmospheric gas by means of low power RF plasma. The oxygen radicals remove hydrocarbon contamination by converting them into CO_2, CO, and H_2O gas molecules that are pumped out of the system by the evacuation system. An EVACTRON® treatment at a pressure of 53 Pa and a RF power of 14W for 30 minutes before beginning the EBIE process was found to be sufficient to remove hydrocarbon contamination and yield a stable EBIE process.

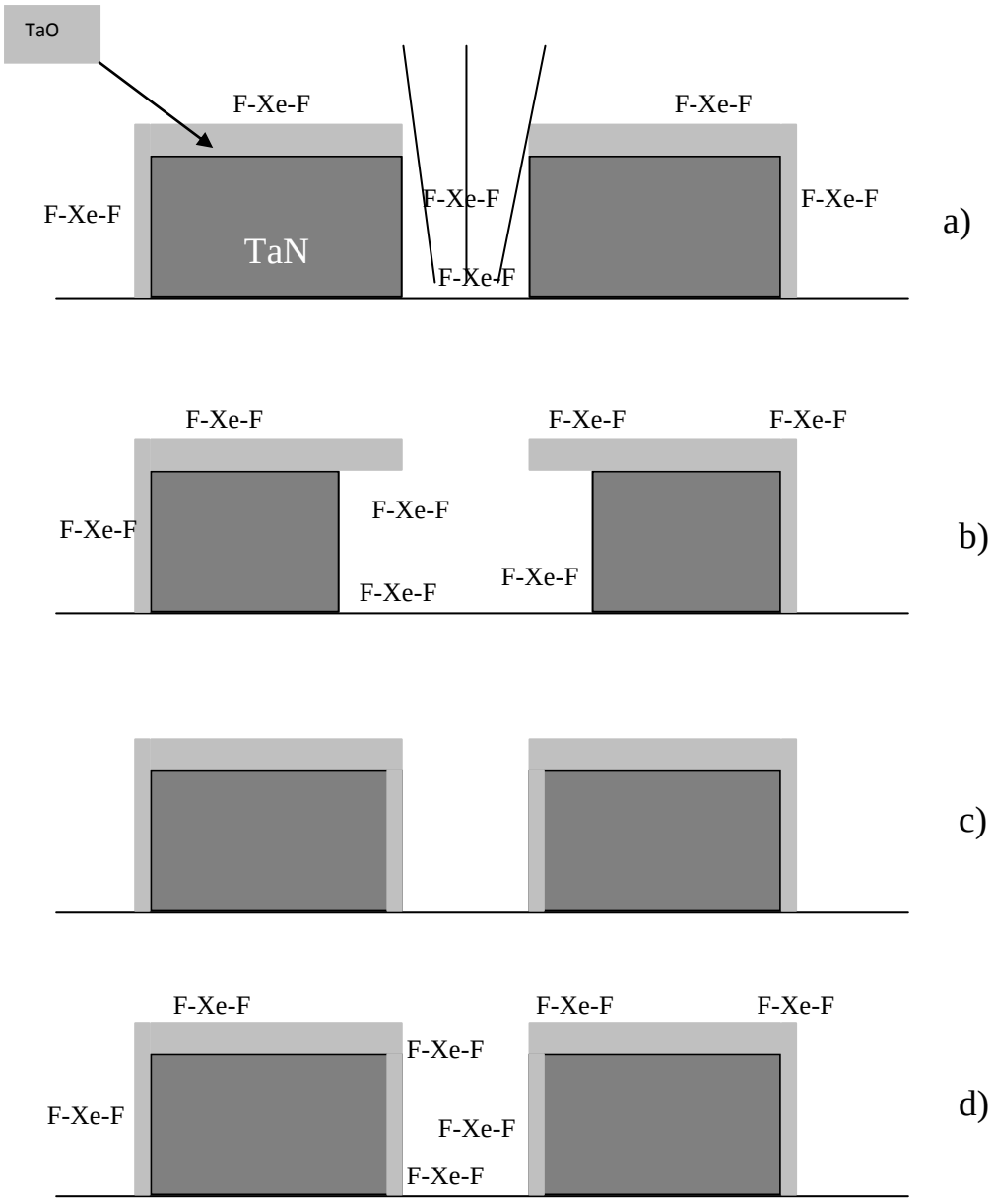

Figure 96

(a) After electron beam induced etching of the film, the sidewalls of the etched feature are exposed TaN. (b) The exposed TaN etches when exposed to XeF_2, undercutting the TaO_xN_y surface layer. (c) Passivation of the TaN sidewalls; (d) The passivated sidewalls inhibit spontaneous etching after subsequent exposure of XeF_2.

The EBIE of the TaN mask film is accomplished by flowing XeF_2 gas through an injection needle 2 mm above the surface of the mask at an approximate angle of 30 degrees to the surface[75]. The flow is adjusted using a metering valve until the chamber background pressure equilibrates to 2.0 x 10^{-2} Pa. Although the localized pressure of the processed region is not precisely known, it is expected to be enhanced by at least an order of magnitude based on capillary flow data[76] and estimates based on flow modeling of a similar injection system[77]. Lines 6.85μm long and 40nm wide were etched into the TaO_x/TaN absorber layers using a focused 5keV, 10 pA electron beam from a thermal field emitter source, 411 μm/sec scan rate and 3 minute process time (Figures 97 & 98). Calculating the diffraction limited probe size based on the aperture in the electron lens, working distance, and electron energy; the probe has a minimum FWHM about 31nm, in good agreement with the ~ 40nm etch line width demonstrated below.

Oxygen Plasma Passivation

The initial strategy for passivating the TaN sidewalls was to expose an electron beam etched feature to an oxygen plasma created by the EVACTRON® system so oxygen radicals could oxidize the tantalum nitride sidewalls. Initially a line was etched as previously described via a XeF_2 EBIE, and subsequently the EVACTRON® system was used at a pressure of 53 Pa (air) and a RF power of 14W for 30 minutes. The atmosphere contains about 20% oxygen, and if the plasma system converts only ~1% of O_2 molecules into O^* radicals, the partial pressure of O^* should be ~ 0.2 Pa (neglecting preferred recombination of O* radicals). The molecular impingement rate (I) is given by:

$$I = \frac{p}{\sqrt{2\pi mkT}}$$

Where p is the pressure in Pa, m is the gas particle mass in kg, k is the Boltzmann constant, and T is the temperature in K. This results in an impingement rate of 7.6 x10^{17} $cm^{-2}s^{-1}$. Assuming a unity sticking coefficient and a surface site density of ~ 1x10^{15} cm^{-2}, the monolayer formation time is ~ 1.3 milliseconds. While the sticking coefficient is likely less than 1 and the partial pressure likely less than 0.2Pa, the 30 minute exposure should be adequate to saturate the TaN surface with the oxygen radicals.

After the oxygen radical treatment, the system was evacuated to a base pressure of less than 2.0 x 10^{-4} Pa. Then, it was exposed to the XeF_2 EBIE flow conditions (background XeF_2 pressure of 2.0 x 10^{-2} Pa) without the incident electron beam for 20 minutes to emulate the gas exposure time of additional mask repairs. The XeF_2 gas flow was stopped, base pressure reached, and the EBIE line was re-imaged in the SEM. Figure 97 reveals that significant spontaneous etching of the TaN film occurred, and that the TaN has undercut the TaO_x top layer as the original shape of the EBIE line can still be

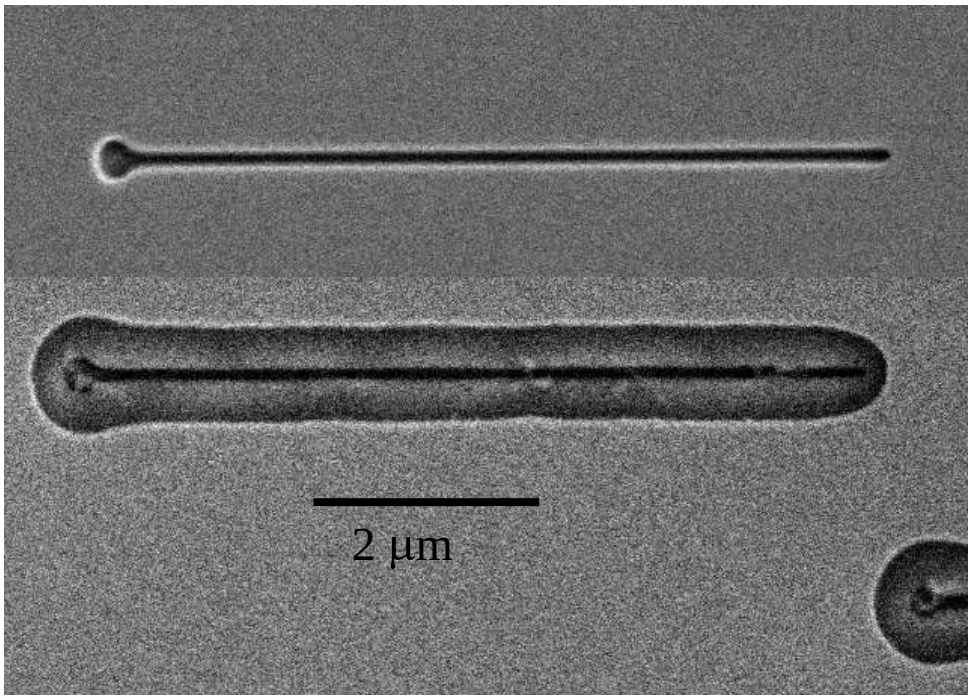

Figure 97: Spontaneous etching of an EBIE feature after oxygen radical exposure.

(top) A 40nm wide line etched by EBIE using XeF_2, then exposed to oxygen radicals for 30 minutes. (bottom) Note the undercutting of the residual Ta_2O_5 surface.

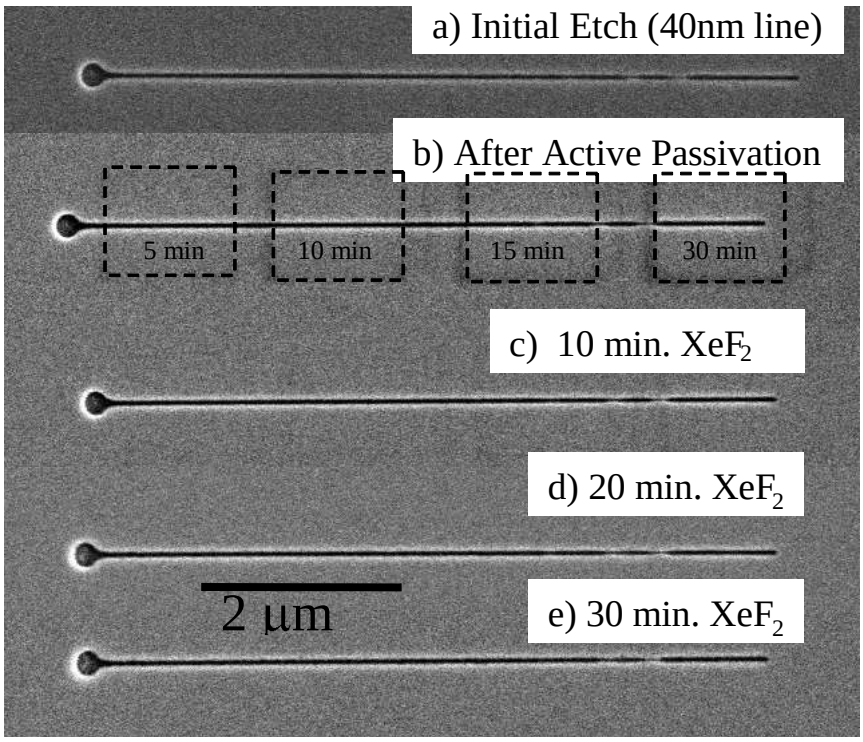

Figure 98

An EBIE line was passivated by scanning an electron beam over the edited feature while flowing H_2O. Sucessive SEM images after XeF_2 exposure demonstrates successful passivation.

observed. A similar effect can be observed when EBIE of SiO_2 films on Si substrates[78]. The bottom image in Figure 97 is representative of an unpassivated feature after a subsequent 20 minute XeF_2 exposure. At room temperature, the reaction kinetics of the oxygen radicals on the TaN surface appear to be insufficient to oxidize the TaN sidewalls and prevent subsequent spontaneous XeF_2 etching. In order to oxidize the TaN surface to inhibit spontaneous etching, some additional activation is required than simply supplying oxygen radicals to the surface.

Electron Beam Induced H_2O Passivation

The second technique that was explored was to expose H_2O to the edited feature while "actively" scanning the electron beam. Based on the failed oxygen plasma treatment approach, it is likely that the TaN is stable to the oxygen radicals at room temperature. However, it is assumed that under the electron beam, electron stimulated desorption of N could reduce the near surface TaN to Ta metal, which would more readily oxidize by H_2O or the O^* radicals created via an electron beam induced dissociation of H_2O.

Another line was etched by XeF_2 EBIE into the TaO_x/TaN EUV absorber film (Figure 98a). The system was evacuated to a pressure less than 2.0 $x10^{-4}$ Pa before starting the H_2O flow through the gas injection system. The H_2O flow was increased to bring the background pressure in the SEM to 2.0 $x10^{-2}$ Pa. Different parts of the etched line were scanned using a 1.30μm x 0.95μm box for 5, 10, 15, and 30 minutes from left to right (Figure 4b). After active H_2O passivation, the H_2O gas flow was stopped, the system was evacuated to less than 2.0 x 10^{-4} Pa, and the XeF_2 flowed through the gas injection system to a background system pressure of 2.0 x 10^{-2} Pa. Figures 98c-e are SEM images after 10, 20, and 30 minutes of XeF_2 exposure, respectively. Based on Figure 98, the active H_2O passivation was successful in passivating the TaN sidewall and it is believed that the sidewalls are converted to TaO_x or TaO_xN_y making it resistant to spontaneous etching in XeF_2.

It was observed that even after the XeF_2 flow was off for several hours and the passivated line is imaged with the SEM (approximately 30 seconds of electron beam exposure), electron beam induced etching of the passivation layer occurs. This observation lead us to two conclusions: 1) the passivation layer is very thin, and 2) the XeF_2 residence time is relatively long (on the order of hours) on the Ta_2O_5 surface. The fact that the passivation layer is very thin is not surprising, as the growth of the passivation layer requires diffusion of the oxygen or tantalum atoms through the passivation layer. Similar to any native oxide, this is slow at room temperature, as bulk diffusion coefficients are very low. Subsequent exposure of electron imaged passivated features to XeF_2 gas flow results in spontaneous etching of the TaN in the imaged regions of the passivated line (Figure 99). This problem can be mitigated given sufficient time (overnight). Additionally, the residual XeF_2 can be removed by purging the chamber at a high pressure (50 Pa) with air. We assume that the impingement of other

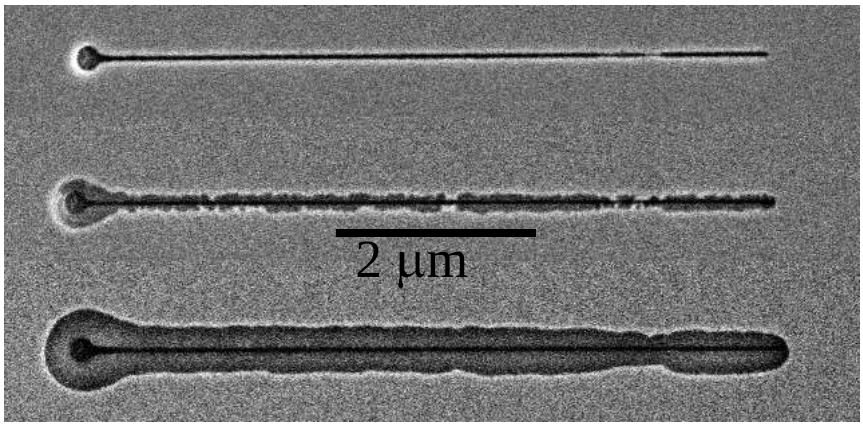

Figure 99

(top) SEM image of passivated EBIE line after 30 minutes of XeF_2 exposure. (middle) SEM image of passivated structure not exposed to high atmospheric gas load prior to SEM imaging which has been de-passivated and spontaneously etched for 10 minutes. (bottom) Further exposure to XeF_2 flow for 10 more minutes shows evidence of significant spontaneous etching.

room temperature gases assists in desorption of the XeF_2 species from the passivation surface. Once the residual XeF_2 is removed, the EBIE trench and passivation layer can be safely imaged using the electron beam without damaging the passivation layer. This approach was used to collect the 10 min. and 20 min. images of the EBIE line shown in Figure 98c and 98d.

Adsorbed Water

The final approach that was explored to passivate the TaN sidewalls was to flow water into the system without the simultaneous electron radiation. While oxidation of the TaN sidewalls was not expected in lieu of the oxygen plasma results, it was speculated that the polar nature of the water molecules could adsorb onto the sidewalls and effectively passivate the TaN sidewalls if the residence time was long enough. After an EBIE edit of the mask was made, the XeF_2 gas flow was stopped, and the chamber was evacuated to a pressure of less than 2.0×10^{-4} Pa. H_2O flow was introduced through the gas injection system and the pressure in the chamber was increased to ~10 Pa. After the water is adsorbed on the surface of the TaN, the surface is protected against spontaneous etching in XeF_2 (images not shown). The H_2O residence time is apparently on the order of hours because water exposed edits were stable during this time, however structures were not stable after pumping overnight. Care must also be taken to avoid imaging the passivated feature after the water is adsorbed on the surface. The electron beam scanning apparently causes electron stimulated desorption of the H_2O molecules[79], leaving sites available for XeF_2 adsorption and spontaneous etching.

Summary

The problem of spontaneous etching of TaN in XeF_2 can be greatly reduced or eliminated by actively scanning the electron beam in a water vapor environment to create a passivation layer on the surface. This passivation layer will protect the underlying TaN from spontaneous etching so long as it remains intact. Residual XeF_2 must be removed before any electron beam imaging of the passivation layer or it will be inadvertently etched and no longer protect the TaN film. Also, flowing H_2O into the SEM chamber after EBIE will protect the TaN film for a long enough time to allow additional editing using XeF_2, as long as the water protected TaN surface is not electron imaged before or during XeF_2 exposure. This strategy is the easiest to implement, as it only requires changing gas flows between repairs rather than actively scanning each repaired site again.

Chapter 5: Carbon Nanotube Manipulation by Electron Beam Induced Etching

Introduction and Theory

Experiments were conducted at the University of Tennessee - Materials Science and Engineering Department to investigate the etching of carbon nanotubes (CNT) by focused electron beam induced chemistry. The CNTs, provided by Xidex Corp. of Austin, Texas, were grown onto the surfaces of silicon atomic force microscopy (AFM) cantilevered tips. Depending upon the process conditions during deposition of the carbon, the CNTs grow in a variety of number densities, sizes, and shapes. Some are loops extending from one part of the cantilever to another, some are free standing with only one end of the tube attached to the silicon, and still others are lying down on the silicon surface. In addition to the CNTs there is a film coating of carbonaceous material elsewhere on the silicon cantilever. Ideally, the e-beam induced chemistry would provide the user the ability to edit a specific CNT as well as clean the surface of the carbonaceous material, leaving only the edited CNT. The edited CNT could be used as the probe tip for atomic force microscopy, as a field emitter, or for other novel applications.

Experiments were carried out in a Hitachi S/E-4300 scanning electron microscope. The etching process consists of supplying a stable precursor gas vapor into the SEM chamber. Some of the precursor gas molecules adsorb onto the surface of the CNT. A primary beam electron, a backscattered electron, or a secondary electron emitted from the surface of the CNT inelastically collides with the adsorbed precursor molecule. The dissociated atoms of the precursor molecule react with the surface and form volatile etch product species. The etch product species desorbs from the surface of the CNT by thermal desorption or electron stimulated desorption. This removes material from the CNT and provides a new adsorption site for precursor vapor molecules to adsorb. The process is selective in that it requires the electron beam to induce the process (Figure 100).

Yuzvinsky *et al*[80] studied the e-beam induced cutting of nanotubes using an SEM with various precursor combinations, and they reported the best precursor was H_2O. The chemistry of choice for etching carbon is oxygen based. Water was chosen as the precursor gas to supply the oxygen for etching of the CNT. An electron induced dissociation of adsorbed water on the CNT surface likely results in carbon monoxide or carbon dioxide etch products, both of which are volatile molecules. If a water vapor is supplied to the SEM chamber, there will be a surface coverage of adsorbed water that

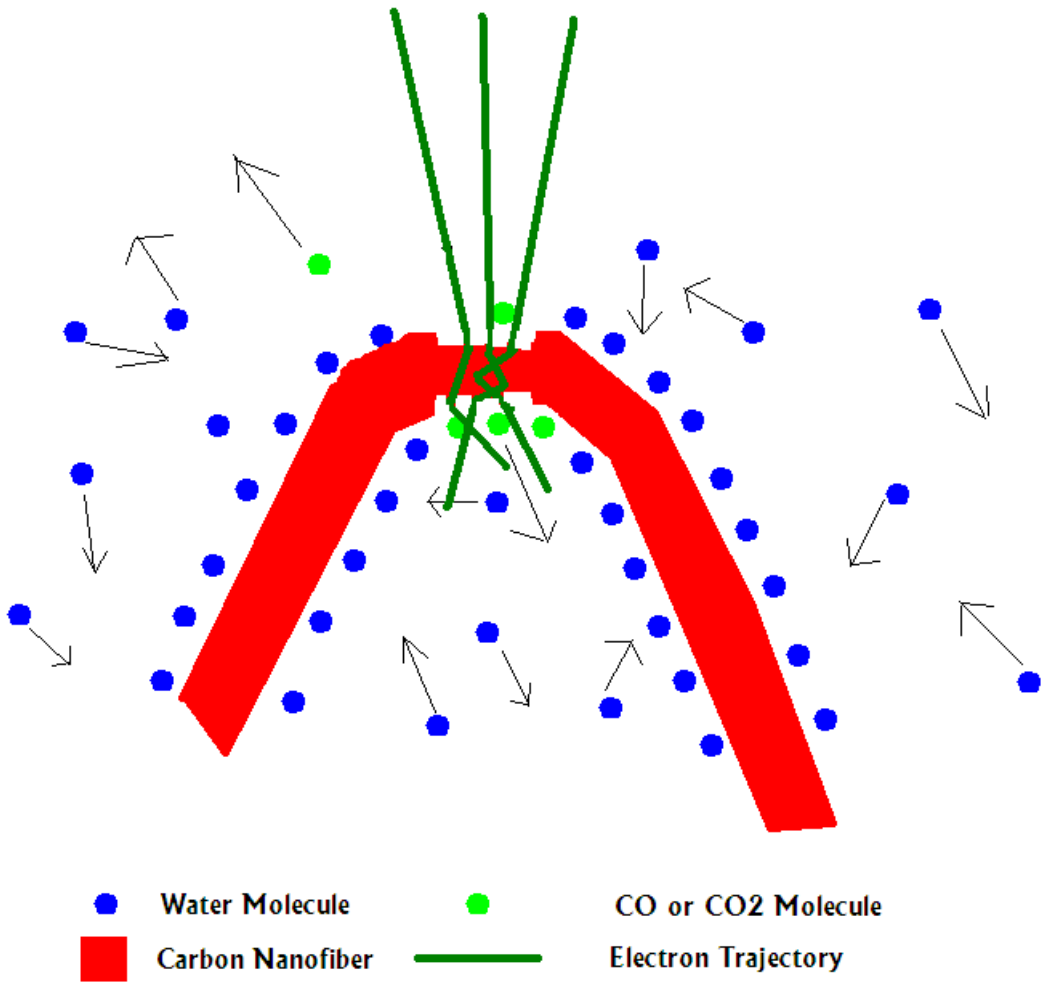

Figure 100: Schematic of CNT Etching Process

depends upon the bonding energy between the CNT surface and the pressure of the water vapor at the surface. The Henry adsorption isotherm gives coverage (θ) as:

$$\theta = \frac{g I_{H_2O} \tau_{ads}}{Z}$$

Where g is the sticking coefficient of the impinging water to the surface, I_{H2O} is the molecular impingement rate of water, τ_{ads} is the average residence time of the water on the surface of the CNT, and Z is the surface density of adsorption sites. Maximizing the rate of etching requires maximizing the water coverage on the surface of the CNT. τ_{ads} is a function of adsorption energy and temperature. Without a temperature controlled stage, this becomes a constant factor. This leaves molecular impingement rate as the only factor remaining for the engineer to increase the surface coverage. Molecular impingement rate is directly proportional to pressure as:

$$I = \frac{p}{\sqrt{2\pi m k T}}$$

Where p is the pressure in Pascals, m is the molecular mass in kilograms, k is the Boltzmann constant in Joules/Kelvin, and T is the absolute temperature of the gas in Kelvin. Under high vacuum mode, the maximum background pressure is 2.50×10^{-2} Pa. In order to increase the pressure, and thus the coverage of water vapor on the surface of the CNT the water is injected into the chamber by a needle less than 1mm above the surface of the substrate. While it is not precisely known, simulation of the gas flow indicates that the local pressure at the surface under the injection needle is 10-1000 times the background pressure in the chamber.

It is common in all SEMs to have carbon pinning during exposure to the electron beam. There is a base pressure of carbon containing species in the chamber, mostly due to back streaming oil from the roughing pumps. These carbon species adsorb on the surface in the chamber and are mobile. Electrons impacting with these mobile species result in dissociation to amorphous carbon or cross-linking of chains to create immobile deposits of carbon. These processes are competitive to the etching process, and in order to result in a net etching rate, the competitive deposition must be eliminated if possible or otherwise minimized. Figure 101 illustrates an example of carbon deposition by the e-beam while imaging a CNT. The CNT was continuously imaged for 30 minutes at a using a 5.0 kV beam and a beam current of 8 pA. Note that there is a significant deposition on the CNT.

Toth *et al*[81] observed that deposition versus etching switching is controlled by the electron flux. For either deposition or etching, the rate of reaction is limited by and proportional to the flux of electrons at low electron flux until the electron flux is sufficient to deplete the precursor gas coverage and the rate becomes limited by the

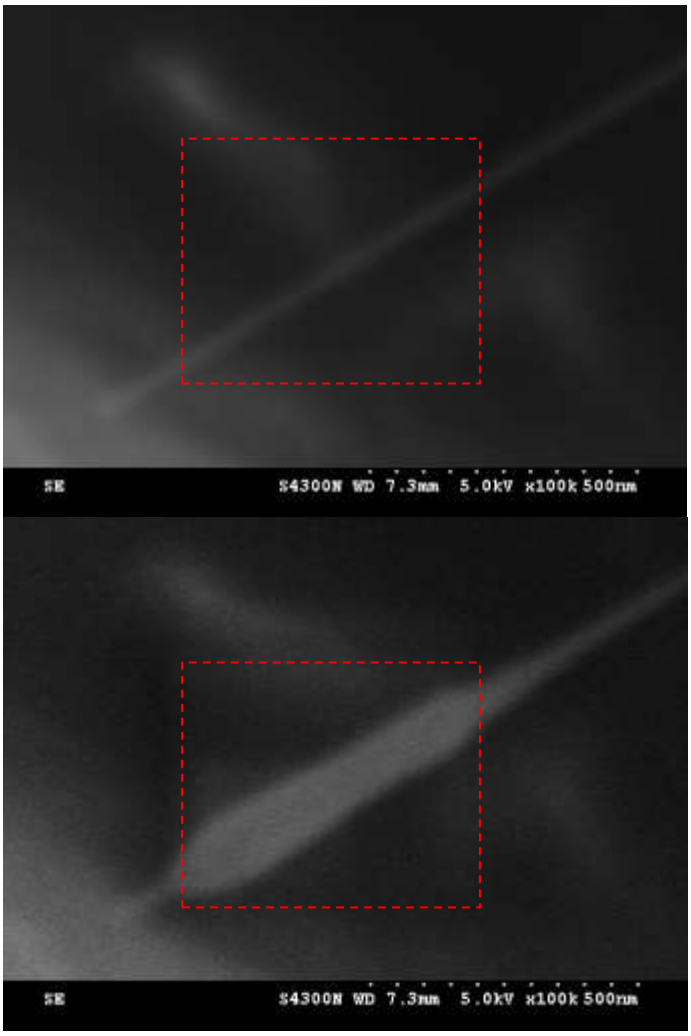

Figure 101: The CNT was imaged by the SEM scanning the region highlighted by the dotted red line. There was significant deposition on the CNT due to carbon contamination in the SEM chamber deposited during exposure to the electron-beam.

mass transport of new precursor to the surface. This results in a constant rate of reaction for higher electron fluxes. At low electron fluxes, the deposition process is more efficient than the etching process due to a higher dissociation probability of the carbon deposition precursor than the dissociation probability of the water. As electron flux increases, the deposition process becomes mass transport limited by the arrival rate of deposition precursor. Provided that there is a sufficiently high pressure of etch precursor; as electron flux continues to increase, the etch process rate continues to increase proportional to electron flux. The etching process then becomes more efficient than the deposition and net etching results (Figure 102 - left).

The net etching rate can be improved by removing the source of hydrocarbon contamination. This lowers the deposition rate enabling a larger net etching rate (Figure 102 – right). Increasing the local water pressure increases the gas coverage on the surface resulting in a higher etching rate, improving the net rate towards etching (Figure 103 – right).

The etching rate can be most improved by cleaning volatile carbon containing species out of the SEM chamber, increasing as much as possible the precursor pressure at the CNT surface, and increasing the electron flux as high as possible.

Modeling

A continuum model can be used to model the etch rate of the CNT. The rate equation for the precursor gas concentration is:

$$\frac{dN_A}{dt} = gI_A\left[1 - \frac{N_A}{Z}\right] - \frac{N_A}{\tau_A} - \frac{A_\sigma \Gamma_e N_A}{Z}$$

Where N_A is the precursor gas concentration, g is the sticking coefficient, I_A is the molecular impingement rate, Z is the surface adsorption site density, τ_A is the surface residence time of the precursor gas molecule, A_σ is the probability of electron induced dissociation, and Γ_e is the electron flux. The steady state solution for the etching rate is:

$$EtchRate \propto \frac{xA_\sigma \Gamma_e g I_A}{\left(gI_A + \frac{Z}{\tau_A} + A_\sigma \Gamma_e\right)}$$

Where x is the stoichiometry factor relating the number of etch product molecules generated per precursor molecules consumed. The surface residence time can be calculated from:

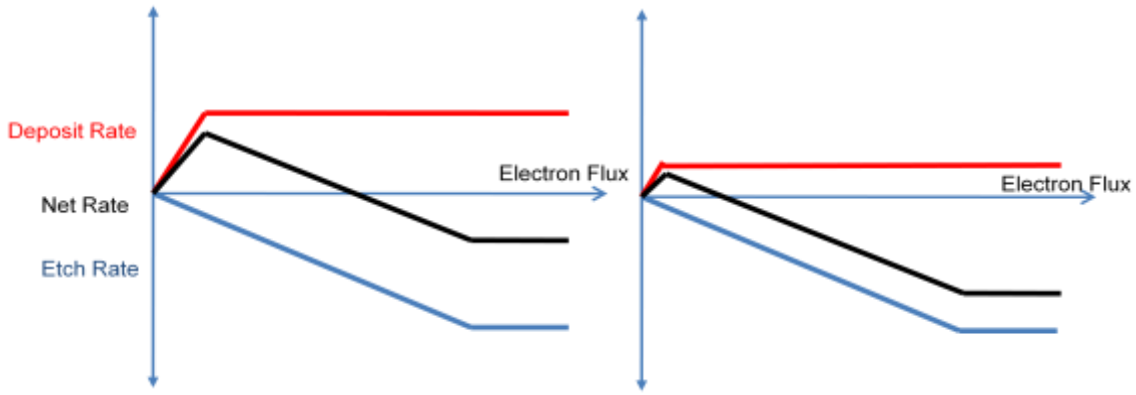

Figure 102: Deposition Rate, Etching Rate, and Net Rate versus Electron Flux

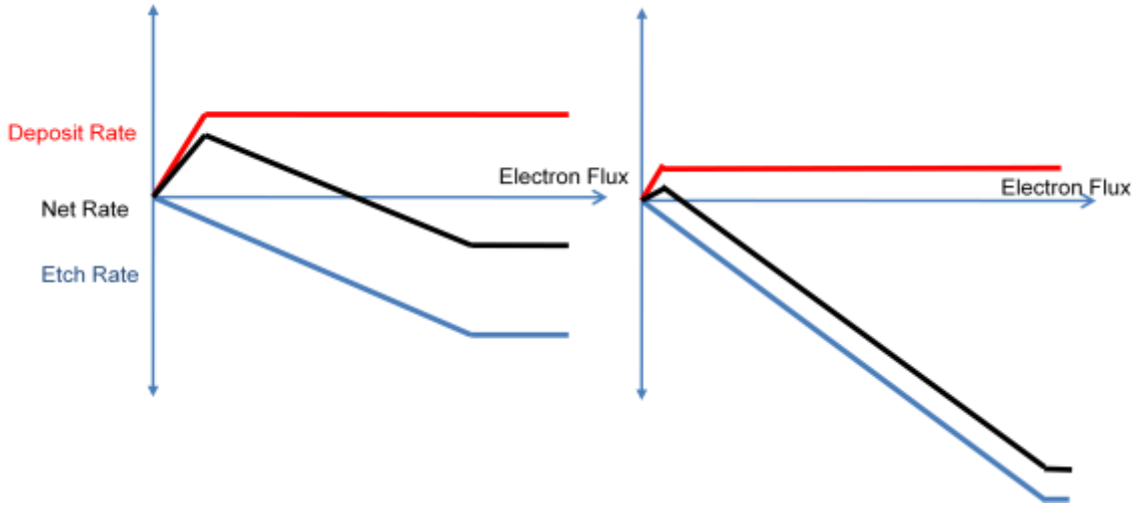

Figure 103: Deposition Rate, Etching Rate, and Net Rate versus Electron Flux

$$\tau_A = \frac{1}{\nu} e^{\frac{E_{ads}}{kT}}$$

Where ν is the fundamental vibrational frequency on the order of $10^{13}s^{-1}$. Using a published value of the energy of adsorption for water on carbon nanotubes of around 30kJ/mol, we arrive at a surface residence time about 15 nanoseconds. If we assume a site density around $10^{15}cm^{-2}$, then the middle term of the denominator in the etch rate equation (Z/τ_A) is around 6.4 x $10^{22}cm^{-2}s^{-1}$. The pressure of water in the chamber is 2.0 x 10^{-2} Pa, this corresponds to a molecular impingement rate around 9.6 x $10^{16}cm^{-2}s^{-1}$. Even using a sticking coefficient of 1.0, the first term in the denominator is very small compared to the second term, and so it can be ignored. Calculating a peak electron flux of about 8.5 x $10^{21}cm^{-2}s^{-1}$ for a 1nA beam at 20keV, the third term ($A_\sigma\Gamma_e$) is about an order of magnitude (or more depending on A_σ) less than (Z/τ_A), so the etch rate equation can be simplified to:

$$EtchRate \propto \frac{xA_\sigma\Gamma_e g I_A}{\left(\frac{Z}{\tau_A}\right)} = \frac{xA_\sigma\Gamma_e g I_A \tau_A}{Z}$$

Inspection reveals that the etch rate is proportional to the electron flux, the pressure, and the surface lifetime of the precursor gas molecule. This follows the observed experimental behavior. As the beam current increased, the electron flux increased and the etch rate increased. At lower pressures, we could not etch the CNTs because the rate was too low and it would not overcome the competitive deposition. Lastly, a different precursor with a longer surface residence time could be considered. Published values of the energy of adsorption for O_2 on carbon nanotubes are lower at about 18.5kJ/mol compared to H_2O at about 30kJ/mol. This is likely due to the permanent dipole nature of the H_2O molecule having a stronger van der Waals interaction force with the CNT than the non-polarized O_2 molecule. These correspond to surface residence times of about 15ns for H_2O and about 0.16ns for O_2. Based on the relationship described above, we expect that all else being equal, the etching rate using water would be 50-90 times faster than the etch rate using oxygen (depending upon the reaction stoichiometry). It is likely that this would never be able to overcome the competitive deposition, so oxygen was not tried as a viable precursor.

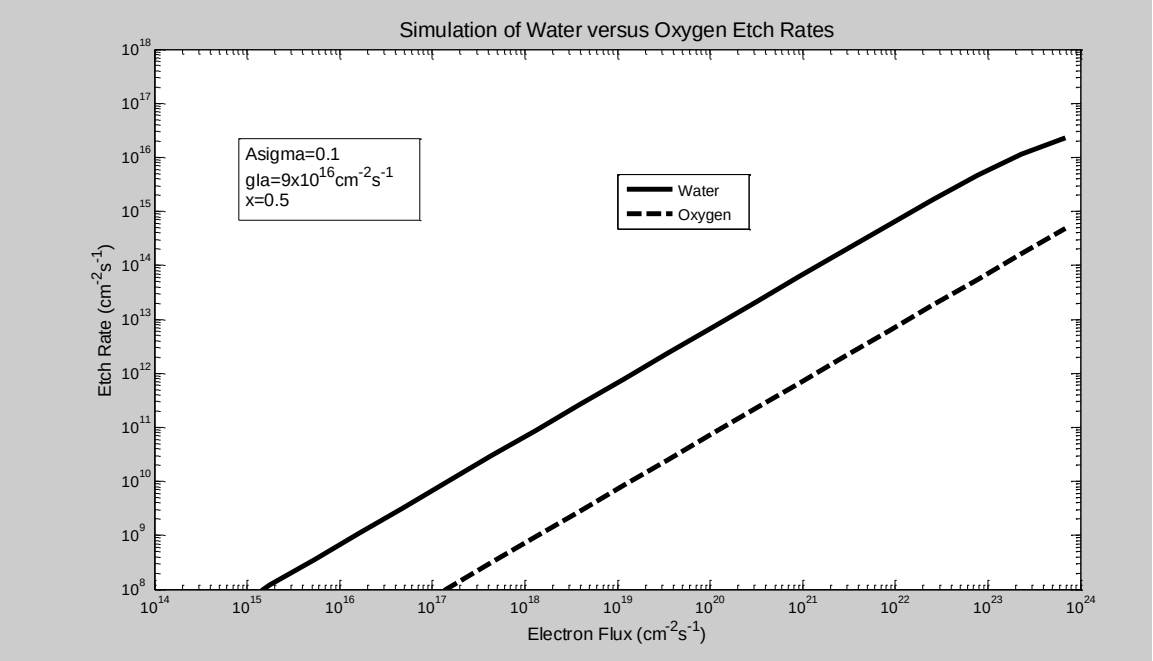

Figure 104: Comparison of Water versus Oxygen Precursors

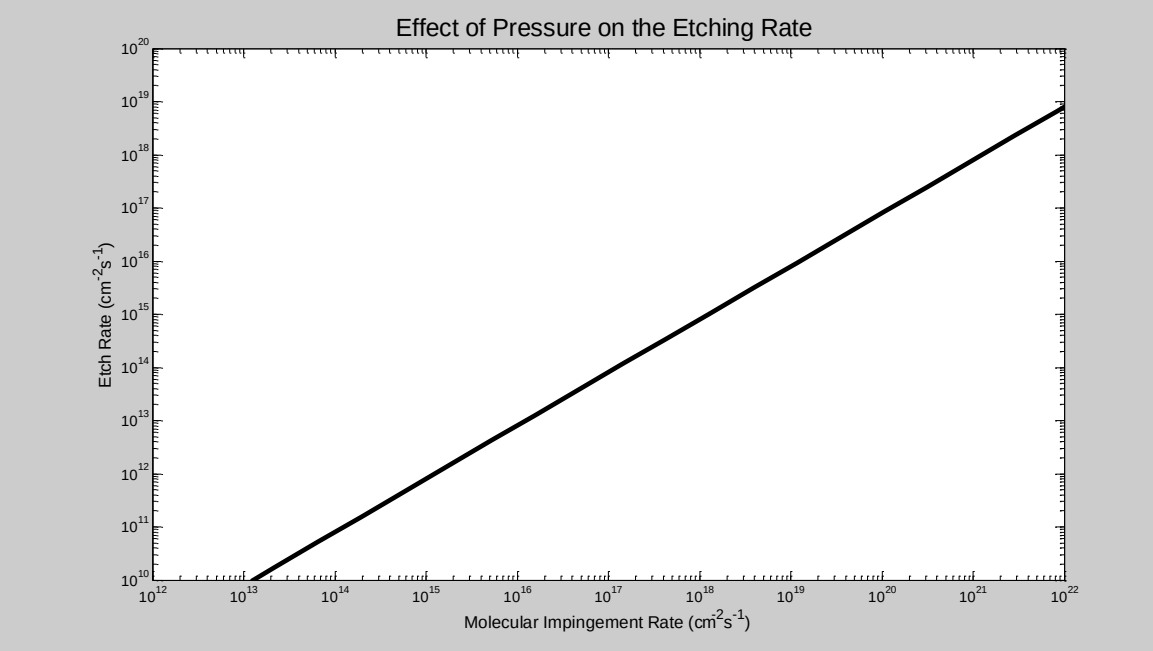

Figure 105: Effect of Pressure on the Etching Rate

Experimental Work

An initial experiment was conducted to determine the etching behavior as a function of beam current. Several CNTs of various sizes were cut by scanning the e-beam across the CNT at a high rate (30 loops per second) in a line scan mode. The secondary electron image was observed during the line scanning and the CNTs were observed to etch with an obvious endpoint where the secondary electron image becomes a flat line where the CNT was observed. Figure 106 illustrates a line scanning secondary electron image during etching and immediately after reaching end point.

The background pressure was maintained at 2.0×10^{-2} Pa, and the beam current was changed by adjusting the condenser lens in the SEM while the limiting aperture and working distance remained constant. The time to cut was observed by the end point of the secondary electron image during etching and the etch rate was calculated by dividing the diameter of the CNT by the time to cut. The results from this etching are plotted in Figure 107 below. Observe that the etch rate improves with increasing probe current. We assume that the probe size is diffraction limited and therefore the peak electron flux is proportional to the beam current. In this assumption, it is seen that the etching is electron flux limited, that is the reaction rate increases proportional to electron flux and does not reach a mass transport limited regime. That is not to say that under a fixed beam that a mass transport rate limited regime would not occur, but rather that the scanning rate is fast enough that the precursor does not deplete during the beam dwell time. Note that the y-axis (net deposit/etch rate) intercept is positive, indicating that there is a competitive deposition process that would dominate at low beam currents, and the behavior is similar to the theory described above. Also, it should be noted that these CNTs were cut in a relatively clean chamber that had been thoroughly cleaned of hydrocarbon contaminants.

Carbon containing species can be removed from the SEM chamber by the use of an EVACTRON™ cleaning system from XEI Scientific, Inc. (Figure 108). The system provides low power RF plasma to atmospheric gases leaked into the chamber through a metering valve. The low power plasma provides enough power to ionize and dissociate O_2 but not enough to do the same with N_2. This provides a supply of oxygen radicals to the chamber. XEI Scientific suggests a power setting of 14W forward RF power and a pressure of 0.4 Torr (~53 Pa) to maximize the creation of oxygen radicals. The oxygen radicals react with the mobile carbon-containing species in the chamber, forming carbon monoxide, carbon dioxide, water, and hydrogen molecules. These volatile gas species are subsequently pumped from the chamber by the vacuum system. The result is the removal of species from that chamber that lead to unwanted carbon deposition.

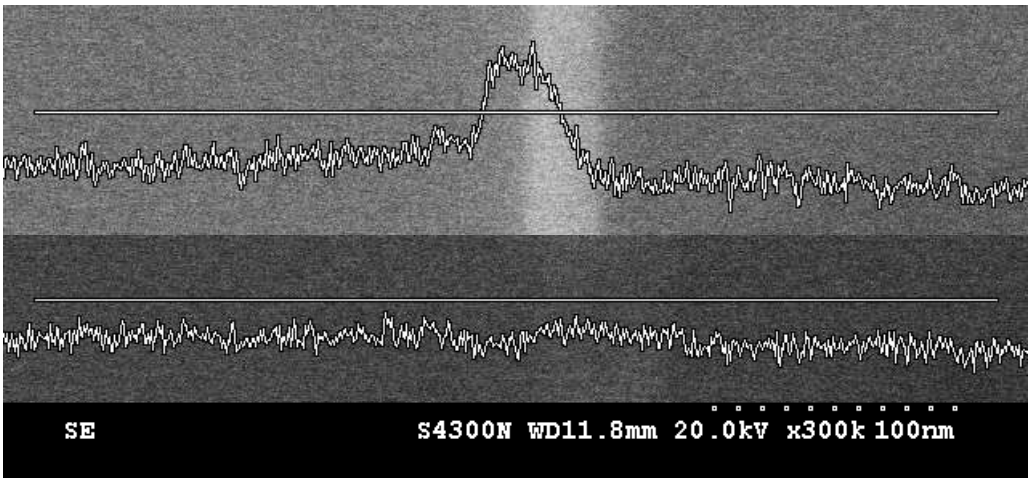

Figure 106: Secondary electron imaging example during line scanning across a CNT (top) and after CNT is cut (bottom)

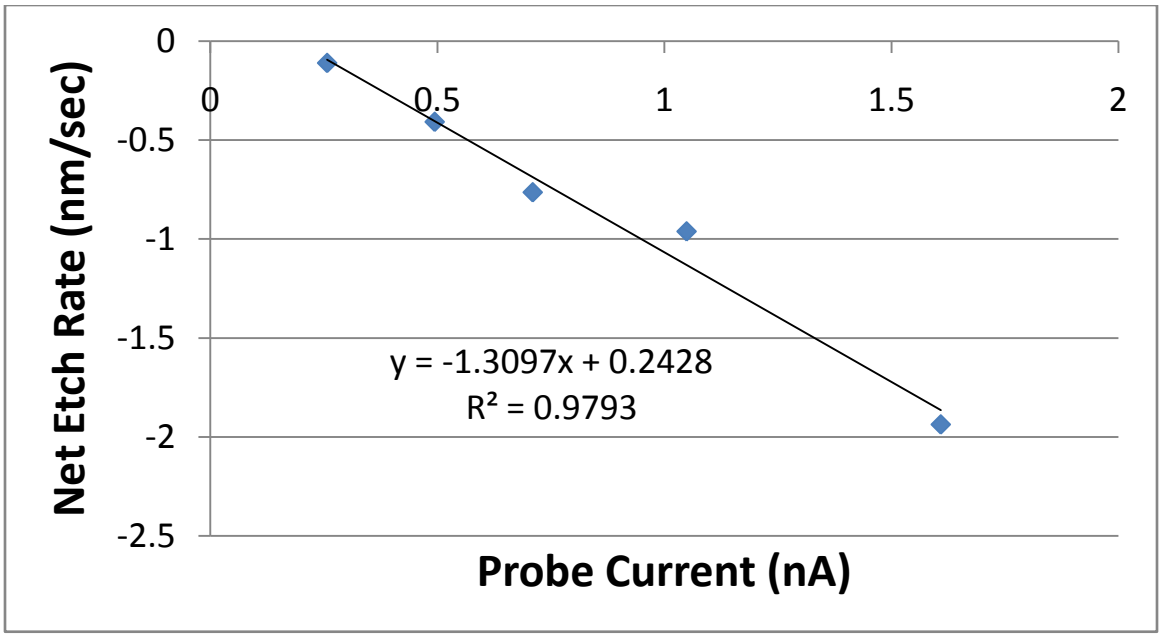

Figure 107: CNT etch rate versus beam current

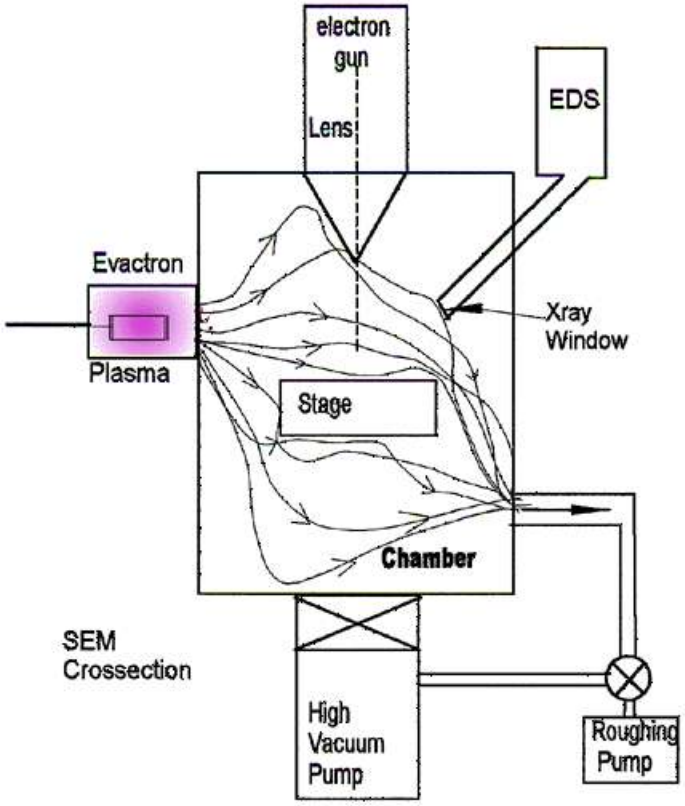

Figure 108: XEI Scientific EVACTRON™ System Schematic

In an effort to determine a reasonable range for the amount of EVACTRON™ cleaning time required to cut the CNTs, a single-factor experiment was performed with cleaning time while cutting a single CNT in multiple places. The entire SEM chamber was vented to atmosphere and the chamber doors opened and left to atmosphere for 1 hour. The system was then pumped to a base pressure of $5.0x10^{-4}$ Pa. The beam was set to a 100pA current at an energy of 20keV. The CNTs were cut at a chamber background pressure of $2.0x10^{-2}$ Pa of water, with the exception of the control run with zero water flow and a chamber background pressure of $5.0x10^{-4}$ Pa. The cutting time was 120 sec or CNT cut endpoint, whichever came first. The images of the processed CNTs are seen in Figure 109 below. Observe that for the control, a net deposit is observed due to the carbon contamination in the SEM chamber. With little or no cleaning, the competitive deposition is not overcome by the etch process, and a net deposit is observed. With sufficient cleaning time the CNT is able to be cut. The 4 minute cleaning time was chosen as the lower clean time for a subsequent full factorial design of experiments. The results from the initial cleaning time experiment are plotted in Figure 110.

A full factorial experiment was designed to investigate the effects of beam current, beam energy, and EVACTRON™ cleaning time. The experimental parameter space was as follows:

Beam Energy – 5keV, 12.5keV, 20keV

Beam Current – 10pA, 45pA, 80pA

Cleaning Time – 4min, 20min

The results indicate all three main effects are statistically significant. Also, there are two interactions with significance: Energy-Current and Energy-Cleaning Time. The main effects are plotted in Figure 111, and it can be seen that the beam current and cleaning time have strong linear effects. As expected, increasing the beam current gives a switching from net deposition to net etching. Increasing the cleaning time gives improved performance as the source of carbon contamination is reduced. The energy dependence shows a quadratic effect that likely is explained by the energy dependence of the dissociation probabilities of the deposit and etch precursors.

Based on the results of the designed experiment, processing conditions were chosen to maximize the beam current and use at least a 20 minute cleaning time. Since the brightness of the electron source is proportional to the accelerating voltage, a 20keV electron beam was used for continued experimentation to allow for as high a beam current as possible.

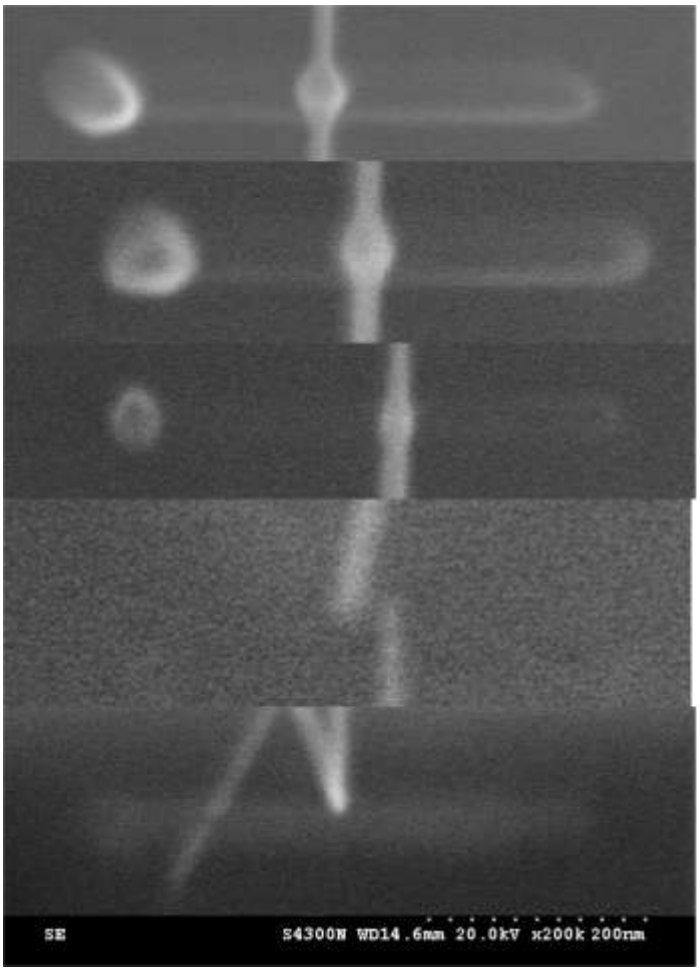

0min EVACTRON (0 flow of H_2O)
+38nm net deposit width on 17nm CNT
120sec process time

0min EVACTRON
+35nm net deposit width
120sec process time

1min EVACTRON
+15nm net deposit width
120sec process time

2min EVACTRON
-17nm net deposit width
90sec process time

4min EVACTRON
-17nm net deposit width
46sec process time

Figure 109: Initial EVACTRON™ Cleaning Experiment

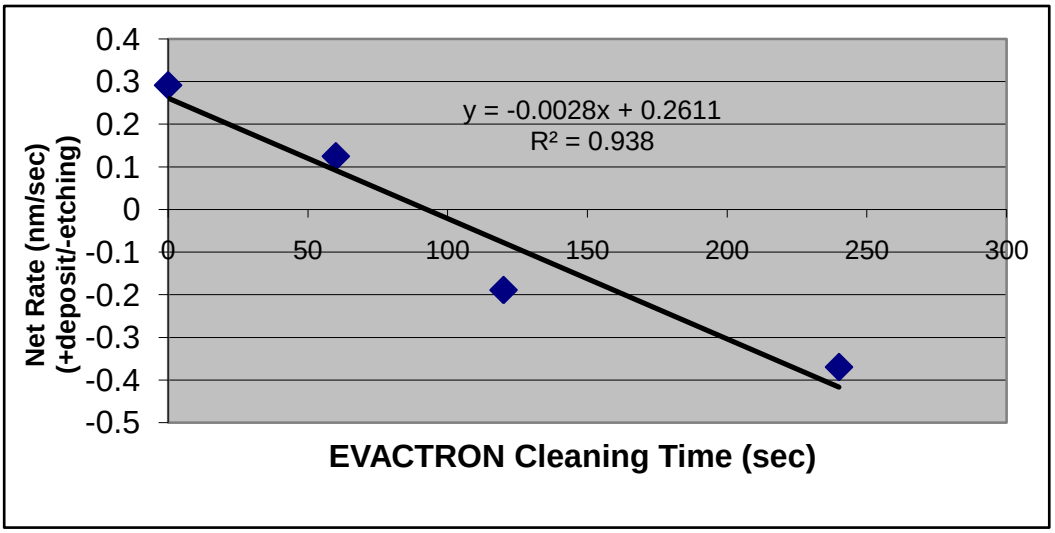

Figure 110: Initial EVACTRON™ Cleaning Experiment

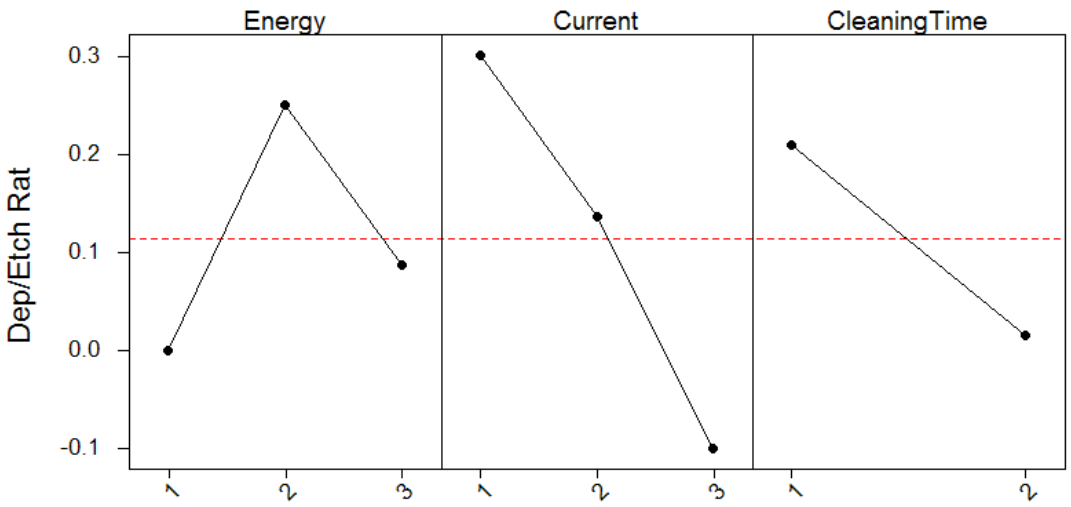

Figure 111: Main Effect Plot from Full Factorial DOE

Practical Considerations

Using a 754pA measured sample current at 20keV beam energy and a $2.0x10^{-2}$Pa of background water pressure; several different CNTs were cut on various occasions and various locations on the AFM cantilever. The time to cut each CNT varied widely based upon the size of the CNT. Often while attempting to cut two large CNTs beside each other, one will cut while the other will not. Small CNTs tend to cut rapidly. It is our speculation that there is some compositional differences between small CNTs and larger ones. The larger ones may contain some Si incorporated from the AFM cantilever during growth, this could significantly slow down or stop the etching process using water as the precursor gas, as no volatile molecule is formed with Si. Future research into cutting these CNTs should consider using fluorine based precursors with the aim of forming CF_x and SiF_x volatile etch products. Figures 112 through 115 show various CNTs before (top) and after cutting (bottom). Note that in each case the remaining CNT size has grown during the cutting process. We attribute this to the backscattered electrons and secondary electrons from the backscattered electrons emitting from the substrate in a large range as the beam is scanned.

We found that often some tubes did not cut after a considerable amount of time. The cause of this was most often drifting of the beam up and down the tube. As the beam drifts around the areas that had seen some etching would then see deposition as the beam drifted away and the electron flux lowered to a range where deposition dominates over etching. Care must be used to remove any mechanical drifting in the stage and the AFM tips and injection needle must be well grounded in order to eliminate any charging and subsequent beam drift. Once a steady beam is acquired, then CNT cutting is a fairly routine procedure. The time to cut the tube is roughly linear in relationship to the beginning size of the tube, as seen in Figure 116.

The variability in cutting time from tube to tube is not a difficulty due to the use of a visual end point. Figure 117 illustrates a time series of 1 minute intervals during the cutting of a CNT showing the size of the tube shrinking and the obvious endpoint signal.

The H_2O electron beam induced etching of carbon can be also be used to clean up areas of carbon debris from the surface of the silicon. An area can be scanned using same conditions as the CNT cutting and most of the carbon material in the field of view is cleaned within 10 minutes. Large CNTs in the field of view remain, as they would require a substantially longer period of time to etch under these conditions, considering that some deposition also occurs due to the electron range. Figures 118 and 119 illustrate 2 different size area cleans by a before and after image. The area inside the red dotted lines was scanned for 10 minutes, and then the wider image was captured to show that the non-scanned areas remain intact.

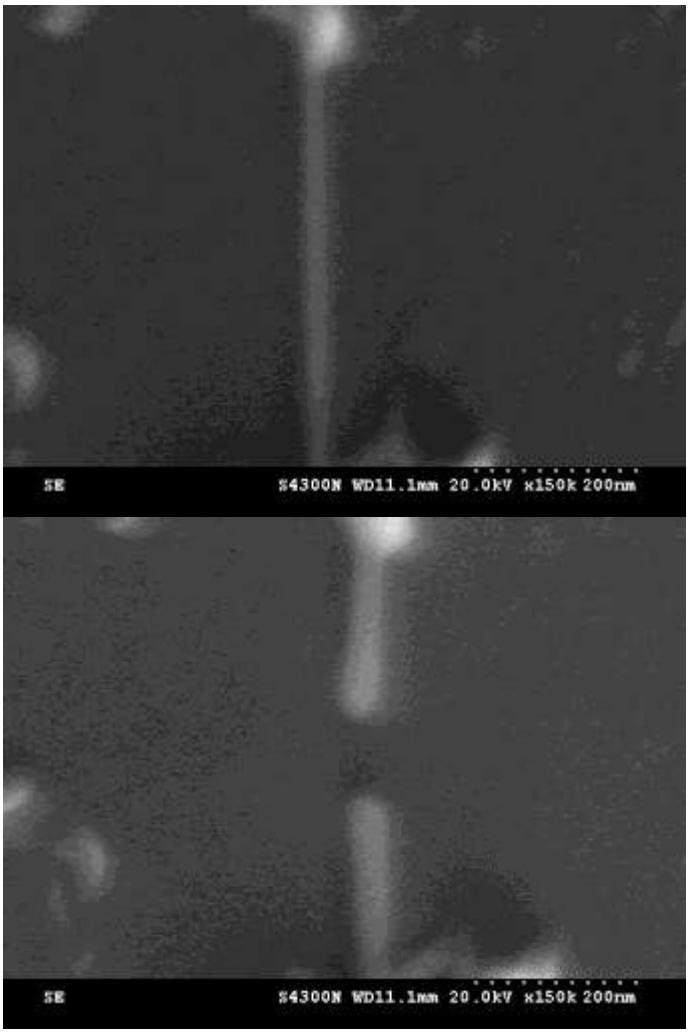

Figure 112: CNT Before and After Cutting

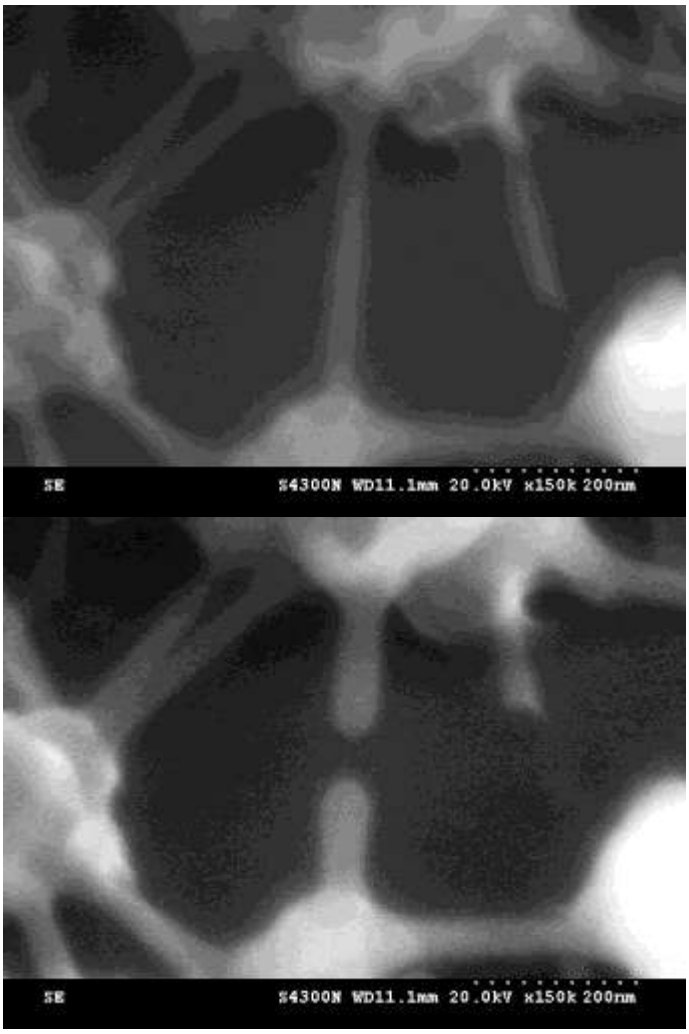

Figure 113: CNT Before and After Cutting

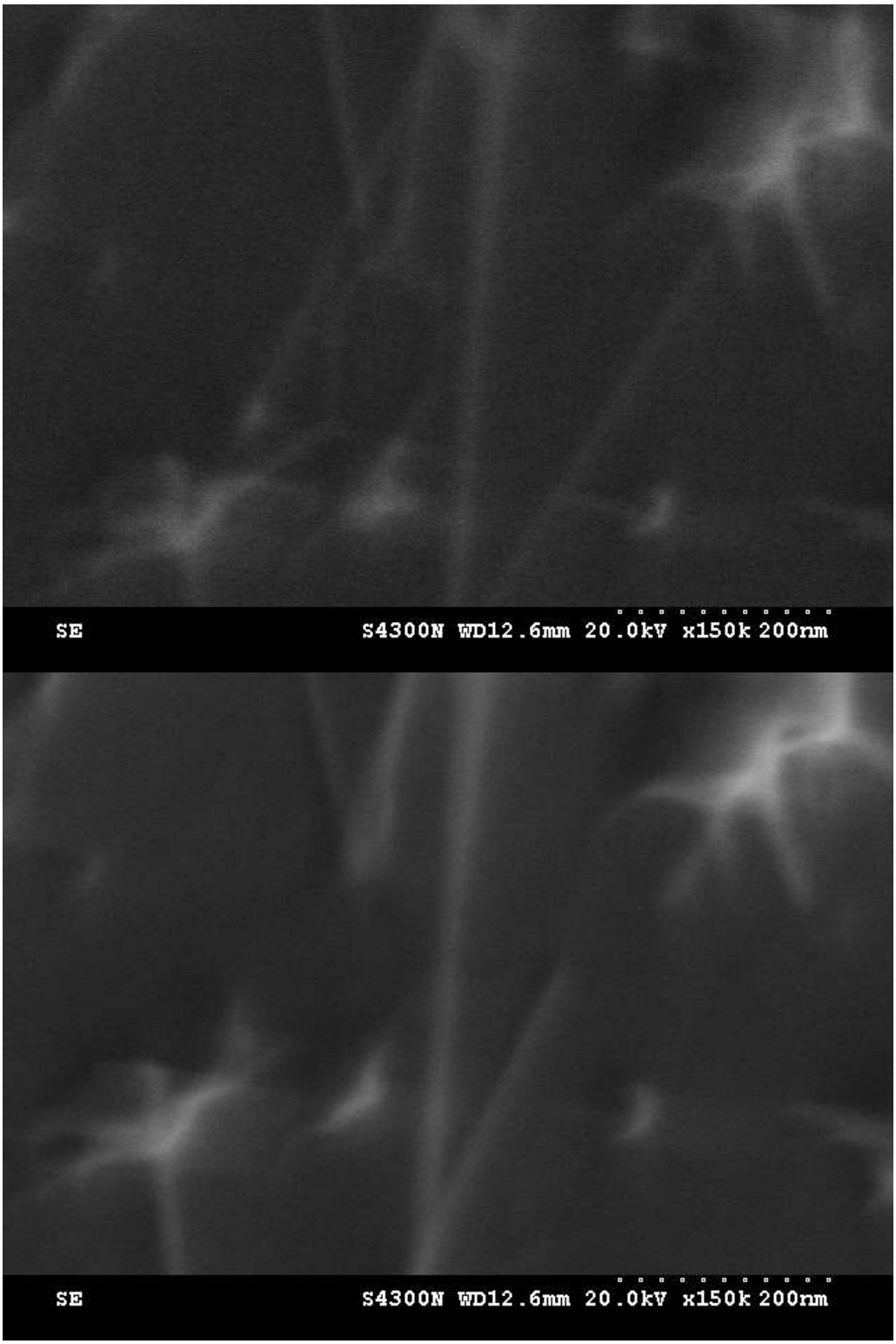

Figure 114: CNT Before and After Cutting

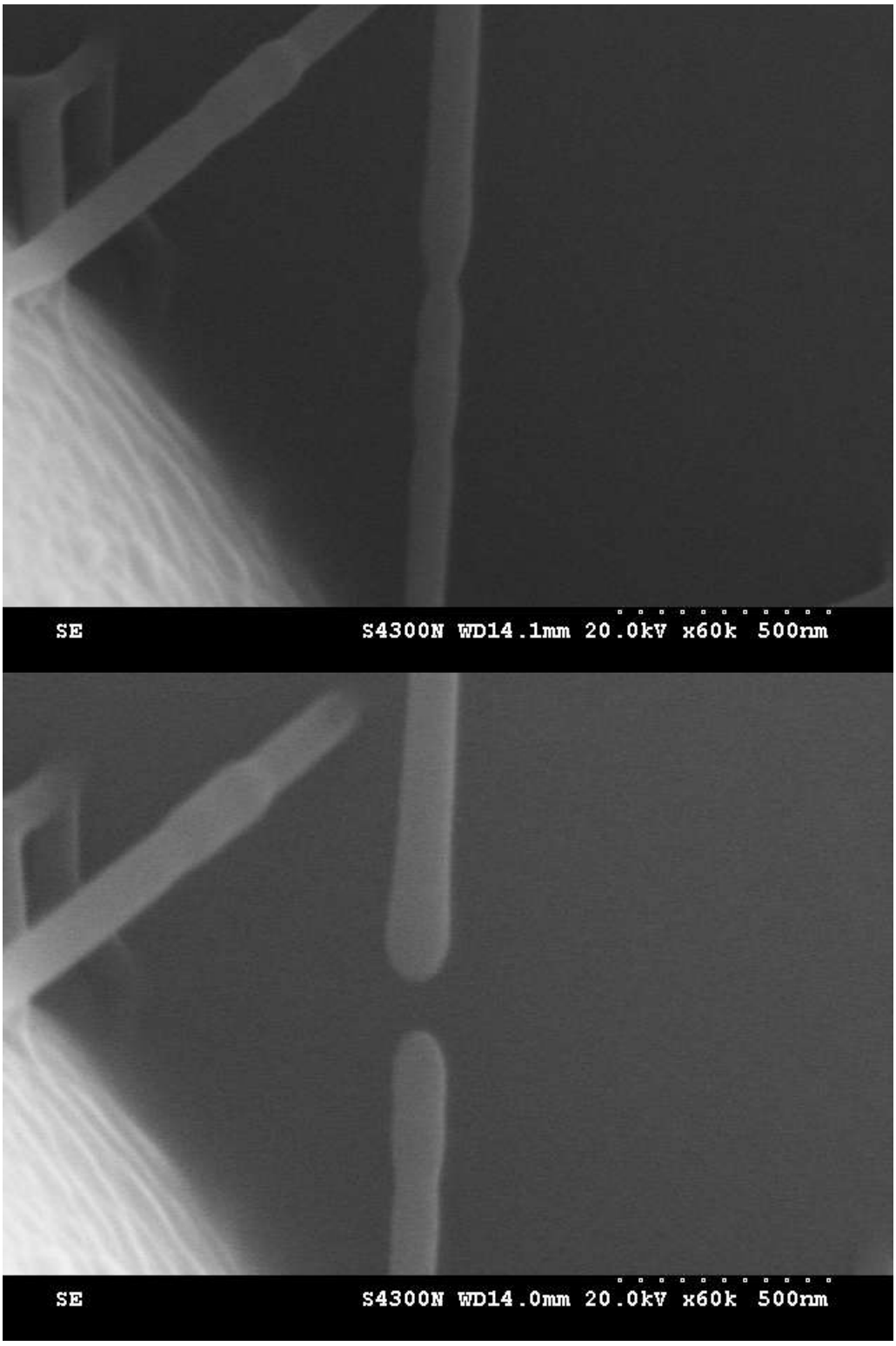

Figure 115: CNT Before and After Cutting

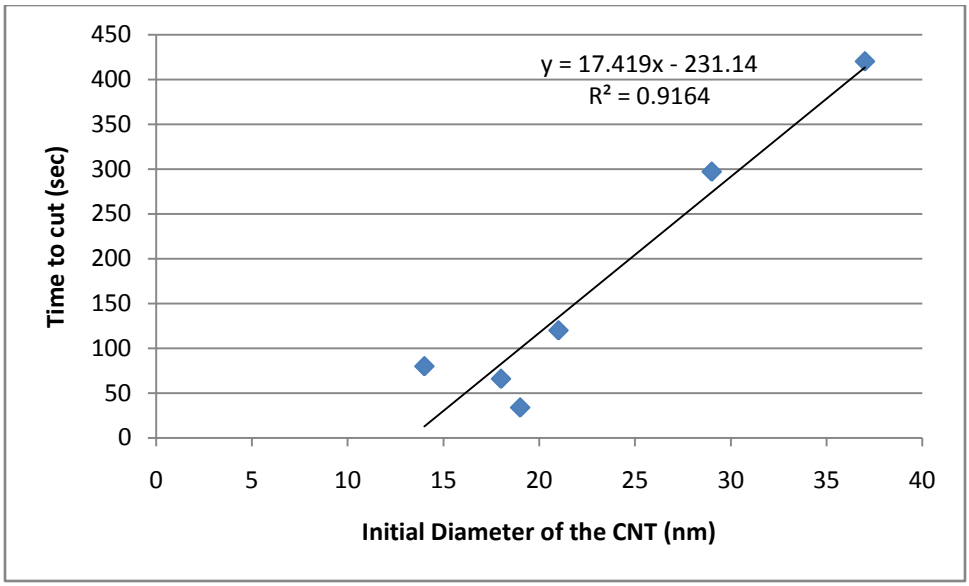

Figure 116: Relationship Between Time to Cut and the Initial Diameter of the CNT

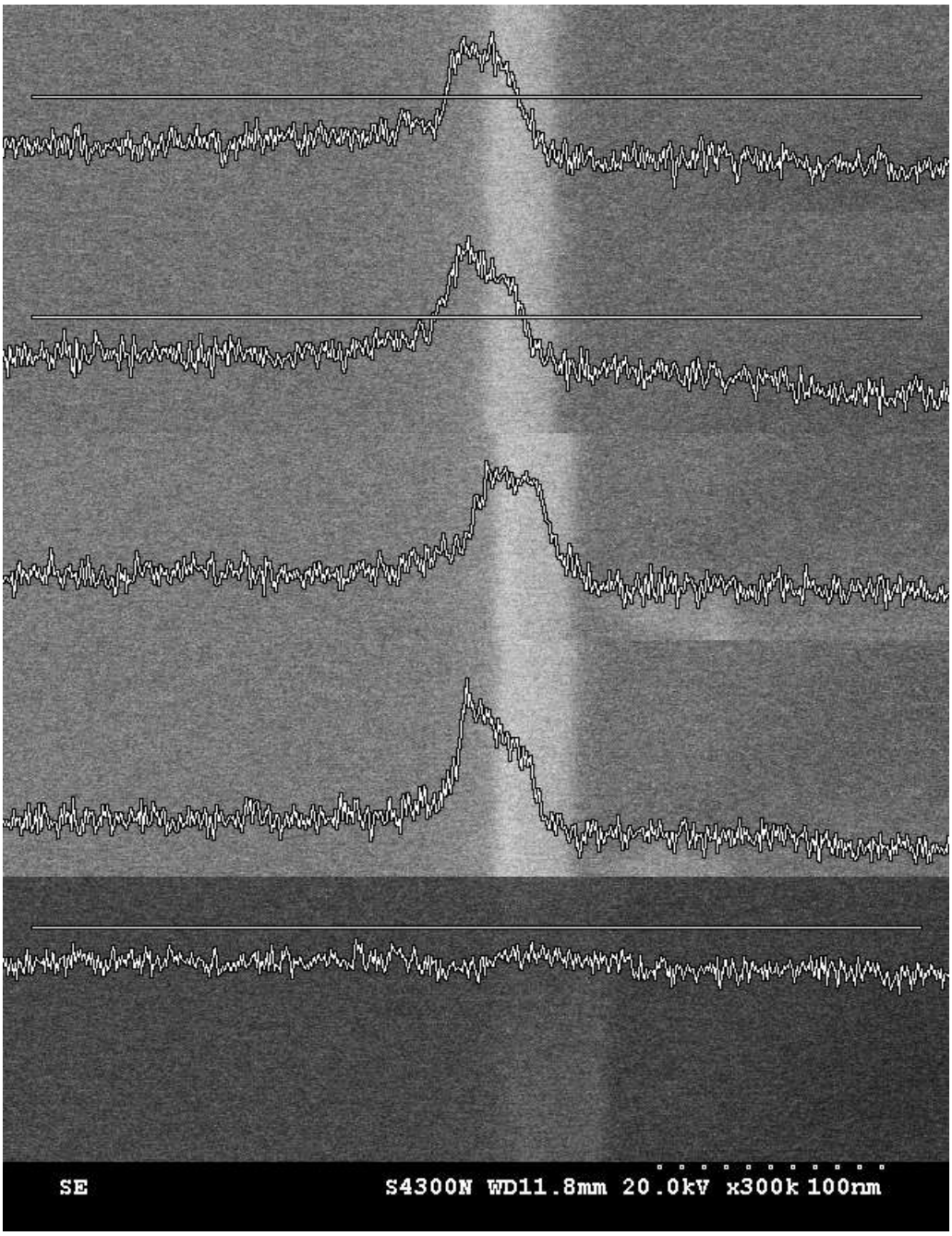

Figure 117: Progression of Line Scanning Secondary Electron Image Towards End Point

Figure 118: Before (top) and After (bottom) Area Cleaning

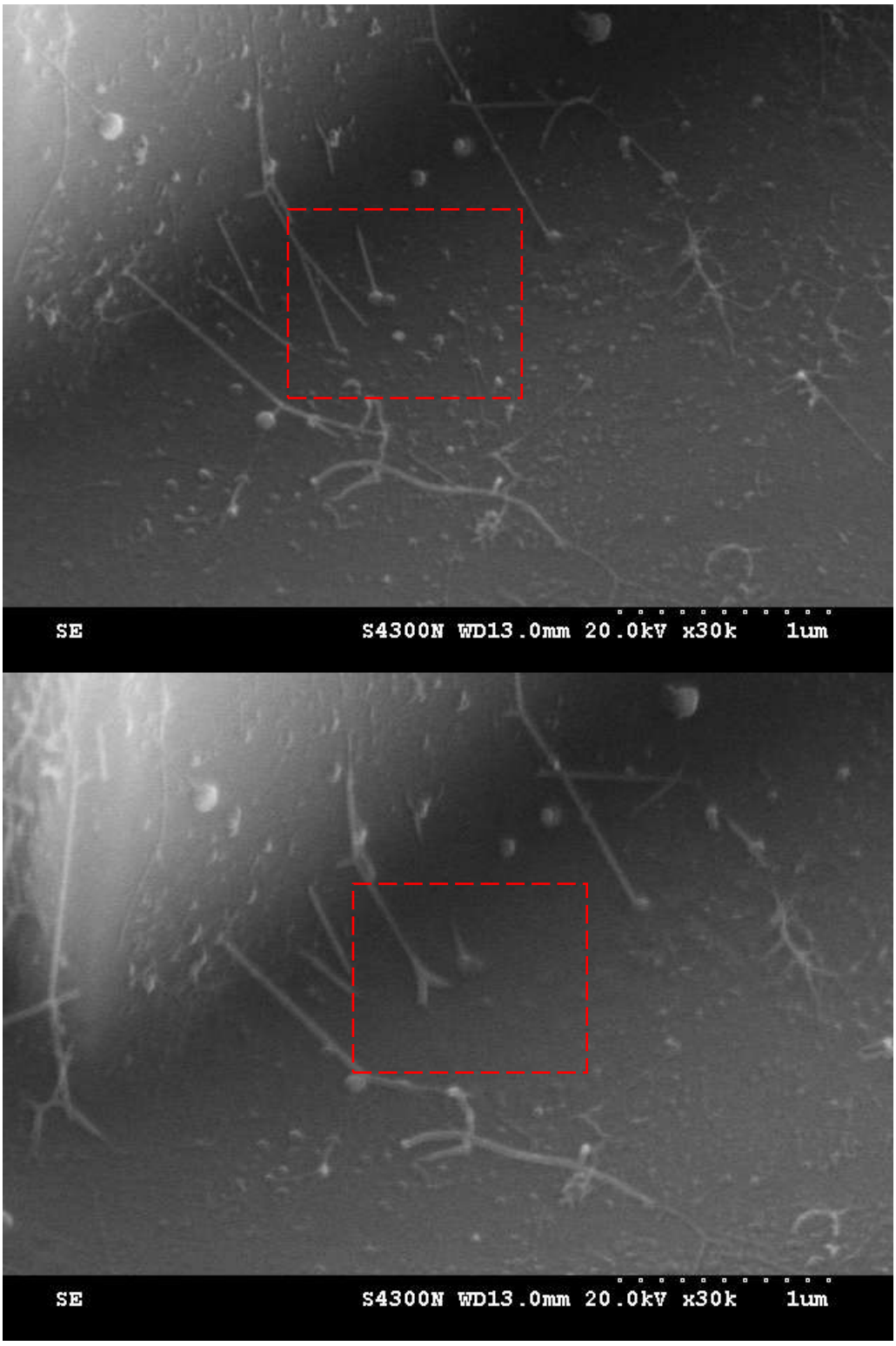

Figure 119: Before (top) and After (bottom) Area Cleaning

List of References

[1] I Utke, et al, *Journal Vacuum Science Technology B*, **25**, 6, 2007

[2] M Toth, et al, *Journal of Applied Physics*, **101**, 054309, 2007

[3] B Bokstein, et al, "Thermodynamics & Kinetics In Materials Science: A Short Course", Oxford University Press, 2005, pp. 99-100

[4] I Langmuir, "Monolayers on Solids", The Seventeenth Faraday Lecture, Delivered Before The Chemical Society on December 15th, 1938, published 1940.

[5] B Bokstein, et al, "Thermodynamics & Kinetics In Materials Science: A Short Course", Oxford University Press, 2005, pp. 212-213

[6] M Plischke, B Bergersen, "Equilibrium Statistical Physics", World Scientific Publishing, 2006, pp. 145

[7] Adapted from J. Hudson, "Surface Science: An Introduction"

[8] T. Hill, "An Introduction to Statistical Thermodynamics", Dover Publications, 1986, pp. 125-128

[9] D. Zill, M. Cullen, "Advanced Engineering Mathematics", PWS-Kent Publishing, 1992, pp. 693-724

[10] H Petzold, P Heard, *Journal Vacuum Science Technology B*, **9**, 5, 1991

[11] M Lassiter, T Liang, P Rack, *Journal Vacuum Science Technology B*, **26**, 3, 2008

[12] T Hill, "An Introduction to Statistical Thermodynamics", Dover Publications, 1986, pp. 125-128

[13] S Kasap, "Principles of Electronic Materials and Devices", McGraw Hill, 2006 pp. 47-49

[14] P Shewman, "Diffusion in Solids", TMS, 1989

[15] I Utke, et al, *Journal Vacuum Science Technology B*, **25**, 6, 2007

[16] S Kasap, "Principles of Electronic Materials and Devices", McGraw Hill, 2006 pp. 330

[17] D Langmuir, Proc. IRE, **25**, 977, 1938

[18] J Goldstein et al, "Scanning Electron Microscopy and X-ray Microanalysis", Springer Science, 2003, p. 48

[19] J Goldstein et al, "Scanning Electron Microscopy and X-ray Microanalysis", Springer Science, 2003, p. 50

[20] S Thornton, A Rex, “Modern Physics for Scientists and Engineers”, Saunders College Publishing, 1993, p. 179

[21] J Gaskill, “Linear Systems, Fourier Transforms, and Optics”, Wiley, 1978

[22] O Wells, “Scanning Electron Microscopy”, McGraw-Hill, 1974

[23] Y Novikov, A Rakov, I Stekolin, *Measurement Techniques*, **38**, 1, 1995

[24] M Bronsgeest, J Barth, L Swanson, P Kruit, *Journal Vacuum Science Technology B*, **26**, 3, 2008

[25] R Edgerton, P Crozier, *Micron*, **28**, 2, 1997

[26] M Bronsgeest, J Barth, L Swanson, P Kruit, *Journal Vacuum Science Technology B*, **26**, 3, 2008

[27] D Joy, CP 788, “Characterization and Metrology for ULSI Technology 2005”, AIP, 2005

[28] J Goldstein et al, “Scanning Electron Microscopy and X-ray Microanalysis”, Springer Science, 2003, p. 63

[29] H Bethe, *Ann. Phys.* (Leipzig), **5**, 325

[30] H Seiler, Secondary Electrons, “Journal of Applied Physics”, **54**, R1-R18, 1984

[31] J Goldstein et al, “Scanning Electron Microscopy and X-ray Microanalysis”, Springer Science, 2003, p. 93

[32] S Randolph, J Fowlkes, P Rack, *Critical Reviews in Solid State and Materials Sciences*, **31**, 55-89, 2006

[33] H Petzold, P Heard, *Journal Vacuum Science Technology B*, **9**, 5, 1991

[34] V Scheuer, H Koops, T Tschudi, *Microelectronic Engineering*, **5**, 423, 1986

[35] P Blauner, J Ro, Y Butt, J Melngailis, *Journal Vacuum Science Technology B*, **7**, 4, 1989

[36] M Toth, C Lobo, G Hartigan, W Knowles, *Journal of Applied Physics*, **101**, 054309, 2007

[37] M Lassiter, T Liang, P Rack, *Journal Vacuum Science Technology B*, **26**, 3, 2008

[38] M Lassiter, P Rack, *Nanotechnology*, **19**, 455306 (2008)

[39] I Utke, et al, *Journal Vacuum Science Technology B*, **25**, 6, 2007

[40] M Lassiter, P Rack, *Nanotechnology*, **19**, 455306 (2008)

[41] C Lobo, M Toth, R Wagner, B Thiel, M Lysaght, *Nanotechnology*, **19**, 025303, 2008

[42] S. J. Randolph, J. D. Fowlkes, P. D. Rack, *Critical Reviews in Solid State & Materials Science*, **31**, 3, pp. 55-89, 2006

[43] T. Liang, E. Frendberg, B. Lieberman, A. Stivers, *Journal of Vacuum Science and Technology B*, **23**, 6, pp. 3101-3105, 2005

[44] J. Wang, D. Griffis, R. Garcia, P. Russell, *Semiconductor Science and Technology*, **18**, 4, pp.199-205, 2003

[45] D. Smith, J. Fowlkes, P. Rack, *Nanotechnology*, **18**, 26, 2007

[46] K. Mitsuishi, Z. Q. Liu, M. Shimojo, M. Han, K. Furuya, *Ultramicroscopy*, **103**, 1, pp. 17-22, 2005

[47] N. Silvis-Cividjian, C. W. Hagen, P. Kruit, *Journal of Applied Physics*, **98**, 8, 084905, 2005

[7] J. D. Fowlkes, S. J. Randolph, P. D. Rack, *Journal of Vacuum Science and Technology B*, **23**, 6, pp. 2825-32, 2005

[49] H. -C. Petzold, P. J. Heard, *Journal of Vacuum Science and Technology B*, **9**, 5, pp. 2664-69, 1991

[50] F. G. Rudenauer, W. Steiger, D. Schrottmayer, *Journal of Vacuum Science and Technology B*, **6**, 1542, 1988

[51] P. G. Blauner, J. S. Ro, Y. Butt, J. Melngailis, *Journal of Vacuum Science and Technology B*, **7**, 609, 1989

[52] P. J. Heard, P. D. Prewett, *Microelectronic Engineering*, **11**, 421, 1990

[53] M. Toth, C. J. Lobo, G, Hartigan, W. R. Knowles, *Journal of Applied Physics*, **101**, 5, 054309, 2007

[54] C. J. Lobo, M. Toth, R. Wagner, B. L. Thiel, M. Lysaght, *Nanotechnology*, **19**, 025303, 2008

[55] I. Utke, V. Friedli, M. Purrucker, J. Michler, *Journal of Vacuum Science and Technology B*, **25**, 6, pp. 2219-23, 2007

[56] K. Rykaczewski, W. White, A. Federov, *Journal of Applied Physics*, **101**, 054307, 2007

[57] V. Friedli, C. Santschi, J. Michler, P Hoffmann, I. Utke, *Applied Physics Letters*, **90**, 053106, 2007

[58] F. Rugamas et al, *Meas. Sci. Technol*., **11**, 1750, 2000

[59] K. T. Kohlmann, M. Thiemann, W. H. Brunger, *Microelectronic Engineering*, **13**, 279, 1991

[60] H. F. Winters, J. W. Coburn, *Journal of Vacuum Science and Technology B*, **3**, 5, pp. 1376-83, 1985

[61] S. J. Randolph, J. D. Fowlkes, P. D. Rack, *Journal of Applied Physics*, **98**, 034902, 2005

[62] M. G. M. Vugts, G. J. P. Joosten, A. van Oosterum, H. A. J. Senhorst, H. C. W. Beijerinck, *Journal Vacuum Science Technology A*, **12**, 2999, 1994

[63] D. E. Ibbotson, D. L. Flamm, J. A. Mucha, V. M. Donnelly, *Applied Physics Letters*, **44**, 1129, 1984

[64] http:\\www.azom.com

[65] D. Smith, J. Fowlkes, P. Rack, *Nanotechnology*, **18** (2007)

[66] J. Hudson, "Surface Science: An Introduction", 1992

[67] M. G. Lassiter, T. Liang, P. Rack, *Journal Vacuum Science Technology B*, **26**, 3, 2008

[68] S. J. Randolph, J. D. Fowlkes, P. D. Rack, *Critical Reviews in Solid State and Materials Sciences*, **31**, 55-89, 2006

[69] T. Liang et al. *Proc. of SPIE* 5567-49, 2004

[70] Klaus Edinger et al., *Journal of Vacuum Science Technology B*, **22**, 6, 2004

[71] M. J. M. Vugts, G. J. P Joosten, A. van Oosterum, H. A. J. Senhorst, H. C. W. Beijerinck, *Journal of Vacuum Science & Technology A*, **12**, 6, 1994, pp. 2999-3011

[72] Ibbotson, D. E.; Flamm, D. L.; Mucha, J. A.; Donnelly, V. M.; *Appl. Phys. Lett*. **44**, 1129, 1984

[73] Sewell, P. B.; Mitchell, D. F.; Cohen, M.; *Surface Science*, **29**, 1972, pp. 173-188

[74] Toth, M.; Lobo, C.J.; Hartigan, G.; Knowles, W.R., *Journal of Applied Physics*, **101**, 5, 2007, p 54309-1-6

[75] Rack, P.D.; Randolph, S.; Deng, Y.; Fowlkes, J.; Choi, Y.; Joy, D.C. Source: *Applied Physics Letters*, **82**, 14, 2003, p 2326-8

[76] Rugamas, F.; Roundy, D.; Mikaelian, G.; Vitug, G.; Rudner, M.; Shih, J.; Smith, D.; Segura, J.; Khakoo, M.A. *Measurement Science & Technology*, **11**, 12, 2000, p 1750-65

[77] Kohlmann, K.T.; Thiemann, M.; Brunger, W.H. *Microelectronic Engineering*, **13**, 1-4, 1991, p 279-82

[78] S. J. Randolph, J. D. Fowlkes, P. D. Rack, *Journal of Applied Physics*, **98**, 034902, 2005

[79] T. E. Madey, J. T. Yates, Jr., *Journal of Vacuum Science Technology*, **8**, 4, 1971

[80] T. D. Yuzvinsky, A. M. Fennimore, W. Mickelson, C. Esquivias, A. Zettl, *Applied Physics Letters*, 86, 053109 (2005)

[81] M. Toth, C. Lobo, G. Hartigan, W. Knowles, *Journal of Applied Physics*, **101**, 054309 (2007)

Vita

Matthew Gordon Lassiter was born December 3, 1976 in Winston-Salem, North Carolina. He earned his B.S. in Microelectronic Engineering in 2000 at the Rochester Institute of Technology in Rochester, New York. After working in semiconductor research and development in Austin, Texas and Dallas, Texas, he moved in 2006 to Knoxville, Tennessee to pursue a PhD in Materials Science and Engineering at the University of Tennessee - Knoxville. He completed the PhD in August 2009, and he is currently working as a post-doctoral fellow for Professor Philip D. Rack at the University of Tennessee – Knoxville. Matthew and his wife Melissa were married in 1998. They have two children: Zachary born in 2002 and Samuel born in 2004, adopted in 2005.